FACULTY OF SCIENCES

Superconducting $YBa_2Cu_3O_{7-\delta}$ nanocomposite films using preformed metal oxide nanocrystals

Hannes Rijckaert

Supervisor: Prof. Dr. Isabel Van Driessche

A dissertation submitted to Ghent University in partial fulfilment of the requirements for the degree of Doctor in Sciences: Chemistry

Academic year: 2017 - 2018

GHENT UNIVERSITY

Universiteit Gent
Faculteit Wetenschappen
Vakgroep Chemie

Promotor
Prof. Dr. Isabel Van Driessche

Leden van de Jury	Affliatie
Prof. Dr. Klaartje De Buysser	Ghent University
Dr. Katrien De Keukeleere	Ghent University
Prof. Dr. Christophe Detavernier	Ghent University
Prof. Dr. Ir. Roumen Petrov	Ghent University
Prof. Dr. Pieter Vermeir	Ghent University
Prof. Dr. Petriina Paturi	University of Turku
Prof. Dr. Michael Bäcker	Deutsche Nanoschicht GmbH
Dr. Glenn Pollefeyt	Dow Benelux B.V.

Universiteit Gent
Faculteit Wetenschappen

Vakgroep Chemie
Krijgslaan 281 S3 B-9000 Gent, België

Tel.: +32-9-264.44.49
Fax.: +32-9-264.49.83

Proefschrift tot het behalen van de graad van
Doctor in de Wetenschappen:
Chemie
Academiejaar 2017-2018

I have no special talents.
I am only passionately curious

Albert Einstein

This dissertation is dedicated to my auntie Rita and unkie Marnix.
My lovely family who untimely passed away.

Dankwoord

Negen jaar geleden startte ik mijn hoger onderwijs aan de Universiteit Gent. Biochemie & biotechnologie was mijn keuze. Mijn allereerste les in auditorium 2 van de Ledeganck was Algemene Chemie van Prof. Dr. Isabel Van Driessche. Meteen kreeg ik in de eerste les al haar slides uitgeprint. Je wou me toen reeds alle kansen geven. Naarmate het academiejaar vorderde werd ik er mij van bewust dat ik biochemie zou ruilen voor een technisch gekleurde opleiding chemie omdat de Master Industrieel Ingenieur de mogelijkheid bood om "Supergeleidende Materialen" op te nemen als keuzevak. Ik was zo geboeid door deze materie dat ik solliciteerde voor een onderzoek in dit domein en voor ik het goed en wel besefte, mocht ik mij een "doctoraatsstudent supergeleiding" van Isabel noemen. Ik kan het moeilijk uitdrukken hoe dankbaar ik ben voor de kans die je me gaf en het vertrouwen dat ik de voorbije vier jaar kreeg van jou als promotor. Mijn oprechte dankjewel voor jouw enthousiasme en inzet om het maximum uit ons onderzoek te halen. Ik kan niet genoeg benadrukken hoe belangrijk je bent voor m'n wetenschappelijke loopbaan. Bij deze kan ik vermoeden wat je nu denkt: "Op naar de volgende uitdaging, Hannes!".

Deel uitmaken van 'SCRiPTS' is een hele eer. De collega's binnen deze onderzoeksgroep zijn niet alleen hele competente wetenschappers maar zijn in de loop van de jaren ook echte vrienden geworden. Eerst en vooral zijn er de mensen die een grote invloed hadden in mijn vierjarige queeste. Dr. Feys, jij was de eerste die mij heeft geleerd welke vaardigheden ik zou nodig hebben om genietend te overleven in de wereld van een doctoraatsonderzoek. Tot mijn grote spijt ben je reeds na een paar maanden weggegaan. Glenn, een dankjewel is vandaag eigenlijk veel te weinig want door jou ben ik een gedreven onderzoeker geworden. De TEM en FIB skills die je mij doorgegeven hebt zijn van onschatbare waarde gezien de vele uren die ik aan de FIB en TEM doorgebracht heb. Je wil echt niet weten hoeveel TEM lamella ik ondertussen gemaakt heb! Een zitje in m'n doctoraatsjury heb je zeker verdiend… al was het wel even schrikken toen ik jouw commentaren/suggesties las. Katrien, ook jij was een evidentie in mijn doctoraatsjury want "zonder nanodeeltjes, geen nanocomposiet laag". Jouw fundamenteel wetenschappelijke en persoonlijke bijdragen hebben mijn onderzoek naar een hoger niveau gebracht. Een dikke merci hiervoor! JJ, we zijn samen aan een doctoraat begonnen en hebben ondertussen al het één en ander meegemaakt (niet alleen op het minivoetbal). Dankjewel voor jouw vriendschap en reisadviezen! Joni aka Dr. Gincubator, met jou op een conference heb ik nog nooit zoveel gegeten en zoveel gedronken! Een luisterend oor en altijd paraat met een gepast advies op mijn vaak storende en lastige vragen/frustraties.

Vazeel, moet ik nog altijd jouw nanorods gaan bekijken? ’t Was ook fijn om met jou samen te werken, hopelijk kunnen wij iets uit SIMS halen. Kennyyyy, jouw enthousiasme is zo aanstekelijk dat ik altijd vrolijk word als ik jou zie. Wanneer is er nog eens een teambuilding? Mieke, dankjewel voor al jouw steun tijdens mijn doctoraat. Ik waardeer dat ten zeerste! Jonathan, het is ongelofelijk hoe je steeds weer een andere kijk hebt op al die wetenschappelijke artikels. Dankzij jou heb ik veel bijgeleerd over hoe een wetenschappelijk artikel te schrijven. Klaartje, dankjewel voor al jouw wetenschappelijk advies en de korte maar inhoudelijk sterke babbels! Jan aka Hitman, you are the rookie of the SCRiPTS team but I’m very glad that we share the office because we always have a small or big talk about everything every morning, afternoon, …. Thank you for motivating me to speak English and to write my PhD without using ghostwriter. You are an amazing and trustworthy friend!

Tijdens mijn doctoraat heb ik ook geluk gehad dat er extra helpende krachten kwamen van bachelor- en masterstudenten. Jelle, jouw onverzettelijke wilskracht heeft tot een geprinte supergeleidende laag geleid wat zeker één hoofdstuk waard is in dit manuscript. Sidney, onze dip-coating master. Het was zeer plezant om met jou samen te werken, te discussiëren, … . Ik vond het heel jammer dat je niet bleef maar Innologic heeft er nu alvast een toponderzoeker bij. We eten zeker nog eens samen een KFC bucket voor twee personen en niet voor vier personen! Ewout en Kasper, mijn meest energieke bachelorstudenten. Het was fijn om jullie te mogen begeleiden, ook al was het maar voor een korte periode. Wie weet in de toekomst voor een langere periode? Ik kijk er alvast naar uit!

During my PhD research, I had the opportunity to collaborate with different people in various European countries. In particular I want to thank my advisors, colleagues and friends from the superconductor world, both in Finland and in Germany. Many thanks to Mika Malmivirta, Dr. Hannu Huhtinen and Prof. Dr. Petriina Paturi from the Wihuri Physical Laboratory for the warm welcome during my (very cold) stay at Turku and the large number of magnetically measurements. Mika, I hope you have already found the sample which was magically disappeared in the cleanroom. And of course, the most important of all are the people from Deutsche Nanoschicht because without them, I would not have achieved the same level of results during my PhD research. If I look at the sample database, I noticed that I have sent more than 400 samples to Deutsche Nanoschicht for several measurements. Sorry for giving you such a lot of work but thank you very much! Special thanks to Prof. Dr. Michael Bäcker, Dr. Martina Falter, Dr. Jan Bennewitz and Dr. Mark Rikel for the fruitful collaboration and giving me the opportunity to become part of Deutsche Nanoschicht! I'm looking forward to work with all of you in the follow-up project, SynFoNY. This SynFoNY was an idea of Dr. Maximilian Hemgesberg and it is a pity that he left us. Max, you were a reliable person that I could always count on. It was amazing to work with you and thank you for your confidence in me. This PhD is also thanks to you and I hope we meet again one day. Max Sieger, the PLD-guy from IFW

Dresden, you appeared during my PhD research and helped me a lot with the transport measurements. I cannot thank you enough because you brought me in contact with Dr. Jens Hänisch from Karlsruhe institute technology. Jens, I want to thank you for sharing your infinite knowledge concerning pinning properties! You have opened a new world for me and improve my articles/results. I'm glad to have the opportunity to work with you again in several follow-up projects.

Het zou een schande zijn mocht ik het administratieve en technische personeel vergeten. Ze zijn het kloppend hart van S3. Balt voor zoveel keren de gasflessen te vervangen en voor het oplossen van mijn technische problemen (Lees: mijn fiets). Pat en Kathleen voor de vele aangename gesprekken in de vroege ochtend. Katrien H. en Funda voor jullie interesse in mijn onderzoek. Pierre voor al die administratie en al die onvergetelijke momenten! Tom, omdat je juist Tom bent! Allemaal een dikke merci voor alle hulp, de vele leuke momenten samen en jullie vriendschap. Jullie zijn nog niet van mij af! Dankjewel Vitaliy en Liesbet voor de goede zorg en onderhoud van de TEM en FIB. Sandy, Hannes DP & Jeroen van de onderzoekgroep COMOC, dankjewel voor zoveel leuke babbels en zoveel meer! Also thanks to Fady for sharing the office and for your friendship! Ik weet dat ik niet iedereen expliciet heb genoemd die direct of indirect hebben bijgedragen aan het succes van mijn doctoraat en daarom aan al deze mensen, mijn oprechte dank!

I would also like to thank the members of the dissertation jury for their suggestions, comments and relevant remarks for improving my manuscript: Prof. Dr. Klaartje De Buysser, Prof. Dr. Isabel Van Driessche, Dr. Katrien De Keukeleere, Prof. Dr. Christophe Detavernier, Prof. Dr. Pieter Vermeir, Prof. Dr. Ir. Roumen Petrov. Prof. Dr. Michaël Bäcker, Prof. Dr. Petriina Paturi and Dr. Glenn Pollefeyt. I hope you somewhat enjoyed reading this work and hopefully we can work together in the future.

Er is ook natuurlijk ook een leven naast het werk. Dankjewel aan alle vrienden Jakob, Johan, Michael, Christof, … voor jullie jarenlange vriendschap, interesse en veel leuke momenten samen. Mijn oud medestudenten die ondertussen al ver wonen, ééntje in Zuid-Afrika, de andere in Zwevegem. Luke en Niels kan ik niet genoeg bedanken voor al hun interesse, aanmoedigingen, eindeloze discussies en ontspannende gesprekken.

De Laatste, en zeker niet de minste die ik hier zou willen bedanken is m'n familie. Mama, papa, ik weet dat ik niet altijd een modelleerling was tijdens m'n prille schooljaren maar dankzij alle kansen die jullie mij gaven kon ik mijn opleiding met succes afwerken met op een einde van de rit een doctoraat in de wetenschappen. Zonder jullie, zou ik dat nooit verwezenlijkt hebben. Daar blijf ik jullie eeuwig dankbaar! M'n broer Jorn, ik heb nu mijn doctoraat afgewerkt, het is nu aan jou om jouw eerste film af te werken. Ik kijk er al naar uit!

Dan rest mij nog de belangrijkste persoon te bedanken: m'n vriendin Nathalie, zonder jou was alles wel wat chaotischer verlopen. Bedankt om er altijd voor mij te zijn, mij te steunen waar nodig en me een zetje te geven wanneer ik het kon gebruiken. Ik kijk al uit naar onze volgende hoofdstukken samen met onze katjes Lily en Pumba. Ik zie je graag!

Kortom, dankjewel aan iedereen!

Hannes Rijckaert, december 2017

List of Acronyms

AFM	-	Atomic-force microscopy
APCs	-	Artificial pinning centers
ATR-IR	-	Attenuated total reflection-infrared
BnO	-	Benzyl alcohol
BSC	-	Bardeen Cooper Schrieffer
BSSC-2223	-	$Bi_2Sr_2Ca_2Cu_3O_{10+\delta}$
CCs	-	Coated conductors
CSD	-	Chemical solution deposition
D	-	Dimension
DAA	-	Diacetone alcohol
DLS	-	Dynamic laser scattering
d-Nano	-	Deutsche Nanoschicht
DOD	-	Drop-op-demand
DOSY	-	Diffusion-ordered spectroscopy
DTA	-	Differential thermal analysis
EDX	-	Energy-dispersive x-ray
FFT	-	Fast Fourier transform
FIB-SEM	-	Focused ion beam-scanning electron microscopy
FWHM	-	Full width at half maximum
GC-MS	-	Gas chromatography–mass spectrometry
HAADF	-	High-angle annular dark-field
HMBC	-	Heteronuclear multiple-bond correlation spectroscopy
HRTEM	-	High-resolution transmission electron microscopy
HSQC	-	Heteronuclear single-quantum correlation spectroscopy
HTS	-	High temperature superconductor
HU	-	Heating-up
IBAD	-	Ion beam assisted deposition
ICP	-	Inductively coupled plasma
iPr	-	Isopropanol
ISD	-	Inclined substrate deposition
LF	-	low-fluorine
LTS	-	Low temperature superconductor
LZO	-	$La_2Zr_2O_5$
M	-	Molariteit
ME	-	2-methoxyethoxide
MEE	-	2-(2-methoxyethoxy)ethoxide
MO	-	Mesityl oxide
MOCVD	-	Metal-organic chemical vapor deposition
MOD	-	metal- organic deposition
MRI	-	Magnetic resonance imaging
MW	-	Microwave
Ni5W	-	5 at-% W in Ni
NMR	-	Nuclear magnetic resonance

nOe	-	Nuclear Overhauser effect
NOESY	-	Nuclear Overhauser effect spectroscopy
Oct	-	1-Octanol
OES	-	Optical emission spectrometry
Oh	-	Ohnesorge number
OPiT	-	Oxide powder in tube
PLD	-	Pulsed laser deposition
PPMS	-	Physical property measurement system
RABiTS	-	Rolling-assisted biaxial texture substrate
RE	-	Rare earth
SAED	-	Selected area electron diffraction
SEMS	-	Superconducting magnetic energy storage system
SF	-	Stacking faults
SF104	-	Surfactis™ 11-104
STEM	-	Scanning transmission electron microscopy
STO	-	$SrTiO_3$
TOF-SIMS	-	Time-of-flight secondary ion mass spectrometry
TEM	-	Transmission electron microscopy
TFA	-	Trifluoroacetate
TFAA	-	Trifluoroacetic acid anhydride
TFAH	-	Trifluoroacetic acid
TGA	-	Thermogravemetric analysis
TOPO	-	Tri-*n*-octylphosphine oxide
XRD	-	X-ray diffraction
XPS	-	X-ray photoelectron
Y124	-	$YBa_2Cu_4O_8$
Y247	-	$Y_2Ba_4Cu_7O_{15}$
YBCO	-	$YBa_2Cu_3O_{7-\delta}$

Content

Nederlandse samenvatting

-Summary in Dutch-

De bezorgdheid van de mensen over de opwarming van de aarde en het grote tempo waarmee de wereldbevolking groeit hebben wetenschappers ertoe aangezet hernieuwbare elektrische energie te ontwikkelen en nieuwe technologieën te vinden met een minimale uitstoot van koolstofdioxide. Technologieën die gebruik maken van hoge-temperatuur supergeleiding hebben de mogelijkheid om de elektriciteit zonder weerstand te vervoeren. Bovendien maken hun superieure eigenschappen het mogelijk om generatoren te produceren met een hoger vermogen dan de conventionele gebruikte ontwerpen. De implementatie van deze hoge-temperatuur supergeleiders in elektrodynamische toepassingen wordt echter beperkt door de aanwezigheid en de beweging van de vortices bij de aanwezigheid van een matig tot hoog magnetisch veld.

In dit doctoraatswerk richten we ons op de verbetering van de eigenschappen van het supergeleidend $YBa_2Cu_3O_{7-\delta}$ (YBCO) door het immobiliseren van de vortices via het inbouwen van metaaloxide nanokristallen als kunstmatige pinning centra in de YBCO matrix. Voorgaande experimenten, die in reeds gepubliceerde wetenschappelijke artikels werden onderzocht, zijn gebaseerd op YBCO-nanocomposiet films die groeien via de *pulsed laser deposition* (PLD) methode. Deze nanocomposiet films worden meestal gecreëerd met een niet-supergeleidende perovskiet-type $BaMO_3$ (M = Zr, Hf en Sn) fase als nanokolommen, gevormd door *self-assembling* in de YBCO films. Dit wordt gerealiseerd door de parameters van het filmafzettingsproces te manipuleren. Deze nanokolommen kunnen goede kritische stroomdichtheden (J_c) genereren en hebben goede prestaties wanneer het magnetische veld parallel aan de kolommen wordt uitgelijnd. Ze vertoont echter een beperkt J_c-isotropiegedrag wat een belangrijke beperking is voor elektrodynamische toepassingen. Bovendien heeft de gebruikte technologie het nadeel gecompliceerd te zijn, duur en traag. De controle over de groei van de nanokolommen is ook niet gegarandeerd.

Bijgevolg is een verbetering van de J_c voor de gehele rotatie in het magnetisch veld noodzakelijk. Dit was mogelijk door introductie van niet-gecorreleerde pinning centra zoals nanodots. Niettegenstaande de PLD-gebaseerde methoden films van hoge kwaliteit kunnen leveren en onderzoek geleid heeft tot diep inzicht in de controle over de grootte, vorm en dichtheid van de pinning centra, is deze PLD-gebaseerde methode echter te duur vanwege het vereiste hoge vacuümsysteem tijdens de afzetting. Hierdoor is de toepasbaarheid op industriële schaal sterk belemmerd. Voor de commerciële doorbraak van de implementatie van hoge-temperatuur supergeleiders is een efficiënt en goedkoop proces cruciaal. In de afgelopen jaren heeft de *chemical solution*

deposition (CSD) methode veel belangstelling gekregen vanwege zijn lage kosten en de gemakkelijk schaalbaarheid met een hoge efficiëntie. Deze methode leidt tot aanzienlijke vooruitgang in de economisch schaalbare producties van hoogwaardige supergeleidende films, teneinde de YBCO-gecoate geleiders over de hele energiemarkt te implementeren.

Ons onderzoek begon met de bereiding van de YBCO dunne film op het $LaAlO_3$ substraat, wat leidde tot uitstekende eigenschappen. Als eerste stap richtten we ons op de bereiding van een stabiele YBCO precursor oplossing, aangezien dit een essentiële stap is in de CSD benadering. De bereiding van de trifluorazijnzuur (TFA) gebaseerde YBCO precursoroplossing, zoals beschreven in het werk van Roma *et al*., maakt gebruik van een conventionele verwarming met een oliebad en duurt 72 uur. In onze onderzoeksgroep is de verwarming met microgolven reeds geïntroduceerd voor nanokristalsynthese, wat resulteert in een duidelijke vermindering van de synthesetijd. Daarom hebben we geprobeerd microgolfverwarming te introduceren om commercieel YBCO-poeder op te lossen met behulp van TFA-anhydride in een watervrije TFA-gebaseerde YBCO precursor. Het resultaat was een vermindering van de voorbereidingstijd met een factor van 72 in vergelijking met conventionele verwarming in een oliebad. De reactie verloopt niet alleen sneller maar belangrijk is dat ook de vorming van ongewenste bijproducten als mogelijke onzuiverheden onderdrukt wordt, zoals blijkt uit nucleaire magnetische resonantie (NMR) en massaspectroscopie (MS). Deze aanpak leidt tot zeer stabiele, zuivere en watervrije organometallische precursoroplossingen die een zeer reproduceerbare bereiding van supergeleidende coatings mogelijk maken. Deze snelle en betrouwbare methode kan ook een aangepast fluorgehalte van YBCO precursor leveren door de verhouding tussen TFA anhydride en propionzuur aan te passen.

Verder werd de succesvolle precursorpreparatie bevestigd door de spin-coating en de thermische verwerking van de TFA-YBCO dunne films op éénkristal substraten, resulterend in hoge kritische stroomdichtheden. Bovendien moet het YBCO CSD-onderzoek evolueren tot het gebruik van precursoren met lager fluorgehalte (gebaseerd op propionaten in plaats van TFA) om de vrijgave van giftige gefluoreerde verbindingen tijdens het thermische proces te verminderen. Als zodanig zijn processen met een laag fluorgehalte (LF) milieuvriendelijker en minder corrosief en dus beter geschikt voor industriële productie. In dit werk richten we ons op het gebruik van de LF-YBCO methode voor de fabricage van de YBCO dunne film. Verschillende CSD technieken zijn geïmplementeerd door middel van spin-coating, ink-jet printing en dip-coating om de YBCO dunne film aan te brengen op een monokristal substraat en op technische metalen substraten.

Deze CSD benadering leidde tot een goede YBCO textuur met goede supergeleidende eigenschappen in het *self-field*. Helaas vervallen de J_c-prestaties van deze LF-YBCO dunne film als het magnetische veld verhoogd

wordt, ten gevolge van de beweging van de vortex. Het is van cruciaal belang om de vortexen op een vaste positie te immobiliseren of te *pinnen.* Bijgevolg moet *vortex pinning* de prestaties van elektrodynamische apparaten verbeteren. Dit betekent dat het doel van dit werk verder was om de *pinning force densities* van de LF-YBCO dunne film te verhogen. Op dit moment zijn er al wetenschappelijke artikelen gepubliceerd over de introductie van niet-supergeleidende secundaire fasen in de YBCO-matrix via een spontane segregatie tijdens de fabricage van de TFA-YBCO dunne film. Deze secundaire fasen worden geïntroduceerd door toevoeging van extra organometallische zouten aan de TFA-YBCO precursoroplossing om de gewenste secundaire fasen laten te groeien (bvb. Y_2O_3, $BaZrO_3$, $BaHfO_3$, $BaCeO_3$ en Ba_2YTaO_6). Deze aanpak toont verbeterde *in-field* prestaties ten opzichte van niet-gedopeerde YBCO films. Deze aanpak biedt echter een beperkte controle op de vorming en grootteverdeling van de nanostructuren en ondervindt problemen met de reproduceerbaarheid. Deze *in-situ* benadering vereist ook een hoge gecontroleerde warmtebehandeling van *roll-to-roll* systeem waardoor het productieproces moeilijk te realiseren is.

Om betere controle te hebben over de uiteindelijke microstructurele eigenschappen van de YBCO nanocomposite films worden colloïdaal stabiele nanokristallen geïntroduceerd als kunstmatige pinning centra. Deze benadering met voorgevormde nanokristalen biedt meer controle over de uiteindelijke eigenschappen van de nanodeeltjes (bvb. grootte en grootte-verdeling) in de YBCO matrix. Tot nu toe zijn er slechts enkele pogingen gepubliceerd voor de synthese van supergeleidende nanocomposietfilms met behulp van voorgevormde nanokristallen (Au, CeO_2 en ZrO_2) als kunstmatige pinning centra, in de TFA-gebaseerde YBCO-methode. Het succes is beperkt omdat de nanokristallen ofwel naar het YBCO-oppervlak worden geduwd of op de substraatinterface geaccumuleerd worden. Het laatste belemmert de epitaxiale groei van YBCO, wat leidt tot slechte supergeleidende eigenschappen.

De bijbehorende vorming van de nanocomposiet film uit voorgevormde nanokristallen blijft onduidelijk omdat de stabilisatie in de TFA-gebaseerde precursoroplossingen (pH = 2) onverenigbaar is met de hogere pH van de LF-YBCO precursoroplossing (pH = 6). Liganduitwisseling en een goede stabilisatieprocedure zijn belangrijke aspecten in dit werk omdat we ons concentreren op het gebruik van LF-YBCO precursoroplossing in plaats van TFA. Door het delicate groeiproces van de getextureerde YBCO-lagen en het risico op 'vergiftiging' van de supergeleider door diverse chemische elementen zoals metalen, halogeniden (behalve F), zwavel en fosfor, zijn er ernstige beperkingen voor het uiteindelijke ligand van de voorgevormde nanokristallen.

In dit werk werden kleine kristallijne metaaloxide nanokristallen (bijvoorbeeld ZrO_2 en HfO_2) gesynthetiseerd met diameters in een bereik van 4-10 nm en bedekt met hydrofobe liganden om colloïdale stabiliteit in apolaire oplosmiddelen te waarborgen. We konden deze nanokristallen stabiliseren in

verschillende types van fluor-gebaseerde YBCO precursor oplossingen door een sterisch polaire ligand (Copolymer en Surfactis™) of korte carboxylaten (citroenzuur en wijnsteenzuur), wat leidt tot zeer stabiele nanocomposiet precursoren met langdurige stabiliteit. Vervolgens werden de YBCO oplossingen met nanokristallen gedeponeerd op éénkristal $LaAlO_3$ substraten via spin-coating. De belangrijkste focus van dit werk was het begrijpen van de factoren die de ontwikkeling van de microstructuur en de fysische eigenschappen van de nanocomposietfilms beheersen. Interessant genoeg leidden nanokristallen die gestabiliseerd werden door korte carboxylaatliganden tot slechte supergeleidende nanocomposieten terwijl het copolymeer leidde tot uitstekende supergeleiders. Dit is een tegen-intuïtief resultaat, omdat men zou verwachten dat hoe meer koolstof in de laag wordt ingevoerd, des te slechter de supergeleiding zou zijn. Zo hebben we met succes een nanocomposiet film van hoge kwaliteit van LF-YBCO precursoroplossingen gedeponeerd en belangrijke relaties tussen stabilisatie van nanokristal en finale eigenschappen van de supergeleider ontdekt, waarbij het gebruik van liganden cruciaal is om een goede supergeleidende film te verkrijgen met de mogelijkheid om de vortexen te pinnen.

Door strenge optimalisatie van zowel de YBCO nanosuspensie met geschikte stabiliserende liganden als het verwerkingsniveau via de introductie van een tussenliggende *dwelling* stap, hebben we nanocomposiet dunne films met uitstekende eigenschappen bekomen. Hierbij is het interessant om te weten wat het effect is van de verschillende morfologieën en groottes van de HfO_2 nanokristallen in de YBCO matrix. In dit werk zijn we erin geslaagd om verschillende HfO_2 nanokristallen te synthetiseren via een microgolf-geassisteerde (MW) synthese en een solvothermische opwarming (HU) synthese. Beiden synthesemethodes leveren kleine monoklinische HfO_2 nanokristallen, zoals bevestigd door röntgendiffractie, maar zijn verschillend in nanokristalgrootte. HfO_2 nanokristallen bekomen via HU synthese leveren kleine nanostaafjes op met een diameter van 2.6 nm en een lengte van 8 nm, terwijl de MW synthese sferische nanokristallen met een diameter van 6-8 nm leverde. Na het thermische proces resulteren de HU-gebaseerde HfO_2 nanokristallen in kleine $BaHfO_3$ deeltjes van 5-20 nm in de YBCO matrix terwijl MW-gebaseerde HfO_2 nanokristallen resulteren in grote $BaHfO_3$ deeltjes van 15-30 nm. Deze laatste zal de supergeleidende eigenschappen afbreken als gevolg van de vorming van meer ongewenste lijnfouten zoals stapelfouten. De kleine deeltjes zouden geneigd zijn om een gebied van korte *intergrowths* te bevorderen, die de deeltjes omringen, wat resulteert in een toename van microspanning en daarmee de pinning eigenschappen. In dit werk hebben we aangetoond dat de nanokristalgrootte en de verdeling ervan de sleutelparameters zijn om een betere controle te krijgen over de *intergrowths* en lijndefecten.

Uiteindelijk richten we ons, ten gevolge van de grote reactiviteit van enkelmetaaloxide-nanokristallen tijdens de YBCO-groei, met negatieve supergeleidende eigenschappen als gevolg, op de microgolf-geassisteerde

synthese van dubbele metaaloxide nanokristallen, d.w.z. $SrTiO_3$, via de benzylalcohol route. Deze $SrTiO_3$ nanokristallen zullen niet reageren tijdens het thermische proces van de YBCO dunne film. In deze synthese onderzochten we de mogelijkheid om de kristalgrootte af te stemmen door gebruik te maken van verschillende soorten bimetaal Sr(II)-Ti(IV) alkoxiden. Alle gesynthetiseerde $SrTiO_3$ nanokristallen hebben een gemiddelde diameter in een bereik van 3-7 nm en zijn agglomeraatvrij in apolair oplosmiddel via een post modificatie behandeling met oliezuur.

Voorafgaand aan de synthese van de YBCO nanocomposite film was een faseoverdracht mogelijk tot polaire oplosmiddelen via een liganduitwisseling met Surfactis™. Na deze spin-coating heeft deze $SrTiO_3$-gedoteerde YBCO-precursoroplossing op $LaAlO_3$-substraat, na een thermische behandeling, geleid tot een goede epitaxiale textuur van YBCO met goede supergeleidende eigenschappen. De finale laag vertoonde echter geen *pinning*-eigenschappen omdat de $SrTiO_3$ nanokristallen naar het YBCO oppervlak geduwd werden of zich vestigden op de interface tijdens de YBCO-groei. Er is ruimte voor verdere optimalisatie, maar hierbij is een eerste studie geleverd met betrekking tot het gebruik van voorgevormde dubbelmetaaloxide nanokristallen in YBCO nanocomposiet films, optimalisatie van het thermische proces en het begrijpen van nanokristal oppervlaktechemie.

Samengevat, zijn we in dit werk geslaagd met succes een YBCO precursoroplossing met voorgevormde nanokristallen via CSD-techniek te deponeren. We kunnen, voor de YBCO nanocomposiet film, hoge kritische stroomdichtheden bereiken, evenals een veel vlotter verval van J_c in functie van het magnetisch veld. Dit wordt weerspiegeld door een uitgesproken versterking van de *pinning force* en een verminderde effectieve anisotropie in vergelijking met niet-gedoteerde YBCO films. We hebben ook het gedrag van nanokristallen in combinatie met de gebruikte stabiliserende liganden tijdens de YBCO-groei verduidelijkt. Verder onderzoek zal nodig zijn om homogeen verdeelde dubbel metaaloxide nanokristallen te verkrijgen over de hele YBCO matrix met uitstekende supergeleidende en pinning eigenschappen. Dit zou ons een stap dichter moeten brengen bij een economisch-efficiënte en milieuvriendelijke synthesemethode voor YBCO nanocomposiet films om aan de eisen voor stroomtoepassingen te voldoen.

English summary

People's concern about global warming and the rapid growth of the world population has prompted scientists to develop renewable electrical energy and to find new technologies with a minimum of carbon dioxide emissions. High-temperature superconducting technologies have the potential to transport electricity without resistance. In addition their superior properties allow the development of generators with a higher power output than the conventional used designs. However, the implementation of these high-temperature superconductors in power applications is constrained due to the presence and movement of vortices in the presence of a medium to high magnetic field.

In this thesis, we focused on the improvement of the superconducting $YBa_2Cu_3O_{7-\delta}$ (YBCO) properties by immobilizing the vortices via the incorporation of metal oxide nanocrystals as artificial pinning centers in the YBCO matrix. However, the first experiments investigated in previously published scientific articles are based on YBCO nanocomposite films, growing via pulsed laser deposition (PLD) method. These nanocomposite films are commonly created with a non-superconducting perovskite-type $BaMO_3$ (M = Zr, Hf and Sn) compound as nanocolumns into the YBCO films. This is done by modifying the film deposition process using the self-assembly process. These nanocolumns can generate good critical current densities (J_c) and its in-field performance is good, when the magnetic field is aligned parallel to them. However, it shows a limited Jc isotropy behavior which is an important restriction for power applications.

So, an enhancement of the J_c for the whole rotation in the magnetic field is necessary. This was possible through the introduction of non-correlated pinning centers such as nanodots. Nevertheless, the PLD-based methods can deliver high quality films and research has already led to deep insight into the control over the size, shape and density of pinning centers,. However, this PLD-based method is considered to be too expensive due to the required high vacuum system during the deposition, hampering its applicability on industrial scale. For the commercial breakthrough of the implementation of high-temperature superconductors, an efficient and low-cost process becomes crucial. Over the last years, the chemical solution deposition (CSD) method has gained a lot of interest due to its low-cost and easy scalability with high efficiency. This method leads to significant advances towards economically scalable productions of high-

quality superconducting films, to implement the YBCO coated conductors throughout the energy market.

Our research began with the fabrication of the YBCO thin film on the $LaAlO_3$ substrate leading to excellent properties. First, we focused on the preparation of a stable YBCO precursor solution as it is the essential step towards the CSD approach. The preparation of the trifluoroacetic (TFA) based YBCO precursor solution, as described in the work of Roma *et al.,* takes 72 hours due to the conventional heating by an oil bath. In our research group, microwave heating was already introduced for nanocrystal synthesis which results in an obvious reduce of the synthesis time. So, we tried to introduce microwave heating to dissolve commercial YBCO powder using TFA anhydride to an anhydrous TFA-based YBCO precursor. The result was a reduction in preparation time by a factor of 72 compared to conventional heating by an oil bath. The reaction is not only faster, also more importantly, the formation of undesirable by-products as possible impurities is suppressed, as shown by Nuclear Magnetic Resonance (NMR) and Mass Spectrometry (MS). This approach leads to highly stable, pure and anhydrous organometallic precursor solutions, which allow a highly reproducible preparation of superconducting coatings. This fast and reliable method can also deliver a modified fluorine content of YBCO precursor by adjusting the ratio between TFA anhydride and propionic acid.

Further on, the successful precursor preparation was confirmed by the spin-coating and the thermal processing of the TFA-YBCO thin films on single-crystal substrates, resulting in high critical current densities. In addition, the YBCO CSD research has to evolve towards the use of precursors with lower fluorine content – based on propionates instead of TFA – to reduce the release of toxic fluorinated compounds during the thermal process. As such, low-fluorine (LF) processes are more environmentally benign and less corrosive and thus better suited for industrial production. In this work, we focused on the use of the LF-YBCO method for the fabrication of YBCO thin film. Several CSD techniques have been introduced by means of spin-coating, ink-jet printing and dip-coating to deposit the YBCO thin film on a single-crystal and on technical metallic substrates.

This benign CSD approach led to good YBCO texture with good superconducting properties in self-field. Unfortunately, the J_c performances of this LF-YBCO thin film start to drop when the magnetic field is increased, due to the vortex motion. It becomes crucial to immobilize or to pin the vortices at a fixed position. So *vortex pinning* has to enhance the performances of electrodynamic devices. This means that the goal of this work is to increase the pinning force

densities of the LF-YBCO thin film. At the moment, there are already scientific articles published concerning the introduction of non-superconducting secondary phases in the YBCO matrix via a spontaneous segregation during the fabrication of the TFA-YBCO thin film. These secondary phases are introduced via the addition of extra metal-organic salts to the TFA-YBCO precursor solution to grow the desired secondary phases (e.g. Y_2O_3, $BaZrO_3$, $BaHfO_3$, $BaCeO_3$ and Ba_2YTaO_6). This approach demonstrates enhanced in-field performances compared to undoped YBCO films. However, this approach offers limited control on the formation and size distribution of the nanostructures and faces issues with reproducibility. This *in-situ* approach also requires a highly controlled heat treatment of the roll-to-roll processing equipment which makes it hard-to-reach.

To offer better control over the final microstructural properties of the YBCO nanocomposite films, colloidally stable nanocrystals are introduced as artificial pinning centers. This preformed nanocrystal approach can provide more control over the final nanoparticles properties (e.g., size and distribution) in the YBCO matrix. As this approach is very complicated, a new challenge has appeared for the researchers which have been thoroughly discussed in this work. Up to now, only a few attempts have been made at the synthesis of superconducting nanocomposite film using preformed nanocrystals (Au, CeO_2 and ZrO_2) as artificial pinning centers in the TFA-based YBCO method. The success has been limited because the nanocrystals are either pushed to the YBCO surface or accumulated at the substrate interface. The latter hampers the epitaxial growth of YBCO, leading to poor superconducting properties.

However, the corresponding formation of the nanocomposite film from preformed nanocrystals remains elusive since the stabilization in the TFA-based precursor solutions (pH = 2) is incompatible with the higher pH of the LF-YBCO precursor solution (pH = 6). Ligand exchange and the appropriate stabilization procedure are important aspects in this work as we focused us on the use of LF-YBCO precursor solution instead of TFA. Due to the delicate growth process of textured YBCO layers and the risk of poisoning the superconductor by many chemical elements like metals, halides (except F), sulphur and phosphorus, there are severe restrictions on the final ligand of the preformed nanocrystals.

In this work, small crystalline single (e.g. ZrO_2 and HfO_2) metal oxide nanocrystals were synthesized with diameters in the range of 4-10 nm and capped with hydrophobic ligands to ensure colloidal stability in apolar solvents. However, we were able to stabilize these nanocrystals in different types of fluorine-based YBCO precursor solutions by a steric polar ligand (Copolymer and Surfactis™) or short carboxylates (citric acid and tartaric acid), leading to highly

stable nanocomposite precursors with long shelf-lives. Afterwards, the YBCO nanosuspensions were deposited on single crystal $LaAlO_3$ substrates via spin-coating. The main focus of this work pointed to understand the factors which control the microstructure development and the physical properties of the nanocomposite films. Interestingly, nanocrystals stabilized by short carboxylate ligands resulted in poorly superconducting nanocomposites while the copolymer lead to excellent superconductors. This is a counter-intuitive result as one would expect that the more carbon is introduced in the layer, the worse the superconductor would be. So, we successfully deposited a high-quality nanocomposite film from LF-YBCO precursor solutions and uncover important relations between nanocrystal stabilization and final performance where the use of ligands is crucial in order to obtain a good superconducting film with the ability to pin the vortices.

By strict optimization of both the YBCO nanosuspension with suitable stabilizing ligands and the processing level through the introduction of an intermediate dwelling step, we have achieved nanocomposite thin films with excellent properties. But it is interesting to know what the effect of the different morphology and size of HfO_2 nanocrystals in the YBCO matrix are. In this work, we were able to synthesize different HfO_2 nanocrystals via a microwave-assisted (MW) synthesis and a solvothermal heating-up (HU) synthesis. Both synthesizes deliver small monoclinic HfO_2 nanocrystals as confirmed by x-ray diffraction but are different in the nanocrystal size. HfO_2 nanocrystals synthesized via HU deliver small nanorods with a diameter of 2.6 nm and 8 nm in length while the MW synthesis delivered spherical nanocrystals with a diameter of 6-8 nm. After thermal process, the HU-based HfO_2 nanocrystals result in small $BaHfO_3$ particles of 5-20 nm in the YBCO matrix while MW-based HfO_2 nanocrystals result in large $BaHfO_3$ particles of 15-30 nm. This latter will degrade the superconducting properties due to the formation of more undesired line defects such as stacking faults. The small particles would tend to promote a region of short intergrowths, surrounding the particles, yielding in an increase of microstrain and thus pinning properties. So, in this work, we have shown that the nanocrystal size and its distribution are the key parameters to a better control of the intergrowths and line defects.

Finally, due to the reactivity of single metal oxide nanocrystals during the YBCO growth, we focused on the microwave-assisted synthesis of double metal oxide nanocrystals, i.e. $SrTiO_3$, via benzyl alcohol route. These $SrTiO_3$ nanocrystals will not react during the thermal process of the YBCO thin film. In this synthesis, we examined the ability of tuning the crystal size by using different types of bimetallic Sr(II)-Ti(IV) alkoxides. All the as-synthesized $SrTiO_3$ nanocrystals have

an average diameter in a range of 3–7 nm and are agglomerate-free in apolar solvent via a post modification treatment with oleic acid. Prior to the fabrication of the YBCO nanocomposite film, a phase transfer was possible to polar solvents via a ligand exchange with Surfactis™. After spin-coating this $SrTiO_3$-doped YBCO precursor solution on $LaAlO_3$ substrate, following a thermal treatment, it resulted in a good epitaxial texture of YBCO with good superconducting properties. But it did not show any pinning properties because the $SrTiO_3$ nanocrystals were pushed to the YBCO surface or settled on the interface during the YBCO growth. There is room for further optimization but it is only a first proof concept regarding the use of preformed double metal oxide nanocrystals in YBCO nanocomposite films, optimization of the thermal process and understanding of nanocrystal surface chemistry.

In conclusion, we are able to deposit a YBCO precursor solution with preformed nanocrystals via CSD technique and can achieved, for the YBCO nanocomposite film, high critical current densities as well as a much smoother decay of J_c in function of magnetic field. This is reflected by a strong pinning force enhancement and a reduced effective anisotropy compared to undoped YBCO films. We also elucidated the behavior of nanocrystals in the combination with the used stabilizing ligands during the YBCO growth. Further research will be required to obtain homogenously distributed double metal oxide nanocrystals throughout the YBCO matrix with excellent superconducting and pinning properties. This should bring us one step closer to a benign and economically YBCO nanocomposite films in order to meet the requirements for power applications.

Chapter one

From theory of superconductivity to $YBa_2Cu_3O_{7-\delta}$ nanocomposites

A brief overview of the history and theory of the phenomena "Superconductivity" and its $YBa_2Cu_3O_{7-\delta}$ nanocomposites for applications

1.1. Introduction

Due to a growing population, it has been predicted that over the next four decades global power usage will almost double. Much of the power we consume is in the form of electricity but during the transmission, more than 10% of the energy is lost in the form of heat due to the effects of electrical resistance. This predicament has many effects on deforestation, global warming and other environmental issues like pollution and acid rain.[1] However, in order to address the steadily increasing demand for more clean and non-polluting power, high temperature superconductors offer a number of advantages that are expected to address some of these concerns. A superconductor is a real physical phenomenon provided by quantum mechanics: superconductivity.

1.2. Superconductivity, phenomenon

During the quest for absolute zero, somewhere in 1908, the Dutch physicist Heike Kamerlingh Onnes succeeded liquefying Helium, which opened the possibility to study the temperature dependence of the electrical resistance in metals at extremely low temperatures.[2, 3] To H. K. Onnes' great surprise in 1911, the resistance showed a discontinuous decrease to zero, which he called superconductivity. The temperature at which this superconducting state occurred was called transition or critical temperature (T_c). It offers opportunities for revolutionizing energy applications as the superconductivity does not show any ohmic resistance and delivers highest energy density.

In the normal conductor, ohmic heating occurs when an electrical current passes through a conductor due to the Joule's first law. This ohmic heating is not only energy loss but also requires an additional installation to release the heat. The fact is that there is no resistance in the superconductivity and thus no ohmic heating. What a perspective! So, the ultimate dream of H. K. Onnes was "*The use of the superconducting materials to transmit electricity without losses and also to build magnets with unprecedentedly high magnetic fields.*" This concept was tested using Sn and Pb wires but H.K. Onnes himself concluded that any of these materials, used in his experiments, could not carry any current at magnetic fields exceeding 50 mT.[4] So, his dream to build powerful magnets went up in smoke because the physics of superconductivity in magnetic fields were seriously misunderstood. Nevertheless, scientists were still busy to understand the phenomenon of superconductivity.

In 1933, Meissner and Ochsenfeld revealed that the superconductor shows a perfect diamagnetism below its transition temperature which expels the

externally applied magnetic fields completely as shown in Figure 1.1a. This phenomenon results in the levitation of a superconducting material above a magnet, when it is cooled below its characteristic critical temperature (Figure 1.1b). This is usually called the Meissner effect and is completely reversible.[5]

In 1957, J. Bardeen, J. N. Cooper, and J. R. Schrieffer gave a theoretical explanation of this phenomenon, known as the BCS-theory.[6] This theory described a microscopic model for superconductivity characterized by the presence of electron pairs, so-called Cooper-pairs, below the critical temperature. Cooper pairing is a quantum effect and can be explained in a simplified description. These pairs are formed by electron-phonon interactions and move freely through the crystal lattice without energy dissipation. These Cooper-pairs are separated by the coherence length (ξ) and are responsible for the superconducting charge carries.[7] However, the BCS-theory is only applicable for metals and simple alloys. Until now the theory has been inadequate to fully explain the superconducting state of other superconducting materials.[3, 8]

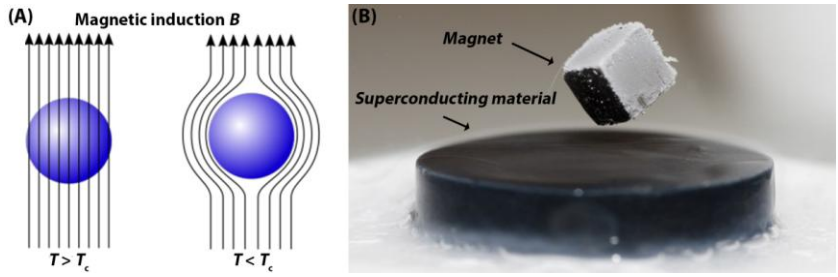

Figure 1.1. *(A) Behavior of the superconducting material above ($T > T_c$) and below ($T < T_c$) its transition temperature in an external magnetic field.[9] (B) A magnet can levitate above a superconducting material, supported by the force expelling the magnetic field.[10]*

The real breakthrough was made in 1986 by Bednorz and Müller. They discovered that the superconducting state was not limited to metals and alloys. A new class of superconducting materials was arisen by the preparation of a ceramic $La_{2-x}Ba_xCuO_4$ compound. The materials show superconductivity at an unusually high temperature of 35 K.[11] One year later, inspired by this discovery, Paul Chu replaced lanthanum by yttrium and found superconductivity at 92 K in the $YBa_2Cu_3O_{7-\delta}$ (YBCO) compound.[12] This last discovery was very considerable because, now cooling with cheap liquid nitrogen became possible. From that moment on, the realisation of H.K. Onnes' dream came very close. So, the search for high-temperature superconducting compounds had started. Another

ceramic compound with superconducting properties is a Bi-Sr-Cu-O system wherein calcium is added to the crystal lattice to increase the transition temperature to 110 K for $Bi_2Sr_2Ca_2Cu_3O_{10+\delta}$ (BSSC-2223) compound.[13] Until now the highest transition temperature of 134 K was observed in a $HgBa_2Ca_2Cu_3O_8$ compound. Recently, a new class of superconducting compounds is discovered in Japan: the iron-based superconductors (RE-Fe-P-O and RE-Fe-As-O with Rare Earth (RE) = La, Ce, Sm, ...) with transition temperature up to 85 K.[14] Despite all of these discoveries (Figure 1.2), the binary compound MgB_2 is used in many applications due to the high abundance of the starting materials and its simple composition.[15]

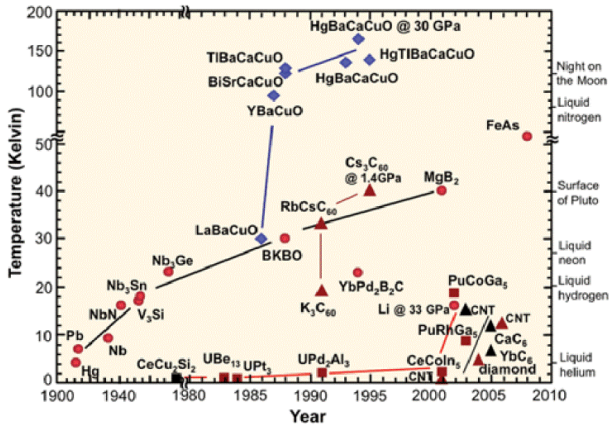

Figure 1.2. *Evolution of the transition temperature over the years.*[16]

1.3. Superconductivity, properties

As mentioned previously, the superconductors have some interesting properties that are controlled by three features: temperature, strength of the external magnetic field and current density.[17] The superconducting state could also be destroyed by a sufficiently high current or magnetic fields, i.e. a critical current (I_c) and a critical magnetic field (H_c). The three critical parameters depend on each other, which means there are actually three critical parameters namely $T_c(H,I)$, $I_c(T,H)$ and H_c (T,I). Figure 1.3 shows the relationship between these parameters in the superconducting state diagram, which in its turn presents the practical operation area of a superconductor. Improvement of those critical parameters is an important goal in the research and development of the superconductivity fields.

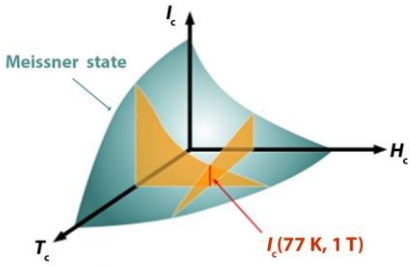

Figure 1.3. *Superconducting (Meissner) state diagram defined by its critical parameters critical temperature T_c, critical current I_c and critical magnetic field H_c.*[18]

1.3.1. Critical temperature

A clear transition between normal and superconducting state is characterized by the critical temperature (T_c). Based on 30 K as border temperature, two groups of materials (Table 1.1) can be determined: below this border temperature, the materials are classified as Low Temperature Superconductors (LTS) while above this temperature are called High Temperature Superconductors (HTS). The metals Nb and V, alloys (except Nb_3Sn), all ceramic oxide (cuprate)-based and MgB_2 are HTS. With a transition temperature above 77 K (the boiling point of liquid nitrogen at atmospheric pressure), the small group of the ceramic oxide-based materials (Table 1.1) is very interesting to be used in energy related applications, because they exhibit higher critical properties than LTS.[3]

Table 1.1. *Critical temperature of several superconducting materials.*[19]

Material	T_c (K)
Nb_3Sn	18
Nb-Ti	9
MgB_2	39
$YBa_2Cu_3O_{7-\delta}$	92
$Bi_2Sr_2Ca_2Cu_3O_{10}$	110
$TlBa_2Ca_2Cu_3O_9$	123
$HgBa_2Ca_2Cu_3O_8$	135

1.3.2. Critical current

The critical current is defined as the maximum current that can flow through the superconducting material without any losses of energy, which means no resistance. If the maximum value of the current in a superconducting material is exceeded, the material will pass into the normal or non-superconducting state. Since the normal state has a certain finite electric resistance, dissipation of the

energy in the current takes place during the transition, which results in heating the material. However, for electrical engineering applications, the critical current is calculated as the critical current density (J_c) as it depends on the size and area of the superconducting material. Take into consideration that the current flow through the superconducting material must be as high as possible at several magnetic fields as function of their use in power applications. However, it is noteworthy that the current has an influence on physical phenomena of the mixed state of type II superconductor where the current will start to drop by an increasing magnetic field. This phenomenon will be discussed in the following section.

1.3.3. Critical magnetic field and irreversibility field

Based on their behavior in a magnetic field, superconductors can be classified into type I and type II. As shown in Figure 1.4, there is only one critical magnetic field (H_c) in type I superconductors. The transition from the superconducting state changes instantly to the normal (non-superconducting) state when the externally magnetic field strength surpasses H_c. In type II superconductors there are two critical magnetic fields: the lower (H_{c1}) and the upper (H_{c2}). Above the H_{c1} (Figure 1.5) the magnetic flux starts to penetrate into the superconductor but the material remains superconductive. Only above H_{c2} the superconductivity is totally disappeared. This behavior can be characterized by the Ginzburg-Landau parameter (κ) defined as $\kappa = \frac{\lambda}{\xi}$ (Eq. 1.1) with λ as the London penetration depth of a magnetic field into the superconducting material and ξ as a superconducting coherence length. This parameter determines whether a superconductor is type I ($0 < \kappa < 1/\sqrt{2}$) or type II ($\kappa > 1/\sqrt{2}$).

H_c is an important feature characterized by the fact that the critical field remains zero at the critical temperature and increases if the temperature decreases. Plots of the critical field versus temperature for several superconducting materials are shown in Figure 1.5. The temperature dependence of the critical field can be described approximately by:

$$H_c(T) = H_c(0)\left[1 - \left(\frac{T}{T_c}\right)^2\right] \qquad \text{Eq. 1.2}$$

where $H_c(0)$ is the critical field at absolute zero temperature. In general, type I superconductors are metals, such as aluminum and mercury. They are perfectly diamagnetic below a critical field $H_c(T)$ whereas the critical fields of type I superconductors are generally quite low (well below one tesla). For this reason,

they cannot be used in applications requiring the production of high magnetic fields, which would destroy their superconducting state.

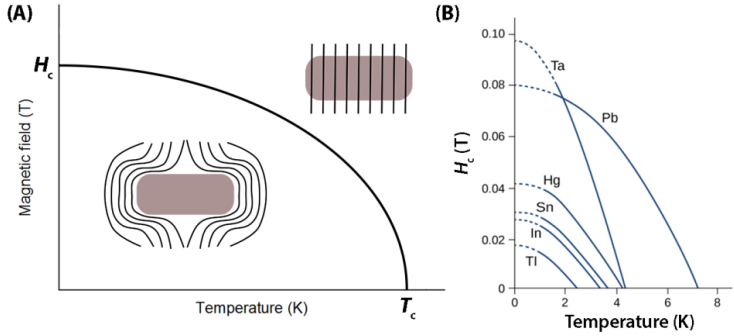

Figure 1.4. *(A) Type I superconductor phase diagram and (B) the temperature dependence of the critical field for several superconductors. Superconductivity occurs for magnetic fields and temperatures below the curves shown.*

Interestingly, type II superconductors are generally compounds or alloys involving transition metals or actinide series elements. Almost all superconductors with relatively high critical temperatures are type II. When the field is below H_{c1}, type II superconductors are perfectly diamagnetic, and no magnetic flux penetration into the material can occur. For a field exceeding H_{c2}, they are driven into their normal state. Moreover, when the field is greater than H_{c1} but less than H_{c2}, type II superconductors are said to be in a mixed state, known as the Shubnikov phase. From H_{c1} on, the magnetic flux starts to penetrate homogeneously distributed in the superconducting material in the form of small cylindrical flux lines called vortices. A vortex is non-superconducting (or normal) area surrounded by a supercurrent that circulates around the normal core of the vortex. As the magnetic field increases from H_{c1} to the H_{c2}, more and more vortices are introduced in the superconducting material and start to overlap. The magnetic field penetrates the material uniformly throughout resulting in a loss of all superconducting properties. In general, H_{c2} is very large compared to the critical fields of type I superconductors, so wire made of type II superconducting material is suitable for most practical applications.

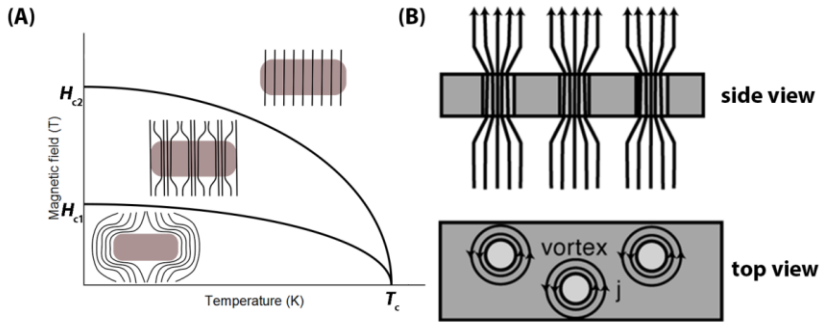

Figure 1.5. *(A) Type II superconductor phase diagram and (B) schematic visualization of a vortex.*[9]

However, when a current density (*J*) flows through a superconducting material in a mixed state, while a magnetic field is applied, the resistance will increase due to the Lorentz force ($F_L = J\ x\ B$, Eq. 1.3) acting on the vortices. As a result, the vortices will move in the perpendicular direction of the current causing non-desirable energy dissipation and will no longer be able to transport the current.

This undesired movement may be prevented by pinning the vortices to avoid energy dissipation. Effective pinning centers are non-superconducting (normal) materials with a similar dimension of vortex's cores. The force that holds the vortex's core at the pinning centers is called the pinning force (F_P). These F_P values should be higher or equal to F_L. For two reasons: Firstly, to pin the vortices and secondly, to carry the current without vortices motions and so eliminating energy losses.

The irreversibility field H_{irr} is the critical value where the vortices motions or flux-creeps start. Below H_{irr}, the vortices are in a flux-solid state and depend on the nature of the effective pinning centers in the material defects. Hence, the vortices become immobilized and the current can flow ($J_c > 0$) without energy dissipation. On the other hand, above $H_{irr,}$ the flux-solid state starts to form a flux-liquid state due to the overcome of the pinning centers by the thermal activation energy. In this state, the vortices start to move resulting in $J_c = 0$. Therefore, the power applications of type II superconductors are limited by H_{irr} and not by H_{c2}. H_{irr} is an important characteristic depending on different parameters such as the anisotropy and temperature. (Figure 1.6)

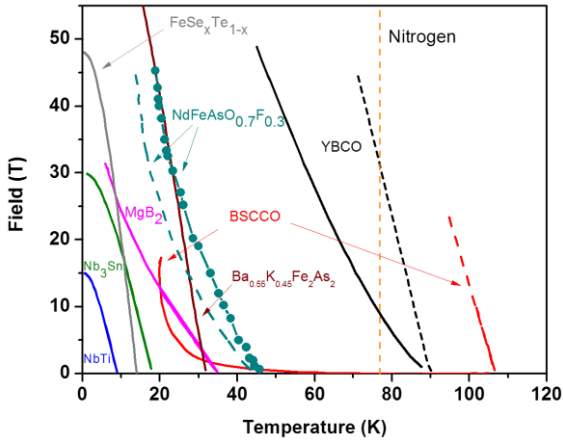

Figure 1.6. *Relationship between the upper critical magnetic field H_{c2} (indicated as a dashed line) and irreversibility field H_{irr} (indicated as full line) for several type II superconductors.*[4]

1.4. Applications

Scientists had already started dreaming of practical applications after the discovery of the superconducting state. Especially, H. K. Onnes saw the enormous potential of superconducting materials building up magnets with extremely high magnetic fields as well as the transport of electricity without any loss of energy.[4, 20] Nevertheless, this realization does not seem to be so simple because superconducting properties depend on several critical parameters. Conventional equipment is already highly efficient but can be further improved by the implementation of superconducting materials.

Nowadays, a part of the dream becomes a reality using type II LTS materials. Most of these LTS are intermetallic compounds such as Nb_3Sn and NbTi-alloys operating at 2 K, and are produced for the magnet technology market since the superconducting electromagnets are used in medical and scientific applications such as Magnetic Resonance Imaging (MRI) and Nuclear Magnetic Resonance spectroscopy (NMR).[7] At this moment, the largest application of these LTS is used for international high energy physics (e.g. The Large Hadron Collider at CERN in Switzerland)[21] and fusion projects (The ITER Tokamak in France, Figure 1.7).[22] Concerning the ITER Tokamak fusion reactor, operational testing is expected to start in 2025. The realization of deuterium-tritium fusion reactions is expected to be realized in 2035.

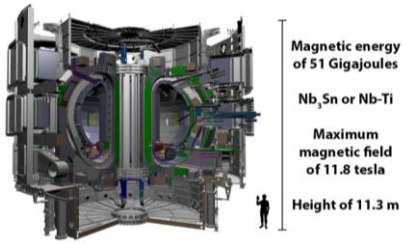

Figure 1.7. *Illustration of ITER Tokamak fusion reactor in France.*[22]

Another interesting application is the Superconducting Magnetic Energy Storage system (SMES) where the energy could be indefinitely stored in a superconducting coil when it is charged. The stored energy can be released back to the network by discharging the coil. The advantage of a SMES is the fast and highly efficient storage of electrical energy.

Superconducting magnets can also be used in the transport industry to levitate a train above magnetic tracks due to the magnetic repulsion between like poles. Facing only air resistance, these so-called MagLev trains can easily reach velocities over 500 km h^{-1}. There are some short-distance MagLev services operational in Korea, Japan and China.[23]

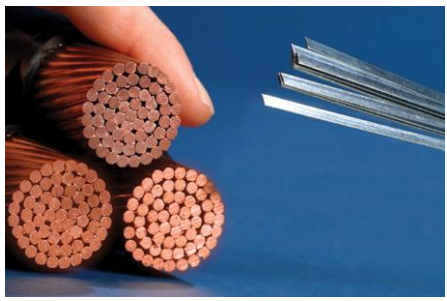

Figure 1.8. *Conventional copper wire (left) versus superconducting wires (right). Courtesy of American Superconductor*

However, the need of the refrigeration of Nb_3Sn and NbTi-alloys LTS wires with liquid helium as their T_c is low and the low performance of LTS wires at high magnetic fields, have forced scientists to focus on the HTS wires, changing the paradigms in energy technology. Due to their moderate cooling requirements, HTS wires offer unique features in highly efficiency and reduced weight/size.[24] Energy applications can be divided into electric grid applications such as power cables, bus bars and fault current limiters and rotating machines such as motors and generators. Furthermore, HTS materials allow current densities of 10.000 to

50.000 A mm^{-2} at operating conditions, a great advantage compared to the currently used in copper-based equipment that operates at a current density of 1 to 5 A mm^{-2}.[3, 24] To illustrate, the few HTS wires pictured on the right in Figure 1.8 are able to carry as much power as all of the conventional copper wires pictured on the left.

The use of HTS wires results in less weight for the same output, so the high current density in the HTS wires allows a more compact winding and a smaller and lighter design of the machines with, on average, 35 % to 50 % of the weight of conventional motors (Figure 1.9). Due to their higher current carrying capacity of more than 150 times of conventional copper, particularly in the wind turbine market, the superconductive windings can generate a higher magnetic induction which is more economical than the common copper wire or permanent magnet technology. In rotating machines HTS materials offer the chance of overcoming technical restrictions arising from conventional technology and open up new potentials with improvements in the magnetic field behavior in the range of 1 to 5 T. Worldwide various real scale prototypes have been manufactured and tested in fields such as wind power generators[25] and ship propulsion motors.[26]

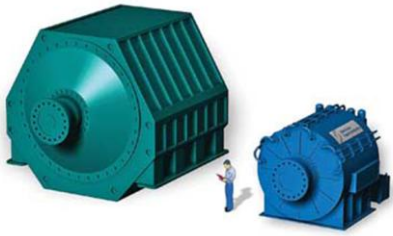

Figure 1.9. *Conventional copper wire (left) versus superconducting wires. Courtesy of American Superconductor.*

Due to the increasing worldwide demand for electricity, it is not certain if our conventional copper based equipment will be able to meet the requirements of our everyday energy demand. As pointed out in the previous paragraph, HTS promise a highly effective and environmental friendly extension of tomorrow's use of energy as they can increase the output power of renewable energy sources such as windmills. Also, efficient and safe transmission and distribution of electric energy is the most important task of electrical infrastructure. However, during the transportation of electric current via conventional copper cables, approximately 10 to 20 % of energy is lost during its transmission towards the consumer due to the unavoidable resistive properties.[24] Since the HTS materials have no ohmic resistance which results into superior energy

efficiency, HTS wires are a viable alternative option for power cables compared to the existing conventional systems. But in order to be usable in electric devices of HTS materials have to be processed to windable wires or tapes. There are only two ceramic cuprate-based materials (YBCO and BSSCO-2223) which really acquire technical relevance with a critical temperature of resp. 92 and 110 K.[4, 18, 20] The fabrication of these HTS materials is very challenging due to two main disadvantages namely brittleness and anisotropy.

1.5. High temperature superconductor $YBa_2Cu_3O_{7-\delta}$

The aim of materials search was to reach a superconductor with highest T_c as close as possible to room-temperature. Yet, by itself, higher T_c does not ensure successful application of the superconductor material. $YBa_2Cu_3O_{7-\delta}$ ($YBCO_{7-\delta}$) superconductor has a T_c of approximately 92 K and is known to be the most suitable superconductor for usage in power applications due to its non-toxic elements (no Tl and Hg-containing), high critical field, high irreversibility and subsequently high critical current density. This gives researchers the opportunity to face a new challenge.

The $YBCO_{7-\delta}$ crystal structure is based on three modified perovskite unit cells stacked along the c-axis (the perovskite structure has the general formula ABO_3). The $YCuO_3$ cube is situated in the center and is surrounded by two $BaCuO_3$ perovskite unit cells, as shown in Figure 1.10. The $YCuO_3$ unit cell is slightly deformed due to the absence of 4 O-atoms around the Y^{3+}-ion. The copper atoms are in mixed oxidation states (Cu^{2+} and Cu^{3+}) and are subdivided into two classes depending on their position in the lattice: CuO chains at the top and the bottom of the cell and CuO_2 basal planes, which are responsible for superconductivity. These CuO_2 planes are located between the Ba^{2+} and Y^{3+} containing perovskite cells. The CuO chains or charge reservoirs have a variable oxygen content (denoted by δ in the chemical formula) which can change the crystal structure of $YBCO_{7-\delta}$. When the oxygen content (δ) is less than 0.6, the oxygen sites in CuO chains along the *b*-axis are filled and the $YBCO_{7-\delta}$ material becomes orthorhombic (Pmmm) with the lattice parameters of a = 3.82 Å, b = 3.88 Å and c = 11.67 Å. This latter is the superconducting state. Otherwise, the $YBCO_{7-\delta}$ material can be non-superconducting or isolator when $\delta > 0.6$ where the oxygen sites in the CuO_2 basal plane are equally occupied and $YBCO_{7-\delta}$ structure has a tetragonal structure (P4/mmm).[3, 7]

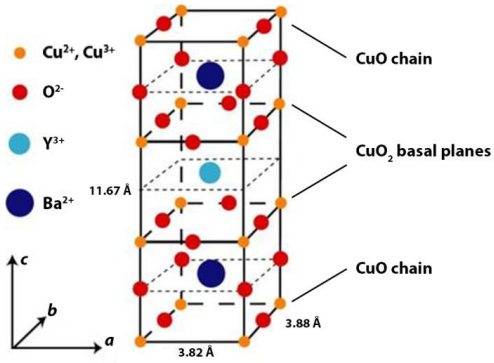

Figure 1.10. *$YBa_2Cu_3O_{7-\delta}$ orthorhombic unit cell.*

Here, the BCS-theory became inadequate to fully explain the superconducting state of cuprate-based HTS because it is strongly believed that the CuO_2 planes lead to electron-holes pairs, which are responsible for the superconducting state, while the CuO chains provides charge carriers to the CuO_2 planes. Nevertheless, no conclusive theory has been found yet.

Hence, the current will mainly flow along the *ab*-plane and CuO_2 planes lie normal to the crystallographic *c*-direction. Thus, the layered structure of the $YBCO_{7-\delta}$ unit cell is highly anisotropic. The anisotropy (γ) is due to the laminar crystalline structure of $YBCO_{7-\delta}$ and is defined in the framework of Ginzburg-Landau theory as following equation (Eq. 1.4):[27]

$$\gamma = \frac{\lambda_c}{\lambda_{ab}} = \frac{\xi_{ab}}{\xi_c} = \frac{H_{c_1}^c}{H_{c_1}^{ab}} = \frac{H_{c_2}^{ab}}{H_{c_2}^c} \qquad \text{Eq. 1.4}$$

Since γ is related to effective mass of the electrons, it dependent on the coherence length (ξ) and penetration depth (λ) depending on the magnetic field orientation relative to the crystallographic axis of the $YBCO_{7-\delta}$ material. For $YBCO_{7-\delta}$ the values of ξ and λ at T = 0 K are shown in Table 1.2.[28]

Table 1.2. *Coherence length (ξ) and penetration depth (λ) for $YBCO_{7-\delta}$ at T = 0 K.*

direction	ξ (nm)	λ (nm)
c-axis	0.24	890
ab-plane	1.60	135

Based on the values of ξ and λ, the value of γ = 6.6 is calculated which is the lowest value for HTS materials[29] and results in a higher H_{irr} for $YBCO_{7-\delta}$ compared

to other HTS materials. For example, BSSCO has γ value of approx. 30 and results in a low H_{irr}. This makes YBCO HTS materials a good candidate for power applications in which high magnetic fields are used.

Hence, the CuO_2 basal planes and their anisotropy have a key role in the superconducting state of YBCO. This anisotropic behavior needs to be taken into account for the use of YBCO HTS materials for power applications, because the critical current densities along the *ab*-plane are 500 times higher than when they are parallel to the *c*-axis.[30] Thus, it is considerable that all the $YBCO_{7-\delta}$ grains show perfect *c*-axis orientation to have a current that flows freely with good properties.

1.6. Coated conductor architecture

After the discovery of high temperature superconductors, lots of research was focused on the fabrication of long, strong and flexible HTS tapes. As mentioned before, the two main disadvantages are the brittleness and the anisotropy of the material. Nowadays, there are several techniques to surmount these practical issues. The first approach was the first generation (1G) HTS tape where BSCCO-2223 wires were prepared using the *Oxide Powder in Tube* (OPiT) process. In this process, the malleable silver cladding tube are filled with the desired metal oxide powders and drawn into thin wires. These resulting small, individual wires are enclosed by a large silver tube and further drawn into a wire. This process results into fine parallel filaments of individual wires in a silver matrix, leading to the BSCCO-2223 superconductor (10^5 A cm^{-2}) with uniaxial crystal alignment with parallel aligned CuO planes after the multi-stage annealing and rolling processing.[24] Most prototypes and early stage commercial HTS systems are realized with 1G-HTS tapes. However, the use of 1G-HTS tape conductor for commercial equipment has already been greatly restricted by the high production price of the tape, due to the requirement of a large amount of silver (60 % of total volume). So, it is desirable to reduce the production cost. Besides, BSCCO-2223 has a very high anisotropy (γ = 30) and a low H_{irr} which decreases the superconducting properties drastically when a small applied magnetic field is applied. This means that the operating conditions of these 1G-HTS tapes are limited to temperatures lower than 25 K.[31, 32]

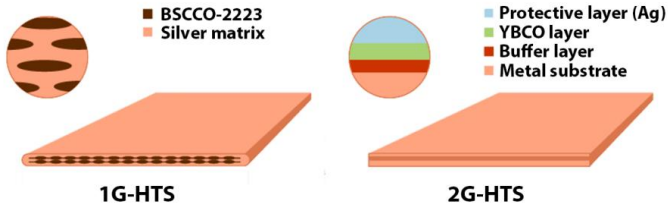

Figure 1.11. *Illustration of architecture of 1G (left) and 2G (right) conductor. Courtesy of SuperOx.*

To offer the perspective for a more economical mass production and to overcome the low performances in high magnetic fields, second generation (2G) HTS tapes or so-called "Coated Conductors" (CCs) architecture, was developed to fabricate flexible YBCO-HTS tapes. In contrast to 1G-HTS tapes, where the processing to thin filaments was preferred, 2G-HTS tapes are now based on thin film technology with multilayer architectures (e.g. protective layer/epitaxial YBCO layer/buffer layers) deposited onto metallic substrates as shown in Figure 1.11. But this process is more complicated compared to the OPiT process for the production of BSCCO due to the necessity of the epitaxial texture of YBCO. When the deposited YBCO is grown directly on the metallic substrate, it leads to a polycrystalline film with high-angle grain boundaries due to the high lattice mismatch, resulting in poor superconducting properties. In addition, the metallic substrates must also contribute to the stability and flexibility of the 2G-HTS tapes. Taking this into account, the substrates can be created according to three different strategies: *Ion Beam Assisted Deposition* (IBAD), *Inclined Substrate Deposition* (ISD) and *Rolling-Assisted Biaxial Texture Substrate* (RABiTS).[33] The IBAD and ISD approach deliver high quality CCs where the desired texture is induced via the growth of buffer layers on polycrystalline stainless steel or Hastelloy substrate. However, IBAD uses ion beam bombardment while ISD uses electron beam evaporation in high vacuum conditions which is not interesting for industrial scalability due to the high investment costs.[7, 34] The RABiTS approach was introduced to allow growing of textured buffer layers without using vacuum conditions. Here, an untextured face centered cubic metallic substrate was multiple cold rolled and recrystallized to obtain a biaxial (*h*00)-texture upon which epitaxial buffer layers can be deposited.[35] Thereby, the ceramic buffer layers are required to act as a texture template or texture transfer layer depending on the substrate approach. For this purpose, the lattice mismatch between buffer and superconducting layers should be as low as possible. These buffer layers can also act as a barrier in order to prevent the outdiffusion of metal ions from the substrates into the

superconducting layer or the indiffusion of oxygen to avoid undesirable substrate oxidation during processing, which would cause problems in terms of mechanical stability.[18, 36] In addition, the thermal expansion of the buffer layer needs to be similar to the one of the superconducting layer in order to reduce the risk of cracking the architecture.

In general, CCs architecture is a delicate approach where buffer layers are commonly stacked on the substrate to meet all the requirements to make the growth of the biaxial textured YBCO thin film with excellent superconducting properties. Furthermore, state-of-the-art CCs are now being introduced by a variety of companies, including American Superconductor, SuperPower, Nexans, Deutsche Nanoschicht, SuNam Co. and Bruker. This path towards economic scalable productions of high-quality superconducting films allows us to implement the coated conductors throughout the energy market.

1.7. $YBa_2Cu_3O_{7-\delta}$ nanocomposite architecture

The challenge is to achieve a cost-effective and high performance YBCO coated conductor with strict requirements for power applications as generators, motors or magnets at high external magnetic fields. Unfortunately, the J_c performances start to drop in the mixed state of type II superconductor due to the vortex motion (Figure 1.12) as discussed in section 1.3.3 (*vide supra*). It becomes crucial to immobilize or to pin the vortices at a fixed position so *vortex pinning* has to enhance the performances of these devices. This means that the goal is to increase the pinning force and to displace the irreversibility field to a higher magnetic field. Vortex pinning is possible by the presence of pinning centers and can be divided into two categories: intrinsic defects in superconductor and artificial non-superconducting phases. As the vortex is depending on the Ginzburg-Landau parameters, namely the superconducting coherence length ξ (the core of vortex) and the London penetration depth λ, the size of the pinning center should be in the range of 2ξ (few nm) and homogeneously distributed in the superconducting matrix. The pinning centers can pin strongly or weakly according to the strength of the pinning force. Pinning is strong when the force is strong enough to deform the vortex. On the other hand, pinning centers smaller than 2ξ give a weak pinning. This means that many weak pinning centers (collective pinning) are needed to pin a vortex. So, the capability to pin vortex depends on the shape, size and distribution of the pinning centers present in the superconducting matrix. The latter also has an influence on the superconducting matrix and its superconducting properties (*vide infra*). Figure 1.12 (red curve) shows a simplified magnetic field dependence of J_c to represent the pinning behavior in three different regions. The first region is a low magnetic field where

the single vortex pinning is dominant and the J_c will remain constant. When the vortex-vortex interactions start above the accommodation field B^* (determined by the criterion $J_c(B^*) = 0.9J_c(0)$), the J_c will decrease according to the power law α.[37] In this region, several vortices are pinned to each pinning center which it is called as small vortex bundle pinning (α = 0.5). When the magnetic field increases, large vortex bundle pinning (α = 1) makes the J_c decrease faster.[38]

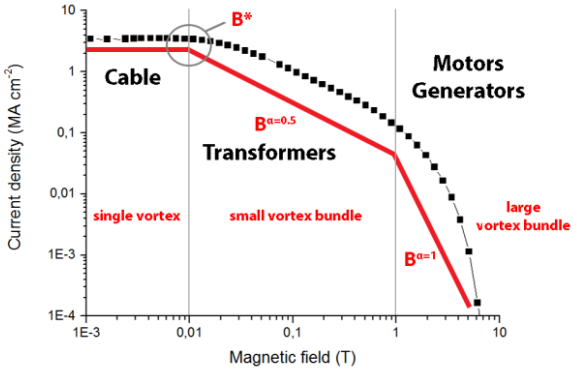

Figure 1.12. *Log-log plot showing the decay of critical current density in the presence of an external magnetic field. The requirements for devices clearly exceed the present performance at this temperature thus limiting the use of YBCO coated conductors in high field power applications. Red curve shows a simplified magnetic field dependence of J_c to represent the pinning behavior in three different regions.*

1.7.1. Intrinsic defects

Intrinsic or natural defects are the crystalline defects generated during the hetero-epitaxial thin film growth. These defects are typically oxygen vacancies, columnar defects, dislocations, twin boundaries, antiphase boundaries, stacking faults, intergrowths, ...[39] (Figure 1.13) and are created in a YBCO thin film. It is important to know that the defects are never superconducting and that they can act as vortex pinning. Noteworthy, it is not necessary that vortex pinning centers are non-superconducting but can just be worse superconducting if the order parameter is limited. The microstrained regions around the particles in the YBCO matrix (*vide infra*) are not the pinning center but they effectively increase the pinning size and thus the pinning force of the particles. So, YBCO performances depend on the capabilities of the vortex pinning centers as well as on a good texture quality of the film. Because the introduction of a higher concentration of natural defects will result in a poorer texture and thus degrade the superconducting properties.

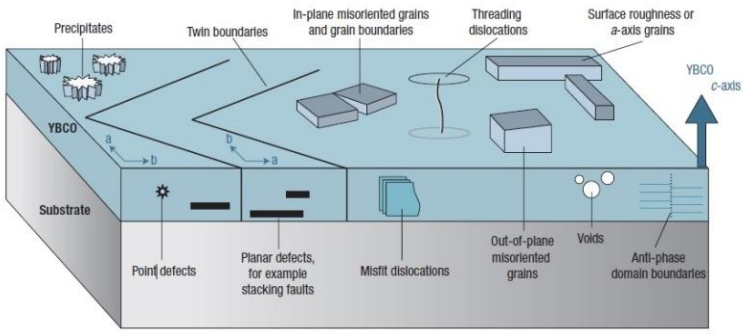

Figure 1.13. *The defects types that can act as pinning centers.*[39]

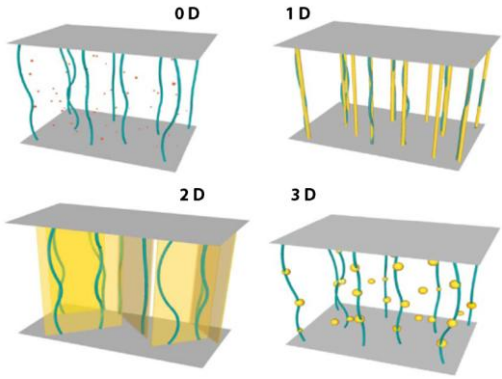

Figure 1.14. *Sketch of the dimensionality of artificial pinning centers (APCs): 0D, 1D, 2D, and 3D-APCs.*[40]

These defects can be classified on the basis of their dimensionality (Figure 1.14).[41]

- 0D (punctual defects as atomic vacancies and cation disorder),
- 1D (dislocations and columnar defects),
- 2D (planar defects as grain boundaries, twin boundaries and stacking faults),
- 3D (precipitates, secondary phases and voids).

The dimensionality and orientation of the defects must also be taken into account as an important criterion known as anisotropic pinning behavior. In this kind of pinning behavior, linear and planar defects are anisotropic pinning centers where the vortex pinning depends on the orientation of the magnetic field and is the strongest when it is in alignment with the defects. If the pinning

centers are not depending on the relative orientation of the magnetic field, they are called isotropic pinning centers.[42] These pinning centers should be distributed throughout the superconducting material to pin a number of vortices as they are present with an average distance of 10-30 nm in between.[3, 9]

The effectiveness of these defects as pinning centers is also depending on the temperature and the magnetic field. The main conclusion is that the distribution, anisotropy and dimension of the defects have an influence on the vortex pinning properties and thus also on the performances of the YBCO. However, the intrinsic defects of superconducting materials are not strong enough to pin the vortices at high magnetic fields for the required applications. This leads to the next challenge to enhance the YBCO performances at high magnetic fields, by introducing artificial pinning centers in the superconducting materials without deterioration of the YBCO texture.

1.7.2. Artificial pinning centers

The incorporation of nano-sized defects has proven to be an effective approach to achieve the immobilization of vortices, i.e. vortex pinning. Besides rare-earth substitution[43], irradiation[44], template modification[45] and optimizing natural growth defects[46], the introduction of nanoparticles or even self-aligned nanocolumns were achieved via pulsed laser deposition and metal-organic chemical vapour deposition. These so-called artificial pinning centers (APCs) can be introduced in different dimensions and shapes, preventing the drastic decrease of J_c at moderate-to-high magnetic fields as well as its anisotropy with respect to the magnetic field direction.[47] Nanocolumns effectively pin the vortices especially at the magnetic field parallel to the columns.[48-50]

In recent years, significant advances in chemical solution deposition (CSD) of both the buffer layer architecture and the superconducting layer have led to high-quality coated conductors and have shown the potential of CSD-based superconductors for a wide range of technological applications.[51, 52] This solution approach offers a less expensive route to coated conductors, being more scalable and faster compared to vacuum deposition methods. Recently, CSD has explored the fabrication of nanocomposite films with formation of effective APCs by the addition of extra metal salts to the YBCO precursor solution, resulting in the spontaneous segregation of non-superconducting secondary phases (called as the *in-situ* approach) such as Y_2O_3, $BaSnO_3$, $BaHfO_3$, $BaZrO_3$ and Ba_2YTaO_6.[53-58] However, this approach offers limited control on the formation and size distribution of the nanostructures and faces issues with reproducibility.

This *in-situ* approach also requires a high controlled heat treatment of roll-to-roll processing equipment which makes it hard-to-reach.

To offer better control over the final microstructural properties of YBCO nanocomposite films, preformed nanocrystals are introduced as APCs. This nanocrystal approach can provide more control over the final nanoparticles properties (e.g., size and distribution) in the YBCO layer. A new challenge has appeared for the researchers as this approach is very complicated and will be discussed more thoroughly in this work.

1.8 Aim of the research

Although we have come closer to H.K. Onnes' dream to build a powerful magnet, the search for a low-cost and scalable process to produce high-quality YBCO nanocomposite based on the coated conductor architecture, is still viable. In recent years, high-temperature superconducting YBCO coated conductors have reached the potential to change the paradigm in large-scale energy applications due to their moderate cooling requirements, unique efficiency and low weight/size ratio. One of the aims in applied-superconductivity research and development has been the low-cost and scalable processing of high-quality YBCO coated conductors in order to meet the requirements for energy applications. Unfortunately, YBCO thin films typically exhibit a strong reduction of the J_c with increasing magnetic field strength caused by vortex motion. To immobilize these vortices, the incorporation of nano-sized defects as so-called artificial pinning centers can be introduced in different dimensions and shapes, preventing the drastic decrease of J_c at moderate-to-high magnetic fields as well as its anisotropy with respect to the magnetic field direction.

In this work, we aim to incorporate single or double metal oxide preformed nanocrystals in the YBCO matrix as artificial pinning centers. The size of the nanocrystals should be between 3 and 10 nm to be able to lead to optimal pinning forces. The novel approach of using preformed nanocrystals, can offer a better control over the size distribution and the composition of nanoparticles during YBCO growth compared to the less efficient self-assembled nanoparticles. We will focus on the behavior of the preformed nanocrystals on the pinning properties and the critical parameters during YBCO growth.

1.9. Outline

In this work, two types of nanocrystals were chosen, i.e. small crystalline single (ZrO_2 and HfO_2) and double ($SrTiO_3$) metal oxide nanocrystals. They were synthesized with diameters in the range of 4-10 nm and capped with hydrophobic ligands to ensure colloidal stability in apolar solvents. However, as the YBCO precursor solution typically provides a more polar environment, e.g., methanol, an important aspect of this research also involves ligand exchange and the appropriate stabilization procedure. For that reason, it is important to stabilize these nanocrystals in low-fluorine based YBCO precursor solutions, leading to highly stable nanocomposite precursors with long shelf-lives. These nanocrystal-containing precursor solutions are deposited on single crystal $LaAlO_3$ substrates via chemical solution deposition technique in order to study the factors which control the microstructure development and the physical properties of the YBCO nanocomposite films.

In chapter two, the basic concepts of the chemistry of the YBCO precursor solution and its chemical solution deposition method are introduced. The chemical solution deposition of YBCO nanocomposite thin films from environmentally benign low-fluorine precursors with the addition of preformed ZrO_2 nanocrystals is discussed in chapter three. In the first part, the careful ligand exchange and phase transfer the oxide nanocrystals is investigated. Secondly, the influence of an appropriate ligand to stabilize the nanocrystals in YBCO precursor solution is observed and in the final part of this chapter, the microstructure and its properties are characterized.

In chapter four, we report on the improvement of the YBCO microstructure and its superconducting properties in nanocomposite thin films by introducing an intermediate dwelling step during the thermal process. This approach improves the formation of the YBCO nuclei density before the YBCO growth. Counter-intuitively, the distribution as well as the miniaturization of ZrO_2 nanocrystals in the YBCO matrix were studied at several intermediate dwelling steps. In view of the implementation of these YBCO nanocomposite films in power applications such as generators and other rotating devices, the superconducting properties of ZrO_2-doped YBCO film were investigated via transport measurements in chapter five to confirm the success of the addition of preformed nanocrystals in the YBCO matrix via CSD-based method.

As it is still unclear what the influence of nanocrystal morphology and its size on the YBCO matrix is, the influence of two different types of HfO_2 nanocrystals is explored in chapter six. An exploration to the use of double metal oxide

nanocrystals is discussed in chapter seven. In this chapter, the microwave-assisted synthesis of double metal oxide $SrTiO_3$ nanocrystals is first introduced and the preformed $SrTiO_3$ nanocrystals are finally introduced in the YBCO matrix in order to improve their compatibility with the YBCO layer.

The work concludes with an overview of the achieved results for a full commercial breakthrough of the formation of YBCO nanocomposite coated conductor on industrial metallic Ni-W substrates in order to verify or not our preformed nanocrystals are capable of meeting the strict requirements for the successful implementation and distribution of coated conductors throughout the energy market.

1.10. References

1. J. Urry, "Climate change and society," pp. 45-59. in Why the social sciences matter**.** Springer, 2015.
2. H. Kamerlingh Onnes, "Further experiments with Liquid Helium. D. On the change of Electrical Resistance of Pure Metals at very low Temperatures, etc. V. The Disappearance of the resistance of mercury," *Proceedings, KNAW,* **14** 113-15 (1911).
3. H. Rogalla and P. H. Kes, "100 years of superconductivity." Taylor & Francis, (2011).
4. D. Larbalestier, A. Gurevich, D. M. Feldmann, and A. Polyanskii, "High-T_c superconducting materials for electric power applications," *Nature,* **414** [6861] 368-77 (2001).
5. W. Meissner and R. Ochsenfeld, "Ein neuer effekt bei eintritt der supraleitfähigkeit," *Naturwissenschaften,* **21** [44] 787-88 (1933).
6. J. Bardeen, L. N. Cooper, and J. R. Schrieffer, "Theory of superconductivity," *Phys. Rev.,* **108** [5] 1175 (1957).
7. J. Feys, "Digitally printed superconducting coatings and patterns." in. Ghent Unversity, 2014.
8. P. Vermeir, "Chemical solution deposition of superconducting $YBa_2Cu_3O_{7-\delta}$ layers in coated conductors." in. Ghent University, 2012.
9. K. De Keukeleere, "Incorparation of metal oxide nanocrystals in high temperature $YBa_2Cu_3O_{7-x}$ superconductors." in. Ghent University, 2016.
10. UAF via http://ffden-2.phys.uaf.edu/webproj/212_spring_2015/
11. G. Bednorz and K. A. Muller, "Possible high-T_c superconductivity in the Ba-La-Cu-O system," *Z. Phys. B,* **64** 189-93 (1986).
12. M. K. Wu*, et al.*, "Superconductivity at 93 K in a new mixed-phase Y-Ba-Cu-O compound system at ambient pressure," *Phys. Rev. Lett.,* **58** [9] 908-10 (1987).
13. H. Maeda, Y. Tanaka, M. Fukutomi, and T. Asano, "A new high-T_c oxide superconductor without a rare earth element," *Jpn. J. Appl. Phys.,* **27** [2A] L209 (1988).
14. I. I. Mazin, "Superconductivity gets an iron boost," *Nature,* **464** [7286] 183-86 (2010).
15. S. Kang*, et al.*, "High-Performance High-T_c Superconducting Wires," *Science,* **311** [5769] 1911-14 (2006).
16. Coalition for the Commercial Application of Superconductors, (CCAS) Superconductivity. Present and Future Applications
17. W. Buckel and R. Kleiner, "Superconductivity: Fundamentals and Applications," pp. 443-45. Wiley-VCH: Berlin, (2004).
18. M. Bäcker, M. Falter, O. Brunkahl, and B. Holzapfel, "Superconducting Films," pp. 673-705. in Chemical solution deposition of functional oxide thin films**.** Edited by T. Schneller, R. Waser, M. Kosec, and D. Payne. Springer, 2013.
19. C. K. Poole, H. A. Farach, and R. J. Creswick, "Handbook of superconductivity." Academic Press, (1999).
20. X. Obradors and T. Puig, "Coated conductors for power applications: materials challenges," *Supercond. Sci. Technol.,* **27** [4] 044003 (2014).
21. CERN via http://home.web.cern.ch/
22. ITER via https://www.iter.org/

23. J. Wang*, et al.*, "The first man-loading high temperature superconducting Maglev test vehicle in the world," *Physica C Supercond,* **378** 809-14 (2002).
24. M. Bäcker, "Energy and superconductors–applications of high-temperature-superconductors," *Z. Kristallogr. ,* **226** [4] 343-51 (2011).
25. A. B. Abrahamsen*, et al.*, "Design study of 10 kW superconducting generator for wind turbine applications," *IEEE Trans. Appl. Supercond.,* **19** [3] 1678-82 (2009).
26. S. S. Kalsi*, et al.*, "Development status of rotating machines employing superconducting field windings," *Proc. IEEE,* **92** [10] 1688-704 (2004).
27. L. Landau and E. Lifschitz, "LD Landau, Collected Papers," (1965).
28. J. Waldram, "Superconductivity of Metals and Cuprates Institute of Physics Publishing." in. London, 1996.
29. H. Takei, H. Asaoka, Y. Iye, and H. Takeya, "Growth of polyhedral $YBa_2Cu_3O_x$ single crystals and their anisotropic properties," *Jpn. J. Appl. Phys.,* **30** [6B] L1102 (1991).
30. Y. Jia*, et al.*, "C-axis critical current density of second-generation YBCO tapes," *Supercond. Sci. Technol,* **23** [11] 115017 (2010).
31. K. H. Sandhage, G. N. Riley, and W. L. Carter, "Critical issues in the OPIT processing of high-J_c BSCCO superconductors," *JOM,* **43** [3] 21-25 (1991).
32. J. Maguire*, et al.*, "Progress and status of a 2G HTS power cable to be installed in the Long Island Power Authority (LIPA) grid," *IEEE Trans. Appl. Supercond.,* **21** [3] 961-66 (2011).
33. M. P. Paranthaman and T. Izumi, "High-performance YBCO-coated superconductor wires," *Mater. Res. Soc. Bull.,* **29** [08] 533-41 (2004).
34. A. Malozemoff*, et al.*, "Low-cost YBCO coated conductor technology," *Supercond. Sci. Technol.,* **13** [5] 473 (2000).
35. A. Goyal*, et al.*, "High critical current density superconducting tapes by epitaxial deposition of $YBa_2Cu_3O_x$ thick films on biaxially textured metals," **69** [12] 1795-97 (1996).
36. G. Pollefeyt, "Chemical Solution Deposition of alternative buffer materials for coated conductors." in. Ghent University, 2015.
37. H. Huhtinen, K. Schlesier, and P. Paturi, "Growth and c-axis flux pinning of nanostructured YBCO/BZO multilayers," *Supercond. Sci. Technol.,* **22** [7] 075019 (2009).
38. G. Blatter*, et al.*, "Vortices in high-temperature superconductors," *Rev. Mod. Phys.,* **66** 1125-388 (1994).
39. S. R. Foltyn*, et al.*, "Materials science challenges for high-temperature superconducting wire," *Nat. Mater.,* **6** [9] 631-42 (2007).
40. X. Obradors*, et al.*, "Growth, nanostructure and vortex pinning in superconducting $YBa_2Cu_3O_7$ thin films based on trifluoroacetate solutions," *Supercond. Sci. Technol.,* **25** [12] 123001 (2012).
41. M. Kaname and M. Paolo, "Artificial pinning center technology to enhance vortex pinning in YBCO coated conductors," *Supercond. Sci. Technol.,* **23** [1] 014001 (2010).
42. T. Puig*, et al.*, "Vortex pinning in chemical solution nanostructured YBCO films," *Supercond. Sci. Technol.,* **21** [3] 034008 (2008).
43. T. Harada and K. Yoshida, "The effect of rare-earth substitution at the Ba site on the flux pinning properties of $Y(Ba_{2-x}R_x)Cu_3O_{7-x}$(for R = La, Pr, and Nd)," *Phys. C,* **391** [1] 1-7 (2003).
44. L. Civale, "Vortex pinning and creep in high-temperature superconductors with columnar defects," *Supercond. Sci. Technol.,* **10** [7A] A11-A28 (1997).

45. K. Develos-Bagarinao*, et al.*, "Enhanced flux pinning in MOD $YBa_2Cu_3O_{7-\delta}$ films by ion milling through anodic alumina templates," *Supercond. Sci. Technol.,* **25** [6] 065005 (2012).
46. S. H. Wee, Y. L. Zuev, C. Cantoni, and A. Goyal, "Engineering nanocolumnar defect configurations for optimized vortex pinning in high temperature superconducting nanocomposite wires," *Sci. Rep.,* **3** 2310 (2013).
47. X. Obradors*, et al.*, "Nanostructured Superconductors with Efficient Vortex Pinning," pp. 303-49. in Comprehensive Nanoscience and Technology**.** Edited by D. L. Andrews, G. D. Scholes, and G. P. Wiederrecht. Academic Press, Oxford, 2011.
48. T. Haugan*, et al.*, "Addition of nanoparticle dispersions to enhance flux pinning of the $YBa_2Cu_3O_{7-x}$ superconductor," *Nature,* **430** [7002] 867-70 (2004).
49. F. J. Baca*, et al.*, "Interactive Growth Effects of Rare-Earth Nanoparticles on Nanorod Formation in $YBa_2Cu_3O_x$ Thin Films," *Adv. Funct. Mater.,* **23** [38] 4826-31 (2013).
50. J. Hänisch*, et al.*, "Formation and pinning properties of growth-controlled nanoscale precipitates in $YBa_2Cu_3O_{7-\delta}$/transition metal quasi-multilayers," *Supercond. Sci. Technol.,* **19** [6] 534-40 (2006).
51. X. Obradors*, et al.*, "Progress towards all-chemical superconducting $YBa_2Cu_3O_7$-coated conductors," *Supercond. Sci. Technol.,* **19** [3] S13-S26 (2006).
52. J. Feys*, et al.*, "Ink-jet printing of $YBa_2Cu_3O_7$ superconducting coatings and patterns from aqueous solutions," *J. Mater. Chem.,* **22** [9] 3717-26 (2012).
53. L. Lei*, et al.*, "Influences of Y_2O_3 nanoparticle additions on the microstructure and superconductivity of YBCO films derived from low-fluorine solution," *Mater. Chem. Phys.,* **127** [1] 91-94 (2011).
54. S. Ye*, et al.*, "Preparation of solution-based YBCO films with $BaSnO_3$ particles," *Phys. C,* **471** [7] 265-69 (2011).
55. M. Erbe*, et al.*, "$BaHfO_3$ artificial pinning centres in TFA-MOD-derived YBCO and GdBCO thin films," *Supercond. Sci. Technol.,* **28** [11] 114002 (2015).
56. F. Ding*, et al.*, "Strong enhancement flux pinning in MOD-$YBa_2Cu_3O_{7-x}$ films with self-assembled $BaTiO_3$ nanocolumns," *Appl. Surf. Sci.,* **314** 622-27 (2014).
57. J. Gutierrez*, et al.*, "Strong isotropic flux pinning in solution-derived $YBa_2Cu_3O_{7-x}$ nanocomposite superconductor films," *Nat. Mater.,* **6** [5] 367-73 (2007).
58. M. Coll*, et al.*, "Size-controlled spontaneously segregated Ba_2YTaO_6 nanoparticles in $YBa_2Cu_3O_7$ nanocomposites obtained by chemical solution deposition," *Supercond. Sci. Technol.,* **27** [4] 044008 (2014).

Chapter two

From precursor formulation to epitaxial thin film

In this chapter, the chemistry of the YBCO precursor solution and its chemical solution deposition method will be discussed.

Adapted from:

H. Rijckaert, J. De Roo, K. Roeleveld, G. Pollefeyt, J. Bennewitz, M. Bäcker, F. Lynen, K. De Keukeleere and I. Van Driessche, Microwave-assisted $YBa_2Cu_3O_7$ precursors: fast and reliable method towards chemical precursors for superconducting film. Journal of the American Ceramic Society, 2017. 100(6). 2407–2418

H. Rijckaert, J. Pelemans, J. Hänisch, R. Nast, J. Bennewitz, G. Pollefeyt, J. De Roo, M. Bäcker, M. Hemgesberg, K. De Keukeleere and I. Van Driessche, Ink-jet Printing of Nanocomposite film: From Low-Fluorine $YBa_2Cu_3O_7$ inks with Preformed Nanocrystals to Superconducting Films. In preparation.

2.1. Introduction

As mentioned in the previous chapter, YBCO coated conductors are considered to be very promising materials for a variety of technological applications such as motors, generators, transmission cables and other power systems. However, it is complicated to achieve a highly biaxially YBCO texture on the desired substrates. Several methods are introduced to prepare a thin film with the desired properties. Up to now, textured superconducting YBCO films with good properties for the coated conductor architecture are realized via *in-situ* or *ex-situ* growth techniques. These techniques are characterized, based on their way to form the desired phase (i.e. YBCO) during the deposition.

2.2. *In-situ* vs. *ex-situ* growth techniques

The *in-situ* growth techniques such as pulsed laser deposition (PLD), sputtering, thermal co-evaporation, liquid phase epitaxy and metal-organic chemical vapor deposition (MOCVD) produce YBCO thin films with excellent properties due to the ability of the atomic-level control. This *in-situ* growth method is a layer-by-layer process where the mobility of adatoms via surface diffusion is essential and is a non-equilibrium process. However, this method is considered too expensive due to the required high vacuum system during the deposition, hampering its applicability on industrial scale.[1] For the commercial breakthrough of coated conductors, an efficient and low-cost process becomes crucial. Over the last years, chemical solution deposition (CSD) has gained a lot of interest due to its low-cost and easy scalability with high efficiency. This CSD method is an *ex-situ* approach which means that the desired phase is not directly formed after the deposition but formed after a subsequent annealing process at specific temperature.

2.3. Chemical solution deposition

Among these different techniques, CSD is the best alternative for large-scale production of YBCO CCs because of its high efficiency and high speed at low processing costs. This *ex-situ* CSD deposition method offers control over the film composition on a molecular level through the control over the precursor solution chemistry and its stoichiometry. Typically, the YBCO precursor solution (Figure 2.1, stage I), containing the required metal-organic salts and additives, is deposited on the substrate at ambient pressure. The as-deposited wet film is partially evaporated and decomposed (stage II) and subsequently crystallized into the desired crystalline YBCO thin film via an appropriate thermal processing

procedure (stage III). The key to successful YBCO thin film starts with a precursor solution synthesis to obtain a stable and homogeneous precursor solution.

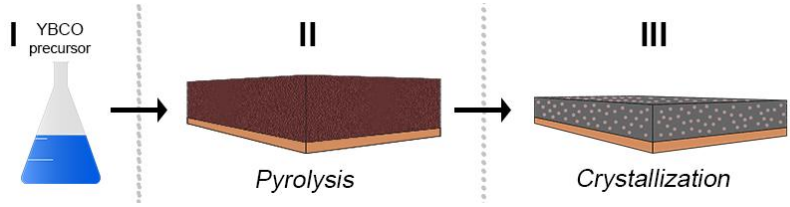

Figure 2.1. *Schematic illustration (not scaled) of the procedure for fabricating YBCO thin layer via CSD process. The process begins with (Stage I) the formulation of YBCO precursor solution. (Stage II) Deposition of YBCO precursor solution on desired substrate and its thermal decomposition. (Stage III) The pyrolyzed layer is thermally treated to crystallize epitaxial YBCO thin film.*

The most established CSD approach is based on the *ex-situ* BaF_2 process and uses trifluoroacetate (TFA) salts typically dissolved in an organic solvent such as methanol. Several researchers[1, 2] have already demonstrated that this TFA route is a suitable metal-organic deposition (MOD) method to produce low-cost epitaxial YBCO thin films without the requirement of a high-vacuum system. The TFA-MOD process is based on the formation of BaF_2 as an intermediate phase, which is believed to be beneficial over the formation of $BaCO_3$, as the latter can disrupt the YBCO formation due to its high decomposition temperature.[3] BaF_2 on the other hand, is stable up to high temperatures, but can be decomposed at 650 °C by the addition of a water vapor to the processing atmosphere.[2] This approach has expanded to one of the most successful growth methods of epitaxial YBCO films with a high J_c in self-field at 77 K on single crystal substrates.

Nevertheless, some potential drawbacks can be identified in the YBCO solution preparation which could hamper the commercial implementation. Several authors have shown that the YBCO precursor can be converted into high quality YBCO thin films by heat treatment under controlled conditions.[4, 5] Afterwards, critical current densities J_c of >1 MA/cm^2 were obtained. Thus, a very important feature in TFA-based YBCO processing is controlling the growth of YBCO during the thermal treatment. However, the presence of possible impurities in YBCO precursor solutions can degrade the final microstructure and superconducting properties of the YBCO thin film due to the improper decomposition of the precursor.[6, 7] Araki *et al.*[8] have shown that the synthesis procedure for the preparation of TFA salts which starts from acetates and trifluoroacetic acid (TFAH), as described by Gupta *et al.*[2] exhibits an uncontrolled amount of water

(> 3 wt%) and other chemical impurities (i.e. acetic acid). Thus, they developed a purified YBCO precursor solution with a refining process and obtained a high J_c after a long pyrolysis step of ~12 hours.[8] Therefore, several authors made large efforts towards the optimization of the TFA precursor synthesis procedure and the pyrolysis.[9-11] The synthesis procedure of Roma *et al*.[9] starts from YBCO powder, which is dissolved in a mixture of excess trifluoroacetic acid anhydride (TFAA) and a small amount of TFAH (10 vol%) as catalyst resulting in the TFA metal-salts. This procedure typically generates an almost "anhydrous" TFA precursor with a water content of less than 1 wt%. However, this synthesis procedure still suffers from some disadvantages such as a long reaction time of 72 hours and off-stoichiometry of TFAA. Additionally, the use of a conventional heat source (oil bath heating) results in an inefficient thermal energy transfer which may result in a temperature gradient in the reaction volume as shown in Figure 2.2a. The combination of these disadvantages may result in the formation of by-products other than the TFA metal-salts.

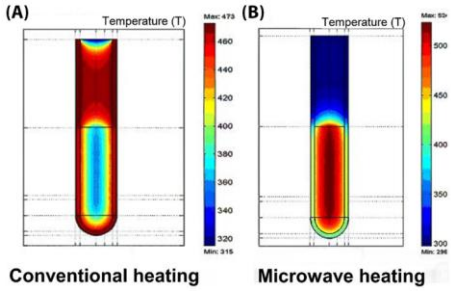

Figure 2.2. *Illustration of (A) conventional and (B) microwave heating.*[12]

The microwave processing method that we are introducing in this thesis can offer a solution to a number of problems stated above. Microwave radiation provides rapid and uniform heating of the reagents and solvents by directly coupling to the molecules, hereby resulting in a more efficient energy transfer (Figure 2.2b) and an enhancement of the reaction rate.[13, 14] By applying microwave radiation, we were able to dissolve commercial YBCO powder in a TFAA-acetone mixture, yielding extremely pure TFA salts. When comparing our microwave-assisted acid dissolution with conventional oil bath heating, it becomes clear that the drastic shortening of the synthesis time by a factor of 72 and the high purity of the precursor solution led to significant advances towards more viable YBCO solution processing. This fast and reliable method can equivalently be used for the preparation of a low-fluorine (LF) YBCO solution by changing the ratio of trifluoroacetic and propionic acid.

2.3.1. Thermal process of fluorine based $YBa_2Cu_3O_{7-\delta}$ layer.

The overall thermal process of fluorine based YBCO film is already described in literature[15, 16] and can be divided in three stage: (1) the thermal decomposition (pyrolysis), (2) crystallization (growth) and (3) the annealing process. The decomposition of the metal organic precursor is one of the critical steps in CSD-based growth of fluorine based YBCO films. The pyrolysis step (Figure 2.3a) is implemented to remove organic constituents which have a detrimental effect on the final superconducting properties. The pyrolysis process consists of a heating rate (3-5 K min^{-1}) up to 190 °C under humid O_2 atmosphere. This wet atmosphere is introduced at 100 °C to avoid the early sublimation of Cu metal salts. The inlet gas is humidified by passing it through a water bath maintained at room temperature. In the region between 190 and 220 °C, the densification [1] process starts which is an endothermic drying that can lead to a buckling effect. Therefore, a slow heating rate of 1 K min^{-1} was introduced to avoid the buckling effect. Next, the metal-organic precursors [2] start to decompose between a temperature range of 220 and 400 °C (*Vide infra*) and is an exothermic process, which can lead to a cracking effect.[11] After the pyrolysis step, the microstructure consists of CuO nanoparticles embedded in an amorphous matrix of $Ba_{1-x}Y_xF_{2-x}$.

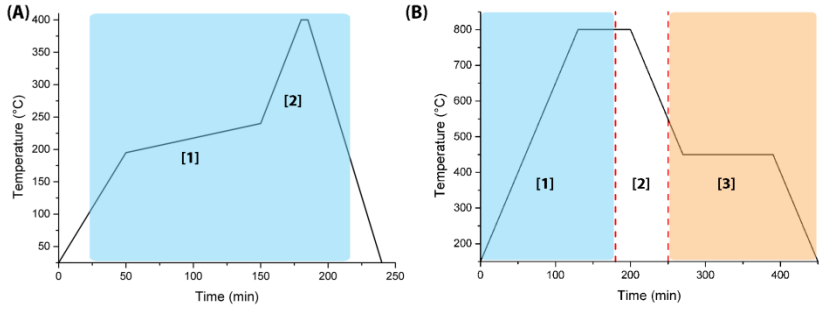

Figure 2.3. *Schematic representation of (A) the pyrolysis process and (B) the thermal process of fluorine based YBCO layer. The regions marked in blue indicate that the flowing gas is humidified.*

To fabricate an YBCO layer (Figure 2.3b), the pyrolyzed layers are heated [1] to a high temperature between 790-840 °C to crystallize the tetragonal phase of YBCO. A temperature of 840 °C cannot be exceeded because a decomposition of the YBCO phase will occur. During this heat treatment, a wet O_2 in N_2 atmosphere was introduced to decompose the BaF_2 phase (blue marked region in Figure 2.3b) and is known as the *ex-situ* BaF_2 process.[1, 2] However, the

nucleation starts during the heating up to the crystallization temperature and takes place at the substrate interface. The YBCO growth rate depends on the water pressure, oxygen pressure, gas flow rate and growth temperature. YBCO formation will not occur when the wet atmosphere is switched to a dry atmosphere and when cooling down [2].

The *ex-situ* BaF_2 process is reported in literature where the $Y_2Cu_2O_5$, BaF_2 and CuO are converted into YBCO by the release of HF by introducing H_2O at the growth interface. The overall reaction in the fluorine based process is proposed as:

$$0.5\ Y_2Cu_2O_5\ (s) + 2\ BaF_2(s) + 2\ CuO\ (s) + 2\ H_2O\ (g) \rightarrow YBa_2Cu_3O_{7-\delta} + 4\ HF\ (g) + \frac{x}{2}O_2(g) \qquad \text{Eq. 2.1}$$

After the crystallization, the oxygenation [3] process follows, under a dry oxygen atmosphere, to convert finally the tetragonal $YBa_2Cu_3O_6$ phase into the superconducting orthorhombic YBCO phase. This process takes place between 350-600 °C. The dwell time is depending on the used oxygenation temperature. Theoretically a lower temperature gives rise to better superconducting properties. However, a low temperature leads to a decrease in O_2 diffusion in the YBCO layer.

2.3.2. Preparation of YBCO precursor solution

In this research, the TFA-YBCO precursor solution is prepared by dissolving desiccated commercial $YBa_2Cu_3O_x$ powder (x ~ 6.7-9.5) with a controlled stoichiometry of TFAA in acetone as solvent. First, the YBCO powder was dried in a vacuum oven at 150 °C for 24 h to remove any adsorbed water. The 0.75 mmol dried YBCO powder was mixed with 6.5 equivalents TFAA and 3 mL dry acetone in a 10 mL microwave vial for the preparation of TFA-YBCO. This mixture was subjected to microwave heating under an inert atmosphere (Argon, to avoid the water absorption from the ambient) for 30 minutes at 100 °C using a Discover SP CEM microwave operating at 2.45 GHz with a maximum power of 20 W. After the dissolution, a dark blue-green solution was obtained, which is centrifuged for 2 minutes at 3000 rpm or at a relative centrifugal force of 1620 x g. The supernatant was filtered with 5 µm filter and transferred to a 10 mL boiler flask and the solvent was evaporated under vacuum using a rotary evaporator. The desired mixture of TFA-YBCO became a viscous dark-green gel and is diluted with anhydrous methanol to obtain a total metal ion concentration of 1.5 mol L^{-1}. This solution is kept in sealed vials and can be stored for several months under an inert atmosphere without precipitation.

Table 2.1. *ICP measurements of different TFA-YBCO precursor solution obtained after the microwave-assisted method indicating the Y^{3+}, Ba^{2+}, Cu^{2+} and total metal concentration.*

Sample	$[Y^{3+}]$ mol L^{-1}	$[Ba^{2+}]$ mol L^{-1}	$[Cu^{2+}]$ mol L^{-1}	$[M^{x+}]$ mol L^{-1}
TFA-YBCO 1	0.253	0.490	0.729	1.472
TFA-YBCO 2	0.253	0.492	0.735	1.479
TFA-YBCO 3	0.252	0.489	0.728	1.470
TFA-YBCO 4	0.226	0.500	0.751	1.478
Average	0.246	0.493	0.736	1.475
Error of the average	0.013	0.005	0.011	0.004
Stoichiometric	1.000	2.004	2.992	

This microwave-assisted method leads to a yield of about 98 %, thus the YBCO powder almost completely dissolved in a stoichiometry of Y:Ba:Cu = 1±0.01:2±0.01:3±0.01 as confirmed by ICP-OES analysis (Table 2.1). Compared to the conventional synthesis procedure as described by Roma *et al.*[9], we only used a stoichiometric amount of TFAA and removed the TFAH catalyst because microwaves themselves can be used to overcome high activation energies for product formation by selectively coupling to intermediates in the transition states.[14] Due to this efficient energy transfer of microwave heating, the synthesis time can be facilitated.[17, 18] It results in a reduction of preparation time by a factor of 72 compared to conventional heating by oil bath as described by Roma *et al.*[9] Instead, the chemical reaction of YBCO powder with TFAA via the microwave-assisted treatment is given in Eq. 2.2.

$$YBa_2Cu_3O_x + 6.5\,TFAA \rightarrow Y(TFA)_3 + 2\,Ba(TFA)_2 + 3\,Cu(TFA)_2 \qquad \text{Eq. 2.2}$$

As TFAH is very hygroscopic[19] and is not introduced as catalyst in this microwave synthesis, it leads to the great advantage of the lack of water in this chemical reaction. Consequently, the water content depends now on the used solvents and starting precursors. Therefore, this microwave-assisted approach leads to a precursor solution with a very low H_2O content (<0.5 wt%, determined via the Karl Fischer method) when high purity starting products are used. Moreover, the microwave-assisted dissolution of YBCO powder always delivered highly stable TFA precursors with low water content, suitable for the deposition of YBCO films and potentially interesting for their industrial scalability.

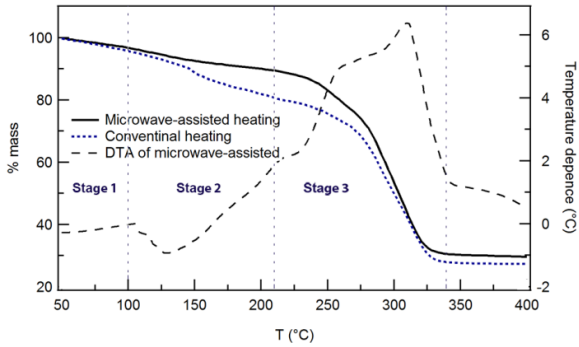

Figure 2.4. *TGA-DTA record of TFA-precursor derived from microwave-assisted and conventional heating with heating ramp of 10 K/min and air atmosphere.*

The decomposition of the metal organic precursor is one of the critical steps in CSD-based growth of high quality ceramic films. TGA-DTA analysis can give detailed insights in the temperature dependency of the decomposition. Early works affirmed that TFA metal-salts start to decompose at the range between 200 and 250 °C.[1] From the TGA analysis (full black line), shown in Figure 2.4, it can be seen that the weight loss starts at 100 °C and the precursor is fully decomposed at 340 °C with a total mass loss of around 70 %. The mass loss as a function of the temperature can clearly be divided in three separate stages.[7] The first stage (from 50 to 100 °C) shows the dehydration and evaporation of organic solvents with a very small mass loss of around 2 %, which is lower compared to the mass loss of 8 % for non-purified TFA-YBCO precursor obtained via the conventional preparation method,[8, 9] confirming the small water content. The second stage between 100 and 210 °C was previously attributed to the evaporation of coordinated solvents and results in a mass loss of approximately 10 %. Starting at 210 °C, the thermo-oxidative decomposition of the TFA metal-salts takes place with a broad exothermic peak in the DTA signal which indicates the successful decomposition of the three TFA-precursors, $Y(TFA)_3$, $Cu(TFA)_2$ and $Ba(TFA)_2$, leading to a large mass loss (~60 %). As this can induce a large shrinkage during thin film processing the third stage is considered to be the critical step in the decomposition of TFA precursors.[9, 11]

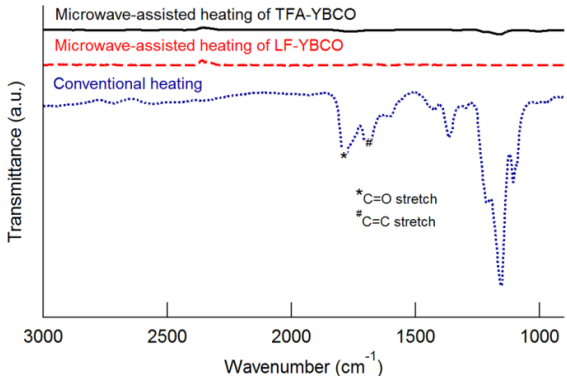

Figure 2.5. *ATR-FTIR spectra of microwave-assisted (black full line) and conventional heating (blue dotted line) synthesis of TFAA-acetone mixture compared with microwave-assisted (red dashed line) synthesis of TFAA/propionic acid-acetone mixture.*

The TGA analysis of both microwave-assisted (full black line) and conventional (blue dotted line) heated TFA precursors shows a difference in the decay in the second stage (between 100 and 210 °C), as seen in Figure 2.4. We hypothesized that the mass loss in the sample prepared by conventional heating, is due to high boiling impurities, formed during the dissolution. To facilitate the analysis of the organic content, both dissolution methods (microwave and conventional) were repeated in the absence of YBCO powder. After the microwave-assisted dissolution of the TFAA-acetone mixture, a yellow solution was obtained compared to a dark orange-brown solution after the conventional heating treatment, confirming the occurrence of by-products in the latter. The resulting solutions were evaporated at 80 °C, resolved in acetone and investigated via ATR-FTIR (Attenuated total reflection-Fourier transform infrared) spectroscopy, given in Figure 2.5. The microwave-assisted solution (full black line) showed no characteristic peaks which means that all the volatiles (acetone and TFAA) were removed during evaporation and no high boiling molecules were formed during the microwave heat treatment. The IR spectrum of the conventional heated solution (blue dotted line) contained characteristic peaks. The C=O stretching (marked with symbol *) peak at 1780 cm^{-1} is related to an unsaturated ketone. Moreover, the C=C stretch (marked with symbol $^{\#}$) is clearly visible on the spectrum at 1684 cm^{-1}. NMR analysis is used to determine the structure of unknown by-products in the conventional heating solution.

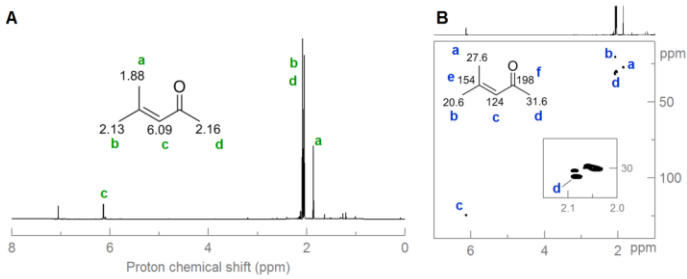

Figure 2.6. *^{1}H NMR and (B) ^{1}H-^{13}C-HSQC spectra of the conventional heating solution.*

From the ^{1}H-NMR spectrum of the solution prepared via conventional heating without adding YBCO powder (Figure 2.6a), the predominant compound 4-methylpent-3-en-2-one or mesityl oxide (MO) is recognized. This is also confirmed by 2D NMR techniques such as HSQC (Figure 2.6b) and HMBC (see Figure A2.1 in Appendix A). It confirms the presence of characteristic peaks of unsaturated ketone shown on ATR-IR spectrum (Figure 2.5).

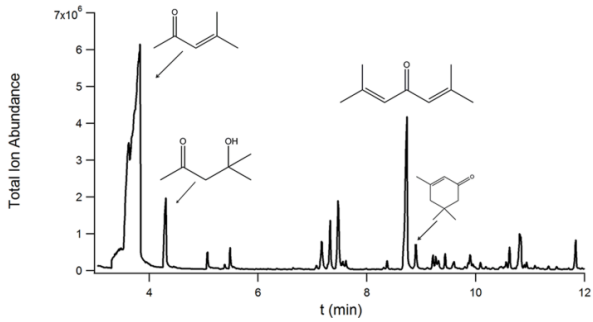

Figure 2.7. *GC spectrum of the conventional heating solution (other small peaks are degradation of the products or system/sample related).*

Table 2.2. *Quantitative relative ratio of the by-products with their boiling point from acetone condensation.*

Reactant	Relative ratio (%)	Boiling point (°C)
Diacetone alcohol	6.1	168
Mesityl oxide	77.8	130
Phorone	14.2	197
Isophorone	1.9	215

Thus, the conventional heating mainly leads to the formation of MO which originates from the aldol condensation of acetone. As described by Nikolopoulos *et al.*[20], acetone condensation does not only lead to MO but also to 4-hydroxy-4-

methylpentan-2-on or diacetone alcohol (DAA). To clarify the condensation reaction using conventional heating, GC-MS was investigated to identify other by-products. It is clear in the GC spectrum (Figure 2.7) and MS-spectra (see section A1.2 in Appendix A) that other products than MO are formed, namely DAA, phorone (2,6-dimethylhepta-2,5-dien-4-on) and isophorone (3,5,5-trimethyl-2-cyclohexene-1-one). The relative ratio of these by-products is given in Table 2.2. Actually, MO is the predominant compound with the relative ratio of 77.8 % and is also confirmed by NMR analysis. This elucidates the next reaction pathway in the acetone condensation process (Figure 2.8). The first step is the self-condensation of acetone to DAA and the second step is the dehydration of DAA to MO. The condensation of acetone to DAA can be catalyzed by either basic or acidic sites while the dehydration of DAA to MO is acid-catalyzed. Here, we study the dissolution of YBCO powder to metal salts using TFAA, because TFAA is the acid anhydride of TFA and can act as a catalyst. Thus, the MO is mainly formed via the condensation of acetone acid-catalyzed by TFAA with DAA as an intermediate product which is quickly converted to MO. The minor by-products phorone and isophorone are formed due to over-condensation. However, these by-products are not observed in the microwave-assisted solution without TFA metal salts, and thus the microwave-assisted method provides a highly stable TFA precursor solution with less impurities. Furthermore, a viscosity of 3.5±0.1 cP for 1.5 M TFA-YBCO solution is obtained for the microwave-assisted solution. This is lower compared to the viscosities of 4 cP for 0.75 M TFA-YBCO reported by Roma *et al.*[9] using conventional heating. This could be explained by the absence of the condensation by-products in microwave-assisted method which could influence the viscosity of the total solution. Although, higher viscosities can be desirable for the preparation of thicker YBCO films, a more accurate control over the rheological properties can be obtained as one can start from a high purity YBCO precursor solution.[21]

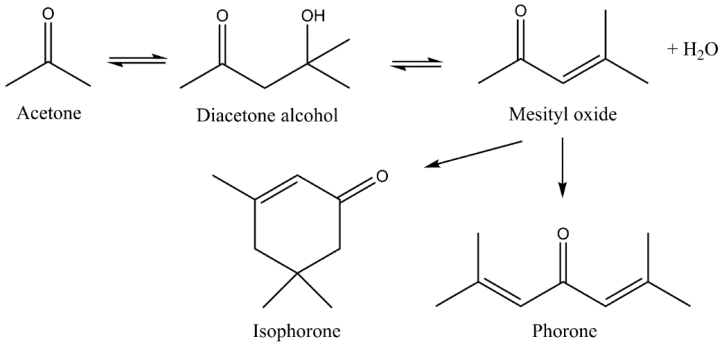

Figure 2.8. *Main reaction pathways in the acetone condensation process.*

2.3.3. Generalization for the preparation of the YBCO precursor

Currently, CSD research is evolving towards the use of an YBCO precursor with a lower fluorine content to reduce the release of fluorinated compounds during the thermal process.[10] In general, complex additives or solvent mixtures are necessary during the preparation of low fluorine solutions to improve the stability of metal ions (mainly for copper).[22, 23] Especially, the stabilization of the metal ions can lead to an improved growth mechanism, resulting in thin films with high quality.[24, 25] In this work, a LF-YBCO precursor solution with a 66 % reduction in fluorine content is synthesized via microwave heating. The precursor is prepared by mixing TFAA and propionic acid in acetone. This results in the formation of highly pure metal salts with less impurities (or by-products) as confirmed in the ATR-IR spectrum (Figure 2.5, red dashed line) of the purified solution without the presence of YBCO powder. Thus, the aldol condensation is not catalyzed by the presence of propionic acid. This microwave-assisted method also results in stable YBCO precursor solution without the formation of precipitates and remains stable for several weeks without additives (Figure 2.9). It shows that the microwave-assisted method could result in YBCO precursor solutions with different contents of fluorine by adjusting the ratio between TFAA and propionate acid. However, the microwave-assisted method does not give the ability to tune YBCO stoichiometry. For this latter, we work in this thesis with LF-YBCO precursor solution prepared by dissolving Y-propionate, Ba-TFA and Cu-propionate in a desired Y:Ba:Cu ratio plus additives in methanol. This reaction mixture is heated to 60 °C for 30 min on a hot plate and the total metal concentration of YBCO is subsequently adjusted to desired concentration (1.5 mol L^{-1}) by adding methanol.

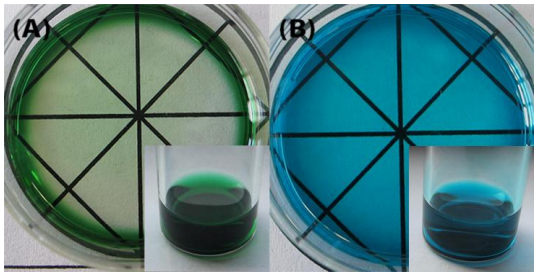

Figure 2.9. *Images of the different YBCO precursor solution after one week: (A) TFA-YBCO and (B) LF-YBCO, indicating its stability as precipitations remain absent.*

2.4. Non-vacuum deposition techniques.

After obtaining a stable and reliable precursor solution, it has to be deposited on the appropriate substrate via different non-vacuum deposition techniques. These different techniques can be applied to obtain a homogeneous wet thin film which can be transformed to the crystalline thin film through thermal process. In this thesis, the spin-coating technique is commonly used because it is a rapid and useful technique for depositing thin films. However, spin-coating is a typical lab-scale technique and shows a limited scalability with regards to the processing. In contrast to spin-coating, other techniques such as dip-coating and ink-jet printing can further strengthen the industrial feasibility as these techniques can offer the opportunities for the deposition of large-scale production of coated conductors.

2.4.1. Spin-coating.

Spin-coating has three important aspects: wetting, thinning and drying of the wet coating. In the first aspect, a quantity of the desired precursor solution is deposited onto an appropriate substrate via a pipette or syringe. It is important to ensure a good wetting of the precursor solution on the substrate as it results in a good coverage of the solution and thus a good coating quality. Next, the spin-coater is accelerated to a faster spinning speed (in the range of a couple thousand rotations per minute, rpm) to spread out the precursor solution on the substrate and to remove the excess amount of precursor solution. The ramping rate and final spin speed have an impact on the final coating thickness (thinning) and may also have an influence on the uniformity of wet coating. Finally, this spin speed is kept constant for a period to dry of the wet coating via the solvent evaporation (often methanol). After spin-coating, the as-deposited substrates are subjected to further thermal processing.[26] For Newtonian fluids, the final coating thickness (h_f) can be predicted in terms of the key solution parameters according to:

$$h_f = c_0 \left(\frac{e}{2(1 - c_o)K} \right)^{1/3} \qquad \text{Eq. 2.3}$$

where e is the evaporation depending on the spin speed (ω) and $K = \rho\omega^2(3\eta)^{-1}$ depending on the density (ρ) and viscosity (η) of the precursor solution. Thus, the coatings have the best quality when the precursor solutions fulfill the fluid properties and when the solvent is not evaporating too quickly. In this thesis, the precursor solutions were deposited using a spin coater model CHEMAT.

2.4.2. Experimental spin-coating of YBCO precursor solutions.

In this thesis, we only show the ability to fabricate a TFA-YBCO thin film to confirm the introduction of microwave dissolution of YBCO powder and focus further on the use of LF-YBCO (66 % fluorine reduction) precursor solutions as environmentally benign precursors. First, the TFA-YBCO precursor solutions were deposited on (100)-$LaAlO_3$ single crystal substrates by means of spin-coating. Prior to coating, the parameters of cleaning, deposition and thermal procedure of Roma *et al*.[9] were used and are described as followed. Before the deposition, the $LaAlO_3$ substrates were ultrasonic cleaned with acetone and methanol to remove adsorbed organics. The 1.5 M TFA-YBCO precursor solutions were spin-coated with the spin rate of 6000 rpm and a spin time of 2 min. The as-deposited layer was preheated at 65 °C for 3 minutes to evaporate the solvent. The coated gel films were pyrolyzed in a humidified oxygen atmosphere. The sample temperature was increased from room temperature at a heating rate of 3-5 °C/min to 310 °C with a dwell time of around 30 min at 310 °C. The standard pyrolysis results in a layer without any inhomogeneities such as buckling or cracks. Subsequently, the pyrolyzed thin film of TFA-YBCO on $LaAlO_3$ substrate undergo a high temperature thermal treatment (sintering and annealing) at 795 °C in a humid 200 ppm oxygen/nitrogen atmosphere for 2.5 hours. A water bath was used to humidify the gas by bubbling it through water at 23 °C. The gas was humidified until the dwelling at the crystallization temperature of 795 °C for 45 min and switched back to the dry gas mixture for 15 min before the cooling down to the annealing step. During the annealing step, it was switched to dry oxygen at 450 °C for 2 hours to change the YBCO crystal structure from tetragonal into orthorhombic to obtain good superconducting properties.

The epitaxial quality of the YBCO thin film was analyzed by θ-2θ diffraction patterns. The XRD spectrum of TFA-YBCO (Figure A2.6, Appendix A) shows very strong (00ℓ) YBCO reflections - 2θ = 22.8° (003), 30.6° (004), 38.5° (005) and 46.6° (006) - without any sign of random YBCO or impurities. Next, the thin film should exhibit a smooth and homogeneous microstructure in order to achieve a J_c. FIB-SEM analysis shows that the thickness of the YBCO film is 50-100 nm determined from the cross-sectional view. However, a thickness of 200-250 nm is obtained from a TFA-YBCO precursor prepared via conventional heating. The relatively low thickness of the microwave-assisted TFA-YBCO layer is believed to be caused by the low viscosity of the precursor solution. Thicker films can, however, be achieved by enhancing the viscosity and/or metal concentration of the precursor and by controlling the wetting behavior and the deposition

parameters. In this thesis, we focused on the latter parameters. The substrates were first rinsed with isopropanol and afterwards heated to 400 °C on a hot plate in air, instead of using ultrasonic cleaning. The spin rate was decreased to 2000 rpm while the spin rate described in the work of Roma *et al.*[9] was 6000 rpm. These mentioned modifications led to a thickness of 250-300 nm after the crystallization step as confirmed by the cross-section determined via FIB-SEM (see inset Figure 2.10a). More importantly, it is also clear from this cross-section and surface (Figure 2.10a) that the film is homogeneous and crack-free without the presence of any *a/b*-oriented grains, which could decrease the superconducting properties. In Figure 2.10b, the $LaAlO_3$/YBCO interface was studied by HRTEM, which confirms that the YBCO layer grows fully (00ℓ)-oriented without the formation of secondary phases. The selected area electron diffraction (SAED) pattern is shown in the inset of Figure 2.10b which further confirms the excellent biaxial alignment and the cube-on-cube orientation relationship between YBCO and LAO. These excellent structural properties yielded YBCO films with J_c up to 3.5 MA cm^{-2} in self-field at 77 K (measured inductively with a voltage criterion of 50 µV), similar to the results obtained via the conventional TFA precursors by Roma *et al.*[9]

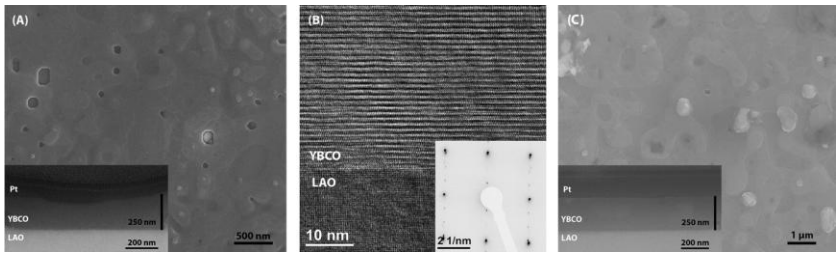

***Figure 2.10**. TFA-YBCO thin film obtained after modifying the wetting behavior and the deposition parameters: (A) Topographical SEM image with cross-sectional view as inset and (B) HRTEM of LAO [100]/YBCO [001] interface (inset shows diffraction pattern). LF-YBCO thin film: (C) Topographical SEM image with cross-sectional view as inset.*

The YBCO thin film, starting from 1.08 M LF-YBCO precursor solutions, was spin-coated on the $LaAlO_3$ substrate via spin-coating with 2000 rpm for 1 min. Prior to spin-coating, the $LaAlO_3$ substrates were cleaned with isopropanol and heated to 400 °C to improve wettability. Figure A2.7 in Appendix A shows that the θ-2θ spectrum of LF-YBCO thin film is (00ℓ)-oriented without secondary phases. However, a SEM image (Figure 2.10c) of a LF-YBCO thin film shows the presence of a Y-rich secondary phases such as Y_2O_3 and $Y_2Cu_2O_5$ on the YBCO surface. Nevertheless, compared to the standard TFA-YBCO thin film, the YBCO surface of the LF-YBCO film shows better homogenous and dense layers with a

thickness of 250-270 nm (see inset Figure 2.10c). This LF-YBCO film (see inset Figure 2.10c) also shows less film roughness than the standard TFA-YBCO (inset Figure 2.10a), indicating that a lower fluorine content leads to smoother layer. The epitaxial growth was observed for the LF-YBCO precursor, giving rise to superconducting performances with J_c up to 4 MA cm^{-2} in self-field at 77 K compared to Palmer *et al.*[22] However, spin-coating technique offers no possibilities for the up-scalable production of long-length coated conductors. Ink-jet printing technique can fulfill the demands such as cost-effectiveness and easy scalability which makes this technique an ideal candidate.

2.4.3. Ink-jet printing.

Ink-jet printing is a non-contact deposition technique where the ink can be stored in a closed cartridge, leading to lower amounts of ink losses and a drastic increase in precursor lifetime due to avoiding any form of contamination. This technique shows some key advantages, as it (Figure 2.11) can easily deliver small droplets in accurate positions with the ability to control the film thickness precisely, and it enables the multi-deposition of several layers without additional additives. It can also introduce the possibility of depositing either full coating or patterns and structures.[27]

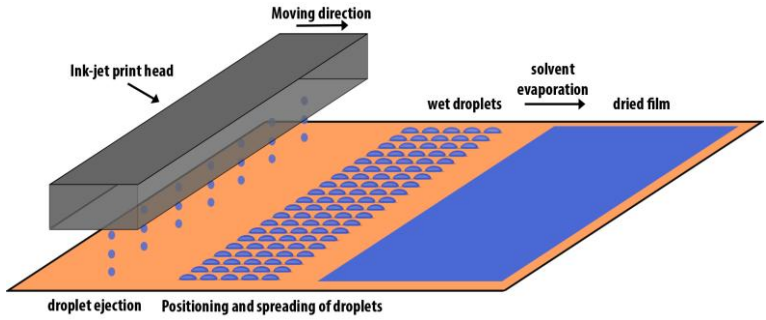

Figure 2.11. *Operating principle of a drop-on-demand ink-jet printing system on a single crystalline or technical substrate.*

There are two different systems to generate the droplet formation, namely continuous ink-jet and drop-on-demand (DOD) systems. However, continuous ink-jet systems have some limitations to electrically conductive inks. In the thesis, we focus on the use of piezoelectric DOD ink-jet printer Dimatix DMP 2800 (Dimatix-Fujifilm Inc.) equipped with a 10 pL cartridge (DMCLCP-11610) with a 22 µm orifice and 16 nozzles. DOD systems only generate droplets when an electric pulse is applied to a piezoelectric $PbZr_xTi_{1-x}O_3$ element in the ink

chamber. This chamber will subsequently expand and push the ink out of the nozzle. The Dimatix printer can induce droplet formation rates up to 80 kHz with a volume of 1 or 10 pL of the droplet.[28]

2.4.4. Experimental ink-jet printing of YBCO precursor solutions.

In most academic projects, methanol-based YBCO precursor solutions are often used for the fabrication of YBCO thin films via spin-coating. When using methanol-based precursor solutions for ink-jet printing, clogging of the nozzle will occur due to fast desiccation and flocculation owing to the low boiling point of methanol.[29] To avoid nozzle blocking, methanol is replaced by 1-butanol to increase the vapor pressure and decrease the evaporation rate. Prior to ink-jet printing, the 0.75 M LF-YBCO precursor solutions were prepared by dissolving Ba-TFA, Cu-propionate and Y-propionate salts in 1-butanol with a Y:Ba:Cu ratio of 1:2:3 at 70 °C for 30 min on a hot plate and were filtered with a 0.20 µm PET filter. However, in order to achieve proper jetting, fluid properties such as viscosity, density and surface tension must be taken into consideration. The jettability of droplets in a DOD print head can be predicted by its fluid dynamics, characterized by the Ohnesorge number ($Oh = \frac{\eta}{\sqrt{\gamma \rho \alpha}}$). This number is related to the Reynolds and the Weber number and consists of surface tension (γ, N m^{-1}), density (ρ, kg m^{-3}), viscosity (η, Pa s) and velocity (v, m s^{-1}) of the ink and the orifice diameter of the nozzle (α, m). The inverse value of Ohnesorge number (Oh^{-1}) is independent of the droplet velocity and should be between 1 and 10 to achieve stable jetting properties.[30] The YBCO ink had a viscosity of 6.4±0.1 mPa s and a surface tension of 22.13±0.16 mN m^{-1}, determined at 21 °C which results in Oh^{-1} value of 3.23 and that means the YBCO ink should be printable.

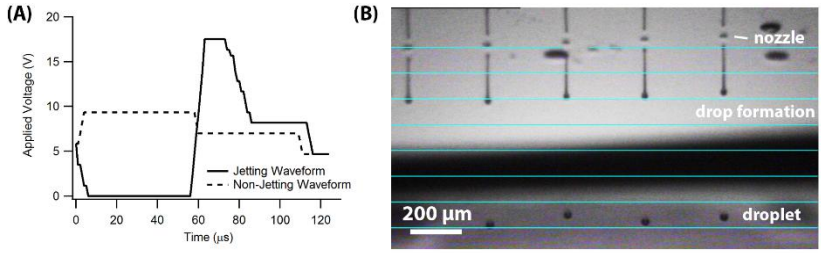

Figure 2.12. *(A) Optimized jetting and non-jetting waveforms used for printing YBCO inks. These waveforms were sequentially applied based on the pattern to be printed. (B) Drop visualization by Dimatix drop watch: Jetting of five spherical YBCO ink droplets from the nozzle in the air.*

(100)-oriented $LaAlO_3$ single crystal substrates were cleaned with isopropanol and heated to 400 °C to improve wettability. The substrates were coated using a piezoelectric DOD ink-jet system. The maximum voltages of the costume waveforms for both cases, jetting and non-jetting, were adjusted for YBCO inks prior to printing the layer, as shown in Figure 2.12. These YBCO inks can be printed reproducibly with the print frequency of 12 kHz using the custom waveform (Figure 2.12a) with the voltage applied in the range of 17-18 V for the jetting waveform and 9-10 V for the non-jetting waveform. This non-jetting waveform was set positive to keep the fluid in the nozzle in motion, preventing it from drying out. The droplet formation break-off results in a droplet with tail but the tail later merges with the droplet to a single spherical droplet, preventing the formation of satellite droplets as shown in Figure 2.12b. Adjustments were optimized by observing the droplet formation with the built-in drop watch camera of the Dimatix.

After characterizing the jetting behavior of the inks, the wetting interaction between the droplets and the cleaned substrates upon impact plays a critical role in forming a homogeneous and continuous coating. The droplets should spread out easily and merge with the neighboring droplets to form a continuous wet coating. In that case, it is of utmost importance that the ink shows good wetting, i.e. low contact angles. The contact angles (θ_{CA}) of YBCO inks on the cleaned $LaAlO_3$ substrate were in the range of 14-15°. The theoretical footprint contact diameter d_{con} of the drop upon impact can be estimated by the following equation 2.4.[30]

$$d_{\mathrm{con}} = {d_0}^3 \sqrt{\frac{8}{\tan\frac{\theta_{\mathrm{CA}}}{2}\left(3+\tan^2\frac{\theta_{\mathrm{CA}}}{2}\right)}} \qquad \text{Eq. 2.4}$$

where θ_{CA} is the equilibrium contact angle and d_0 is the droplet diameter during flight measured via dropwatch (Figure 2.12b, diameter of 23.9±0.2 µm). The theoretical contact diameter was calculated to be 64 µm. The experimental contact diameter as measured by separated droplets on $LaAlO_3$ substrate (distance of 100 µm) via optical micrograph (Figure 2.13) was even slightly larger in the range 70-80 µm. This indicates that the local wetting of the droplets is good on $LaAlO_3$ substrates. In order to get a smooth and continuous wet coating, a drop spacing of 25 µm in both *x* and *y* direction was used.

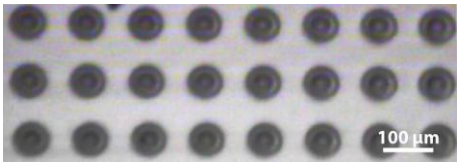

Figure 2.13. *Optical images of the printed arrays on LAO substrate with a separation of 100 µm. The contact diameter of the drops is in the range 70-80 µm.*

After single printing one layer, the wet coating was dried at 85 °C on a hotplate for 5 min and subsequently thermally treaded (pyrolysis, crystallization and annealing) at the same conditions as above for LF-YBCO, leading to a thickness of ~125 nm for YBCO ink verified by cross-sectional view via FIB-SEM (Figure A2.4 in Appendix A). However, from an engineering point of view, it is of utmost importance to have a high critical current I_c for HTS applications. Besides an increase of the J_c by nanoparticle addition as artificial pinning center, the higher current can be achieved by increasing the superconducting layer thickness.[6] The latter is possible through inkjet printing multi-deposition. As described above, a single deposition of YBCO ink produces 125 nm with a self-field J_c of 4.74 MA cm^{-2} at 77 K. The multi-deposition via ink-jet printing was possible by printing one layer on the $LaAlO_3$ substrate and subsequently rotated the as-deposited substrate 90 degrees clockwise for a next layer printing. This was repeated until the desired thickness was reached. This procedure of perpendicularly printing was preferred to avoid an accumulation of liquid at the edges of the substrates. This liquid accumulation can lead to a cracking phenomenon during the pyrolysis step which degrades the superconducting properties. By increasing the number of depositions stepwise to six, the thickness of the YBCO layer after the thermal process was increased linearly. The properties of different layer thicknesses are summarized in Table 2.3. The self-field J_c at 77 K decreased linearly with total thickness. This has mainly two reasons: First, the increased thickness and therefore (critical) currents lead to stronger self-fields resulting in a stronger decrease of self-field J_c.[31] Second, the YBCO growth starting from a thick pyrolyzed layer (obtained from single or multiple printing and finally one thermal processing) gets more and more disturbed resulting in non-ideal microstructures, e.g. increasing *a*-axis content [5, 32] or pore formation [33] and therefore reduced J_c values. $Ba(O,F)_2$ is present in the YBCO layer obtained after 4 depositions as confirmed by XRD - 2θ = 24.9 (111), 28.9 (002) and 41.2 (202) - and cross sectional SEM via FIB (Figure A2.5 in Appendix A). The presence of $Ba(O,F)_2$ may indicate that the YBCO formation is incomplete. Thus, the thermal process of the YBCO growth needs to be optimized for larger thicknesses.

Table 2.3. *Experimental values of thickness, inductively measured self-field critical current density at 77 K and normalized critical current after different deposition runs using YBCO inks.*

Number of depositions	YBCO ink		
	Thickness, nm	J_c (77K, *sf*), MA cm^{-2}	I_c (77K, *sf*), A (cm-width)$^{-1}$
1	125±10	4.74	59
2	235±10	3.93	92
3	340±15	3.56	121
4	450±20	2.73	127
5	595±20	1.99	118
6	730±25	1.59	116

Nonetheless, as clearly seen from the XRD spectrum in Figure 2.14a, the higher deposition numbers, e.g. 4 depositions, exhibit a good (00ℓ) YBCO structure (2θ = 30.6 (004) and 38.5 (005)) with just a small amount of secondary phases such as $Ba_xCu_yO_z$ (2θ = 27.7° and 42°), Y_2O_3 (220) at 29.9° and Y_2O_3 (004) at 34.2°. No (103) YBCO reflection at 32.8° was observed. The surface morphology of this 4-deposition YBCO film, Figure 2.14b, shows a small number of *a/b*-oriented grains. It has a dense and homogeneous cross-section (only occasionally holes are visible) with a thickness of 450±15 nm (Figure 2.14c) and shows a J_c(77 K, sf) of 2.73 MA cm^{-2} and corresponding I_c of 127 A (cm-width)$^{-1}$, which is a promising result compared to Vilardell *et al*.[34] who reported a 400 nm (resp. 600 nm) YBCO layer with 120 A (cm-width)$^{-1}$ (resp. 72 A (cm-width)$^{-1}$) on $LaAlO_3$ substrates via TFA-CSD method.

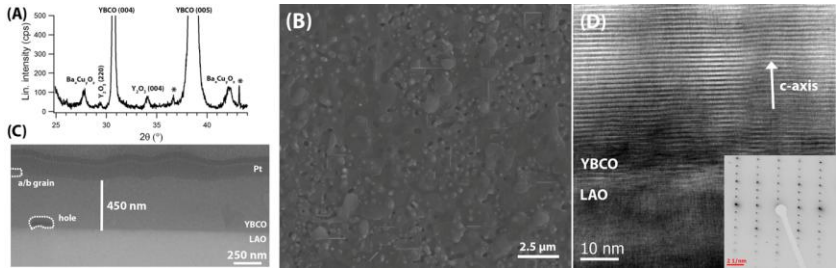

Figure 2.14. *Composition and microstructure after full thermal processing of an ink-jet-printed YBCO film with 4 deposition runs. (A) XRD analysis (asterisk: reflections by the secondary radiation of x-ray tube), (B) topographical SEM image, (C) cross-sectional SEM view of $LaAlO_3$/YBCO architecture and (D) cross-sectional HRTEM image of the interface between $LaAlO_3$ substrate and YBCO thin film derived from four deposition runs. (The inset shows diffraction pattern of LAO [100]/YBCO [001] interface.).*

The cross-sectional HRTEM image of the $LaAlO_3$/YBCO interface, Figure 2.14d illustrates the (00ℓ)-oriented growth of the YBCO layer. It is noteworthy that there are no *a/b* grains visible at the $LaAlO_3$/YBCO interface and in YBCO matrix. However, *a/b* grains (needle shaped structure) can be observed at the top of the YBCO layer, due to the faster growth of *a/b*-grains along the (100)/(010) plane. Some linear defects such as dislocations can be present in YBCO microstructure. Another remarkable feature of multi-deposited YBCO layers with one final thermal processing is the absence of several distinct layers (See Figure A2.6 in Appendix A), commonly formed from multiple deposition and its pyrolysis. The selected area electron diffraction (SAED) pattern, inset of Figure 2.14d, further confirms the excellent biaxial alignment and the cube-on-cube orientation between YBCO and $LaAlO_3$.

In this work, we have shown the possibility to introduce the ink-jet printing method using a low-fluorine YBCO precursor solution for the production of thicker YBCO thin films. The next step is to transfer these results from $LaAlO_3$ substrates to industrial metallic substrates as there are challenges for depositing the YBCO inks due to the different wetting behavior on technical substrates. In this work, we used a state-of-the-art of CCs architecture based on Deutsche Nanoschicht GmbH (d-Nano, a BASF company) which is known as "all-solution coated conductor" due to the introduction of CSD technique for manufacturing buffer layers and (00ℓ)-orientated YBCO layer. This orientated growth is enforced by the orientation of the substrate and the buffer layer. 5 at.% W-doped Ni (Ni5W) tapes are introduced as the orientated substrate to reduced magnetism and hardening of tape, resulting in highly quality cube-textured and non-magnetic substrates. It shows a good ability for texturing and a good match of lattice parameters to the subsequently deposited buffer layer and YBCO layer. The properties of the buffer layer were described in section 1.6 of chapter one and in this work, the CSD buffer layer system is so far, the combination of lanthanum zirconate ($La_2Zr_2O_7$, LZO) and cerium oxide (CeO_2). These buffer layers offer advantages (e.g. good lattice mismatch) and are stable in wide temperature and atmosphere. Thus, the texture quality of substrate and buffer layers is very crucial as they can deliver the maximal critical current densities of YBCO layer. As spin-coating is not suitable for continuous coating of industrial metallic long tapes while the ink-jet printing technique is very challenging for depositing YBCO inks as several parameters (e.g. wetting, drop formation, etc.) must taken into account. So, to deposit YBCO coating on metallic tape without any issues, we will introduce the dip-coating technique as it is very simple.

2.4.5. Dip-coating

The dip-coating method is known as one of the simplest scalable deposition techniques and can be divided into three important stages, namely (1) immersion and dwell time, (2) drainage and (3) evaporation of the solvent. The substrate is first immersed in the precursor solution reservoir with a constant speed followed by a certain dwell time for completing the wetting. The substrate is subsequently withdrawn from the precursor solution with a constant speed. The thin wet film of precursor solution is entrained on the substrate and excess liquid will drain. The solvent will start to evaporate, forming the as-deposited thin film. This technique looks simple, however, the thickness of wet thin film is controlled by the Landau-Levich equation (Eq. 2.5) which describes the experimentally thickness via the withdrawal speed (v, mm min^{-1}), gravitational forces (g, 9.81 m s^{-2}) and the rheological parameters (e.g. the viscosity and the surface tension) of the solution precursor.

$$d = \frac{0.94(\eta v)^{2/3}}{\gamma^{1/6}(\rho g)^{1/2}} \qquad \text{Eq. 2.4}$$

In this coating process, there is an important link between the structure of the solution and the final thickness of the deposited film. The critical thickness may not be exceeded as it results in cracking or less uniformity of the wet thin film on the substrate. It is worth noting that this simple dip-coating is limited for this application due to fast evaporation of solvents (e.g. methanol) and contamination by the atmosphere due to open coating reservoir and long term operation, resulting in the complete use of the precursor solution. In this work, we will use this dip-coating technique on industrial metallic substrates because it is very close to the slot-die coating technique of d-Nano due to their similar uniformity of coating and solvent evaporation rate.

2.4.6. Experimental dip-coating of YBCO precursor solutions.

As described in chapter one section 1.6, the major issue for high superconducting performance is the orientated growth of the superconducting layer on a desired substrate. Therefore, a technical substrate (Ni5W tapes) with a chemical solution deposited LZO and a CeO_2 buffer layer were used. However, the major drawback of the CeO_2 thin layer as a growth template for YBCO is the formation of barium cerate ($BaCeO_3$) as a secondary phase at the CeO_2/YBCO interface during the thermal process, resulting in barium deficiency into the YBCO film. It subsequently leads to poorer superconducting properties due to the presence of YBCO misorientation and the formation of undesired secondary

phases. However, the fact is that CeO_2 layer is essential for the epitaxial growth of CSD based YBCO layer. So, it is desirable to suppress the formation of $BaCeO_3$ phase by accurate control of the optimized process parameters of YBCO crystallization. When introducing a typical YBCO crystallization process at 800 °C with a slow heating rate (5 K min^{-1}) under 100 ppm O_2 in N_2 atmosphere, as described in section 2.3.1 on the pyrolyzed YBCO on Ni5W tapes, it results to more formation of the secondary phases - $BaCeO_3$ and $Ba_xCu_yO_z$ phases - and less (00ℓ) YBCO texture compared to YBCO on $LaAlO_3$ substrate (see Figure A2.7 in Appendix A). So, a strict optimization of the YBCO crystallization for YBCO layer on Ni5W tape is essential.

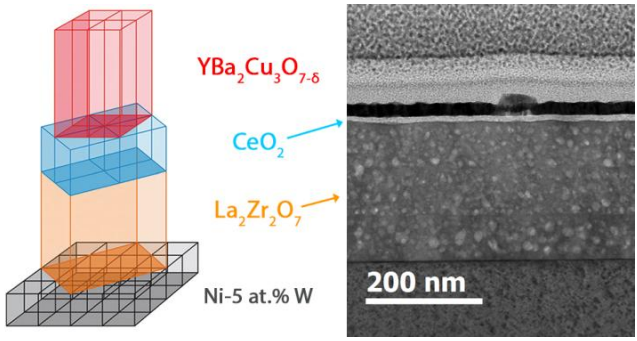

Figure 2.15. *Relative orientation of the layer-layer system of Ni5W-LZO-CeO_2-YBCO and its HAADF-STEM overview. Courtesy from d-Nano.*[35]

In this work, a highly textured Ni5W tape with triple LZO buffer layers and a CeO_2 cap layer was used, shown in Figure 2.15. These buffer layers were coated in reel-to-reel processes on 10 nm wide rolling assisted biaxially textured substrate (RABiTS) at d-Nano. To build a thicker YBCO film via the dip-coating technique without any formation of cracks during the pyrolysis, Falter *et al.*[36] has shown four different methods: (1) Increasing the thickness using higher concentration of YBCO precursor solution, multiple deposition of YBCO precursor solution with (2) a pyrolysis step between each coating step or (3) without any pyrolysis step between, (4) withdrawing the substrate faster out the precursor solution.

In this work, we describe how to increase the YBCO film's thickness up to 450 nm via method (4). The YBCO precursor solution is prepared with dissolving Y-propionate, Ba-TFA and Cu-propionate in methanol at 60 °C for 30 min on a hot plate in the ambient with a stoichiometric Y:Ba:Cu ratio of 1.3:1.8:3 and YBCO concentration of 0.15 M, resulting in a viscosity of 8.5 cP. This off-stoichiometric leads to Y-rich and Ba-poor films and results in high critical

current density.[37] Priority to the dip-coating, the Ni5W substrates are cleaned by then washing with isopropanol and subsequently heat treated at 400 °C for 5 min to remove organic adsorbents. Afterwards, the substrates are dipped into the precursor solution and withdrawn out vertically with a speed in the range of 40-160 mm min^{-1} (Table 2.4). After the dip-coating procedure, the back-side of Ni5W substrate was cleaned with acetone to remove the excess wet film. Subsequently, the as-deposited Ni5W substrates undergo thermal process (pyrolysis, YBCO crystallization and annealing). The thickness after pyrolysis and after YBCO crystallization was verified via FIB cross-sectional SEM images. The increase in thickness of YBCO layer is in line with the higher drawing speed while the pyrolyzed films are reduced with the factor after YBCO crystallization.

Table 2.4*. The relationship between drawing speed of dip-coating and its thickness after pyrolysis and YBCO crystallization.*

Drawing speed mm min^{-1}	**Film thickness (nm)**	
	after pyrolysis	**after crystallization**
160	1200	660
130	800	455
100	500	315
70	400	245
40	300	200

As mentioned in section 2.4.4, the limit of the thickness is around 500 nm. So, we dipped the cleaned Ni5W substrate into the YBCO precursor solution, left it there for 10 seconds and vertically drawn it out upwards with a drawing speed of 100 mm min^{-1}. After drying at 65 °C on a hot plate in the ambient to evaporate methanol for 5 min, the procedure is repeated with a drawing speed of 60 mm min^{-1}. This second procedure does not increase the film's thickness twice but makes the wet film more compact which leading to a better surface homogeneity after the thermal process. After full thermal process with a heating rate of 100 K min^{-1}, the thickness is 450 nm as verified via cross-sectional SEM image. The fast heating rate of 100 K min^{-1} was obtained via direct insertion of the decomposed films into a preheated tube furnace at 815 °C for 45 min in a flowing N_2 atmosphere containing 500 ppm O_2. The inlet gas was humidified by passing it through a water bath maintained at 25 °C. After YBCO crystallization, the samples underwent an annealing procedure under pure O_2 atmosphere for 2 hours. This fast heating rate and 500 ppm O_2 atmosphere during YBCO crystallization were introduced to accelerate the YBCO growth because the slow heating rate of 5 K min^{-1} results in more formation of large secondary phases such as $Ba_xCu_yO_z$ and $Y_2Cu_2O_5$. These secondary phases can be ruled out by

introducing the modified thermal process as shown on XRD θ-2θ pattern (Figure 2.16). There are also strong (00ℓ) YBCO reflections - 2θ = 15.2° (002), 22.8° (003), 30.6° (004), 38.5° (005), and 46.6° (006) -, indicating good epitaxial quality of the YBCO film.

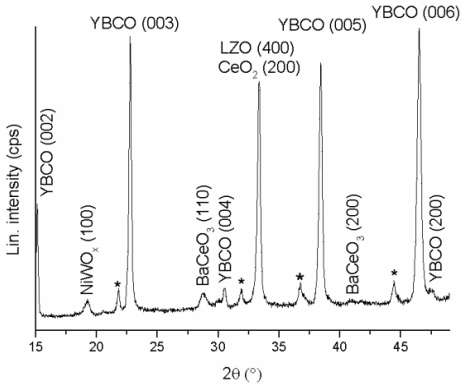

Figure 2.16. *XRD θ-2θ patterns of a fully processed YBCO film on Ni5W substrate, indicating good epitaxial quality. (Reflections by the secondary radiation of x-ray tube are marked with an asterisk.)*

This excellent epitaxial growth leads to a T_c of 87.5 K and a critical current density of 0.2 MA cm^{-1}. These poor superconducting properties are due to the presence of secondary phases (such as $Ba_xCu_yO_z$ and $Y_2Cu_2O_5$) in the YBCO matrix as observed in the HAADF-STEM image (Figure 2.17). However, the YBCO layer shows the typical YBCO topographical structure (Figure 2.18a and diffraction patterns on Figure 2.17b), but with the presence of very large $Y_2Cu_2O_5$ phase (Figure 2.18b in the YBCO matrix and 2.18c close to the YBCO/CeO_2 interface) as confirmed via EDX analysis. This additional phase is probably formed due to a higher amount of Y in the YBCO precursor solution. It is remarkable that this phase does not induce the region of lots of stacking faults (SF) in YBCO matrix. However, some SF can be observed in YBCO matrix (See Figure 2.18d).

Nevertheless, from the microstructural analysis, we can conclude that epitaxial YBCO can be grown on the coated conductor architecture (Figure 2.18b) with a CeO_2 top layer, three stacked LZO buffer layer (diffraction pattern in Figure 2.16c shows pyrochlore structure) onto tungsten-doped nickel substrate (diffraction pattern in Figure 2.17d shows cubic structure). However, some $BaCeO_3$ phases can be formed due to the reactivity of CeO_2 with Ba^{2+} without affecting the growth of YBCO. Based on these preliminary results, there is still room for further optimization such as adjusting the stoichiometric ratio of Y:Ba:Cu by means of a reduction in the excess of Y in the YBCO precursor solution.

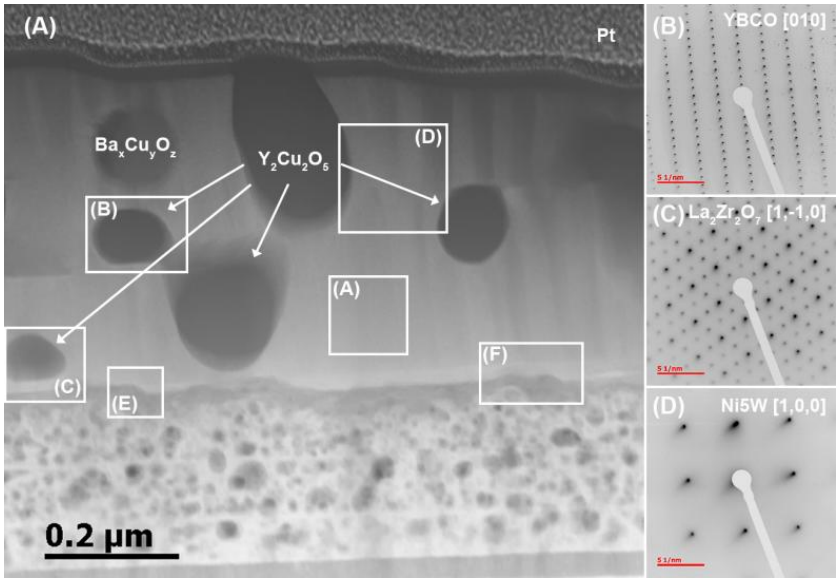

Figure 2.17. *(A) HAADF-STEM overview image of YBCO on Ni5W tape with its diffraction patterns of (B) YBCO film, (C) three stacked LZO buffer layer and (D) nickel substrate. The marked regions in the HAADF image are enlarged in Figure 2.17.*

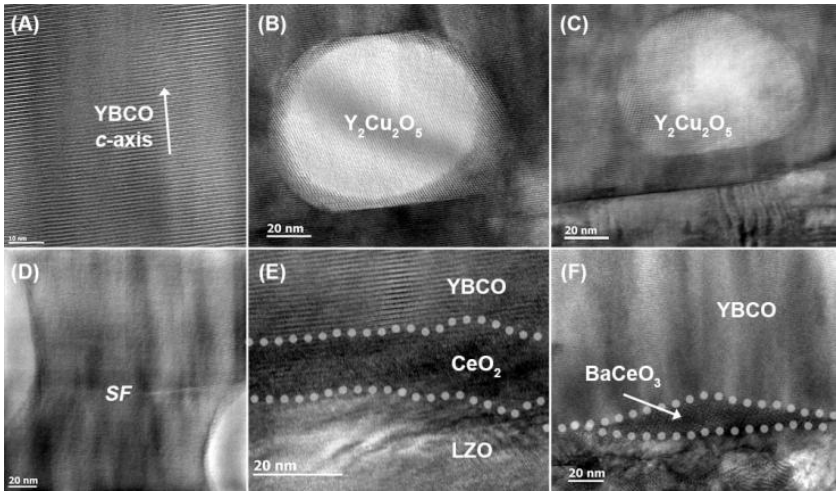

Figure 2.18. *High-resolution TEM images of YBCO film grown on Ni5W tape: (A) YBCO matrix, showing a good (00ℓ)-oriented, the presence of $Y_2Cu_2O_5$ phase in (B) YBCO matrix and (C) close to YBCO/CeO_2 interface, (D) YBCO matrix showing a stacking fault (SF) between two secondary phases in the YBCO layer, (E) YBCO/Ni5W tape interface and (F) the formation of $BaCeO_3$ phase.*

2.5. Conclusion

In this work, we have shown the possibility to introduce the chemical solution deposition technique for the fabrication of the superconducting film. First, the preparation of a stable YBCO precursor solution is the most important step towards CSD approach. It has been demonstrated in this work that microwave heating is efficient in facilitating the dissolution of YBCO powder to an anhydrous TFA precursor with a reduction in preparation time by a factor of 72 compared to conventional heating by oil bath. Other advantages are the use of only a stoichiometric amount of TFAA and the removal of TFAH, resulting in a highly pure precursor as confirmed by a thorough analytical study. This fast and reliable method can also deliver a modified fluorine content of YBCO precursor by adjusting the ratio between TFAA and propionic acid.

Second, TFA-based and LF-YBCO thin film are formed via a CSD-based method by means of spin-coating and thermal growth. This method yields in the epitaxial YBCO thin films with J_c up to 4 MA cm^{-2} in self-field at 77 K for both TFA- and LF-YBCO film. These properties are very promising and indicate that this microwave assisted procedure can improve the standard TFA-based and LF chemical solution deposition of YBCO thin films significantly. We have also shown the possibility to adjust the YBCO inks in order to deposit YBCO inks on single crystal $LaAlO_3$ substrates using a DOD piezoelectric ink-jet printing Dimatix system. This ink-jet printing method leads to critical current densities up to 3.0 MA cm^{-2} (sf, 77 K) with a thickness of 500 nm. This CSD route shows good potential for low-cost long-length industrial production (reel-to-reel deposition).

However, these results from $LaAlO_3$ substrates should be transferred to industrial metallic Ni5W substrates for the commercial market as there are challenges for depositing YBCO inks due to the different wetting behavior on Ni5W substrates. It was possible to deposit an YBCO layer on Ni5W substrate via a dip-coating technique. This method delivers a 450 nm thick YBCO film with maximum J_c of 0.2 MA cm^{-2} via fast withdrawing of 100 mm min^{-1} out of the YBCO precursor solution. These J_c's values were obtained after the adjustment of YBCO crystallization from a slow heating rate (5 K min^{-1}) to 800 °C under 100 ppm O_2 in N_2 atmosphere for $LaAlO_3$ substrates to the direct insertion in the tube furnace (100 K min^{-1}) under 500 ppm O_2 in N_2 atmosphere for Ni5W substrates. This method results in good (00ℓ) YBCO texture with the slightly formation of the $BaCeO_3$ phase. However, compared to obtained results from 1.8-2.5 MA cm^{-1} for 2-3 times 500 nm deposited YBCO layer after thermal reel-to-reel process at d-Nano, there is still room for further optimization of the YBCO crystallization process at a lab scale.

2.6. References

1. T. Araki and I. Hirabayashi, "Review of a chemical approach to $YBa_2Cu_3O_{7-x}$-coated superconductors—metalorganic deposition using trifluoroacetates," *Supercond. Sci. Technol.,* **16** [11] R71-R94 (2003).
2. A. Gupta*, et al.*, "Superconducting oxide films with high transition temperature prepared from metal trifluoroacetate precursors," *Appl. Phys. Lett.,* **52** [24] 2077-79 (1988).
3. P. Vermeir*, et al.*, "Elucidation of the Mechanism in Fluorine-Free Prepared $YBa_2Cu_3O_{7-\delta}$ Coatings," *Inorg. Chem.,* **49** [10] 4471-77 (2010).
4. P. C. McIntyre, M. J. Cima, and M. F. Ng, "Metalorganic deposition of high-J_c $Ba_2YCu_3O_{7-x}$ thin films from trifluoroacetate precursors onto (100) $SrTiO_3$," *J. Appl. Phys.,* **68** [8] 4183-87 (1990).
5. J. Smith, M. Cima, and N. Sonnenberg, "High critical current density thick MOD-derived YBCO films," *IEEE Trans. Appl. Supercond.,* **9** [2] 1531-34 (1999).
6. X. Obradors and T. Puig, "Coated conductors for power applications: materials challenges," *Supercond. Sci. Technol.,* **27** [4] 044003 (2014).
7. X. Obradors*, et al.*, "Growth, nanostructure and vortex pinning in superconducting $YBa_2Cu_3O_7$ thin films based on trifluoroacetate solutions," *Supercond. Sci. Technol.,* **25** [12] 123001 (2012).
8. T. Araki*, et al.*, "Coating processes for $YBa_2Cu_3O_{7-x}$ superconductor by metalorganic deposition method using trifluoroacetates," *Supercond. Sci. Technol.,* **14** [9] 783 (2001).
9. N. Roma*, et al.*, "Acid anhydrides: a simple route to highly pure organometallic solutions for superconducting films," *Supercond. Sci. Technol.,* **19** [6] 521-27 (2006).
10. A. Llordes*, et al.*, "Evolution of metal-trifluoroacetate precursors in the thermal decomposition toward high-performance $YBa_2Cu_3O_7$ superconducting films," *Chem. Mater.,* **22** [5] 1686-94 (2010).
11. K. Zalamova*, et al.*, "Smooth Stress Relief of Trifluoroacetate Metal-Organic Solutions for $YBa_2Cu_3O_7$ Film Growth," *Chem. Mater.,* **18** [25] 5897-906 (2006).
12. K. De Keukeleere, "Incorparation of metal oxide nanocrystals in high temperature $YBa_2Cu_3O_{7-x}$ superconductors." in. Ghent University, 2016.
13. J.-S. Schanche, "Microwave synthesis solutions from personal chemistry," *Mol. Divers.,* **7** [2] 291-98 (2003).
14. J. A. Gerbec, D. Magana, A. Washington, and G. F. Strouse, "Microwave-Enhanced Reaction Rates for Nanoparticle Synthesis," *J. Am. Chem. Soc.,* **127** [45] 15791-800 (2005).
15. H. Rijckaert*, et al.*, "Microwave-assisted $YBa_2Cu_3O_7$ precursors: A fast and reliable method towards chemical precursors for superconducting films," *J. Am. Ceram. Soc,* **100** [6] 2407–18 (2017).
16. X. Obradors*, et al.*, "Progress towards all-chemical superconducting $YBa_2Cu_3O_7$-coated conductors," *Supercond. Sci. Technol.,* **19** [3] S13-S26 (2006).
17. K. De Keukeleere*, et al.*, "Fast and Tunable Synthesis of ZrO_2 Nanocrystals: Mechanistic Insights into Precursor Dependence," *Inorg. Chem.,* **54** [7] 3469-76 (2015).

18. J. Watté*, et al.*, "Highly Crystalline Nanoparticle Suspensions for Low-Temperature Processing of TiO_2 Thin Films," *ACS Appl. Mater. Interfaces,* **8** [20] 13027-36 (2016).
19. P. Cayado*, et al.*, "Epitaxial superconducting $GdBa_2Cu_3O_{7-d}/Gd_2O_3$ nanocomposite thin films from advanced Low-Fluorine solutions," *Supercond. Sci. Technol.* (2017).
20. A. Nikolopoulos, B.-L. Jang, and J. Spivey, "Acetone condensation and selective hydrogenation to MIBK on Pd and Pt hydrotalcite-derived Mg Al mixed oxide catalysts," *Appl. Catal. A-Gen.,* **296** [1] 128-36 (2005).
21. J. Feys*, et al.*, "Ink-jet printing of $YBa_2Cu_3O_7$ superconducting coatings and patterns from aqueous solutions," *J. Mater. Chem.,* **22** [9] 3717-26 (2012).
22. X. Palmer*, et al.*, "Solution design for low-fluorine trifluoroacetate route to $YBa_2Cu_3O_7$ films," *Supercond. Sci. Technol.,* **29** [2] 024002 (2016).
23. L. Jin*, et al.*, "Optimization of fluorine content in TFA-MOD precursor solutions for YBCO film growth," *Supercond. Sci. Technol.,* **29** [1] 015001 (2015).
24. G. Pollefeyt*, et al.*, "Influence of Aqueous Precursor Chemistry on the Growth Process of Epitaxial $SrTiO_3$ Buffer Layers," *Inorg. Chem.,* **53** [10] 4913-21 (2014).
25. V. Narayanan*, et al.*, "Aqueous CSD approach for the growth of novel, lattice-tuned $La_xCe_{1-x}O_\delta$ epitaxial layers," *J. Mater. Chem.,* **22** [17] 8476-83 (2012).
26. D. P. Birnie III, "Spin Coating: Art and Science," pp. 263-74. in Chemical solution deposition of functional oxide thin films**.** Edited by T. Schneller, R. Waser, M. Kosec, and D. Payne. Springer, 2013.
27. J. Feys, "Digitally printed superconducting coatings and patterns." in. Ghent Unversity, 2014.
28. Fujifilm via www.fujifilmusa.com
29. I. Van Driessche*, et al.*, "Chemical solution deposition using ink-jet printing for YBCO coated conductors," *Supercond. Sci. Technol.,* **25** [6] 065017 (2012).
30. B. Derby, "Inkjet printing of functional and structural materials: fluid property requirements, feature stability, and resolution," *Ann. Rev. Mater. Res.,* **40** 395-414 (2010).
31. F. Hengstberger, M. Eisterer, and H. Weber, "Thickness dependence of the critical current density in superconducting films: A geometrical approach," *Appl. Phys. Lett.,* **96** [2] 022508 (2010).
32. M. Boubeche*, et al.*, "Thick REBaCuO superconducting films through single-coating of low-fluorine metallorganic solution," *Cryogenics,* **79** 49-52 (2016).
33. S. Kim*, et al.*, "Mechanisms of weak thickness dependence of the critical current density in strong-pinning ex situ metal–organic-deposition-route $YBa_2Cu_3O_{7-x}$ coated conductors," *Supercond Sci. Technol.,* **19** [9] 968 (2006).
34. M. Vilardell*, et al.*, "Flexible manufacturing of functional ceramic coatings by inkjet printing," *Thin Solid Films,* **548** 489-97 (2013).
35. M. Bäcker, M. Falter, O. Brunkahl, and B. Holzapfel, "Superconducting Films," pp. 673-705. in Chemical solution deposition of functional oxide thin films**.** Edited by T. Schneller, R. Waser, M. Kosec, and D. Payne. Springer, 2013.
36. M. Falter*, et al.*, "Chemical solution deposition (CSD) of $YBa_2Cu_3O_{7-x}$ films and oxide buffer layers by dip coating," *IEEE Trans. Appl. Supercond.,* **13** [2] 2751-54 (2003).
37. P. Paturi, H. Huhtinen, K. Laajalehto, and R. Laiho, "Reason for high critical current in thin YBCO films prepared by laser ablation from nanostructured target," *Supercond. Sci. Technol.,* **13** [5] 622 (2000).

Chapter three

A crucial step during the $YBa_2Cu_3O_{7-\delta}$ nanocomposite formation:

Surface chemistry

In this chapter, we report on the chemical solution deposition of YBCO nanocomposites from environmentally benign low-fluorine precursors and show the relationship between the nanocrystal surface chemistry and final nanocomposite performance.

Adapted from:

H. Rijckaert, G. Pollefeyt, M. Sieger, J. Hänisch, J. Bennewitz, J. De Roo, K. De Keukeleere, R. Hühne, M. Bäcker, P. Paturi, H. Huhtinen, M. Hemgesberg and I. Van Driessche, Optimizing Nanocomposites through Nanocrystal Surface Chemistry: Superconducting $YBa_2Cu_3O_7$ Thin Films via Low-Fluorine Metal Organic Deposition and Preformed Metal Oxide Nanocrystals. Chemistry of Materials, 2017. 29(14), 6104-6113

3.1. State-of-art

As described in chapter one, the incorporation of nano-sized defects in the YBCO matrix can immobilize the vortices and thus create an effective pinning. Recently, several authors have already published a lot of papers based on PLD-grown YBCO nanocomposite films, resulting in good properties. These nanocomposite films are commonly created with a non-superconducting perovskite-type BaMO_3 (M = Zr, Hf and Sn) compound as nanocolumns into the YBCO films due to the self-assembling process via modifying the film deposition process. These nanocolumns can generate a good in-field performance when the magnetic field is aligned parallel to them (i.e. $H||c$). Such defects are correlated pinning centers along the c-axis and produce an enhancement of J_c at $H||c$ with a pinning force density of more than 25 GN m^{-3} at 77 K.[1]

To increase J_c at whole applied magnetic rotation, non-correlated pinning centers (Y_2O_3 or $BaCeO_3$) were introduced as nanodots. PLD-based methods are able to deliver high quality films. This PLD-based research is already advanced to deep understanding in control of the size, shape and density of pinning centers.[2-5] Current research however tends to shift to the synthesis of trifluoroacetates based CSD-grown YBCO films with embedded nanoparticles, as the latter offer high deposition speeds and low processing costs. First experiments in that area were performed based on a spontaneous segregation of secondary phases in the YBCO matrix during the thermal process. These secondary phases are introduced via the addition of extra metal-organic salts to the YBCO precursor solution to grow the desired secondary phases (e.g. Y_2O_3, $BaZrO_3$, $BaHfO_3$, $BaCeO_3$ and Ba_2YTaO_6).[6-11] This approach demonstrates enhanced in-field performances compared to undoped YBCO films but the pinning force densities (77 K, $H||c$) are still lower than the PLD-grown nanocomposite films. The nanoparticles must remain small, in the range of 3-10 nm and homogenously distributed in the YBCO matrix, which requires a high control of the thermal process during YBCO formation. This technique offers a limited control on the formation and size distribution of the nanostructures and faces issues with reproducibility. To reproducibly gain control over the final microstructure of the nanocomposite films, we opted to synthesize colloidally stable nanocrystals and add these to the YBCO precursor solution (Figure 3.1, stage I).

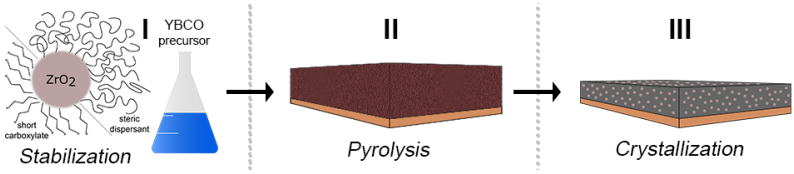

Figure 3.1. *Schematic illustration (not scaled) of the procedure for fabricating YBCO-nanocrystals nanocomposite. The process begins with (Stage I) the stabilization of nanocrystals with desired ligands in the YBCO precursor solution. (Stage II) Deposition of the YBCO precursor solution on a single crystalline or technical substrate and its thermal decomposition. (Stage III) The pyrolyzed layer is thermally treated to crystallize the YBCO matrix.*

Up to now, only a few attempts have been made at the synthesis of superconducting nanocomposites using preformed nanocrystals (Au, CeO_2 and ZrO_2)[12-14] as APCs in trifluoroacetates based YBCO. The success has been limited because the nanocrystals are either pushed to the YBCO surface or accumulated at the substrate interface. The latter hampers the epitaxial growth of YBCO, leading to poor superconducting properties.[13]

In addition, YBCO CSD research should evolve towards the use of precursors with lower fluorine content – based on propionates instead of trifluoroacetates – to reduce the release of toxic fluorinated compounds during the thermal process.[15,16] As such, low-fluorine processes are more environmentally benign and less corrosive, thus better suited for industrial production. However, the corresponding formation of nanocomposites from preformed nanocrystals remains elusive since the developed nanocrystal surface chemistry for the stabilization in trifluoroacetate-based precursor solutions (pH = 2) is incompatible with the higher pH of the low-fluorine (LF) solution (pH = 6).[13, 14, 17] Therefore, ligand exchange and the appropriate stabilization procedure are important aspects in nanocomposite research. Due to the delicate growth process of textured YBCO layers and poisoning of the superconductor by many chemical elements like metals, halides (except F), sulphur and phosphorus, the restrictions on the final ligand for the preformed nanocrystals are severe.[17] In this work, we successfully deposit a high-quality nanocomposite thin film from low-fluorine precursors and uncover important relations between nanocrystal stabilization and final performance. A 5 mol-% ZrO_2 nanocomposite was chosen as a model system to study the effect of ligands and preformed nanocrystals on the microstructure and physical properties of the nanocomposite films since a higher loading of nanocrystals leads to poor superconducting properties. This comprehensive study can initiate the improvement of many functional and structural properties of nanocomposite films in several material classes,

including solar cells[18], ferroelectrics[19], multiferroics[20], biosensors[21] and metamaterials[22, 23]. Each of these materials have a huge potential to be refined through microstructure engineering[24, 25].

3.2. ZrO_2 nanocrystals

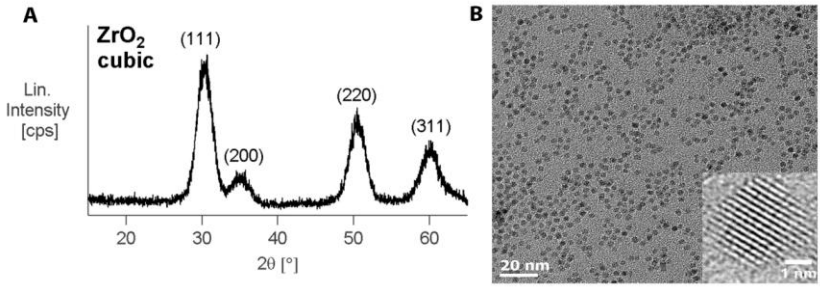

Figure 3.2. *ZrO_2 nanocrystals synthesized in tri-n-octylphosphine oxide: (A) XRD spectrum showing only reflections of the cubic phase. (B) TEM image of the ZrO_2 nanocrystals after heating-up synthesis. The inset shows (111) lattice fringes.*

Spherical ZrO_2 nanocrystals are obtained via the heating-up solvothermal synthesis - as described by Joo *et al.*[26] - using 5 mmol $ZrCl_4$, 4 mmol $Zr(OiPr)_4 \cdot iPrOH$ and 20 g tri-*n*-octylphosphine oxide (TOPO). This specific concentration ratio was used because a ligand exchange between $ZrCl_4$ and $Zr(OiPr)_4 \cdot iPrOH$ was induced during nonhydrolytic sol-gel process. So, the number of ligands should be identical. The temperature of this mixture is carefully raised until tri-n-octylphosphine oxide is melted under Ar atmosphere. The temperature of the homogenous solution is increased to 340 °C under vigorous stirring and kept at this temperature for 2 hours. After the heating-up synthesis, the reaction mixture is cooled to 80 °C (TOPO becomes solid below 60 °C). Toluene (4:1 by volume) and acetone (1:5 by volume) is added to precipitate the nanocrystals. The nanocrystals appear to be capped with hydrophobic ligands after synthesis and can be redispersed in toluene, yielding a clear suspension. These nanocrystals have a cubic crystal structure, confirmed by X-ray diffraction (XRD, Figure 3.2a). A crystallinity of 85 % was obtained via Rietveld quantitative analysis (See section A2.1 in Appendix A). The ZrO_2 nanocrystals are colloidally stable in nonpolar solvents (e.g. toluene), featuring a solvodynamic diameter of 5.9 nm in Dynamic Light Scattering measurements (DLS, Figure 3.3). This is consistent with the nanocrystal core diameter of 3.5±0.4 nm (TEM, Figure 3.2b) and an organic ligand shell of 1.2 nm. The high crystallinity of the ZrO_2 nanocrystals is further corroborated by high resolution

(HR) TEM of a ZrO_2 nanocrystal (inset of Figure 3.2b) where (111) lattice fringes are clearly visible.

3.3. Ligand exchange and phase transfer to YBCO precursor solutions

Since the nanocrystals are capped with hydrophobic ligands, a ligand exchange is indispensable for stabilization in the methanol based LF-YBCO precursor solution (Figure 3.1, stage I).[17, 27] We have found that short carboxylic acids (citric acid or tartaric acid) as well as a steric dispersant (a polar copolymer containing a phosphate group and Surfactis™11-104) are able to stabilize the ZrO_2 nanocrystals in methanol and in the LF-YBCO precursor solution. Table 3.1 shows the chemical structure of the ligands. In a ligand exchange step, the 1 mL ZrO_2 dispersion (concentration of 0.3 M) is first precipitated by the addition of acetone (1:3 by volume). In a second step, the precipitate (obtained after centrifugation at 5000 rpm for 2 min) is transferred to 1 mL methanol via the addition of a 35 mg steric dispersant or 15 mg short carboxylate, leading to a transparent and stable nano-suspension after an ultrasonic treatment of 30-60 minutes.

Table 3.1. *The chemical structure of the ligands.*

Name	Structure
Tartaric acid	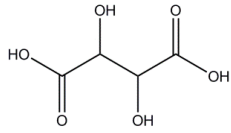
Citric acid	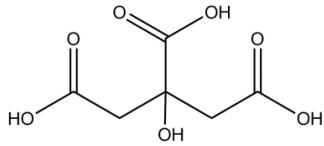
Surfactis™ 11-104	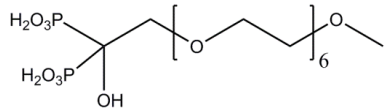
Copolymer[(a)]	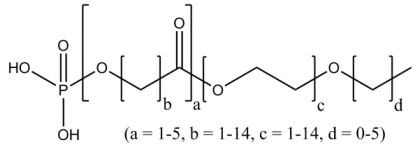 (a = 1-5, b = 1-14, c = 1-14, d = 0-5)

[(a)] The copolymer is a commercially available polar copolymer with phosphate groups which may be given in the form of its alkylolammonium salt.

DLS analysis (Figure 3.3) confirms the successful ligand exchange and phase transfer to methanol with a solvodynamic diameter of 6.4 nm for the copolymer,

8.1 nm for Surfactis™, 5.9 nm for tartaric acid and 5.8 nm for citric acid. It is noteworthy that the colloidal integrity of the copolymer capped nanocrystals is maintained in the highly ionic LF-YBCO precursor solution even at high loadings (up to 30 mol-%), since the solution remains stable for more than six months and no precipitates are observed. In contrast, Surfactis™ and short carboxylate capped nanocrystals (5 mol-%) remain stable for only one week in the LF-YBCO precursor solution. ^{1}H NMR measurements in methanol-d_4 reveal that the phosphonate group of copolymer effectively interacts with the nanocrystal surface as evidenced by negative nOe (nuclear Overhauser effect) cross peaks in the NOESY spectrum (see Figure 3.2a in Appendix A).[28] In diffusion-ordered spectroscopy (DOSY), we observe two sets of resonances for the copolymer (see Figure A3.2b in Appendix A). The slowly diffusing species feature a diffusion coefficient of 107 µm² s^{-1}, corresponding to a solvodynamic diameter of 7.5 nm. This is in agreement with the solvodynamic diameter from DLS and we conclude that the copolymer is tightly bound to the nanocrystal. The other set of resonances with a higher diffusion coefficient corresponds with free copolymer. The principle of coordination is the same as for Surfactis™ 11-104 and is described in section A2.3 in Appendix A. For the citric acid or tartaric acid stabilization, the acidic group coordinates to the surface. This principle is thoroughly described in the work of De Keukeleere *et al*.[29] In comparison with the stabilization with short carboxylates, the steric bulk of the steric dispersant screens the interaction with other particles more effectively. This is also reflected in the polydispersity index (obtained via DLS analysis, Table 3.2) which is significantly smaller in the copolymer stabilized dispersion, indicating a better stabilization. In addition, when the dispersions are drop casted onto TEM grids, the short carboxylate stabilization shows aggregates and individual particles whereas the copolymer stabilization features only individual particles (See Figure A3.4 in Appendix A).

Table 3.2. *Overview of the LF-YBCO nanocomposite precursors with different ligands, their solvodynamic diameter and polydispersity index in methanol and their decomposition temperature of pure ligands, indicating the different critical current densities (self-field, inductively measured at 77 K,* voltage criterion of 50 µV*).*

Ligand	d_s **nm**	**Polydispersity index**	T_{decomp} **°C**	$J_{c,sf}$ **(77 K) MA cm^{-2}**
Copolymer	6.4	0.32	340	3.1±0.1
Surfactis™ 11-104	8.1	0.45	800	2.8±0.3
Citric acid	5.8	0.86	250	2.0±0.8
Tartaric acid	5.9	0.91	265	1.6±0.4

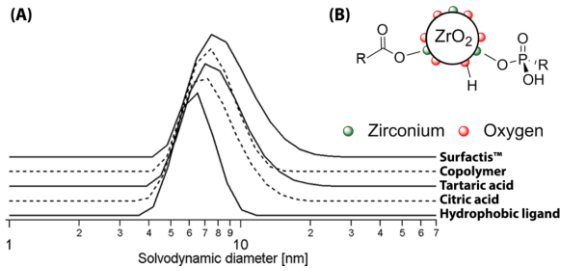

Figure 3.3. *(A) DLS volume percent analysis of ZrO_2 nanocrystals before (black line), after ligand exchange with citric acid (green dashed line) and after ligand exchange with the steric dispersant (blue dotted line). (B) The principle of coordination on nanocrystal surface.*

3.4. Nanocomposite formation and the influence of ligands.

After spin-coating of undoped and ZrO_2-doped YBCO precursors on $LaAlO_3$ substrates, the layers were pyrolyzed in a wet O_2 atmosphere (Figure 3.1, stage II) with a heating ramps of 3 K min^{-1} from 25 to 195 °C, 0.1 K min^{-1} to 240 °C and 5 K min^{-1} to the final temperature of 400 °C. Optically homogeneous layers were obtained without the formation of defects such as buckling or cracks. In earlier attempts at nanocomposites, the nanocrystals were always stabilized with short ligands such as amino acid (e.g. glutamine), triethyleneglycol or a fatty acid (e.g. decanoic acid).[13, 14] These types of ligands are of the same length scale as the short carboxylic acids (citric and tartaric acid) in this work. From thermogravimetric analysis (TGA, Figure 3.4 and Table 3.2), we can conclude that the short carboxylates decompose at lower temperatures (250 °C for citric acid and 265 °C for tartaric acid) compared to the copolymer which decomposed around 340 °C. The fact that the copolymer is a more thermally stable ligand might prevent early coagulation of the nanocrystals in the pyrolyzing matrix and thus lead to a more homogeneous nanocomposite. However, it is remarkable that the Surfactis™ 11-104 is fully decomposed around 800 °C (See Figure A3.5 in Appendix A), which may induce there are some residual products at a temperature up to 800 °C. As the final temperature of the pyrolysis step is 400 °C, the residual weight percentage after 400 °C of Surfactis™ is around 40% while of copolymer is around 10%. It seems that Surfactis™ based pyrolyzed film counts more phosphorus containing residual products, which might disturb the formation of YBCO.

Apart from the stabilization of the nanocrystals, it is important that the ligands do not disturb the decomposition of the LF-YBCO precursor itself. The temperature dependence of the decomposition was investigated by TGA

analysis (Figure 3.4). The weight loss starts earlier for 5 mol-% nanocrystal addition (at 150 °C) compared to undoped YBCO precursor (at 210 °C). In addition, the nanocomposite precursor with copolymer as ligand shows a slightly slower weight loss between 310 and 340 °C, consistent with the slower decomposition of the pure ligand (*vide supra*). It is expected that the Surfactis™ starts to decompose later and shows faster weight loss between 310 and 340 °C because the different decomposition behavior of the YBCO precursor solutions are related to the decomposition behavior of the pure ligands. Nevertheless, both undoped and nanocomposite precursors are fully decomposed at 400 °C, indicating the successful pyrolysis of YBCO precursors in the presence of nanocrystals and ligands (both short carboxylates and steric dispersant). The microstructure of the pyrolyzed layers consists of CuO nanoparticles embedded in a matrix of $Ba_{1-x}Y_xF_{2+x}$.[30]

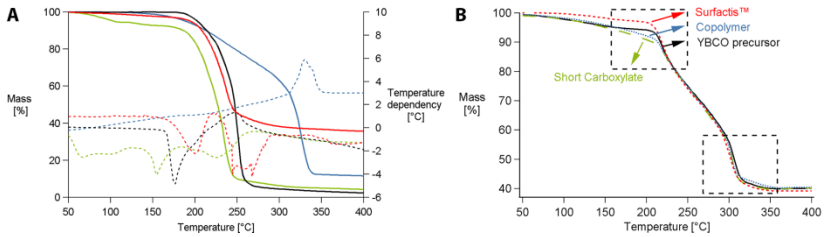

Figure 3.4. *(A) TGA-DTA record of citric acid (green) and tartaric acid (black) in comparison with the steric dispersant Copolymer (blue) and Surfactis™ (red) with heating ramp of 10 K/min and air atmosphere. (B) TGA curves of the LF-YBCO nanocomposite precursor with steric dispersant (Copolymer and Surfactis™) and with short carboxylate in comparison with an undoped LF-YBCO precursor (black line) dried in air atmosphere. More details of rectangle marked are shown in section A2.5 in Appendix A.*

After crystallization (Figure 3.1, stage III), epitaxial YBCO was obtained for all pyrolyzed layers. The pyrolyzed thin films were processed to 790 °C with a heating rate of 5 °C min^{-1} and dwelling for 45 min in a flowing wet nitrogen atmosphere. The inlet gas was humidified by passing it through water bath with a dew point of 23 °C. After 45 min, a switch to dry nitrogen atmosphere containing 100 ppm oxygen takes hold for 15 min. The following oxygenation treatment takes place at 450 °C in a flowing dry oxygen atmosphere for 2 h. The critical current density of the citric acid, tartaric acid and surfactis™ based nanocomposites are only in the range of 1.5-2.5 MA cm^{-2} compared to 2.8 MA cm^{-2} for undoped YBCO, while the copolymer based nanocomposite showed a critical current density of 3.1 MA cm^{-2} (Table 3.1). Clearly, the nature of the ligands is crucial to the final superconducting performance of the

nanocomposite. To study this effect in more detail, we analysed samples that were thermally quenched as soon as they reached the growth temperature of 790 °C. The XRD spectrum (Figure 3.5) features crystalline BaF_2 that is in the process of reacting towards epitaxial YBCO. The difference in BaF_2 intensities is due to the competing reaction with ZrO_2 nanocrystals (*vide infra*). Interestingly, the (005) reflection of YBCO is much lower for the short carboxylate based nanocomposite, indicating a slower growth rate. We infer that the slow growth rate is symptomatic for poor epitaxial growth and higher surface roughness (Atomic-force microscopy (AFM) analysis, Table 3.3) because of the changes in the nucleation process.[31, 32] These changes can generate non-*c*-axis oriented grains, resulting in the lower critical current density. Indeed, the fast decomposition of short carboxylate can interfere with the drying and/or sintering process of the gel as described by Zalamova *et al.*[33] In this regard, it is also worth noting that amino acid capped ZrO_2 nanocrystals[14] settle on the $LaAlO_3$ interface during pyrolysis of the YBCO trifluoroacetate precursor, resulting in a disturbed epitaxial growth of YBCO. To investigate if the same mechanism occurs here, X-ray photoelectron spectroscopy (XPS) measurements were performed on the pyrolyzed films. Interestingly, the ZrO_2 nanocrystals are spread throughout the amorphous matrix for both the copolymer and citric acid based LF-YBCO nanocomposites (See section A2.6 in Appendix A for XPS data). Clearly, the behaviour of nanocrystals during pyrolysis depends on their surface chemistry and the YBCO precursor solution. The lower J_c value of Surfactis™ based YBCO nanocomposites seems due to the presence of a higher phosphorus content after the pyrolysis which might not be removed and remains as phosphorus oxides. It is still unclear what the effect of phosphorus oxide on the superconducting properties is, but it seems that it results in a slight degradation of the superconducting properties (cf. Table 3.2). A follow-up study should be investigated to understand the effect of phosphorus content on the final properties.

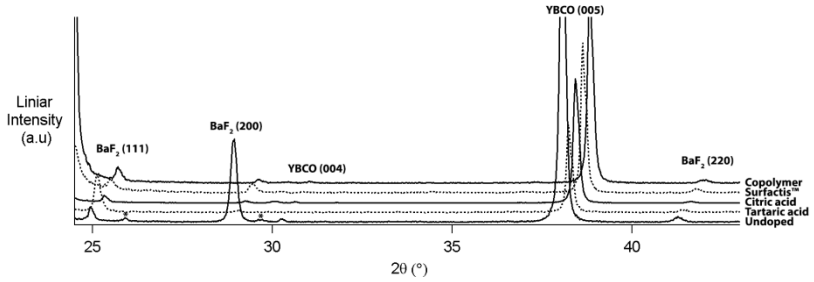

Figure 3.5. *XRD scans of different crystallized YBCO films quenched at 790 °C, indicating the YBCO growth rate is different. (Reflections marked with an asterisk are related to $Ba_xCu_yO_z$ phase.)*

3.5. Secondary ion mass spectroscopy analysis of pyrolyzed samples

As the growth of textured YBCO layers is a delicate process[27, 32], the choice of stabilizing ligands need to be careful. Poorer YBCO growth due to the ligands is probably originated by the presence of possible impurities after the pyrolysis. In general, Y and Ba form an amorphous matrix with oxygen or fluorine atoms while Cu only binds with oxygen atoms during the pyrolysis. Moreover, only Cu content can ripen to become large nanoparticles during the pyrolysis. This can be partly avoided through an early sublimation of Cu organic salts by the introduction of the humidified gas. Llordes *et al.*[15] shows that the coarsening of CuO/Cu_2O particles would form on the YBCO surface if the films were pyrolyzed under low O_2 pressure. These large CuO/Cu_2O particles can lead to undesired phases during the thermal process and thus the degrading J_c of the resulting films. Secondary ion mass spectroscopy (SIMS) has been used to analyze pyrolyzed undoped YBCO film (Figure 3.6) and reveals the ratio of Ba/Y (red line) and Cu/Y (black line) in the amorphous matrix. This analysis indicates that more CuO nanoparticles (probably coarsened or due to surface inhomogeneous) are on top of pyrolyzed matrix with a constant Ba/Y ratio throughout pyrolyzed sample.

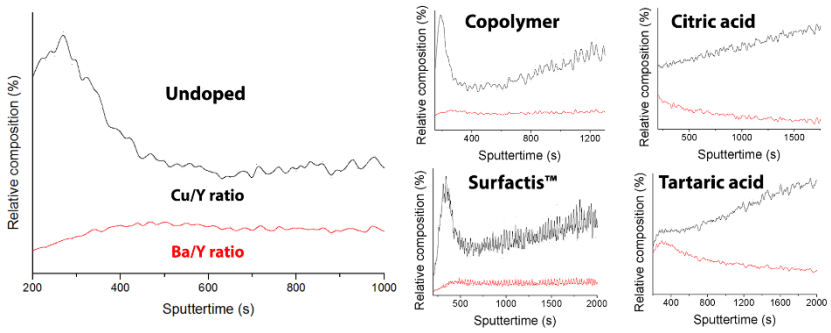

Figure 3.6. *The relative composition of Ba/Y and Cu/Y in pyrolyzed matrix of undoped and ZrO_2-doped YBCO films, determined via SIMS analysis.*

Nevertheless, ZrO_2-doped pyrolyzed YBCO samples starting from different ligands show different metal distributions in the amorphous $Ba_{1-x}Y_xF_{2+x}$ matrix. On the top-surface, there is a Cu-rich zone by copolymer and Surfactis™ based ZrO_2-doped sample with constant Ba/Y ratio. This metal ion distribution into the matrix yields in excellent superconducting properties (e.g. high critical current density). However, short carboxylate based ZrO_2-doped films show an inhomogeneous distribution of metal ions (i.e. irregular ratio of Ba/Y) into the matrix and result in lower superconductivity. It is possible that the quality of

YBCO structure is sensitive to the inhomogeneity of metal content (especially Ba and Y) in the layer. To unravel this effect, all pyrolyzed samples underwent a YBCO crystallization process and were analyzed via XRD (Figure 3.7) and SEM (Figure 3.8). Based on XRD data, short carboxylate based nanocomposite films contain more secondary phases like as $Ba_2Cu_2O_5$ and $Y_2Cu_2O_5$ while steric dispersant based films have minor secondary phases. It is due to the disturbed nucleation mechanism (the details of nucleation and growth are given in the chapter 4) of the epitaxial YBCO film because the formation of the BaF_2 phase on the LAO interface is not beneficial. As SIMS indicates there are less Ba^{2+} present at the bottom layer of the pyrolyzed layer. This is also confirmed via YBCO (005) reflections (Figure 3.5), indicating that the nucleation/growth mechanism is different. It is also remarkable in SEM images of these samples that the surface differs in the film roughness. However, some YBCO *a*-axis can be observed on surface due to the higher rate anisotropy compared to YBCO *c*-axis. So, *a/b*-oriented grains will start first to nucleate at the substrate interface and grown out of the film due to the faster growth along the (100)/(010) plane, leading to more overall roughness and the needle shaped structure on the YBCO surface.[34]

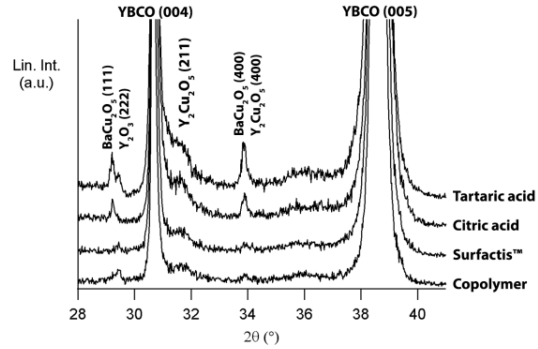

Figure 3.7. *XRD analysis of ZrO_2-doped YBCO films using different ligands after YBCO crystallization.*

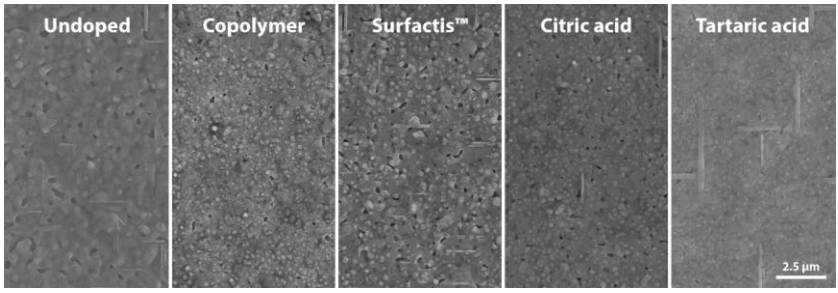

Figure 3.8. *SEM images of undoped and ZrO_2-doped YBCO films using different ligands.*

3.6. Magnetic measurements

Good biaxial YBCO texture is an important matter but it is essential that the nanocrystals are incorporated into YBCO matrix to deliver good pinning properties. For this reason, the magnetic properties were measured with a Quantum Design Physical Property Measurement System (PPMS). The onset T_c values, defined with the AC Measurement System (ACMS) option of the PPMS from the onset temperature of the in-phase component of the AC-magnetization and calculated from the criterion of $\Delta T_c = T_c^{90\%} - T_c^{10\%}$, are listed in Table 3.3. The J_c's of all samples are calculated using the Bean critical state model from the opening of the hysteresis loop up to 8 T, obtained by DC-magnetization.[35] These magnetically measured transitions are very informative in order to get better understanding of overall film quality due to the current percolation throughout the YBCO film. The Bean critical state model is widely used because of the ease of use and its accuracy. However, the obtained J_c values must be carefully compared with the other J_c values obtained by different methods.[36] It can be concluded that the addition of nanocrystals slightly increase the magnetic transition by means of T_c and that there is probably some strain around the particles and structural defects in the YBCO matrix. However, the tartaric acid based ZrO_2-doped YBCO film shows a slight decrease and is probably explained due to lots of the secondary phases in the YBCO matrix. On the other hand, the magnetic field dependences of J_c's were calculated at 77 K in maximum Lorentz force configuration in which the applied magnetic field direction is always perpendicular to the direction of the current flow and the fittings were made using a double logarithmic plot with $J_c(T,H) = A(T)B^{-\alpha}$ and are shown in Figure 3.9. It is clear that the critical current densities are in the range of 1.5-3 MA cm^{-2} except tartaric acid based ZrO_2-doped YBCO film, which only achieved a J_c of 0.74 MA cm^{-2}. This latter is due to a large amount of undesired secondary phases into YBCO matrix as confirmed on HAADF-STEM image (Figure 3.10), which can degrade the superconducting film. To determine if the ZrO_2 nanocrystals in the YBCO matrix acts as the pinning centers, we studied the shape of the J_c(H) curves. Copolymer, citric acid and tartaric acid based ZrO_2-doped YBCO films show a smoother decay compared to undoped YBCO film. This is also confirmed by higher values of accommodation field B^* (determined by the criterion $J_c(B^*) = 0.9J_c(0)$ at 77 K) by lower values of the slope (power-law exponent α) in log-log plot (Table 3.3). The low field plateau below B^* is the single vortex pinning region where each vortex is pinned to a free pinning site.[37] At B^* collective pinning effects take place and a reduction of the slope of α is seen in log–log plot (Figure 3.9).

The values of B^* and α are listed in Table 1. A clear difference between undoped and ZrO_2-doped films (except Surfactis™) can be seen. This means that the addition of preformed nanocrystals increase pinning mechanism (leading to higher B^* values) and results in slower decay (leading to lower α values) of critical current density in function of the magnetic field. However, the J_c value of tartaric acid based ZrO_2-doped YBCO nanocomposite is still lower than another ZrO_2-doped films due to the presence of more secondary phases in the YBCO matrix as confirmed via XRD (Figure 3.7) and HAADF-STEM image (Figure 3.10). Given the high values of the copolymer based nanocomposites, we examined the structural quality and superconducting performance of these materials in detail and compared them to undoped films in the next chapter.

Table 3.3. Collection of critical temperature T_c, critical current densities J_c at self-field and 1 T (magnetically measured at 77 K), accommodation field B^*, the power-law exponent α and roughness measured by AFM in undoped and ZrO_2-doped YBCO films on $LaAlO_3$ substrates.

Ligand	T_c K	$J_{c,mag}$ (0 T) MA cm^{-2}	$J_{c,mag}$ (1 T), kA cm^{-2}	B^* mT	α	RMS Å
Undoped	90.0	2.37	41.54	7.62	0.68	82.2
Copolymer	90.5	2.68	237.00	17.02	0.39	75.9
Surfactis™	91.5	2.14	79.05	9.85	0.58	89.6
Citric acid	90.5	1.65	120.32	15.52	0.40	107.6
Tartaric acid	89.0	0.74	72.76	20.06	0.40	109.4

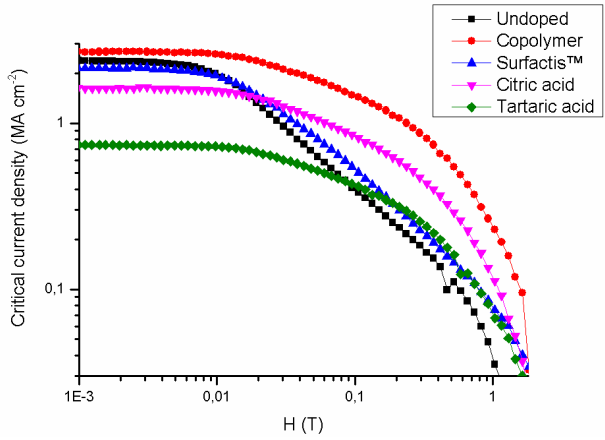

Figure 3.9. *Double logarithmic plots of critical current density vs. magnetic field H measured at 77 K for undoped and ZrO_2-doped YBCO films on $LaAlO_3$ substrates.[Magnetically measured at University of Turku]*

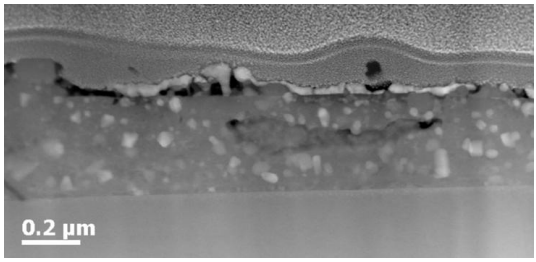

Figure 3.10. *HAADF-STEM cross sectional image of tartaric acid based ZrO_2-doped YBCO film, indicating lots of secondary phases in YBCO matrix.*

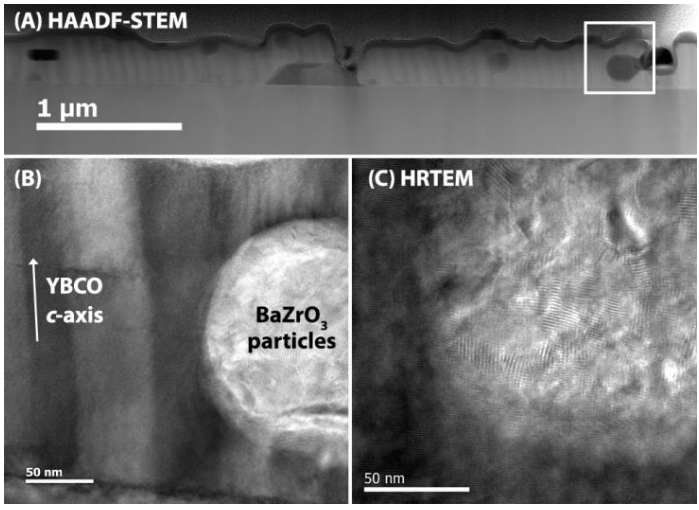

Figure 3.11. *(A) HAADF-STEM image of Surfactis™ capped ZrO_2-doped YBCO film grown on $LaAlO_3$ substrate, indicating big particles into the YBCO matrix, (B) TEM image showing YBCO/$BaZrO_3$ particles interface and (C) HR-TEM image of $BaZrO_3$ particles, showing a coagulation of ZrO_2 nanocrystals.*

It is remarkable that the Surfactis™ based ZrO_2-doped nanocomposite did not show any improvement of pinning forces while the self-field J_c has an acceptable value (in the range of 2-2.5 MA cm^{-1}). As shown on the HAADF-STEM image (Figure 3.11a) and TEM image (Figure 3.11b), whereby the YBCO layer is strongly textured and grows epitaxially on the $LaAlO_3$ substrates which explains the good superconducting properties. Nevertheless, some secondary phases and large $BaZrO_3$ particles in the size range of 150-200 nm can be indicated in the YBCO layer via EDX analysis. In order to have a better understanding of the $BaZrO_3$ particles in the YBCO matrix, HRTEM analysis was investigated. Fig. 3.11c shows that this $BaZrO_3$ particle contains several small nanocrystals in agglomeration.

So, it seems that the nanocrystals are coagulated during the YBCO growth to the size of approximately 200 nm. This particle is too large to act as a pinning center because it is not in the order of superconducting coherence length of 2-4 nm for YBCO at 77 K. The assumption of this coagulation behaviors is that the stabilizing effect of Surfactis™ is probably reduced or annihilated upon the initial decomposition, leading an increased tendency to form agglomerations.

3.7. Conclusion

Highly crystalline ZrO_2 nanocrystals were stabilized by a steric polar ligand (Copolymer and Surfactis™) or short carboxylates (tartaric and citric acid) in low-fluorine YBCO precursor solutions. From the resulting suspension, by a single coating step, we synthesized superconducting ZrO_2-doped YBCO nanocomposites. Interestingly, nanocrystals stabilized by short carboxylate ligands resulted in poorly superconducting nanocomposites while the steric dispersant led to excellent superconductors. This is a counter-intuitive result as one would expect that the phosphorus or/and carbon is introduced in the layer, the worse the superconductor would be. Given the counter-intuitive relation between the nanocrystal surface chemistry and the final nanocomposites performance, we expect that the use of ligands will be crucial in order to obtain a good superconducting film with the ability to pin the vortices. The use of Surfactis™ yields in the coagulation of ZrO_2 nanocrystals during YBCO growth probably due to the reduction of stabilizing effects during the thermal decomposition, resulting in no improved pinning properties.

3.8. References

1. J. MacManus-Driscoll, *et al.*, "Strongly enhanced current densities in superconducting coated conductors of $YBa_2Cu_3O_{7-x}$+$BaZrO_3$," *Nat. Mater.,* **3** [7] 439-43 (2004).
2. T. Haugan, *et al.*, "Addition of nanoparticle dispersions to enhance flux pinning of the $YBa_2Cu_3O_{7-x}$ superconductor," *Nature,* **430** [7002] 867-70 (2004).
3. L. Opherden, *et al.*, "Large pinning forces and matching effects in $YBa_2Cu_3O_{7-\delta}$ thin films with $Ba_2Y(Nb/Ta)O_6$ nano-precipitates," *Sci. Rep.,* **6** 21188 (2016).
4. M. Sieger, *et al.*, "$Ba_2Y(Nb/Ta)O_6$–Doped YBCO Films on Biaxially Textured Ni–5at.% W Substrates," *IEEE Trans. Appl. Supercond.,* **26** [3] 1-5 (2016).
5. J. Hänisch, *et al.*, "Formation and pinning properties of growth-controlled nanoscale precipitates in $YBa_2Cu_3O_{7-\delta}$/transition metal quasi-multilayers," *Supercond. Sci. Technol.,* **19** [6] 534-40 (2006).
6. L. Lei, *et al.*, "Influences of Y_2O_3 nanoparticle additions on the microstructure and superconductivity of YBCO films derived from low-fluorine solution," *Mater. Chem. Phys.,* **127** [1] 91-94 (2011).
7. S. Ye, *et al.*, "Preparation of solution-based YBCO films with $BaSnO_3$ particles," *Phys. C,* **471** [7] 265-69 (2011).
8. M. Erbe, *et al.*, "$BaHfO_3$ artificial pinning centres in TFA-MOD-derived YBCO and GdBCO thin films," *Supercond. Sci. Technol.,* **28** [11] 114002 (2015).
9. F. Ding, *et al.*, "Strong enhancement flux pinning in MOD-$YBa_2Cu_3O_{7-x}$ films with self-assembled $BaTiO_3$ nanocolumns," *Appl. Surf. Sci.,* **314** 622-27 (2014).
10. J. Gutierrez, *et al.*, "Strong isotropic flux pinning in solution-derived $YBa_2Cu_3O_{7-x}$ nanocomposite superconductor films," *Nat. Mater.,* **6** [5] 367-73 (2007).
11. M. Coll, *et al.*, "Size-controlled spontaneously segregated Ba_2YTaO_6 nanoparticles in $YBa_2Cu_3O_7$ nanocomposites obtained by chemical solution deposition," *Supercond. Sci. Technol.,* **27** [4] 044008 (2014).
12. F. Martinez-Julian, *et al.*, "Chemical Solution Approaches to $YBa_2Cu_3O_7$-Au Nanocomposite Superconducting Thin Films," *J. Nanosci. Nanotechnol.,* **11** [4] 3245-55 (2011).
13. P. Cayado, *et al.*, "Epitaxial $YBa_2Cu_3O_{7-x}$ nanocomposite thin films from colloidal solutions," *Supercond. Sci. Technol.,* **28** [12] 124007 (2015).
14. K. De Keukeleere, *et al.*, "Superconducting $YBa_2Cu_3O_{7-\delta}$ Nanocomposites Using Preformed ZrO_2 Nanocrystals: Growth Mechanisms and Vortex Pinning Properties," *Adv. Electr. Mater.,* **2** [10] 1600161 (2016).
15. A. Llordes, *et al.*, "Evolution of metal-trifluoroacetate precursors in the thermal decomposition toward high-performance $YBa_2Cu_3O_7$ superconducting films," *Chem. Mater.,* **22** [5] 1686-94 (2010).
16. X. Palmer, *et al.*, "Solution design for low-fluorine trifluoroacetate route to $YBa_2Cu_3O_7$ films," *Supercond. Sci. Technol.,* **29** [2] 024002 (2016).
17. J. De Roo, *et al.*, "Amino Acid-Based Stabilization of Oxide Nanocrystals in Polar Media: From Insight in Ligand Exchange to Solution ^{1}H NMR Probing of Short-Chained Adsorbates," *Langmuir,* **32** [8] 1962-70 (2016).
18. S. Ren, *et al.*, "Inorganic–organic hybrid solar cell: bridging quantum dots to conjugated polymer nanowires," *Nano Lett.,* **11** [9] 3998-4002 (2011).
19. P. Kim, *et al.*, "High energy density nanocomposites based on surface-modified $BaTiO_3$ and a ferroelectric polymer," *ACS nano,* **3** [9] 2581-92 (2009).

20. R. Ramesh and N. A. Spaldin, "Multiferroics: progress and prospects in thin films," *Nat. Mater.,* **6** [1] 21-29 (2007).
21. C. Shan*, et al.*, "Graphene/AuNPs/chitosan nanocomposites film for glucose biosensing," *Biosens. Bioelectron.,* **25** [5] 1070-74 (2010).
22. B. S. Guiton and P. K. Davies, "Nano-chessboard superlattices formed by spontaneous phase separation in oxides," *Nat. Mater.,* **6** [8] 586-91 (2007).
23. K. A. Bogle*, et al.*, "Synthesis of epitaxial metal oxide nanocrystals via a phase separation approach," *ACS nano,* **4** [9] 5139-46 (2010).
24. S. Komarneni, "Nanocomposites," *J. Mater. Chem. A,* **2** [12] 1219-30 (1992).
25. J. S. Moya, S. Lopez-Esteban, and C. Pecharroman, "The challenge of ceramic/metal microcomposites and nanocomposites," *Prog. Mater. Sci.,* **52** [7] 1017-90 (2007).
26. J. Joo*, et al.*, "Multigram scale synthesis and characterization of monodisperse tetragonal zirconia nanocrystals," *J. Am. Chem. Soc.,* **125** [21] 6553-57 (2003).
27. H. Rijckaert*, et al.*, "Microwave-assisted $YBa_2Cu_3O_7$ precursors: A fast and reliable method towards chemical precursors for superconducting films," *J. Am. Ceram. Soc,* **100** [6] 2407–18 (2017).
28. B. Fritzinger*, et al.*, "In situ observation of rapid ligand exchange in colloidal nanocrystal suspensions using transfer NOE nuclear magnetic resonance spectroscopy," *J. Am. Chem. Soc,* **131** [8] 3024-32 (2009).
29. K. De Keukeleere*, et al.*, "Stabilization of Colloidal Ti, Zr, and Hf Oxide Nanocrystals by Protonated Tri-n-octylphosphine Oxide (TOPO) and Its Decomposition Products," *Chem. Mater.* (2017).
30. X. Obradors and T. Puig, "Coated conductors for power applications: materials challenges," *Supercond. Sci. Technol.,* **27** [4] 044003 (2014).
31. H. Chen*, et al.*, "Growth rate control and solid–gas modeling of TFA-$YBa_2Cu_3O_7$ thin film processing," *Supercond. Sci. Technol.,* **23** [3] 034005 (2010).
32. X. Obradors*, et al.*, "Growth, nanostructure and vortex pinning in superconducting $YBa_2Cu_3O_7$ thin films based on trifluoroacetate solutions," *Supercond. Sci. Technol.,* **25** [12] 123001 (2012).
33. K. Zalamova*, et al.*, "Smooth Stress Relief of Trifluoroacetate Metal-Organic Solutions for $YBa_2Cu_3O_7$ Film Growth," *Chem. Mater.,* **18** [25] 5897-906 (2006).
34. T. Puig*, et al.*, "The influence of growth conditions on the microstructure and critical currents of TFA-MOD $YBa_2Cu_3O_7$ films," *Supercond. Sci. Technol.,* **18** [8] 1141 (2005).
35. E. Gyorgy*, et al.*, "Anisotropic critical currents in $Ba_2YCu_3O_7$ analyzed using an extended Bean model," *Appl. Phys. Lett.,* **55** [3] 283-85 (1989).
36. A. V. Pan, I. Golovchanskiy, and S. Fedoseev, "Critical current density: Measurements vs. reality," *EPL,* **103** [1] 17006 (2013).
37. P. Paturi, M. Malmivirta, H. Palonen, and H. Huhtinen, "Dopant Diameter Dependence of J(c)(B) in Doped YBCO Films," *IEEE Trans. Appl. Supercond.,* **26** [3] (2016).

Chapter four

Optimization of $YBa_2Cu_3O_{7-\delta}$-$BaZrO_3$ nanocomposite films

In this chapter, we report on the improvement of the YBCO microstructure and its J_c properties in nanocomposite thin films by introducing an intermediate dwelling step during the thermal process. This approach improves the formation of the YBCO nuclei density before the YBCO growth, leading to a self-field J_c of 5-6 MA cm^{-2} at 77 K for undoped and ZrO_2-doped YBCO thin films. Counter-intuitively, the distribution as well as the miniaturization of ZrO_2 nanocrystals in the YBCO matrix are independent of this intermediate dwelling step.

Adapted from:

H. Rijckaert, G. Pollefeyt, M. Sieger, J. Hänisch, J. Bennewitz, J. De Roo, K. De Keukeleere, R. Hühne, M. Bäcker, P. Paturi, H. Huhtinen, M. Hemgesberg and I. Van Driessche, Optimizing Nanocomposites through Nanocrystal Surface Chemistry: Superconducting $YBa_2Cu_3O_7$ Thin Films via Low-Fluorine Metal Organic Deposition and Preformed Metal Oxide Nanocrystals. Chemistry of Materials, 2017. 29(14), 6104-6113.

H. Rijckaert, J. Hänisch, G. Pollefeyt, M. Bäcker and I. Van Driessche: Influence of Intermediate Dwelling during $YBa_2Cu_3O_7$ Nanocomposite Formation. In preparation

4.1. Introduction

Despite the established CSD approach based on the *ex-situ* BaF_2 process starting from the trifluoroacetate metal-organic deposition (TFA-MOD) method, several research groups have already reported a more benign modified TFA-MOD method - i.e. low-fluorine (LF) - to reduce the release of fluorinated compounds during the YBCO crystallization.[1-3] However, superconducting performances of the pure YBCO film in function of both the applied magnetic field and direction remain a challenge. The properties can be improved by the introduction of nano-sized secondary phases as artificial pinning centers as they can act as pinning centers for the vortices.[4, 5] Although the pulsed laser deposition-grown method is an already advanced research to elucidate and to restrict the size, shape and density of pinning centers[6-9], there is limited knowledge of the control over the size distribution of nanoparticles via the spontaneous segregation during the CSD process of TFA-MOD methods. An additional intermediate dwell step at lower temperatures before the YBCO crystallization was introduced in several works using of CSD approach to offer an opportunity to tune the particle size during the self-assembled growth of nanoparticles.[10-12] Nonetheless, the reproducibility of the self-assembled nanoparticles was not mentioned in these published works and it is hard to reach a narrow size distribution of these nanoparticles. To tackle this uncontrollable process, the *ex-situ* approach of preformed nanocrystals was introduced in this work, resulting in a high reproducibility which is meaningful for the commercial production. However, the influence of nanocrystal addition on the nucleation and epitaxial growth process of LF-YBCO at the substrate surface is not completely understood. Understanding this process is particularly important for the fabrication of viable YBCO coated conductors. In this work, we present a comprehensive study to elucidate the influence of an additional intermediate dwelling step at several lower temperatures on the mechanism of the LF-YBCO nucleation and the final nanocrystal size in the YBCO matrix after the YBCO crystallization at 800 °C.

4.2. Experimental section

Undoped YBCO precursor solutions were prepared by dissolving Y-propionate, Ba-TFA and Cu-propionate in an Y:Ba:Cu ratio of 1:2:3 in methanol. Small 3-5 nm cubic ZrO_2 nanocrystals were synthesized via a heating-up method as described extensively by Joo *et al.*[13] (also in section 3.2 of chapter three) and are capped with hydrophobic ligands in nonpolar solvents. To transfer these as-synthesized nanocrystals to polar solvents (e.g. methanol), a ligand exchange with a commercially available polar copolymer with phosphonate groups[14] (which may be given in the form of its alkylolammonium salt, details in section 3.3 of chapter

three) was introduced. To obtain a clear colloidal ZrO_2 nanocrystal suspension, 35 mg copolymer was mixed with 0.075 mmol ZrO_2 precipitated nanocrystals in methanol. A transparent nano-suspension was obtained after an ultrasonic treatment. These as-stabilized nanocrystals were added to the YBCO precursor solution, resulting in ZrO_2-doped YBCO precursors solutions. Both precursor solutions have a total metal concentration of 1.08 M. The $LaAlO_3$ substrates were spin-coated with 2000 rpm for 1 minutes with undoped and 5 mol-% ZrO_2-doped YBCO precursor. The layers were successfully pyrolyzed by heating up to 400 °C with a heating rate of 3-5 °C min^{-1} in a wet oxygen atmosphere. Its microstructure consists of CuO nanoparticles embedded in an amorphous matrix of $Ba_{1-x}Y_xF_{2+x}$ (BYF). The pyrolyzed YBCO films were subsequently treated to obtain the desired superconducting film with the high-temperature thermal treatment (Figure 4.X) with a heating rate of 5 K min^{-1} to 600, 650 or 700 °C [1] and dwelling for 60 min with 45 min in a humid 100 ppm O_2 in N_2 atmosphere and 15 min in a dry 100 ppm O_2 in N_2 atmosphere. After the additional dwelling step, fast heating to 800 °C (15 K min^{-1}) was introduced under dry conditions and switched back to humid conditions at 770 °C to avoid the formation of a/b grains (between [1] and [2]). The inlet gas was bubbled through a water bath with a temperature of 23 °C. After this crystallization dwelling step of 60 min with 45 min wet, the flowing atmosphere was switched to dry atmosphere. O_2 atmosphere was introduced during the annealing step [3] at 450 °C for 2 hours

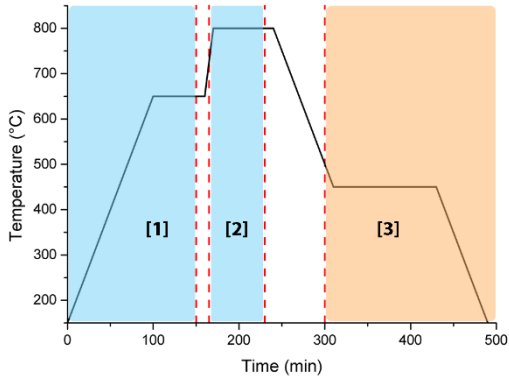

Figure 4.1. *Schematic representation of an YBCO thermal process with additional dwelling step: [1] Slow heating to the dwell temperature and dwelling under wet 100 ppm O_2 in N_2 atmosphere. After this dwelling, a fast heating to the crystallization temperature under dry 100 ppm O_2 in N_2 atmosphere was introduced to avoid the formation of a/b grains. [2] The atmosphere was switched to a wet 100 ppm O_2 in N_2 atmosphere during the crystallization. [3] After this crystallization process, the oxygenation process under an O_2 atmosphere was introduced.*

4.3. The nucleation and growth of $YBa_2Cu_3O_7$ nanocomposite film

The nucleation and growth of fluorine-based YBCO systems can be found in literature[15-17] and is described as the *ex-situ* BaF_2 process (see chapter 2 section 2.3.1) where the BYF phase transforms into $Ba(O,F)_2$ and Y_2O_3 composites while Y_2O_3 reacts with CuO nanoparticles to form $Y_2Cu_2O_5$ which is followed by the nucleation of the tetragonal $YBa_2Cu_3O_6$ ($YBCO_6$) phase at temperatures between 650 and 700 °C. In order to study the nucleation and growth process of undoped YBCO, all pyrolyzed samples with smooth and crack-free surface were crystallized and quenched by quickly pulling them out of the tube furnace at several intermediate temperatures (400, 500, 600, 650, 700, 750 and 800 °C). After XRD analysis on these samples, the XRD pattern of the YBCO layer (Figure 4.2a), starting from LF-YBCO precursors, shows that BYF reflections - (111) (2θ = 24.9°), (002) (2θ = 28.8°) and (202) (2θ = 42.2°) - shift towards lower 2θ angles for increasing temperature. This is due to a compositional change and related to the development of a BaF_2-based superstructure, which has been found to provide a good template for YBCO nucleation.[18] Upon increasing the temperature, Y is removed from the BYF phase to form Y_2O_3 (400) (2θ = 33.7°) which reacts with fine nanocrystals of CuO (11$\underline{1}$) (2θ = 35.5°) to form a submicron-sized $Y_2Cu_2O_5$ phase (peaks at 2θ = 33.4) at ~650 °C. Similar to the results published in literature, the reaction between CuO and Y_2O_3 is almost directly followed by the nucleation of $YBCO_6$. The first trace content of $YBCO_6$ nucleation can be identified at 650 °C with YBCO (005) (2θ = 38.3°). To clarify the influence of ZrO_2 nanocrystals on the nucleation and growth of YBCO, the quenched ZrO_2-doped YBCO films were analyzed via XRD (Figure 4.2b). The results indicat that the formation of the (002)-oriented BaF_2 superstructure is reduced between 650 and 700 °C compared to undoped YBCO. This can most likely be assigned to the reaction between the BYF phase and ZrO_2 nanocrystals, resulting in the formation of $BaZrO_3$ particles, which cannot be observed in XRD probably due to the small size and homogeneous distribution in the YBCO matrix.

As the ZrO_2 nanocrystals react with the BaF_2 structure before they react with $Y_2Cu_2O_5$, it will enhance the feasibility of the hetero-epitaxial growth of $BaZrO_3$ particles on the $LaAlO_3$ interface during growth. This effect can result in worse epitaxial growth of YBCO.[19] Here, no accumulation of ZrO_2 nanocrystals on the $LaAlO_3$ interface can be observed in the pyrolyzed films as confirmed via TOF-SIMS analysis (see Figure A3.1 in Appendix A), indicating a homogenous distribution. This spread-out of nanocrystals in a very important step to avoid the tendency to the agglomerations or accumulations of nanocrystals during the

growth. The change of the intermediate amorphous phases has been estimated from the intensity of XRD peaks - BaF_2 (111) and YBCO (005) - with different quench temperatures as shown in Figures 4.2c and 4.2d. We can conclude that ZrO_2-doped YBCO films exhibit a different evolution of BaF_2 (111) compared to undoped YBCO. Also with increasing temperature, the intensity of the YBCO (005) peak increases although the ZrO_2-doped YBCO seems to display some delay in the YBCO nucleation. It is also remarkable that the intensity of fine CuO (11$\underline{1}$) nanocrystals for YBCO with nanocrystals is higher than for YBCO without nanocrystals, also confirming the delayed reaction mechanism, which results in a delay in YBCO growth. From Figures 4.2c and 4.2d as well as the absence of a $BaZrO_3$ (200) peak in Figure 4.2b, an accumulation and formation of $BaZrO_3$ at the $LaAlO_3$ interface can be ruled out. It is also confirmed via HRTEM image of the quenched sample at 650 °C (Figure 4.2e), where no accumulation of ZrO_2 nanocrystals can be observed.

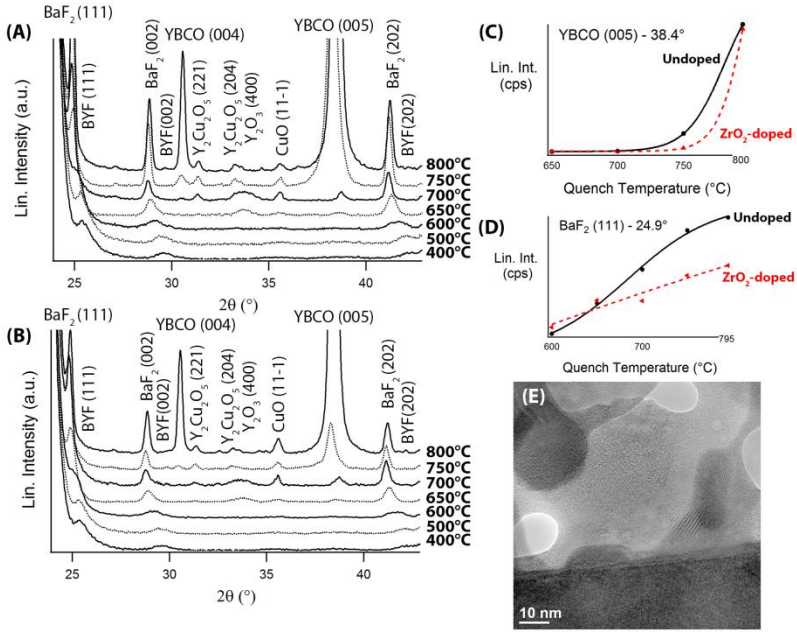

Figure 4.2. *XRD scans of (A) undoped and (B) ZrO_2-doped YBCO films quenched at various intermediate temperatures. Temperature dependence of the intensity of XRD peaks of (C) YBCO (005) (2θ = 38.4°) and (D) BaF_2 (111) (2θ = 24.9°). (E) A HRTEM image of ZrO_2-doped YBCO film quenched at 650 °C.*

4.4. Introduction of an intermediate dwelling step.

As mentioned above the nucleation and growth of YBCO is an important step for achieving a highly (00ℓ) textured YBCO layer with nanocrystal addition. As concluded from the quench study, Ba^{2+} reacts with ZrO_2 nanocrystals to $BaZrO_3$ particles in the temperature range between 650 °C and 700 °C and the nucleation of YBCO occurs at ~650 °C. In order to promote the nucleation of YBCO, we introduced an intermediate heat treatment step at temperatures of 600, 650 and 700 °C with a dwell time of 1 hour with 45' wet and 15' dry 100 ppm O_2 in N_2 atmosphere.[2] Whereas YBCO grains start growing at 700 °C as indicated by the YBCO (005) peak from the XRD data (Figure 4.3) of the quenched samples after dwelling for 1 hour, they remain small and only increase in nuclei density at 650 °C - broader peak of YBCO (005) -, indicating an increased amount of small nucleation sites. When dwelling at 600 °C, no YBCO (005) was observed for both undoped and ZrO_2-doped samples. Remarkably, there is some reduction of the BaF_2 reflections because of their reactivity with ZrO_2 nanocrystals.

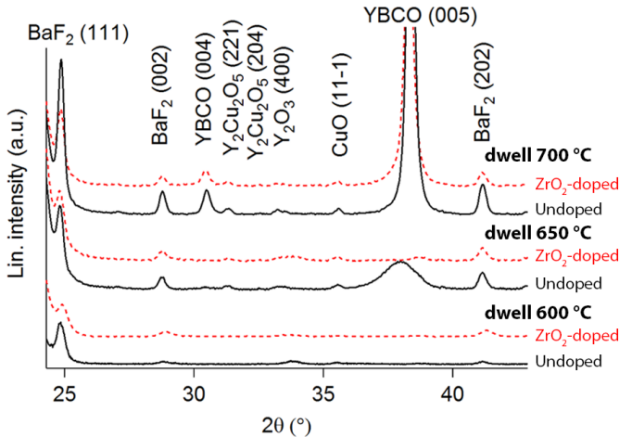

Figure 4.2. *XRD patterns of undoped (black, full line) and ZrO_2-doped (red, dotted line) YBCO samples quenched after dwelling at 600, 650 and 700 °C.*

To confirm the improvement of nucleation, the pyrolyzed samples undergo full crystallization at 800 °C with humid 100 ppm O_2 in N_2 atmosphere followed by an annealing step at 450 °C for 2 hours under pure O_2 atmosphere.[3] After the additional dwelling step, fast heating to 800 °C (15 K min^{-1}) was introduced under dry conditions and switched back to humid conditions at 770 °C to avoid the formation of a/b grains. The inlet gas was humidified with a dew point of 23 °C. Their (inductive) self-field critical current densities are given in Table 4.1.

The intermediate step at 650 °C clearly results in an improved J_c of 5-6 MA cm^{-2} for both precursors. This happens because of the increase of T_c in the range of 91.5 K compared to T_c of both precursors without an intermediate dwelling step. By lowering the temperature of the intermediate step to 600 °C, T_c decreases for both precursors but undoped YBCO still shows a fairly good J_c of 3.31 MA cm^{-2} while ZrO_2-doped YBCO did not a finite J_c due to the bad epitaxial structure. When increasing the temperature of the intermediate step to 700 °C, more secondary phases and *a/b*-oriented YBCO grains are formed which would degrade the superconducting properties by decreasing the superconductive cross section. So, the temperature of the intermediate dwelling step is very crucial to obtain an enhancement of J_c values for both undoped and ZrO_2-doped YBCO films. This enhancement via introduction of the additional dwelling step is comparable to the pulsed laser deposition-grown method where the nuclei density can be controlled by deposition temperature[20], laser frequency[21] or nano-crystallinity of the target.[22] As mentioned in literature[10-12], for CSD the intermediate dwelling step prevents accumulation of particles at the $LaAlO_3$ interface and hence excessive grain growth and also minimizes agglomeration of nanocrystals in the YBCO matrix. However, compared to this work, it has been shown that even during thermal processing without the intermediate dwelling step an accumulation of nanocrystals at the $LaAlO_3$ interface did not occur, as confirmed by HAADF-STEM image (Figure 4.4) and TOF-SIMS analysis (see Figure A4.2 in Appendix A). It is remarkable that the upper layer (approx. 30 nm) of YBCO matrix shows a high density of stacking faults but is probably caused by TEM sample preparation due to the FIB-induced damage during the thinning and the cleaning steps.

Table 4.1. *Self-field critical current density J_c (inductively measured at 77 K) and critical temperature T_c of undoped YBCO and ZrO_2-doped YBCO layer after the complete thermal process with an additional dwell step at different temperatures.*

Dwell temperature	**YBCO**		**ZrO_2-doped YBCO**	
	J_c	T_c	J_c	T_c
°C	**MA cm^{-2}**	**K**	**MA cm^{-2}**	**K**
700	1.25	90.1±0.4	1.10	91.1±0.4
650	5.51	91.4±0.6	5.80	91.6±0.9
600	3.31	90.2±0.5	0.00	90.1±1.3
no dwell	2.52	90.6±0.7	2.39	90.9±0.7

The size distribution of $BaZrO_3$ particles (determined and fitted via two different cross-sectional HAADF-STEM images of nanocomposites) shows a mean

diameter of 13.0±5.5 nm after the thermal process with the intermediate dwelling step while the thermal process without the intermediate dwelling step produced 14.2±5.2 nm average-sized $BaZrO_3$ particles in the YBCO matrix. (See section A3.2 in Appendix A for more data). Interestingly, the preformed ZrO_2 nanocrystals with 3-4 nm diameter have coarsened by four times to $BaZrO_3$ particles during the thermal process. (This effect will be explained in section 4.5) This means that the introduction of the intermediate dwelling step in the range of 640-650 °C does not improve the distribution of nanoparticles in the YBCO matrix but results in the improvement of the superconducting properties of the YBCO matrix itself. This is also confirmed by XRD patterns (Figure 4.4b), indicating that the thermal process with the additional dwelling step of undoped layers reduces the formation of Y_2O_3 (222) ($2\theta = 29.2°$) and increases the $Ba_xCu_yO_z$ ($2\theta = 27.7°$) amount. This formation of the $Ba_xCu_yO_z$ phase is prevented by the introduction of ZrO_2 nanocrystals in combination with the increase of Y_2O_3 (222) which can contribute to pinning.[14] So, the additional dwelling step at 650 °C reduces undesired secondary phases in the YBCO matrix of the nanocomposite film and thus improves the YBCO morphology. This presumption is verified by the SEM images of undoped and ZrO_2-doped layers after the thermal process with additional dwelling step (see Figure A4.4 in Appendix A).

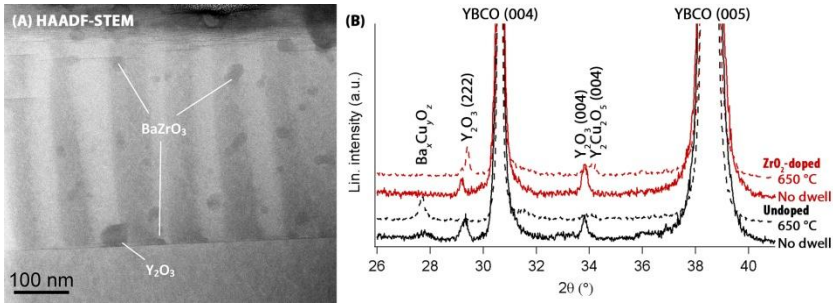

Figure 4.4. *(A) HAADF-STEM image of ZrO_2-doped YBCO after thermal process without a dwell step. $BaZrO_3$ particles are randomly distributed in the YBCO matrix. (B) XRD patterns of undoped and ZrO_2-doped YBCO layer after thermal process with or without a dwell step.*

To determine the improvement of vortex pinning, the magnetic field dependence of the transport critical current densities - at 77 K and magnetic field (B) parallel to c-axis of YBCO ($B||c$) - of an undoped and a ZrO_2-doped YBCO film was shown on Figure 4.5. This indicates that the addition of ZrO_2 nanocrystals has enhanced the capabilities to pin the vortices. However, it is remarkable that the use of the additional dwelling step (red data) results in a higher maximum pinning force density (F_p) of around 7.3 GN m^{-3} at 0.8 T for the

ZrO_2-doped and around 2.9 GN m^{-3} at 1.5 T for the undoped film, while the absence of the additional dwell step (black data) results in F_p of 6.0 GN m^{-3} at 0.9 T for the ZrO_2-doped and 2.1 GN m^{-3} at 1.3 T for the undoped film. Thus, clearly the addition of 5 mol-% ZrO_2 nanocrystals in the YBCO matrix further increases F_p by three times while the introduction of an additional dwelling step increases self-field J_c and does not minimize or prevent the coarsening of the nanocrystals during the thermal process resulting in a further increase in in-field performance and maximum F_p. But it is remarkable that the maximum of F_p is shifted towards the lower magnetic field by the addition of nanocrystals. Based on F_p curves of the undoped and ZrO_2-doped films, it seems that undoped YBCO shows a wider maximum of F_p, indicating a better pinning performance at higher magnetic field compared to ZrO_2-doped YBCO films where a steeper decay of F_p curve is observed. As observed on XRD (Figure 4.4), in-situ Y_2O_3 particles are more present in undoped YBCO layer without an additional dwelling step and as Y_2O_3 particles can contribute to the pinning performance, the F_p is at lower magnetic field (1.3 T) compared to a maximum F_p value at higher magnetic field (1.5 T) of undoped YBCO with additional dwelling step. The addition of preformed nanocrystals or the introduction of self-assembled nanoparticles can lead to a shift of maximum F_p value towards a lower magnetic field. A follow-up study should be essential to understand the origination of this shifting effect.

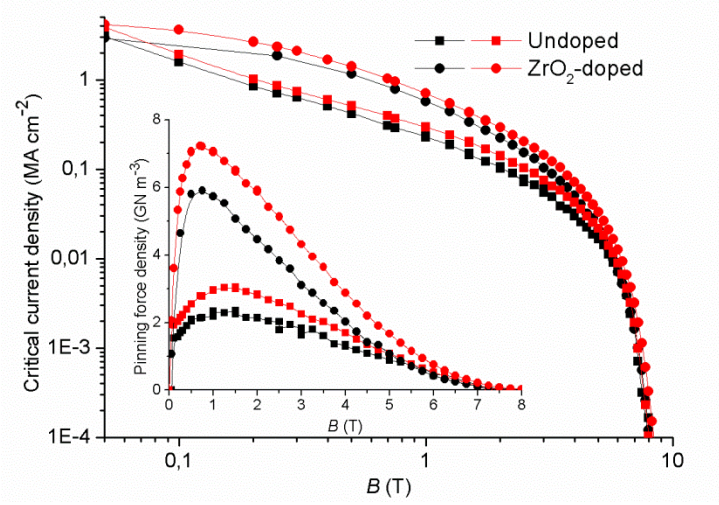

Figure 4.5. *Magnetic field dependence of the transport J_c showing the in-field enhancement of J_c by both the addition of ZrO_2 nanocrystals to the solution (symbol) and/or of a dwelling step at 650 °C in the heat treatment (color). [Measured at Karlsruhe Institute of Technology]*

For an essential breakthrough to commercial production, these results have to be transferred to textured Ni-W tape with an epitaxial oxide buffer stacked layers or polycrystalline Hastelloy tape with a complex sequence of oriented oxide buffer layers.[23] Both types of technical tape have an additional CeO_2 cap layer. Thus, this transfer is challenging because the YBCO growth rate on an oxide buffer layer is different than on single crystal substrates due to less defined (00ℓ) terminations of the CeO_2 oxide layer which will affect the YBCO nuclei density.[24] This limitation can be obviated by the optimization of temperature and duration of the additional dwelling step during the thermal process which is the focus of future studies.

4.5. Copolymer based nanocomposite, a structural investigation.

As described in section 3.6 of chapter three, ZrO_2 nanocrystals stabilized with steric polar ligand by means of copolymer would lead to excellent superconducting properties in combination with the introduction of an intermediate dwelling step. So to unravel these advantages, the pyrolyzed layers of undoped YBCO and copolymer based nanocomposites are crystallized at 790 °C after a 1 hour dwell step at 640 °C. This two-step process is used to improve the nucleation mechanism and therefore to control the microstructure. The surfaces of both undoped YBCO and nanocomposite films are dense and smooth without the presence of any *a*/*b*-oriented grains (Figure 4.6). Cross-sectional SEM analysis shows that the thickness of the YBCO film is 350-375 nm (inset Figure 4.6) with minor secondary phases.

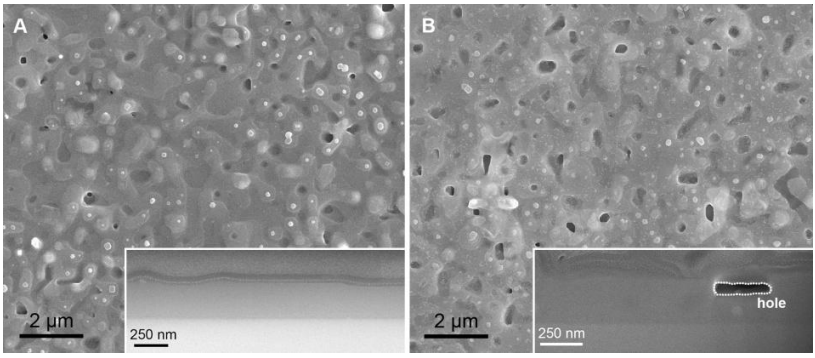

Figure 4.6. *Topographical top-view SEM image of (A) undoped and (B) 5 mol-% ZrO_2 nanocrystals YBCO thin films with cross-sectional side-view as insets.*

The YBCO thin films with and without 5 mol-% ZrO_2 nanocrystals exhibit an (00ℓ) texture, that proves that the YBCO phase grows epitaxially on the $LaAlO_3$

substrate for both precursors (Figure 4.7). Small amounts of secondary phases such as $Ba_xCu_yO_z$ – mostly poorly ordered $BaCu_3O_4$ ($2\theta = 27.7°$ and 42°)[25] – and Y_2O_3 ((222) at 29.9° and (004) at 34.2°) are detected. The $Ba_xCu_yO_z$ content is reduced for 5 mol-% ZrO_2 nanocrystals, most likely due to reaction of Ba^{2+} with ZrO_2 nanocrystals during the crystallization, which results in a higher fraction of biaxially and randomly oriented Y_2O_3 particles. The latter has also shown to contribute to vortex pinning.[26, 27] Nanocomposite films show a reflection at 43.0° for $BaZrO_3$ (200), while ZrO_2 reflections remain absent. This confirms the transformation of the ZrO_2 nanocrystals into $BaZrO_3$ nanocrystals during the heat treatment. The crystallite size of $BaZrO_3$ (200) is 12 nm, calculated via the Scherrer equation. No reflection of YBCO (103) ($2\theta = 32.8°$) can be observed, which would have represented a misoriented fraction.

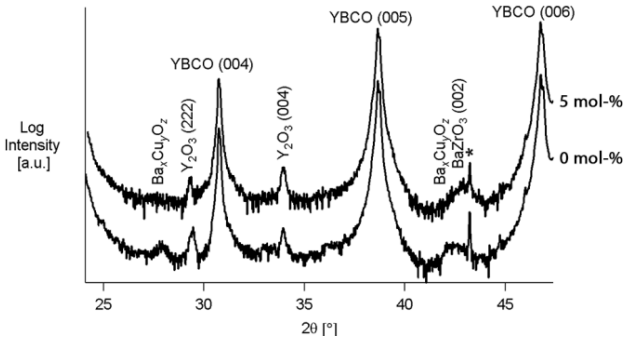

Figure 4.7. *XRD analysis of undoped YBCO and the 5 mol-% ZrO_2- copolymer based nanocomposite after crystallization.*

The YBCO (103) pole figures of the samples with and without nanocrystals (see Figure A4.5 in Appendix A) show a fourfold symmetry, demonstrating that the films are biaxially oriented (cube-on-cube relationship). The FWHM values of the YBCO (103) ϕ-scans (see Figure A4.6 in Appendix A) of undoped YBCO and nanocomposite are about 0.8°, indicating a sharp in-plane alignment. The out-of-plane crystallographic texture of YBCO is determined by measuring the FWHM values of the YBCO (006) XRD rocking curves (ω-scans) (see Figure A4.7 in Appendix A). Undoped samples give 0.43° compared to 0.56° for a nanocomposite film. The widening of the rocking curve can indicate a small increase of microstrain in the nanocomposite.[28] We conclude that the structural integrity of the nanocomposite films is comparable to the undoped YBCO layers.

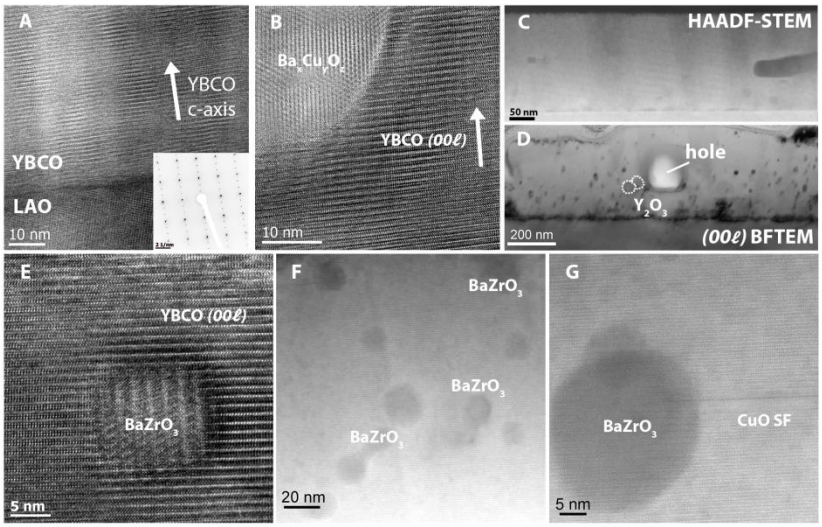

Figure 4.8. *Undoped YBCO film: (A) HR-TEM images of the YBCO/$LaAlO_3$ interface and its diffraction pattern (inset), (B) $Ba_xCu_yO_z$ particles in the YBCO matrix and (C) High angle annular dark field (HAADF)-STEM cross sectional image. Nanocomposite film: (D) Cross-section bright field TEM image taken with a diffraction vector $\vec{g}$ = (003). (E) HR-TEM image of randomly oriented $BaZrO_3$ particles embedded in the YBCO matrix. (F-G) HAADF-STEM Z-contrast image of YBCO-5 mol-% ZrO_2 nanocomposite. Black dots correspond to $BaZrO_3$ particles.*

The fully biaxial (00ℓ) texture of the YBCO layer with cube-on-cube orientation between YBCO and $LaAlO_3$ is further corroborated by the HR-TEM image of the $LaAlO_3$/YBCO interface (Figure 4.8a) with the electron diffraction pattern as inset. There are no defect structures in the YBCO matrix around randomly oriented $Ba_xCu_yO_z$ particles visible in the HR-TEM image (Figure 4.8b) and the FFT pattern (Figure A4.8a in Appendix A). Figure 4.8c shows a cross-sectional STEM image of undoped YBCO with $Ba_xCu_yO_z$ and Y_2O_3 particles embedded in the YBCO layer, which is in agreement with the XRD analysis (Figure 4.7). In the nanocomposite, $BaZrO_3$ particles are mainly homogenously dispersed throughout the film, although some are present at the interface (black dots in Figure 4.8d). An isolated, randomly oriented $BaZrO_3$ particle is shown in Figure 4.8e (FFT pattern in Figure A4.8b). The size distribution of $BaZrO_3$ particles (*vide supra*) shows a mean diameter of 13.0±5.5 nm, which indicates that the initial (3.5±0.4 nm) ZrO_2 nanocrystals have coarsened during the thermal process. The growth can be attributed to both their reactivity with Ba^{2+} and a slight degree of agglomeration in the film (Figure 4.8f). The latter is driven by (i) aggregation in solution (see polydispersity index, Table 4.1), (ii) aggregation upon deposition

and drying (See Figure A3.4) and (iii) aggregation during the thermal process. Given the large polydispersity index for short carboxylates and the observed aggregates in TEM, this is another reason for the worse performance of the short carboxylate based nanocomposites. Regarding the final $BaZrO_3$ nanoparticle size, our results obtained with copolymer stabilized nanocrystals compare favorably with literature reports using zirconium salts in YBCO solution as nanocomposite precursors. In the latter case, the final $BaZrO_3$ particles were in the order of 30 nm in diameter,[29] which is a 12 fold volume difference compared to the 13 nm particles described here.

The $BaZrO_3$ particles are mostly randomly oriented, while YBCO remains epitaxial, thus generating incoherent interfaces which can act as nucleation centers for Y124-type intergrowths. These short (< 10 nm) Y124-type stacking faults are thought to be contributing for pinning[30] and seem to be absent in ZrO_2-doped films as observed in the HRTEM images. However, we observed some local and long order Y124 regions (Figure 4.8g) in the YBCO matrix which are possibly induced by the high amount of Y_2O_3 and non-stoichiometric amount of Ba^{2+}. The strain ε of the YBCO matrix calculated via a Williamson-Hall plot slightly increases for the nanocomposite (0.135%) compared to the undoped YBCO films (0.125%), indicating some nanostrained regions in nanocomposite matrix. In this case, randomly oriented particles in YBCO matrix produced the desired lattice strain due to the large degree of incoherent interface.[31] This additional strain at the $BaZrO_3$ and YBCO interface can lead to the vortex pinning enhancement. In order to reveal this strain effect, an in-depth texture analysis (e.g. offset scans) should be investigated to confirm the existence of a preferential axiotaxial orientation (off-axis alignment) of $BaZrO_3$ particles in the YBCO matrix and their contribution to the pinning mechanism.

4.6. Conclusion

In summary, we have shown that the addition of the preformed ZrO_2 nanocrystals results in a delay in YBCO nucleation and growth because of the nanocrystal reactivity with Ba^{2+} between temperatures of 600 and 700 °C, leading to the formation of $BaZrO_3$ particles. This latter would lead to less BaF_2 (111) superstructure which acts as a template for YBCO nucleation. For this reason, we have introduced an additional dwelling step to improve YBCO nuclei density and to avoid the coarsening of nanocrystals. However, this extra dwelling step does not improve the distribution nor the miniaturization of nanocrystals in the YBCO matrix, but does result in the improvement of superconducting properties. As a result, the intermediate dwelling step at 650 °C has revealed a J_c of 5.5 MA cm^{-2} for undoped and 5.8 MA cm^{-2} for ZrO_2-doped YBCO films. Due to the addition of nanocrystals, the pinning force densities of ZrO_2-doped are threefold increased compared to undoped YBCO films. The present work has shown how to control and improve the performance of YBCO nanocomposites by understanding the stabilization and the growth of pinning-active nanocrystals in the YBCO matrix. This approach results in a high maximum pinning force density of 7.3 GN m^{-3}, which is more than tripled compared to undoped YBCO thin films.

4.7. References

1. X. Palmer, *et al.*, "Solution design for low-fluorine trifluoroacetate route to $YBa_2Cu_3O_7$ films," *Supercond. Sci. Technol.,* **29** [2] 024002 (2016).
2. Y. Chen, C. Wu, G. Zhao, and C. You, "An advanced low-fluorine solution route for fabrication of high-performance YBCO superconducting films," *Supercond. Sci. Technol.,* **25** [6] 062001 (2012).
3. H. Rijckaert*, et al.*, "Microwave-assisted $YBa_2Cu_3O_7$ precursors: A fast and reliable method towards chemical precursors for superconducting films," *J. Am. Ceram. Soc.,* **100** [6] 2407–18 (2016).
4. J. MacManus-Driscoll*, et al.*, "Strongly enhanced current densities in superconducting coated conductors of $YBa_2Cu_3O_{7-x}$+$BaZrO_3$," *Nat. Mater.,* **3** [7] 439-43 (2004).
5. J. Gutierrez*, et al.*, "Strong isotropic flux pinning in solution-derived $YBa_2Cu_3O_{7-x}$ nanocomposite superconductor films," *Nat. Mater.,* **6** [5] 367-73 (2007).
6. M. Malmivirta*, et al.*, "Enhanced flux pinning in YBCO multilayer films with BCO nanodots and segmented BZO nanorods," *Sci. Rep.* 1 (2017).
7. T. Haugan*, et al.*, "Addition of nanoparticle dispersions to enhance flux pinning of the $YBa_2Cu_3O_{7-x}$ superconductor," *Nature,* **430** [7002] 867-70 (2004).
8. M. Sieger*, et al.*, "$Ba_2Y(Nb/Ta)O_6$–Doped YBCO Films on Biaxially Textured Ni–5at.% W Substrates," *IEEE Trans. Appl. Supercond.,* **26** [3] 1-5 (2016).
9. J. Hänisch*, et al.*, "Formation and pinning properties of growth-controlled nanoscale precipitates in $YBa_2Cu_3O_{7-\delta}$/transition metal quasi-multilayers," *Supercond. Sci. Technol.,* **19** [6] 534-40 (2006).
10. K. Nakaoka*, et al.*, "Another approach for controlling size and distribution of nanoparticles in coated conductors fabricated by the TFA-MOD method," *Supercond. Sci. Technol.,* **30** [5] 055008 (2017).
11. M. Coll*, et al.*, "Size-controlled spontaneously segregated Ba_2YTaO_6 nanoparticles in $YBa_2Cu_3O_7$ nanocomposites obtained by chemical solution deposition," *Supercond. Sci. Technol.,* **27** [4] 044008 (2014).
12. H. Horita*, et al.*, "Miniaturization of $BaHfO_3$ nanoparticles in $YBa_2Cu_3O_y$-coated conductors using a two-step heating process in the TFA-MOD method," *Supercond. Sci. Technol.,* **30** [2] 025022 (2016).
13. J. Joo*, et al.*, "Multigram scale synthesis and characterization of monodisperse tetragonal zirconia nanocrystals," *J. Am. Chem. Soc.,* **125** [21] 6553-57 (2003).
14. H. Rijckaert*, et al.*, "Optimizing Nanocomposites through Nanocrystal Surface Chemistry: Superconducting $YBa_2Cu_3O_7$ Thin Films via Low-Fluorine Metal Organic Deposition and Preformed Metal Oxide Nanocrystals," *Chem. Mater.,* **29** [14] 6104-13 (2017).
15. K. Zalamova*, et al.*, "Intermediate phase evolution in YBCO thin films grown by the TFA process," *Supercond. Sci. Technol.,* **23** [1] 014012 (2009).
16. L. H. Jin*, et al.*, "Evolution of low fluorine solution in decomposition and crystallization for $YBa_2Cu_3O_y$ film growth," *J. Alloy. Compd.,* **568** 36-41 (2013).
17. D. Wesolowski, M. Yoshizumi, and M. Cima, "Understanding the MOD process between decomposition and YBCO formation," *IEEE Trans. Appl. Supercond.,* **17** [2] 3351-54 (2007).

18. J. Gazquez*, et al.*, "Precursor Evolution and Nucleation Mechanism of $YBa_2Cu_3O_x$ Films by TFA Metal-Organic Decomposition," *Chem. Mater.,* **18** [26] 6211-19 (2006).
19. K. De Keukeleere*, et al.*, "Superconducting $YBa_2Cu_3O_{7-\delta}$ Nanocomposites Using Preformed ZrO_2 Nanocrystals: Growth Mechanisms and Vortex Pinning Properties," *Adv. Electr. Mater.,* **2** [10] 1600161 (2016).
20. D. Feldmann*, et al.*, "Influence of growth temperature on critical current and magnetic flux pinning structures in $YBa_2Cu_3O_{7-x}$," *Appl. Phys. Lett.,* **91** [16] 162501 (2007).
21. I. A. Golovchanskiy, A. V. Pan, S. A. Fedoseev, and M. Higgins, "Significant tunability of thin film functionalities enabled by manipulating magnetic and structural nano-domains," *Appl. Surf. Sci.,* **311** 549-57 (2014).
22. P. Paturi, H. Huhtinen, K. Laajalehto, and R. Laiho, "Reason for high critical current in thin YBCO films prepared by laser ablation from nanostructured target," *Supercond. Sci. Technol.,* **13** [5] 622 (2000).
23. X. Obradors and T. Puig, "Coated conductors for power applications: materials challenges," *Supercond. Sci. Technol.,* **27** [4] 044003 (2014).
24. V. F. Solovyov*, et al.*, "Nature of Y1Ba2Cu3O7 nucleation centers on ceria buffers," *Supercond. Sci. Technol.,* **23** [1] 014008 (2009).
25. J. Zeng*, et al.*, "HRTEM characterization of $YBa_2Cu_3O_{7-\delta}$ thick films on $LaAlO_3$ substrates," *Phys. C,* **405** [2] 127-32 (2004).
26. S. K. Viswanathan*, et al.*, "Enhancement of critical current density of $YBa_2Cu_3O_{7-\delta}$ thin films by self-assembly of Y_2O_3 nanoparticulates," *Thin Solid Films,* **515** [16] 6452-55 (2007).
27. P. Mele*, et al.*, "High pinning performance of $YBa_2Cu_3O_{7-x}$ films added with Y_2O_3 nanoparticulate defects," *Supercond. Sci. Technol.,* **28** [2] 024002 (2015).
28. S. C. Wimbush*, et al.*, "Interfacial Strain-Induced Oxygen Disorder as the Cause of Enhanced Critical Current Density in Superconducting Thin Films," *Adv. Funct. Mater.,* **19** [6] 835-41 (2009).
29. A. Llordes*, et al.*, "Nanoscale strain-induced pair suppression as a vortex-pinning mechanism in high-temperature superconductors," *Nat. Mater.,* **11** [4] 329-36 (2012).
30. A. Llordés*, et al.*, "Nanoscale strain-induced pair suppression as a vortex-pinning mechanism in high-temperature superconductors," *Nat. Mater.,* **11** [4] 329-36 (2012).
31. E. Solano*, et al.*, "Axiotaxy in oxide heterostructures: Preferential orientation of BaCeO3 nanoparticles embedded in superconducting YBa2Cu3O7− δ thin films," *Thin Solid Films,* **638** 105-13 (2017).

Chapter five

Maximizing the properties of $YBa_2Cu_3O_{7-\delta}$-$BaZrO_3$ nanocomposite films

In this chapter, the superconducting properties of ZrO_2-doped YBCO films were investigated via transport measurements to confirm the success of the addition of preformed nanocrystals in the YBCO matrix via a CSD-based method. This approach seems not straightforward as the higher loading of nanocrystals can affect the structural and superconducting properties of the YBCO film.

5.1. Epitaxial $YBa_2Cu_3O_7$ nanocomposite films, what now?

Generators and other rotating devices used in energy conversion would be an ideal future application for the HTS Ni5W tapes. However, these parts of infrastructure operate at magnetic fields that would normally lower the performance of the superconductor significantly. To maintain the outstanding current transport properties of YBCO, the YBCO inks used to make the thin film need to be doped with preformed nanocrystals. In chapter three, it has been proven that the nanocrystal surface chemistry is a crucial step during the nanocomposite formation, yielding excellent structural properties as discussed in chapter four. However, it is important that the addition of preformed nanocrystals, as so-called artificial pinning centers, can effectively decrease the magnetic field dependence of J_c. To confirm the success of this approach, the superconducting properties of ZrO_2-doped YBCO layers on single crystal substrates were investigated via transport measurements. The reason is that it is easier to study its pinning mechanism on $LaAlO_3$ substrates since extra parameters due to influences of the substrate are eliminated.

5.2. Experimental section

The LF-YBCO precursor solutions were prepared by dissolving Y-propionate, Ba-TFA and Cu-propionate in an Y:Ba:Cu ratio of 1:2:3 plus additives in methanol. The reaction mixture is heated to 60 °C for 30 min on a hot plate. Subsequently, the total metal concentration is adjusted to 1.08 M by adding methanol for undoped YBCO solutions. For 5 mol % ZrO_2 nanocrystals doped YBCO solutions, 1 mL YBCO solution with the total metal concentration of 1.20 M is diluted by adding of 33.3 µL ZrO_2 nanocrystals (0.3 M) and further diluted with methanol to 1.08 M. Those solutions were deposited on (001)-oriented $LaAlO_3$ single crystal substrates by spin-coating with a spin rate of 2000 rpm for 1 min. The substrates were cleaned with isopropanol followed by a heat treatment at 400 °C on a hot-plate in the ambient before deposition to remove adsorbed organics prior to deposition. The deposited layers were heated at 65 °C for 3 min in order to evaporate the solvent.

The as-deposited gel films were pyrolyzed in a humidified O_2 atmosphere with heating ramps of 3-5 K min^{-1} from 25 °C to the final temperature of 400 °C. The pyrolyzed thin films were subsequently processed to an intermediate dwell step at 640 °C for 60 min and then to 790 °C for 70 min in a flowing wet nitrogen atmosphere containing 100 ppm oxygen (a dew point of 23 °C), followed by an oxygenation treatment at 450 °C in flowing dry oxygen for 2 h to convert the tetragonal YBCO phase to the superconducting orthorhombic phase.

5.3. Copolymer based nanocomposite, superconducting properties

The excellent structural properties, as mentioned in the previous chapter, are in accordance with high critical temperatures (T_c) of 90.5 K with a transition width ΔT_c of 1.2 K for undoped YBCO and T_c of 91.0 K with ΔT_c of 0.9 K for the nanocomposite. It is clear that the nanocrystal addition does not reduce T_c which is often observed in nanocomposite films probably due to the strain effects at the particles' interface or due to the structural defects in YBCO matrix.[1] The inductive critical current densities J_c in self-field at 77 K (voltage criterion of 50 µV) are 4.8±0.5 MA cm^{-2} for undoped YBCO (average of 6 samples) and 5.1±0.4 MA cm^{-2} for the nanocomposite (9 samples). This enhancement of J_c in self-field for the nanocomposite is probably explained by the contracted Cu-O bonds, resulting in the increase of the pair breaking energy.[2, 3] To determine the extent of vortex pinning, the magnetic field dependences of J_c were measured at 77 K with an electric field criterion of 215 µV cm^{-1} and fitted as $J_c(T,B) = A(T)B^{-\alpha}$ in the appropriate region (Table 5.1). The averaged J_c value in self-field (0 T, 77 K) for undoped YBCO is 3.3±0.3 MA cm^{-2} and decreases to 16.8±5.1 kA cm^{-2} at 1 T. The incorporation of ZrO_2 nanocrystals resulted in an increase of J_c to about 4.0±0.4 MA cm^{-2} in self-field which is a 1.2 times improvement. However, the true potential of the nanocomposite is revealed at 1 T, having a critical current of 231.1±15.6 kA cm^{-2} which is a 14 times improvement. The excellent performance of the nanocomposite is underscored by the averaged power-law exponent α at 77 K, which is about 0.74±0.03 for undoped YBCO and about 0.44±0.06 for YBCO-5 mol-% ZrO_2 nanocrystals. The smaller power law exponent for the nanocomposite indicates a less steep decay of the critical current with an increasing magnetic field and thus a better performance at high fields. From the obtained results and their low standard deviations, we conclude our approach to be highly reproducible. Often in the literature, a single champion value is reported without information on the reproducibility and we would like to present our averaging of samples as a best practice.

Transport current measurements of undoped YBCO and YBCO-5 mol-% ZrO_2 show a similar trend as the magnetic measurements (Table 5.1 and Figure 5.1a). The $J_c(B||c)$ curves for three different temperatures show clearly a higher performance (higher current) for the nanocomposite compared to undoped YBCO for all temperatures and all magnetic field values (Figure 5.1a).

Table 5.1. *The averaged critical current density in self-field and 1 T as determined from magnetic measurements, the power-law exponent α at 77 K, the critical current density (self-field) as determined from transport measurements at 77 K and maximum pinning force for undoped YBCO and YBCO-5 mol-% ZrO_2 nanocrystals.*

ZrO_2	$J_{c,mag}$ (0 T), MA cm^{-2}	$J_{c,mag}$ (1 T), kA cm^{-2}	α	$J_{c,trans}$ (0 T), MA cm^{-2}	F_P^{max}, GN m^{-3}
0 mol-%	3.3±0.3	16.8±5.1	0.74±0.03	4.65	1.6
5 mol-%	4.0±0.4	231.1±15.6	0.44±0.06	5.20	5.5

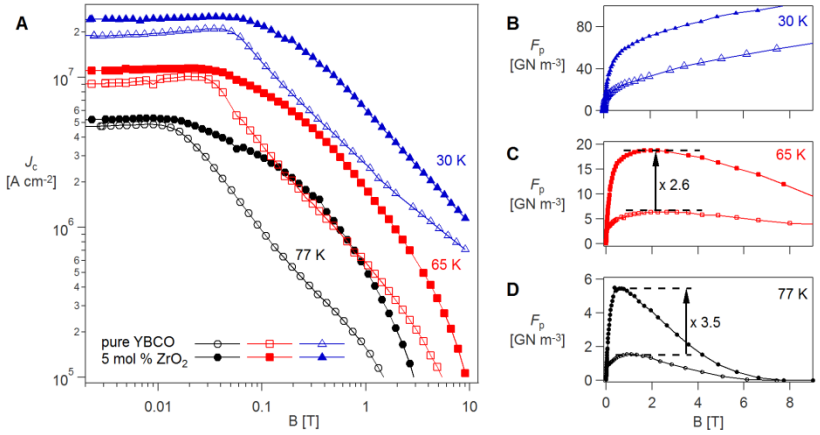

Figure 5.1. *J_c(B) for undoped and 5 mol-% ZrO_2 nanocrystals doped YBCO films at 77, 65 and 30 K (A) and according pinning force curves at 30 (B), 65 (C) and 77 K (D). [Measured at IFW Dresden, E_c = 1 μV cm^{-1}]*

Values of the irreversibility field H_{irr} are extracted from Dew-Hughes-Fits[4] to the pinning force curves $F_P(B)$ with $F_p = j_c \times B$. H_{irr} at 77 K is increased from 7.5 T to 8.4 T, whereas the maximum pinning force density $F_{P,max}$ is more than tripled from 1.6 to 5.5 GN m^{-3} at 77 K (Table 5.1 and Figure 5.1d) by the introduction of 5 mol-% nanocrystal. This is a record pinning force value for LF-YBCO films.[5] At lower temperatures, the increase of F_P is similar but somewhat lower (Figure 5.1b and c). These values are slightly lower than the champion value (10-22 GN m^{-3}, 77 K) reported from the spontaneous segregation of $BaZrO_3$ particles in CSD-YBCO films[6] but improved compared to earlier reports on $BaZrO_3$ particles in LF-YBCO (3.8 GN m^{-3})[5], and our results have the additional advantage of being highly reproducible. The self-field J_c is still high for doped YBCO, so we believe that the $F_{P,max}$ can be increased by the addition of more ZrO_2 nanocrystals in the YBCO matrix provided they remain small in the order of superconducting coherence length (2-4 nm for YBCO structure at 77 K) and

agglomeration-free (to reach a higher number density of defects in YBCO matrix) without affecting the YBCO microstructure.[7]

The anisotropy of the critical current density $J_c(B,\Theta)$ was measured for a similar batch of samples at 77 K / 1 T and 30 K / 3 T (Figure 5.2), two typical regimes for HTS applications, e.g. superconducting transmission cables (high temperature/ low field) or motors/generators (medium temperature/medium field).[8] In both regimes, the maximum J_c at magnetic field parallel to the YBCO *ab*-plane ($\Theta = 90°$) is approximately the same (2.1 MA cm^{-2} at 77 K / 1 T, 17 MA cm^{-2} at 30 K / 3 T, Table 5.2), but the overall performance is increased by nanocrystal addition in a wide angular range aside $B||ab$, and the anisotropy, i.e. the ratio of highest J_c to lowest J_c in the full $J_c(B,\Theta)$, is lowered by the nanocrystal addition.

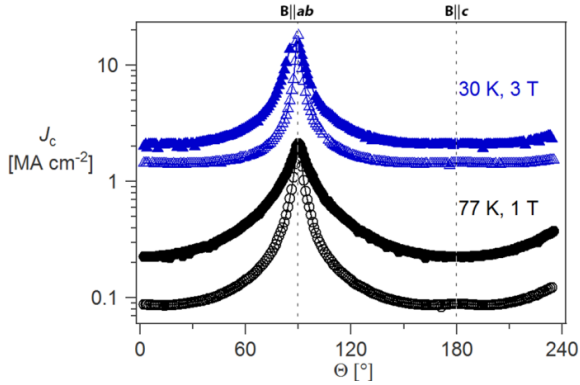

Figure 5.2. *Anisotropy $J_c(\Theta)$ for undoped (open symbols) and 5 mol-% nanocrystal doped (closed symbols) YBCO films at 77 K / 1 T (black) and 30 K / 3 T (blue). [Measured at IFW Dresden, E_c = 1 µV cm^{-1}]*

Table 5.2. *J_c^{max}, J_c^{min} and Anisotropy $A = J_c^{max} / J_c^{min}$ of undoped and 5 mol-% nanocrystal doped YBCO at different temperatures and fields.*

	undoped YBCO			**5 mol-% nanocrystal**		
	J_c^{max}	J_c^{min}	***A***	J_c^{max}	J_c^{min}	***A***
	MA cm^{-2}		**-**	**MA cm^{-2}**		**-**
77 K / 1T	2.1	0.1	25.6	2.1	0.2	10.1
30 K / 3 T	18.0	1.4	13.4	17.1	1.9	9.0

Measurements of $J_c(B,\Theta)$ at 65 K for different magnetic fields (1 to 9 T) are given in Figure 5.3. The ZrO_2-doped YBCO film shows an improved J_c -behavior in the full angular range at low and intermediate fields ($B \leq 7$ T). The J_c values for $B||ab_{YBCO}$ (J_c^{ab}, which is also J_c^{max}) and $B||c_{YBCO}$ (J_c^{c}, which is not necessarily J_c^{min})

are given in Table 5.3 for several fields. Whereas the maximum J_c values for $B||ab_{YBCO}$ are similar for undoped and ZrO_2-doped YBCO, a peak for $B||c$ becomes more pronounced for high magnetic fields due to the twin boundaries (*vide infra*). A peak near Θ = 90° (B||*ab*) is most likely related to stacking faults (extra CuO layer) in YBCO matrix.[9] Up to 5 T the ZrO_2-doped YBCO films' J_c values are higher in the full range of Θ, at 7 T the maximum and minimum J_c are equal, i.e. the anisotropy is unchanged, still J_c is increased for Θ = 90° ± (5…55)°. At 9 T a crossover occurs and the undoped YBCO film shows better performance around $B||c$ (Θ = 140…220°). This is mainly due to correlated pinning at twin boundaries (and to some degree to extended particles). So, the decrease of the relative height of this peak by nanocrystal addition is probably due to the (small) decrease in *c*-axis correlation of the twin boundaries.[10] At this peak, the twin boundaries are active, counterbalancing the higher twin boundary density in ZrO_2-doped YBCO film (Figure 5.4). Undoped YBCO film show a better pinning performance at $B||c$ and 9 T due to the smaller twin boundary density (see Figure A5.1 in Appendix A). However, it is remarkable because the addition of nanocrystals, the presence of secondary phases as well as by intergrowths, often result in a loss of twin boundary coherence along c-axis as reported in Refs.[10, 11] For ZrO_2-doped YBCO film at 1 T, 3 T, 5 T, 7 T and 9 T, it is clear that the *ab* peak broadens in the entire field and this demonstrates the effective stacking fault pinning.[12] However, no (large) stacking faults are observed around $BaZrO_3$ particles in HRTEM image (Figure 4.7e), thus this can be related to the modified microstrain distribution due to the strained interface between particles and the YBCO matrix.[11]

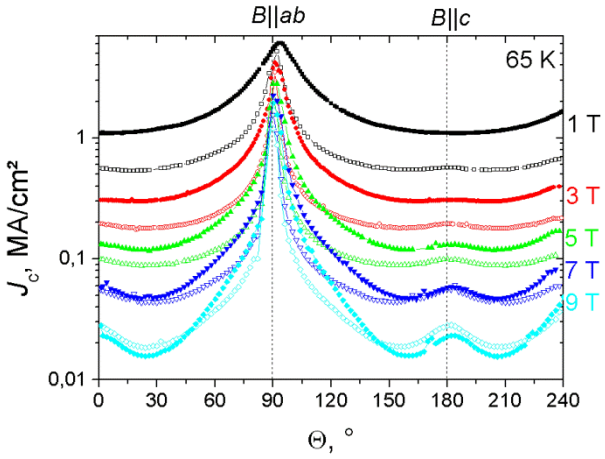

Figure 5.3. *Anisotropy $J_c(Θ)$ for undoped (open symbols) and ZrO_2-doped (closed symbols) YBCO films at 65 K for several magnetic fields. (The shifted peak at 1 T is*

due to the uncorrected rotator of PPMS device.) [Measured at IFW Dresden, E_c = 1 μV cm^{-1}]

Table 5.3. *J_c^{ab}, J_c^{c} and Anisotropy A (A = J_c^{max} / J_c^{min}) of undoped and ZrO_2-doped YBCO at different temperatures and fields (cf. Figure 5.3)*

	undoped YBCO			ZrO_2-doped		
	J_c^{ab}	J_c^{c}	A	J_c^{ab}	J_c^{c}	A
	MA cm^{-2}			MA cm^{-2}		
65 K / 1 T	5.21	0.57	9.1	6.11	1.10	5.6
65 K / 3 T	3.49	0.20	17.5	4.18	0.31	13.5
65 K / 5 T	2.17	0.10	21.7	2.80	0.13	21.5
65 K / 7 T	1.55	0.06	25.8	2.25	0.09	25.1
65 K / 9 T	1.20	0.04	40.0	1.90	0.03	63.3

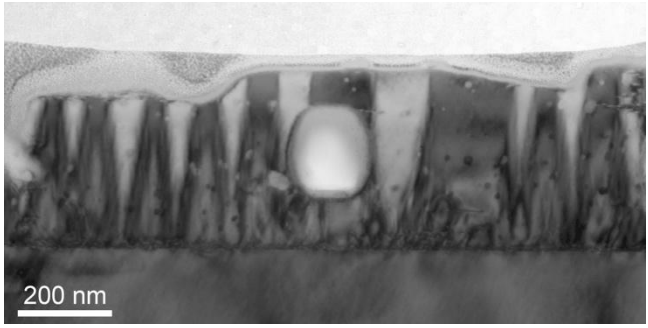

Figure 5.4. *(h00) bright-field TEM showing the (small) decrease in c-axis correlation twin boundaries of ZrO_2-doped YBCO layer.*

5.4. Influence of the reactivity of single metal oxide nanocrystals with Ba^{2+}

As mentioned in section 4.6 of chapter 2, the off-stoichiometric of Y:Ba:Cu in YBCO precursor solution can lead to a higher self-field critical current density. Since the single metal oxide (e.g. ZrO_2) nanocrystals can react with Ba^{2+} during the YBCO growth into $BaZrO_3$ particles, there is also an off-stoichiometric during the YBCO formation due to the Ba^{2+} consumption. This deficiency has one advantage during the YBCO formation as Ba^{2+} deficiency results into less formation of undesired secondary phases like as $Ba_xCu_xO_y$ in combination with more formation of *in-situ* Y_2O_3 which can act as additional pinning centers if they remain small in the size of superconducting coherence length. To confirm that Ba^{2+} deficiency in YBCO growth would lead to higher self-field J_c, the undoped YBCO precursor solution with stoichiometric Y:Ba:Cu ratio of 1:1.8:3 (5 mol-%

Ba^{2+} deficiency) was deposited on $LaAlO_3$ substrate and underwent a complete thermal process without an intermediate dwelling step. The superconducting properties and their magnetic dependency of this YBCO layer with Ba^{2+} deficiency were measured via MPMS system. It is clear that the self-field J_c at 77 K is in the same order of undoped and 5 mol-% copolymer stabilized ZrO_2-doped YBCO films. However, the behavior on increased magnetic field shows worse J_c decay compared to undoped YBCO film, which means that YBCO structure of Ba^{2+} deficiency is not improved.

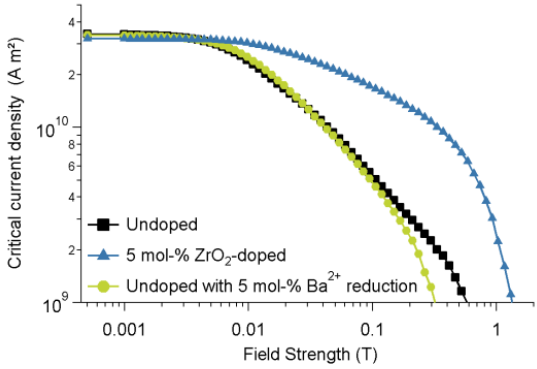

Figure 5.5. *Magnetic dependency of Y:Ba:Cu stoichiometric ratio of 1:2:3 based film without (black) or with (blue) 5 mol-% ZrO_2 nanocrystals and Y:Ba:Cu off-stoichiometric ratio of 1:1.8:3 based film without ZrO_2 nanocrystals. [Magnetically measured at University of Turku]*

5.5. Influence of higher loading of ZrO_2 nanocrystals in YBCO matrix

As more nanocrystals can be added in the YBCO matrix, they can act as pinning centers. However, this seems not straightforward, because of their reactivity with Ba^{2+}. Several mol-% - 0, 5, 7.5, 10, 12.5 and 15 - were investigated to analyze the effect of copolymer stabilized ZrO_2 nanocrystals on the YBCO formation. Figure 5.6 shows more accurate XRD θ-2θ scans of different mol-% copolymer stabilized ZrO_2-doped YBCO layers. It is clear that more secondary phases are formed such as $Y_2Cu_2O_5$ and Y_2O_3, probably due to the higher Ba^{2+} deficiency. A higher Ba^{2+} deficiency can lead to worse epitaxial YBCO texture by means of the formation of the polycrystalline (103) (2θ = 32.6°) and *a*-oriented (200) YBCO (2θ = 47°, not shown on XRD pattern) structures in the YBCO matrix, resulting in a decrease of the superconducting properties (Table 5.4) in function of higher loading of nanocrystals. When 15 mol-% ZrO_2 nanocrystals are added in YBCO matrix, no superconductivity is observed at 77 K via inductive

measurement. However, 7.5, 10 and 12.5 mol-% ZrO_2-doped YBCO films show a trend where the superconducting properties are decreased by the addition of a larger quantity of ZrO_2 nanocrystals. As shown in XRD pattern of 12.5 mol-% ZrO_2-doped YBCO layer, there are some BaF_2 phases present into the layer which means that the YBCO formation is incompletely during the thermal process. This behavior is already described in section 4.3 of chapter 4, whereas the addition of ZrO_2 nanocrystals induces a delay in the YBCO growth mechanism due to the reactivity of BaF_2 with ZrO_2 nanocrystals before it reacts with $Y_2Cu_2O_5$ to the $YBCO_6$ structure and is symptomatic for poor epitaxial growth. This is observed in HAADF-STEM image (Figure 5.7a) where a barium-rich zone is indicated on the top of the YBCO matrix. When 5 mol-% ZrO_2 nanocrystals are added into the YBCO matrix, the $BaZrO_3$ particle size is 13.0±5.5 nm. In the case of 12.5 mol-% ZrO_2-doped YBCO layer, the size distribution shows a mean diameter of 16.7±4.3 nm (Figure 5.7b), which indicates that the nanocrystals are more coarsened during the thermal process. However, based on the statistical relevance, there are no major difference between the particle size of 5 mol-% and 12.5 mol-% ZrO_2-doped as the fact that the relative standard deviation of 5 mol-% (42.3%) is larger than 12 mol-% (25.7%). The addition of more nanocrystals in YBCO precursor solution would lead to more opportunity to form more agglomerations of nanocrystals, e.g. bigger particle size, during the thermal process, which is often observed in CSD-based nanocomposite with higher nanoparticle concentration.[13] This should be avoided by introduction of preformed nanocrystals with low polydispersity index and with thermally stable ligand. More agglomerations and more secondary phases in YBCO matrix result in poor epitaxial YBCO structure and also poor superconducting properties of 0.92 MA cm^{-2}.

Table 5.4. *Self-field critical current densities of different mol-% ZrO_2-doped YBCO films, inductively measured at 77 K.*

ZrO_2 nanocrystals	**J_c (77 K, *sf*) MA cm^{-2}**
0 mol-%	4.65
5 mol-%	5.20
7.5 mol-%	2.18
10 mol-%	2.03
12.5 mol-%	0.92
15 mol-%	-

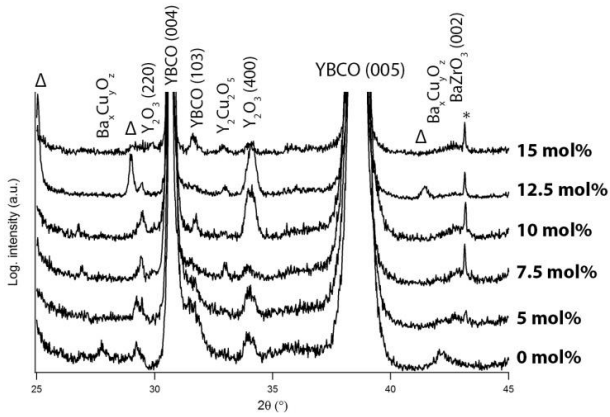

Figure 5.6. *XRD θ-2θ scans of YBCO with different mol-% ZrO_2 nanocrystals. BaF_2 phases are marked with delta (Δ) symbol. ($LaAlO_3$ and YBCO reflections by the secondary radiation of x-ray tube are marked with an asterisk.)*

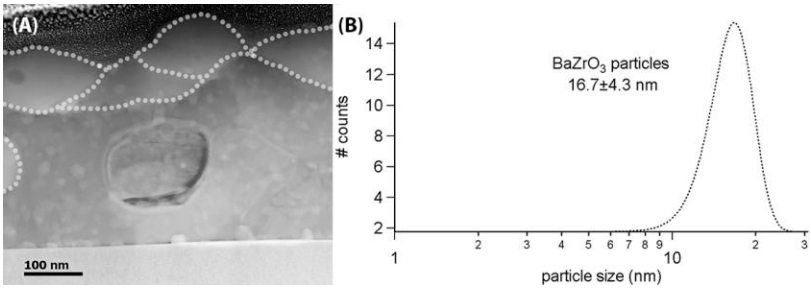

Figure 5.7. *(A) HAADF-STEM image of 12.5 mol-% ZrO_2-doped YBCO layer, indicating lots of secondary phases into YBCO matrix. (B) Fitted curve of histogram of $BaZrO_3$ particles in an YBCO matrix after thermal process. The values of $BaZrO_3$ particles are estimated from cross-sectional image (cf. Figure 5.8a).*

The addition of nanocrystals does not decrease the critical temperature T_c (Table 5.5 and Figure 5.8), although the transition width shows a footnote for 7.5 mol-% and 10 mol-% ZrO_2-doped YBCO film, implying that the higher loading of nanocrystals leads to a degradation of the superconducting properties. However, the power-law exponent α at 77 K of undoped shows a value of around 0.93 while ZrO_2-doped YBCO films show better power-law behavior as shown in Table 5.5. It is remarkable that the 7.5 and 10 mol-% ZrO_2-doped YBCO films shows better α values of around 0.32-0.34 compared to the α value of around 0.46 for 5 mol-% ZrO_2-doped, indicating that more addition of nanocrystals lead to large pinning centers (because of the agglomerations) which turn out to be very effective at higher magnetic fields.[14] Based on pinning

force densities F_p (Figure 5.9b and Table 5.5) as a function of magnetic field for 5, 7.5 and 10 mol-% ZrO_2-doped YBCO films compared to undoped YBCO film, the optimum amount of ZrO_2 nanocrystals for this LF-YBCO CSD based method is 5 mol-% as F_p shows a good enhancement (F_p = 5.5 GN m^{-3} at 0.66 T) compared to undoped (F_p = 1.6 GN m^{-3} at 0.96 T) and higher loaded ZrO_2-doped YBCO films (F_p = 3.5-3.8 GN m^{-3} for both). However, the optimal pinning behavior is obtained for the 7.5 mol-% ZrO_2-doped film due to the less decay of F_p in function of magnetic field and because of the maximum F_p of 7.5 mol-% is situated at higher magnetic field (0.83 T) compared to 5 mol-% ZrO_2-doped film. For this reason, a TEM follow-up should be recommended to analysis and optimize the microstructure of 7.5 mol-% ZrO_2-doped YBCO nanocomposite film. It should be conceivable via adjusting stoichiometric ratio of Y:Ba:Cu in YBCO precursor solution (e.g. addition of more Ba^{2+}) or via modifying the thermal process in function of the higher loading of nanocrystals. It is remarkable that the pinning performance of the 10 mol-% ZrO_2-doped YBCO film is significantly worse at higher magnetic field at B||*c* which indicating that higher loading of nanocrystals can disrupt the formation of twin boundaries. The angular dependency of various mol-% ZrO_2-doped YBCO films is described in section A4.2 in Appendix A where the peak at B||*ab* (Θ = 90°) is broaden because of the addition of nanocrystals and is typical attributed to the effective pinning of stacking faults in YBCO matrix. Nevertheless, the stacking faults around the $BaZrO_3$ particles is not observed on TEM images.

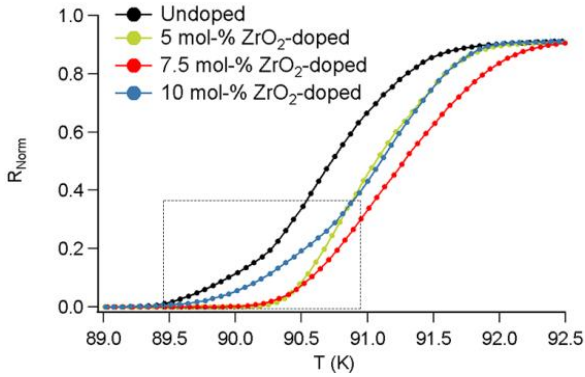

Figure 5.8. *Critical temperature T_c measurements of different mol-% ZrO_2-doped films. Rectangle marked zone shows a footnote of T_c, indicating two different slopes in the transition.*

Table 5.5. *The critical temperature T_c, accommodation field B* and the pinning force densities F_p^{max} at 77 K of various mol-% ZrO_2-doped YBCO film.*

ZrO_2 nanocrystals	T_c K	α	F_P^{max} (77 K) GN m^{-3}
0 mol-%	90.7±1.2	0.93	1.6 at 0.96 T
5 mol-%	91.0±1.0	0.46	5.5 at 0.66 T
7.5 mol-%	91.0±1.3	0.32	3.8 at 0.81 T
10 mol-%	91.0±1.1	0.35	3.5 at 0.63 T

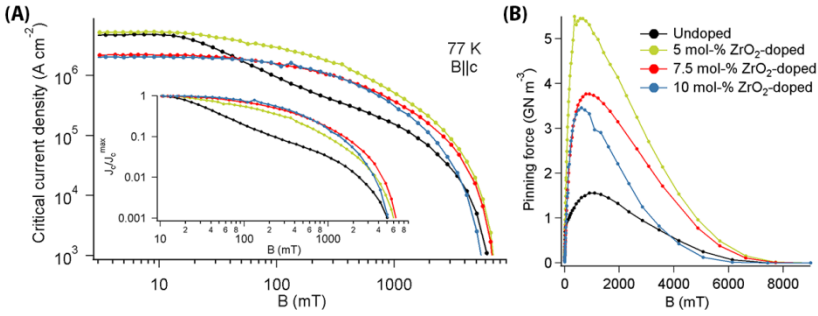

Figure 5.9 *Undoped and different mol-% ZrO_2-doped YBCO layers: (A) J_c in the function of magnetic field at 77 K, determined via transport measurements. The inset shows the J_c curves normalized to self-field J_c. (B) Pinning force densities in the function of magnetic field at 77 K. [Measured at IFW Dresden, E_c = 1 µV cm^{-1}]*

5.6. Transfer to industrial metallic Ni-W substrates

This LF-YBCO CSD based method with 5 mol-% ZrO_2 nanocrystals would be a success if these results could be transferred from $LaAlO_3$ substrates to industrial metallic Ni-W substrates. Despite poor superconducting properties of undoped YBCO film on Ni5W tape, the CSD procedure (described in section 2.4.6 chapter 2) is repeated with the addition of 5 mol-% ZrO_2 nanocrystals. As expected, the addition of ZrO_2 nanocrystals will delay the YBCO growth due to the Ba^{2+}-consumption but nevertheless, as shown in XRD patterns (Figure 5.10), the YBCO layer shows a poor epitaxial texture. It is probably due to the combination of Ba^{2+} deficiency in the YBCO precursor solution, Ba^{2+} reactivity of the CeO_2 buffer layer leading to the formation of a $BaCeO_3$ phase and Ba^{2+} reactivity of ZrO_2 nanocrystals during YBCO growth (*vide supra*). To confirm this effect, the stoichiometric ratio of Y:Ba:Cu is changed from 1.3:1.8:3 to 1.3:1.9:3 where extra 5 mol-% Ba^{2+} was added into YBCO precursor solution which would react with ZrO_2 nanocrystals during the YBCO growth. This extra amount of Ba^{2+}

results in good epitaxial texture but also in more formation of *a/b*-oriented YBCO as confirmed in XRD patterns (Figure 5.10). These results are promising and will be studied in a follow-up project as YBCO film needs a perfect texture like single crystal for the high current density, which is a challenge for metallic substrates. It is due to another YBCO growth kinetic and the presence of grain boundaries. These both can be affected by the incorporation of nanocrystals. So, an in-depth analysis is needed to understand the effect of nanocrystals on the YBCO texture by means of grain boundaries on metallic substrates to bring us a step closer to a commercial breakthrough.

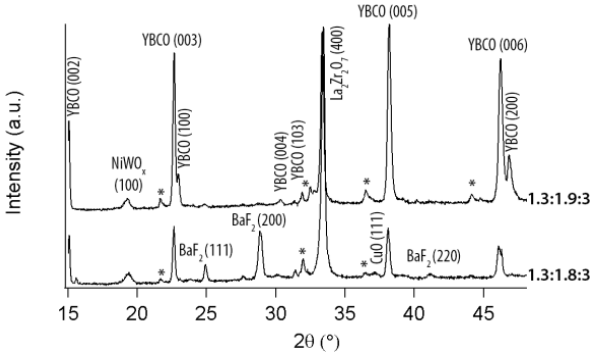

Figure 5.10. *XRD patterns of 5 mol-% ZrO_2-doped YBCO film starting from YBCO precursor solution with Y:Ba:Cu ratio of 1.3:1.8:3 and 1.3:1.9:3. (Reflections by the secondary radiation of x-ray tube are marked with an asterisk.)*

5.7. Conclusion

In this chapter, it is clear that the critical current densities are increased by the 5 mol-% nanocrystal addition. This approach results in a high maximum pinning force density of 5.5 GN m^{-3}, which more than tripled compared to undoped YBCO thin films. The J_c in a moderate-to-high magnetic field is increased, and its anisotropy is lowered by the addition of nanocrystals. A peak near Θ = 90° (B||*ab*) is broaden because of the addition of nanocrystals and is most likely related to the stacking faults. Besides the *ab*-peak, there is a small *c*-axis peak visible, especially at 77 K. This is mainly due to correlated pinning at twin boundaries (and to some degree to extended particles). The decrease of the relative height of this peak by nanocrystal addition is probably explained due to the (small) decrease in *c*-axis correlation of the twin boundaries and due to the higher twin boundaries density compared to the smaller twin boundaries density of undoped YBCO film.

However, by higher loading of the nanocrystals in the YBCO matrix, more nanocrystals result in poorer superconducting properties, probably due to the more Ba^{2+} consumption of single metal oxide nanocrystals. This should cause a slow YBCO growth and Ba^{2+} deficiency in the YBCO matrix, which can result in a worse epitaxial YBCO. Nevertheless, it is remarkable that the more addition of nanocrystals (with a limited amount) can lead to better pinning properties.

So, the preformed nanocrystal approach can be successfully applied to the CSD based LF-YBCO method, yet additional research is required to fully understand the influence of the higher loading of nanocrystals into the YBCO matrix. This should lead to an optimization of the final YBCO nanocomposite films onto industrial metallic substrates. This should bring us one step closer to the effective and economically efficient application of HTS in high and alternating magnetic field applications, relevant in alternative energy generation.

5.8. References

1. H. Huhtinen, K. Schlesier, and P. Paturi, "Growth and c-axis flux pinning of nanostructured YBCO/BZO multilayers," *Supercond. Sci. Technol.,* **22** [7] 075019 (2009).
2. G. Deutscher, "The role of Cu-O bond length fluctuations in the high temperature superconductivity mechanism," *J. Appl. Phys.,* **111** [11] 112603 (2012).
3. L. Lei*, et al.*, "Strongly improved current-carrying capacity induced by nanoscale lattice strains in $YBa_2Cu_3O_{7-\delta}$–$Ba_{0.7}Sr_{0.3}TiO_3$ composite films derived from chemical solution deposition," *J. Mater. Chem. C,* **4** [7] 1392-97 (2016).
4. D. Dew-Hughes, "Flux pinning mechanisms in type II superconductors," *Philos. Mag.,* **30** [2] 293-305 (1974).
5. T. Petrisor Jr*, et al.*, "The Vortex Path Model Analysis of the Field Angle Dependence of the Critical Current Density in Nanocomposite $YBa_2Cu_3O_{7-x}$–$BaZrO_3$ Films Obtained by Low Fluorine Chemical Solution Deposition," *J Supercond Novel Magn,* **27** [11] 2493-500 (2014).
6. J. Gutierrez*, et al.*, "Strong isotropic flux pinning in solution-derived $YBa_2Cu_3O_{7-x}$ nanocomposite superconductor films," *Nat. Mater.,* **6** [5] 367-73 (2007).
7. T. Haugan*, et al.*, "Addition of nanoparticle dispersions to enhance flux pinning of the $YBa_2Cu_3O_{7-x}$ superconductor," *Nature,* **430** [7002] 867-70 (2004).
8. X. Obradors and T. Puig, "Coated conductors for power applications: materials challenges," *Supercond. Sci. Technol.,* **27** [4] 044003 (2014).
9. E. Talantsev*, et al.*, "Hole doping dependence of critical current density in $YBa_2Cu_3O_{7-\delta}$ conductors," *Appl. Phys. Lett.,* **104** [24] 242601 (2014).
10. R. Guzman*, et al.*, "Strain-driven broken twin boundary coherence in $YBa_2Cu_3O_{7-\delta}$ nanocomposite thin films," *Appl. Phys. Lett.,* **102** [8] 081906 (2013).
11. K. De Keukeleere*, et al.*, "Superconducting $YBa_2Cu_3O_{7-\delta}$ Nanocomposites Using Preformed ZrO_2 Nanocrystals: Growth Mechanisms and Vortex Pinning Properties," *Adv. Electr. Mater.,* **2** [10] 1600161 (2016).
12. A. Llordés*, et al.*, "Nanoscale strain-induced pair suppression as a vortex-pinning mechanism in high-temperature superconductors," *Nat. Mater.,* **11** [4] 329-36 (2012).
13. M. Coll*, et al.*, "Size-controlled spontaneously segregated Ba_2YTaO_6 nanoparticles in $YBa_2Cu_3O_7$ nanocomposites obtained by chemical solution deposition," *Supercond. Sci. Technol.,* **27** [4] 044008 (2014).
14. A. Gurevich, "Pinning size effects in critical currents of superconducting films," *Supercond. Sci. Technol.,* **20** [9] S128 (2007).

Chapter six

$YBa_2Cu_3O_{7-\delta}$-$BaHfO_3$ nanocomposite films: nanocrystal synthesis matters

In this chapter, the incorporation of single metal oxide HfO_2 nanocrystals is discussed. As it is still unclear what the influence of nanocrystal morphology and its size on the YBCO matrix is, the influence of two different types of HfO_2 nanocrystals was explored.

Adapted from:

H. Rijckaert, J. Pelemans, J. Hänisch, R. Nast, J. Bennewitz, G. Pollefeyt, J. De Roo, M. Bäcker, M. Hemgesberg, K. De Keukeleere and I. Van Driessche, Ink-jet Printing of Nanocomposite film: From Low-Fluorine $YBa_2Cu_3O_7$ inks with Preformed Nanocrystals to Superconducting Films. In preparation.

J. De Roo, S. Coucke, H. Rijckaert, K. De Keukeleere, D. Sinnaeve, Z. Hens, J. C. Martin and I. Van Driessche, Amino Acid-Based Stabilization of Oxide Nanocrystals in Polar Media: From Insight in Ligand Exchange to Solution ^{1}H NMR Probing of Short-Chained Adsorbates. Langmuir, 2016. 32(8). 1962-1970.

6.1. Introduction

The pathway to fabricate YBCO nanocomposite films with relevant pinning properties does not seem to be easy because of the necessity to solve several critical issues related to YBCO growth. There are many papers in literature concerning the control of the size and the distribution of self-assembled nanoparticles in the YBCO matrix.[1, 2] It has been shown that the nucleation and growth mechanisms of the two different crystalline phases can be controlled by the introduction of an intermediate dwelling step during the thermal process.[1, 3] However, this method did not ensure a high reproducibility of self-assembled nanocomposite film formation. To increase the reproducibility, an alternative pathway was introduced with the incorporation of preformed nanocrystals in the YBCO matrix.[4, 5] A key advantage of this novel approach is a possibility to improved control over the composition, the particle size and the concentration of the nanoparticles.

In this work, the size of 3.5 nm of ZrO_2 nanocrystals was discussed, whereas it has been proven in the chapter three that the nanocrystal surface chemistry is very crucial for the final properties of nanocomposite film. In this chapter, two different methods (solvent- and surfactant-controlled) to synthesize HfO_2 nanocrystals were introduced to reveal the influence of nanocrystal morphology and size on the defect state of YBCO matrix. The solvothermal heating-up (surfactant-controlled) synthesis closely following that of ZrO_2 nanocrystals yielded highly crystalline nanorod-like HfO_2 nanocrystals with a size of 2.6 nm in diameter and 8.0 nm in length. This surfactant-controlled approach can offer a better control over the crystal size control and shape with a low agglomeration tendency compared to solvent-controlled approach.[6]

The microwave-assisted (solvent-controlled) synthesis also delivered highly crystalline HfO_2 nanocrystals but now are spherical with a size of 6-8 nm in diameter. With these two types of monoclinic HfO_2 nanocrystals, the effect of the nanocrystal morphology on the YBCO matrix can be studied. It is presented in this chapter that the nanorod-like HfO_2 nanocrystals led to short intergrowths surrounding the particles while spherical HfO_2 nanocrystals led to more formation of line defects in the YBCO matrix. Thus, these differences in nanocrystal size have an influence on the formation of the intergrowths and the line defects around the particles in the YBCO matrix, leading to different pinning properties.

6.2. HfO_2 nanocrystals

6.2.1. Microwave-assisted synthesis

HfO_2 nanocrystals were synthesized from metal chlorides and benzyl alcohol via a microwave-assisted hydrothermal treatment as described by De Roo *et al.*[7] 0.5 mL dibenzyl ether is added to 0.4 mmol hafnium chloride and 4 mL of benzyl alcohol is rapidly added. This mixture is subjected to microwave heating for 3 hours at 210 °C. After the synthesis, the reaction mixture is rinsed with 4 mL diethyl ether. After mild centrifugation, two phases are obtained. The top phase is an organic phase (diethyl ether, benzylalcohol and dibenzyl ether), while the bottom phase is a stable dispersion of HfO_2 nanocrystals in only 400 µL water. The top phase is removed while 2 mL ethanol is added to the bottom phase, resulting in a stable, clear suspension. The nanocrystals are precipitated and washed once with diethyl ether. Finally, the nanocrystals are redispersed in 4 mL chloroform after the addition of 0.2 mmol dodecanoic acid and 0.15 mmol oleylamine under vigorous stirring to break up agglomerates. This suspension becomes colorless and transparent.

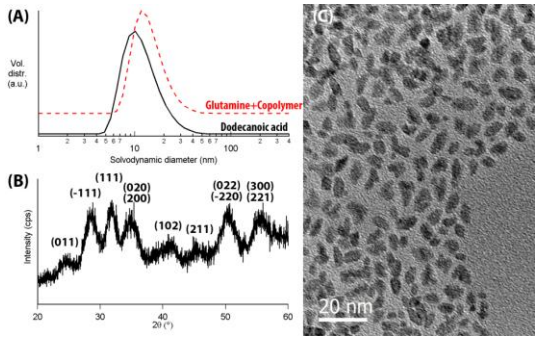

Figure 6.1 *HfO_2 nanocrystals after microwave synthesis: (A) DLS analysis before and after ligand exchange, (B) XRD powders patterns showing only reflections of the monoclinic phase and (C) TEM image.*

The XRD patterns of HfO_2 nanocrystals after microwave-assisted synthesis (Figure 6.1b) affirmed the monoclinic crystal structure. The solvodynamic size distribution of the HfO_2 nanocrystals capped with dodecanoic acid and dispersed in chloroform is focused around 10 nm (Figure 6.1a) while the nanocrystal core size according to TEM is approximately 6-8 nm and is slightly elongated (Figure 6.1c).

6.2.2. Ligand exchange after microwave-assisted synthesis

After the microwave-assisted synthesis, the nanocrystal surface is functionalized with dodecanoic acid, yielding a stable colloidal nanosuspension in a nonpolar solvent, while the YBCO precursor solution mainly contains a polar solvent (e.g. methanol). So, a ligand exchange/phase transfer is essential to transfer these as-synthesized nanocrystals to the desired solvent. Therefore, acetonitrile (1:1 by volume) is added to the chloroform dispersion to precipitate the nanocrystals. The precipitate is mixed with 0.06 mmol of a suitable polar amino acid - glutamine or lysine - and 0.5 mmol TFA in methanol. The mixture is ultrasonically treated for 30-60 minutes until a transparent suspension is obtained. After this treatment, toluene (1:3 by volume) is added to purify the amino acid capped HfO_2 nanocrystals through precipitation. Redispersion in different polar solvents is realized by the addition of 0.25 mmol TFA (Figure A6.1 in Appendix A). When the mixture does not become transparent, an excess of TFA should be added.

The amino acid capped HfO_2 nanocrystals can be introduced in TFA-based YBCO precursor solutions without further precipitation, but do not lead to stable suspensions in LF-YBCO precursor solution. However, it is possible to further stabilize amino acid capped HfO_2 nanocrystals in LF-YBCO precursor solutions when a droplet (35 mg) of copolymer is added after the redispersion of the precipitated amino acid capped HfO_2 nanocrystals in methanol with a final concentration of 0.06 M. After ligand exchange/phase transfer to methanol, a solvodynamic diameter of approximately 11 nm is retrieved in DLS (Figure 6.1a). This phase transfer procedure was introduced because dodecanoic acid stabilized HfO_2 nanocrystals cannot be stabilized with solely copolymer without a ligand exchange with amino acid. Thoroughly NMR studies of amino acid stabilized HfO_2 nanocrystals can be found in the work of De Roo *et al.*[8]

6.2.3. Heating-up solvothermal synthesis

As the microwave-assisted synthesis is a solvent-controlled approach, a heating-up synthesis was introduced because surfactant-controlled approach as it can offer a better control over the nanocrystal size and shape with a narrow size distribution. A heating-up solvothermal synthesis closely following that of Joo *et al.*[9] and in this work (section 3.2 of chapter 3) for the synthesis of ZrO_2 nanocrystals was used to synthesize high crystalline HfO_2 nanocrystals. Here, monodisperse HfO_2 nanocrystals are synthesized by adding 4 mmol $HfCl_4$ and 4 mmol $Hf(OiPr)_4$ to 20 g tri-*n*-octylphosphine oxide at 360 °C for 2 hours under argon atmosphere, according to the work of Tang *et al.*[10] After the heating-up

synthesis, the reaction mixture is cooled to 80 °C and acetone (1:5 by volume) is added to precipitate the nanocrystals. The as-synthesized nanocrystals are redispersed in an apolar solvent, e.g., toluene, yielding a clear suspension with agglomerate-free HfO_2 nanocrystals capped with hydrophobic ligands with a solvodynamic diameter of 10.2 nm as determined via DLS (Figure 6.2a). The nanocrystal core diameter is 2.3 nm in diameter and 8.0 nm in length according to TEM image, (Figure 6.2c) and the monoclinic phase is recognized via XRD (Figure 6.2b).

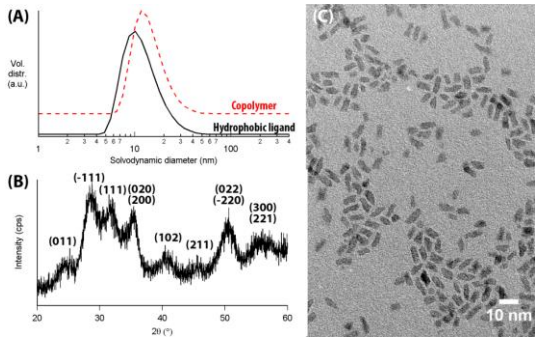

Figure 6.2 *HfO_2 nanocrystals after heating-up synthesis: (A) DLS analysis before and after ligand exchange, (B) XRD powders patterns showing only reflections of the monoclinic phase and (C) TEM image.*

6.2.4. Ligand exchange after heating-up solvothermal synthesis

As known, the YBCO precursor provides a highly ionic and polar environment. Thus, a careful ligand exchange is also needed to transfer and redisperse the as-synthesized nanocrystals into a polar solvent without any precipitation and agglomerations.[8] To achieve a stable YBCO ink nano-suspension, acetone (1:3 by volume) is added to the nanocrystals dispersion to precipitate the HfO_2 nanocrystals. The precipitate is transferred to methanol via the addition of a 35 mg commercially available polar copolymer (see chapter 3), leading to a transparent and stable nano-suspension with a HfO_2 concentration of 0.2 M, as confirmed via TGA analysis, and a solvodynamic diameter of 10.7 nm as confirmed via DLS measurements, Figure 6.2a.

6.2.5. Nanocrystal stabilization

To determine the stabilization method of the copolymer after the ligand exchange for both microwave (MW) and heating-up (HU) based HfO_2 nanocrystals, the nanocrystals' surface was investigated by 1D ^{1}H NMR, 2D

NOESY and DOSY spectra. In the 1D ^{1}H NMR spectra (Figure A6.2 in Appendix A) the copolymer can be recognized (resonances are in the range of 0.5-4.2 ppm) in methanol-d_4, where the ^{1}H NMR spectrum of HU-based HfO_2 nanocrystals is similar to that of the copolymer stabilized ZrO_2 nanocrystals and pure copolymer. However, we note that the ^{1}H NMR spectrum of MW-based HfO_2 nanocrystals shows additional resonances (see resonance around 2 ppm). It is not clear which molecule(s) correspond to those resonances. According to the NOESY spectrum (Figure 6.3a) of HU-based HfO_2 nanocrystals, the copolymer interacts with the nanocrystal surface as evidenced by the negative nOe cross peaks while the NOESY spectrum (Figure 6.3b) of MW-based HfO_2 nanocrystals also shows negative nOe cross peaks, but not for all resonances of the copolymer. This indicates that not the entire copolymer chain interacts with the nanocrystal surface.

In DOSY (Figure 6.4), the copolymer is observed as a free state for both HU- and MW-based HfO_2 nanocrystals. These results together with the results from the NOESY spectrum indicate that the copolymer is interacting with the nanocrystal surface but is not strongly bound, which is different compared to the copolymer stabilized ZrO_2 nanocrystals.

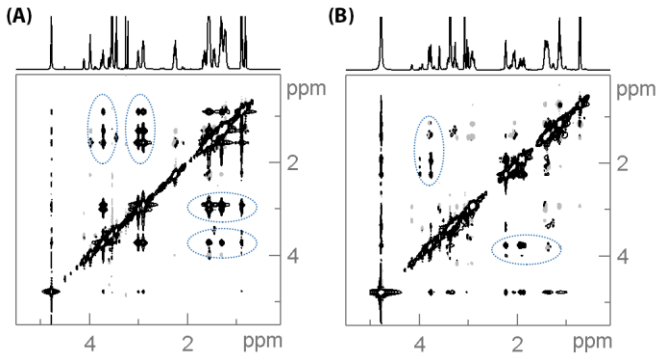

***Figure 6.3**. NOESY spectra of (A) HU-based and (B) MW-based HfO_2 nanocrystals in methanol-d_4. The negative cross peaks indicate interaction of the copolymer with the nanocrystal surface (see dotted circles).*

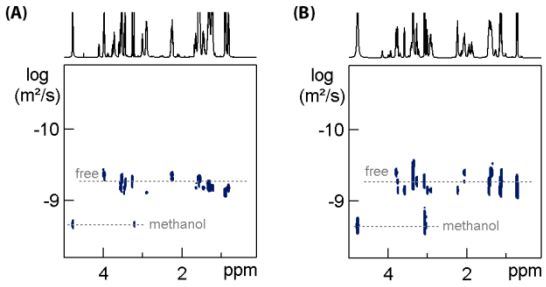

Figure 6.4. *DOSY spectra of (A) HU-based and (B) MW-based HfO_2 nanocrystals in suspension.*

6.3. Does nanocrystal synthesis really matter?

It is interesting that both types of synthesis deliver different nanocrystal surfaces and shapes. As shown in Table 6.1, HU-based synthesis delivers an average nanocrystal size of 2.6 nm in diameter and 8.0 nm in length which looks like a very small nanorod, while MW-based synthesis yields more spherical nanocrystals with an average nanocrystal size diameter of 6-8 nm. These HfO_2 nanocrystals are added with a concentration of 5 mol-% into YBCO precursor solutions prior to unravel their effects in the YBCO matrix.

Table 6.1. *Overview of nanocrystal core and solvodynamic diameter size in methanol of HU-based and MW-based HfO_2 nanocrystals.*

HfO_2 nanocrystals	Nanocrystal core	Solvodynamic diameter
HU-based	2.6 nm in diameter 8.0 nm in length	10.7 nm
MW-based	6-8 nm in diameter	11.0 nm

These undoped, HU-HfO_2 doped and MW-HfO_2 doped YBCO precursor solutions were spin-coated on $LaAlO_3$ substrate. The experimental conditions of the deposition are described in section 2.4.2 of chapter 2. As-deposited YBCO layer on $LaAlO_3$ substrate was heated to 795 °C with an introduction of an intermediate dwelling step at 640 °C to crystallize YBCO under wet 100 ppm O_2 in N_2 atmosphere. After crystallization, the film thicknesses of undoped and HfO_2-doped YBCO films were in the range of 200-230 nm as confirmed via cross-sectional SEM image (not shown).

In the XRD θ-2θ pattern of the undoped and HfO_2-doped YBCO films, Figure 6.5, three strong reflections of YBCO (004), (005) and (006) are exhibited, indicating a good epitaxial texture. However, weak reflections of Y_2O_3 - 2θ = 29.2° (222)

and 2θ = 33.8° (400) are visible for HfO_2-doped YBCO films. This indicates that more Y_2O_3 or $Y_2Cu_2O_5$ is formed during the growth of the YBCO film due to the reactivity of Ba^{2+} with HfO_2 nanocrystals to $BaHfO_3$ particles. The $BaHfO_3$ peak is not visible in the XRD patterns due to the small molar fraction of $BaHfO_3$ (5 mol-%) and the small $BaHfO_3$ particle size (in range of a few nm). The strongest $BaHfO_3$ reflection, (110) at 2θ = 30.3°, is not visible since it overlaps with the dominant YBCO (004) peak at 2θ = 30.6°.

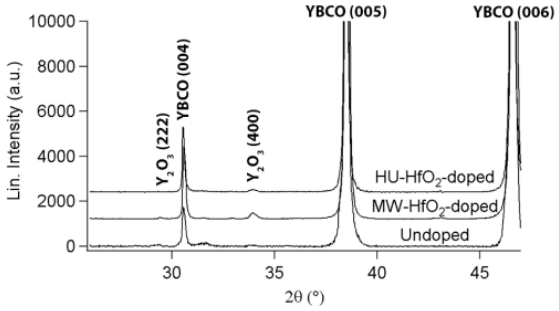

Figure 6.5. *XRD patterns of undoped and HfO_2-doped YBCO films*

To investigate the electrical properties, the films were photolithographically etched to 90±5 µm wide stripes with a solution of 0.15 M phosphoric acid (H_3PO_4) in deionized water. The thicknesses and exact widths of the stripes, needed for the critical current density J_c values, were determined by atomic force microscopy (AFM) after etching. The etched pattern was a standard four-probe measurement circuit where the contacts on these samples were made by tapping with indium. The critical current I_c was measured in a Quantum Design PPMS in the maximum Lorentz force configuration. The values for voltage between the voltage pads as a function of the applied current were recorded with the critical electric field of 215 µV cm^{-1}. The critical temperature was obtained via resistive measurements in function of temperature between 120 and 40 K using a 10 µA current.

Table 6.2. *Critical temperature T_c, self-field critical current densities J_c and pinning force densities F_p^{max} at 77 K of undoped, HU-HfO_2-doped and MW-HfO_2-doped YBCO layers.*

HfO_2 nanocrystals	**T_c K**	**J_c (77 K, *sf*) MA cm^{-2}**	**F_p^{max} (77 K) GN m^{-3}**
Undoped	91.1±0.7	2.92	3.40
HU-based	91.9±1.2	3.04	17.11
MW-based	90.6±1.1	2.88	11.04

The analysis of the superconducting properties of HfO_2-doped YBCO films exhibits a T_c of 91.9±1.2 K for HU-based and 90.6±1.1 K for MW-based. Compared to undoped YBCO film (T_c = 91.1±0.7 K), the addition of HU-based HfO_2 nanocrystals does not reduce T_c and shows similar effects as ZrO_2-doped nanocomposite film. However, the addition of MW-based HfO_2 nanocrystals reduces T_c slightly and may be explained by a greater number of defects in the YBCO matrix. As expected from transport measurements, both HfO_2-doped YBCO films show a better behavior over the magnetic field range compared to undoped YBCO. This indicates that the addition of nanocrystals results in an improvement of the pinning properties. However, it is clear that the HU-HfO_2-doped YBCO film shows a slower decay compared to the MW-HfO_2-doped YBCO film. On the other hand, it also shows an increase of pinning force density F_p^{max} for HU-HfO_2-doped YBCO films with a factor of 5 to 17.11 GN m^{-3} at 2.1 T compared to F_p^{max} of 3.40 GN m^{-3} at 2.1 T for undoped YBCO film. Nevertheless, MW-HfO_2-doped YBCO films show a threefold increase of F_p^{max} to 11.04 GN m^{-3} at 1.6 T. It is worthwhile to note that HU-based HfO_2 nanocrystals deliver a champion F_p^{max} value in this work without a shift of F_p^{max} to the lower magnetic field.

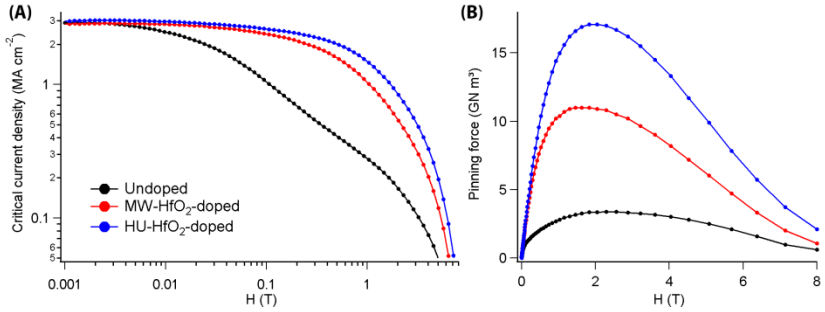

Figure 6.6. *(A) J_c(H) for undoped, HU-HfO_2-doped and MW-HfO_2-doped YBCO layers and (B) according pinning force curves at 77 K.*

The quest for a reason why HU-based HfO_2 nanocrystals deliver better pinning force densities compared to MW-based nanocrystals was studied via a cross-sectional microstructure study of the obtained thin films. TEM-lamellae were produced by FIB and studied with HRTEM (Cs-corrected JEOL 2200FS, operating at 200 kV). The HRTEM image of a HU-HfO_2-doped YBCO film, Figure 6.7, shows $BaHfO_3$ particles embedded in the YBCO matrix with diameters in the range of 5-20 nm. However, some agglomerations of $BaHfO_3$ particles, which lead to larger particles and a non-ideal pinning landscape, can be observed only occasionally in the YBCO matrix (Figure A6.3 in Appendix A). On the other hand,

it is worth noting that $BaHfO_3$ particles in MW-HfO_2-doped YBCO films exhibit diameters with a range of 15-30 nm (cf. Figure 6.8b).

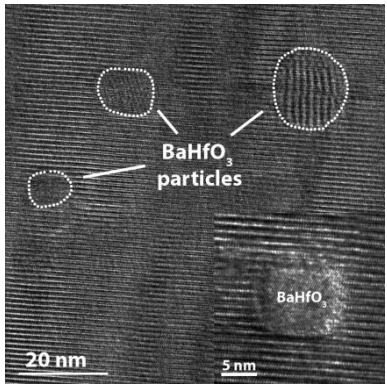

Figure 6.7. *HRTEM image of HU-HfO_2-doped YBCO layer showing isolated, randomly oriented $BaHfO_3$ particles in the YBCO matrix. Inset: close-up of a $BaHfO_3$ particle, showing absence of stacking faults around the particle.*

The HRTEM image of the $BaHfO_3$ particles, inset Figure 6.7, reveals no particular crystallographic relation between the $BaHfO_3$ and the YBCO matrix. However, some $BaHfO_3$ particles show a relational relationship with the YBCO matrix because a rotational Moirée contrast is clearly observed, indicating the presence of some degree of epitaxy. The crystal lattices of $BaHfO_3$ is slightly rotated with 10-20° compared to crystal lattices of YBCO as confirmed via FFT (not shown) of isolated $BaHfO_3$ particle in YBCO matrix. As described in the work of L. Molina-Luna *et al*.[11], misfit interfacial dislocations with a distance less than 2 nm are usually observed at the $BaHfO_3$/YBCO interface in CSD-grown films, which can act as nucleation centers for Ba-Cu-Cu-Ba (Y124-type) stacking faults. To elucidate this interface, TEM-lamellae (prepared via FIB method) were studied with high-resolution HAADF-STEM in the Titan QuantEM probe corrected microscope (operated at 300 kV) combined with EDX in collaboration with EMAT, University of Antwerp. Figures 6.8a and 6.8b show the overview STEM images of HU-HfO_2 and MW-HfO_2-doped YBCO nanocomposite film, indicating both films show homogenously distributed $BaHfO_3$ particles into the YBCO matrix with quite a lot of line defects. But the MW-HfO_2-doped YBCO film shows less particles and more line defects in the whole layer.

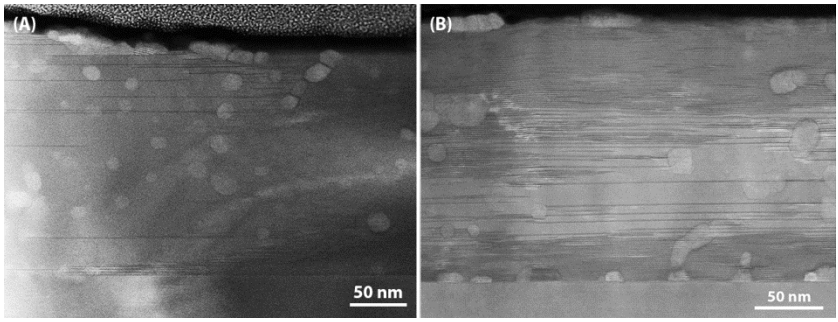

Figure 6.8. *STEM images of (A) HU-HfO_2-doped and (B) MW-HfO_2-doped YBCO films. Black lines correspond to line defects.*

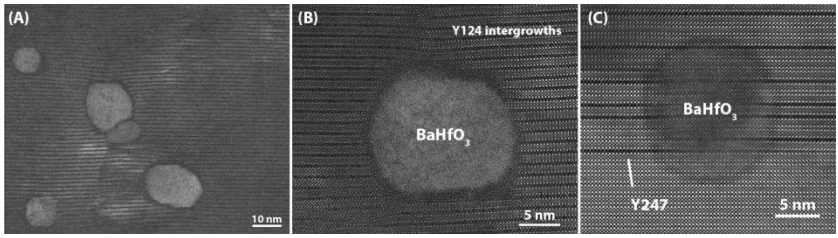

Figure 6.9. *(A) STEM Overview image of HU-HfO_2-doped YBCO microstructure, showing a 1 nm dark region around the particles and (B) the isolated $BaHfO_3$ particles surrounded with Y124 intergrowths. (C) HAADF-STEM image of MW-HfO_2-doped YBCO microstructure shows the line defects are produced around the particles.*

A closer look into the HU-HfO_2-doped YBCO microstructure (shown in Figure 6.9a) of the film with best pinning properties in this work, a 1 nm dark amorphous region is observed at the interface between $BaHfO_3$ particles and the YBCO matrix (Figure 6.9b). This is due to the incoherent interface and the induced $YBa_2Cu_4O_8$ (Y124) structural defects, which consist of an intergrowth of an extra Cu-O chain layer. It has been observed that randomly $BaHfO_3$ particles are surrounded by large clusters of Y124 intergrowths, which means that all YBCO unit cells exhibit an additional CuO layer. This intergrowth is also observed in self-assembled YBCO-$BaZrO_3$ nanocomposite film with small 10-20 nm nanoparticles, promoting short intergrowths which can act as pinning.[12, 13] However, large nanoparticles of MW-HfO_2-doped YBCO film (20-30 nm, Figure 6.9c) seem to be more embedded inside the YBCO matrix, leading to a reduction of the incoherent interface because the dark region around the particles is less observed. This results in the formation of more extended defects such as occasional CuO stacking faults in the YBCO matrix, which locally forms $Y_2Ba_4Cu_7O_{15}$ (Y247) structure. This means that an extra CuO layer is introduced in

every 2 YBCO unit cells. So, the large line defects seem to be produced by the big particles (>25 nm) in the YBCO matrix, which would increase the overall microstrain and thus degrade the critical current densities.[1, 14] It is important to control Y124 intergrowths and Y247 line defects as they can result in negative effects on T_c and J_c.[14-16] Thus, the key parameter to control these defects is the introduction of agglomerate-free preformed nanocrystals in a size range of 5-15 nm.

In addition, only a small portion of the sample can be examined via TEM analysis, so the results may not be representative for the entire sample. XRD analysis was used to provide a rapid, quantitative and nondestructive measurement over a large area of the YBCO film. The stacking faults density was calculated based on an analysis of (00ℓ) peak positions using the Hendrick-Teller method.[17, 18] This method quantitatively links the shift in these peak positions and widths to the density of stacking faults present in the YBCO layer. XRD analysis of HU-HfO_2-doped layers shows the higher density of stacking faults (f = 0.043) compared to MW-HfO_2-doped layers (f = 0.024). As stacking fault is a planar defect, it causes anisotropic vortex pinning at 77 K which is effective for applied magnetic fields aligned the *ab*-plane.

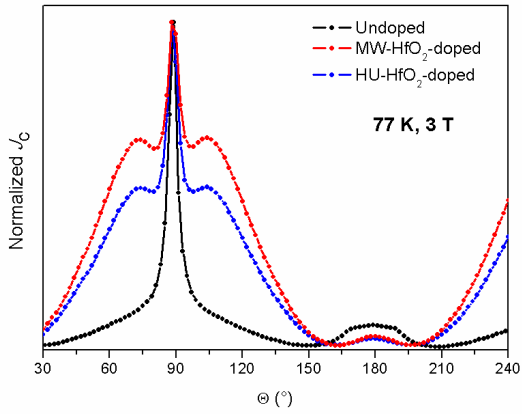

Figure 6.10. *Angular dependence of normalized J_c at 3 T measured at 77 K of undoped and HfO_2-doped layers.*

Figure 6.10 shows the dependence of normalized J_c at 3 T on the magnetic field angle at 77 K for all layers. It is clearly that HfO_2-doped layers show better anisotropic behavior (broaden *ab*-peak) compared to undoped layer due to the addition of nanocrystals. These results suggest that the enhanced *ab*-plane pinning (sharp peak) of the HU-HfO_2-doped layer is due to the combination of

short Y124 intergrowths and $BaHfO_3$ particles. The MW-HfO_2-doped layer shows less strong *ab*-plane pinning due to the presence of large stacking faults but have more shifting of F_p^{max} (1.6 T) to a lower magnetic field compared to undoped (2.1 T). The addition of nanocrystals results in a decrease of twin boundaries, leading to the decrease in the pinning at B||*c*. So, a follow-up study is essential to understand the complex relationship between vortex pinning and microstructural defects.

As shown in Table 5.5, the F_p^{max} values of ZrO_2-doped YBCO films were shifted to a lower magnetic field, which should be explained due to the absence of the stacking faults around the $BaZrO_3$ particles as confirmed via TEM images (Figure 4.8e-g). While the F_p^{max} values of HU-HfO_2-doped YBCO films have shown no shifting effects, which is probably due to the presence of Y124 intergrowths around the $BaHfO_3$ particles, leading to improved pinning properties. However, we were strongly convinced that the pinning properties could be improved by combining the addition of preformed nanocrystals and the formation of short Y124 intergrowths around the particles. Since the formation of stacking faults can be originated from the decomposition of Cu-containing impurity phases (such as Ba–Cu–O) during the oxygenation process[18], a follow-up research should be executed to vary the oxygenation temperature to increase the stacking faults density in the YBCO matrix with nanocrystals. This combination should lead to an enhancement of pinning properties.

6.4. Ink-jet printing of $YBa_2Cu_3O_7$ with preformed nanocrystals

6.4.1. Experimental section

A HU-HfO_2-doped YBCO precursor solution is prepared by dissolving barium trifluoracetic, copper propionate and yttrium propionate in 1-butanol with a Y:Ba:Cu ratio of 1:2:3 and a total concentration of 0.75 M L^{-1}. The HU-HfO_2 nanocrystals are stabilized in methanol via phase transfer/ligand exchange with copolymer. Prior to inkjet printing, the $LaAlO_3$ substrates were first cleaned with isopropanol and heated to 400 °C to remove organic residues. HfO_2-doped YBCO inks were printed reproducibly with a print frequency of 9 kHz using the custom waveform with an ejection voltage applied to the piezoelectric nozzle in the range of 18-19 V for the jetting waveform and 9-10 V for the non-jetting waveform. A wet coating was obtained by printing lines with droplet spacing of 25 µm and a longitudinal spacing between each printed line of 25 µm. After printing, the single- or multi-printed layers were dried at 85 °C on a hotplate for 5 min and subsequently pyrolyzed by heating to 400 °C with heating rate of 3-5 °K min^{-1} in a humidified O_2 atmosphere. The pyrolyzed YBCO thin films were

subsequently treated to obtain the desired superconducting film with the high-temperature thermal treatment at 640 °C for 60 min and 795 °C for 70 min in a humid 100 ppm O_2 in N_2 atmosphere (the details of this thermal process are described in section 4.2 of chapter four) which were switched to dry O_2 at 450 °C for 2 hours during the annealing step. The inlet gas was humidified with a dew point of 23 °C.

6.4.2. Study of fluid properties and its jettability

To maximize the implementation of this HfO_2 nanocrystal approach in the YBCO matrix for power applications, ink-jet printing was introduced as a CSD technique to have a possibility to increase the thickness of YBCO nanocomposite film. The principle of the ink-jet printing method is described in section 2.4.3 of chapter two. YBCO ink nano-suspensions with 5 and 10 mol-% HfO_2 nanocrystals concentration are used to study their resulting fluid properties. The addition of HfO_2 nanocrystals to the YBCO ink increases its density and surface tension slightly while the viscosity remains the same as shown in Table 6.3. This modification leads to a small increase of the Oh^{-1} number while the values remain in the intended range between 1 and 10. Therefore, these inks are printable and the small nanocrystals (in the range of 3-10 nm) do not affect the printability. The small nanocrystals should also be agglomeration-free and have a solvodynamic diameter less than the orifice diameter (22 µm) of the nozzle to avoid nozzle blockage. It is noteworthy that the different inks in the cartridges were stable for at least 5 months when stored in a closed container, indicating a high shelf-life of these nano-suspensions. In this work, we focused on the ink-jet printing deposition of undoped and 5 mol-% HfO_2-doped YBCO inks on $LaAlO_3$ substrates as this mol-% concentration of nanocrystal has given the optimal value of the pinning properties for ZrO_2-doped YBCO nanocomposite film in this work.

***Table 6.3**. Fluid properties of the different YBCO inks for an orifice diameter (α) of 22 µm, determined at 21 °C.*

Type of ink	density kg m^{-3}	viscosity Pa s	surface tension J m^{-2}	contact angle °	Oh^{-1}
Undoped	918	6.4 x 10^{-3}	2.21 x 10^{-2}	14.1	3.23
5 mol-% HfO_2-doped	946	6.4 x 10^{-3}	2.34 x 10^{-2}	14.6	3.37
10 mol-% HfO_2-doped	961	6.4 x 10^{-3}	2.44 x 10^{-2}	15.0	3.47

Despite the negligible difference in Oh^{-1} number, a clear difference in the jetting behavior of the undoped and HfO_2-doped YBCO inks can be seen as their voltage

settings are different. The firing voltage of the piezoelectric nozzles is increased to 18-19 V with a lower print frequency of 9 kHz for HfO_2-doped YBCO ink. The first segment of droplet generation is decreased at slower step of over 1.2 µs to the minimum voltage of 0 V with a shorter dwell time of 25 µs to force the pressure build-up in the nozzle for the droplet ejection. In the second segment, the voltage increases to the maximum of 18 V in 28 µs to cut off the droplet tails. The jetting analysis of HfO_2-doped ink, Figure 6.11, reveals the formation of a droplet tail with very small satellite droplets (red dotted rectangle Figure 6.10), which finally rapidly merges with the main droplet. This means that the addition of nanocrystals can affect the jetting behavior and its droplet formation. Thus, it is clearly visible that the ejection voltage depends on the addition of nanocrystals and not only on the Oh^{-1} number.

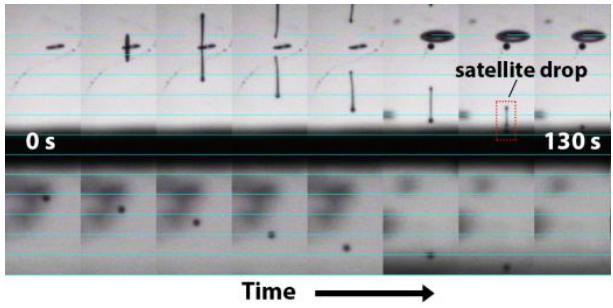

Figure 6.11. *Time-resolved drop formation after ejection of HfO_2-doped ink in the air. A very small satellite droplet can be observed at t = 120 s (red dotted rectangle) but finally recombines with the main droplet. The blue lines are separated by 100 µm and the time step is 15 s.*

6.4.3. Study of HfO_2-doped YBCO nanocomposite films.

In order to obtain a smooth and continuous wet coating, a drop spacing of 25 µm in both *x* and *y* direction was used to deposit a thin film. After a single deposition of HfO_2-doped YBCO ink, resulted in a thickness of 150 nm after full thermal process as confirmed by the cross-sectional SEM view (Figure A6.4 in Appendix A). The HfO_2-doped YBCO nanocomposite film with a similar thickness of 450 nm as described for the undoped YBCO film is obtained after only three ink-jet deposition runs with a thickness of (480±20) nm after a full thermal process, as confirmed in the cross-sectional SEM image in Figure 6.12. Furthermore, this image shows a dense film with a homogeneous dispersion of particles (bright spots) throughout the film. At the surface and to a lesser degree at the interface, some larger particles are visible. The addition of preformed HfO_2 nanocrystals results in self-field J_c values of 3.1 MA cm^{-2} at 77 K for the

YBCO nanocomposite film with 3 deposition runs. It is noteworthy that the self-field critical current is slightly increased compared to the corresponding undoped YBCO films obtained via the ink-jet printing method.

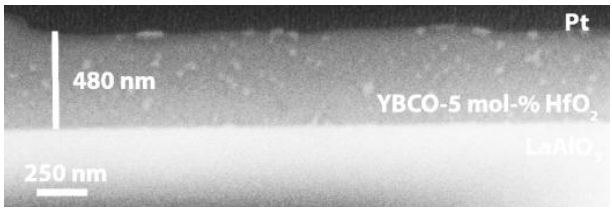

Figure 6.12. *Cross-sectional SEM image of an ink-jet-printed HfO_2-doped YBCO nanocomposite film with 3 deposition runs after full thermal processing.*

6.4.4. Transport properties

Ink-jet printing of both undoped YBCO and HfO_2-doped YBCO nanocomposite films leads to good in-field properties of the critical current density J_c, Figure 6.12, measured via transport measurements with an electrical field criterion of 1 μV cm^{-1}. The additive effect of the $BaHfO_3$ particles in the YBCO matrix to the pinning properties is clearly seen by comparing $J_c(B)$ of both films at 30 and 77 K. The largest effect on J_c occurs around 1 T for the magnetic field parallel to the film ($B||c$), Figure 6.13a. This is a combined effect of the $BaHfO_3$ particles themselves and the concurrent larger density of twin boundaries, as shown in Figure A6.5 in Appendix A. The maximum pinning force $F_{p,max}$ at 77 K of the undoped YBCO film is around 1.3 GN m^{-3} and is comparable to the value observed by M. Erbe *et al.* for similar films prepared by spin-coating TFA-based YBCO.[19] On the other hand, the 5 mol-% HfO_2-doped YBCO film obtained via ink-jet printing shows a $F_{p,max}$ = 6.8 GN m^{-3} at 77 K, a value about 5 times larger than for the undoped YBCO film (Figure 6.13). Similar $F_{p,max}$ values at 77 K have been shown for 10 mol-% ZrO_2-doped YBCO nanocomposite films, fabricating via TFA-based YBCO with preformed ZrO_2 nanocrystals (5.8 GN m^{-3}).[4] However, it is remarkable that there are a difference in a position of F_p^{max} values of spin-coated and ink-jet printed YBCO nanocomposites in the magnetic field, indicating ink-jet printed HfO_2-based nanocomposites should not show an equal amount of Y124 intergrowths as the spin-coated films. A follow-up TEM study should be recommended to verify this hypothesis.

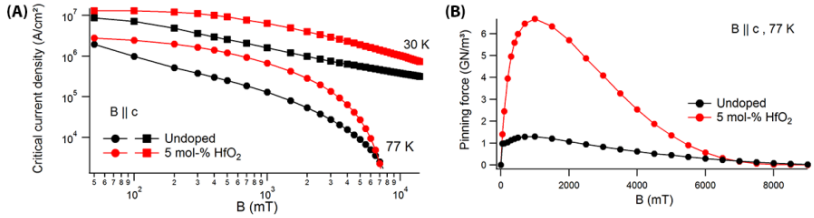

Figure 6.13. *Transport critical current density of the two-deposition films with (red) and without (black) nanocrystal addition at two temperatures, 30 and 77 K (A) magnetic field dependence of J_c, (B) corresponding pinning force density F_p at 77 K. [Measured at Karlsruhe Institute of Technology, E_c = 1 µV cm^{-1}]*

6.5. Conclusion

In this chapter, it has been shown that the nanocrystal size and its distribution are the key parameters for a better control of the intergrowths and line defects. Small particles would tend to promote formation of short intergrowths surrounding the particles in HU-HfO_2-doped YBCO film, yielding an increase of microstrain and pinning properties. Large particles (>25 nm) in the YBCO matrix could lead to formation of large stacking faults leading to degradation of the critical current density in the YBCO nanocomposite films as confirmed by MW-HfO_2-doped YBCO film.

It has been shown that HU-HfO_2-based nanocrystals incorporated in the YBCO matrix lead to $BaHfO_3$ particle size of 5-20 nm combined with a pinning force density F_p^{max} of 17.11 GN m^{-3}. As this F_p^{max} shows highest value in this work, it should be attractive to transfer these results from spin-coated to ink-jet printed samples. It is possible to adjust the printing parameters depending on the addition of nanocrystals in order to deposit HfO_2-doped YBCO inks on single crystal $LaAlO_3$ substrates using a DOD piezoelectric ink-jet printing Dimatix system. This ink-jet printing method leads to self-field critical current densities up to 3.0 MA cm^{-2} at 77 K. By the addition of HfO_2 nanocrystals, the pinning force density at 77 K is increased by a factor of more than 5 due to the combined effect of $BaHfO_3$ particles in a size of ~5-20 nm and a larger density of twin boundaries. So, this chemical solution deposition route shows a good potential for a low-cost, long-length industrial production when using reel-to-reel deposition.

6.6. References

1. M. Coll, *et al.*, "Size-controlled spontaneously segregated Ba_2YTaO_6 nanoparticles in $YBa_2Cu_3O_7$ nanocomposites obtained by chemical solution deposition," *Supercond. Sci. Technol.,* **27** [4] 044008 (2014).
2. K. Nakaoka, *et al.*, "Another approach for controlling size and distribution of nanoparticles in coated conductors fabricated by the TFA-MOD method," *Supercond. Sci. Technol.,* **30** [5] 055008 (2017).
3. H. Horita, *et al.*, "Miniaturization of $BaHfO_3$ nanoparticles in $YBa_2Cu_3O_y$-coated conductors using a two-step heating process in the TFA-MOD method," *Supercond. Sci. Technol.,* **30** [2] 025022 (2016).
4. K. De Keukeleere, *et al.*, "Superconducting $YBa_2Cu_3O_{7-\delta}$ Nanocomposites Using Preformed ZrO_2 Nanocrystals: Growth Mechanisms and Vortex Pinning Properties," *Adv. Electr. Mater.,* **2** [10] 1600161 (2016).
5. P. Cayado, *et al.*, "Epitaxial $YBa_2Cu_3O_{7-x}$ nanocomposite thin films from colloidal solutions," *Supercond. Sci. Technol.,* **28** [12] 124007 (2015).
6. M. Niederberger and N. Pinna, "Metal oxide nanoparticles in organic solvents: synthesis, formation, assembly and application." Springer Science & Business Media, (2009).
7. J. De Roo, *et al.*, "Fast, microwave-assisted synthesis of monodisperse HfO_2 nanoparticles," *J. Nanopart. Res.,* **15** [7] 1778 (2013).
8. J. De Roo, *et al.*, "Amino Acid-Based Stabilization of Oxide Nanocrystals in Polar Media: From Insight in Ligand Exchange to Solution ^{1}H NMR Probing of Short-Chained Adsorbates," *Langmuir,* **32** [8] 1962-70 (2016).
9. J. Joo, *et al.*, "Multigram scale synthesis and characterization of monodisperse tetragonal zirconia nanocrystals," *J. Am. Chem. Soc.,* **125** [21] 6553-57 (2003).
10. J. Tang, *et al.*, "Solid-Solution Nanoparticles: Use of a Nonhydrolytic Sol-Gel Synthesis To Prepare HfO_2 and $Hf_xZr_{1-x}O_2$ Nanocrystals," *Chem. Mater.,* **16** [7] 1336-42 (2004).
11. L. Molina-Luna, *et al.*, "Atomic and electronic structures of $BaHfO_3$-doped TFA-MOD-derived $YBa_2Cu_3O_{7-\delta}$ thin films," *Supercond. Sci. Technol.,* **28** [11] 115009 (2015).
12. J. Gutierrez, *et al.*, "Strong isotropic flux pinning in solution-derived $YBa_2Cu_3O_{7-x}$ nanocomposite superconductor films," *Nat. Mater.,* **6** [5] 367-73 (2007).
13. R. Guzman, *et al.*, "Probing localized strain in solution-derived $YBa_2Cu_3O_{7-\delta}$ nanocomposite thin films," *Phys. Rev. Materials,* **1** [2] 024801 (2017).
14. A. Llordés, *et al.*, "Nanoscale strain-induced pair suppression as a vortex-pinning mechanism in high-temperature superconductors," *Nat. Mater.,* **11** [4] 329-36 (2012).
15. E. Talantsev, *et al.*, "Hole doping dependence of critical current density in $YBa_2Cu_3O_{7-\delta}$ conductors," *Appl. Phys. Lett.,* **104** [24] 242601 (2014).
16. E. Talantsev, *et al.*, "Oxygen deficiency, stacking faults and calcium substitution in MOD YBCO coated conductors," *IEEE Trans. Appl. Supercond.,* **23** [3] 7200205-05 (2013).
17. S. Hendricks and E. Teller, "X-Ray Interference in Partially Ordered Layer Lattices," *J. Chem. Phys,* **10** [3] 147-67 (1942).

18. A. Puichaud, S. Wimbush, and R. Knibbe, "Enhanced low-temperature critical current by reduction of stacking faults in REBCO coated conductors," *Supercond. Sci. Technol,* **30** [074005] 074005 (2017).
19. M. Erbe*, et al.*, "$BaHfO_3$ artificial pinning centres in TFA-MOD-derived YBCO and GdBCO thin films," *Supercond. Sci. Technol.,* **28** [11] 114002 (2015).

Chapter seven

$YBa_2Cu_3O_{7-\delta}$-$SrTiO_3$ nanocomposite films:

An exploration to the use of double metal oxide nanocrystals

This chapter describes the microwave-assisted synthesis of double metal oxide $SrTiO_3$ nanocrystals and its incorporation into the YBCO matrix.

Adapted from:

H. Rijckaert & K. De Keukeleere, J. De Roo, M. Bäcker, M. Hemgesberg and I. Van Driessche, Size-tunable microwave-assisted synthesis of $SrTiO_3$ nanocrystals starting from bimetallic alkoxide precursors. In preparation.

7.1. Introduction

Perovskite double metal oxides - strontium titanate, barium zirconate and barium titanate - exhibit outstanding chemical and physical properties that can be tuned by adding metal dopants or changing crystal phase and size, leading to enhanced or controlled electronic and optical properties.[1, 2] Strontium titanate ($SrTiO_3$) has a band-gap of about 3.2 eV which is attractive for new microelectronic devices because of a high dielectric permittivity[3], ferroelectricity[4] and low leakage current.[5] For example, the incorporation of transition metal ions like trivalent chromium can switch the resistance for solid-state memory by tuning the conduction band, which creates new intermediate band states.[6] The nano-sized $SrTiO_3$ material is also a promising photocatalyst as it offers a higher specific surface area and an activity under UV-VIS light.[7, 8] It is noteworthy that their activity is strongly influenced by the crystal phase, size, morphology and crystallinity. Hence, many of the physical properties of $SrTiO_3$ particles are critically dependent on the particle size as well as on the dimensionality for most of the applications. $SrTiO_3$ material is already introduced in the superconducting field (mainly for academic purpose) as a single crystal substrate for the epitaxial growth of YBCO film, due to its low lattice mismatch (2.36 %) with the orthorhombic $YBCO_{7-\delta}$ structure together with a chemical and physical inertness.[9] Previously in this work, it has been shown that the use of ZrO_2 and HfO_2 nanocrystals as single metal oxide nanocrystals leads to the formation of double metal oxide ($BaZrO_3$ and $BaHfO_3$) particles, which are coarsened during the thermal process because of the reaction with Ba^{2+}, causing a slight degree of agglomeration in the film. Even more at higher loading of nanocrystals would affect the YBCO texture due to their reactivity. This reactivity of the preformed nanocrystals could be avoided by using double metal oxide nanocrystals, acting as completely inert materials in the YBCO matrix. Cubic $SrTiO_3$ nanocrystals can be used as artificial pinning centers and should be an ideal candidate with thanks to the low lattice mismatch, resulting in minor structural defects (i.e. large stacking faults, see chapter six) after the YBCO growth.[10, 11] The lattice mismatch ε is generally defined as:

$$\varepsilon = \left|\frac{a_{\mathrm{m}} - a_{\mathrm{particles}}}{a_{\mathrm{m}}}\right| \times 100 \qquad \text{Eq. 7.1}$$

with a_{m} and $a_{\mathrm{particles}}$ the lattice parameter of the material and the particles respectively. Here, the lattice mismatch between the nanoparticles and the matrix should be as low as possible, because a large mismatch (> 15 %) will generate more structural defects, leading to poor superconducting properties. However, due to the small lattice mismatch, some local strain around the

particles in the YBCO matrix can arise and can act as pinning centers (see section 6.3 of chapter 6). The lattice constants of the materials and the calculated lattice mismatches are represented in Table 7.1.

Table 7.1. *Comparison of the lattice constants and lattice mismatches between the $SrTiO_3$ particles and materials*

Material	Structure	Lattice constant Å	Mismatch vs. $SrTiO_3$ %
$SrTiO_3$	*cubic*	3.91	-
$YBCO_6$	*tetragonal*	3.86	1.30
$YBCO_{7-\delta}$ [(a)]	*orthorhombic*	3.82 (*a*-axis)	2.36
		3.88 (*b*-axis)	0.77
CeO_2 [(b)]	*cubic*	5.41	2.22
$LaAlO_3$	*rhombohedral*	3.81	2.62

[(a)] $YBCO_6$ crystal will change to $YBCO_{7-\delta}$ crystal with the introduction of oxygen in the lattice during the oxygenation step.[12] However, $YBCO_{7-\delta}$ unit cell parameters change continuously when the oxygenation changes.

[(b)] Regarding the calculations of the mismatch between CeO_2 and $SrTiO_3$. Since $YBCO_6$ grows 45° rotated vs. CeO_2 one needs to recalculate the actual lattice parameter for $SrTiO_3$ ($\sqrt{2a^2}$ = 5.53 Å).[13]

As stated in chapter 1 section 7.2, the preformed $SrTiO_3$ nanocrystals should be small in size, stable and agglomeration-free in the YBCO precursor solution. In general, nano-sized $SrTiO_3$ particles are synthesized via conventional solvothermal methods, starting from aqueous or non-aqueous precursors.[8, 14-16] These conventional procedures mainly produce amorphous phases and require an additional crystallization step at temperatures above 900 °C to obtain crystalline $SrTiO_3$, resulting in an extensive aggregation and in the formation of large particles. To avoid this undesired crystallization step, Niederberger *et al*[17] have introduced a non-aqueous synthesis method in benzyl alcohol which results in aggregated nanocrystalline cubic $SrTiO_3$ particles, with sizes varying between 5 and 10 nm, via a non-hydrolyic and halide-free procedure. Some researchers have successfully synthesized aggregate-free and colloidal stable $SrTiO_3$ nanocrystals.[18-21] Nevertheless, this nanocrystal synthesis based on solvothermal methods generally involves a long reaction time up to 6 days, to obtain the desired properties.

In this work, we report a microwave-assisted nanocrystal synthesis using benzyl alcohol as solvent in the combination with bimetallic Sr(II)-Ti(IV) alkoxide precursors. A conventional synthesis, starting from bimetallic Sr(II)-Ti(IV) methoxyethoxide resulting in highly crystalline STO powders obtained after hydrolysis and calcination at 600 °C, is already described.[22] Otherwise, the

solution-based synthesis described in the work of Urban *et al*[23] shows that the use of bimetallic Sr(II)-Ti(IV) alkoxide precursors in the presence of heptadecane and oleic acid, leads to crystalline cubic $SrTiO_3$ nanorods. To obtain colloidally stable $SrTiO_3$ nanocrystals, we introduce the solvothermal microwave-assisted synthesis starting from different types of Sr(II)-Ti(IV) bimetallic precursors. In this microwave procedure, small nanocrystals with the cubic crystal phase are obtained after the synthesis. The $SrTiO_3$ nanocrystals are agglomerated directly after synthesis but can be de-agglomerated via a post-functionalization step with oleic acid, providing stabilization via steric hindrance in an apolar solvent such as toluene. This microwave-assisted method also delivers an advantage to tune the crystal size depending on the used bimetallic precursors and lies between 3 and 6.5 nm. This results in a larger applicability of $SrTiO_3$ nanocrystals as artificial pinning centers.

7.2. Nanocrystal synthesis

Five different bimetallic Sr(II)Ti(IV)-alkoxide precursors are synthesized by HTE (High Throughput Experimentation GmbH, a subsidiary of BASF) and are kept in sealed vials under inert atmosphere to avoid hydrolysis and oxidation. The ratio of Sr:Ti is 1:1, with a stoichiometric alcohol amount. The liquid or viscous-like precursors differ in their alkoxide, i.e., 2-methoxyethoxide (ME), 2-(2-methoxyethoxy)ethoxide (MEE), 1-Octanol (Oct), isopropanol (iPr) or benzyl alcoholate (BnO) and are miscible in benzyl alcohol. This 0.32 mmol bimetallic Sr(II)Ti(IV)-alkoxide precursor was transferred to a 10 mL microwave vial and dissolved in 4 mL anhydrous benzyl alcohol (99.8 % - Sigma-Aldrich) under vigorous stirring, resulting in a clear, orange solution with a concentration of 0.08 M. These vials are subjected to microwave heating for 4 hours at 270 °C using a. 2.45 GHz Discover SP CEM Microwave. After the microwave-assisted solvothermal treatment, all precursors produce a white precipitate and an organic supernatant after synthesis. The precipitate is collected by centrifugation (4000 rpm, 3 min) and is washed twice with ethanol and diethyl ether to remove excess of organic byproducts. These precipitations are dried at 60 °C to determine the crystallinity and crystal phase by XRD.

Figure 7.1a shows that all the Sr(II)Ti(IV) alkoxide precursors result in cubic $SrTiO_3$ (STO) after the microwave treatment. Only the cubic STO phase (JCPDS 35-0734) is found, while impurities or byproducts like $SrCO_3$ and TiO_2 remain absent. Scherrer analysis of the full width at half maximum of the most intense (110) peaks at 32.3° of the STO nanocrystals starting from bimetallic alkoxide precursors has led to different values of the crystallite size (Figure 7.1b). STO-ME and STO-Oct have a small crystallize size of 3-4 nm while STO-BnOH has a large

size of 6.5 nm. The crystallize size of STO-MEE is 5.3 nm. It is clear from Figure 7.1c that the STO powders show a different degree in crystallinity as confirmed via Rietveld refinement on dried powders after synthesis. STO-ME and STO-MEE contain an acceptable degree of crystalline cubic STO with approximately 79 % and 70 %, while STO-iPr shows a poor crystallinity of 12 %. The crystallinity of STO-Oct and STO-BnOH were 58 % and 45 % resp. The conversion from STO precursors to STO powders was almost 90 % as confirmed by TGA, affirming a good efficiency of the microwave synthesis.

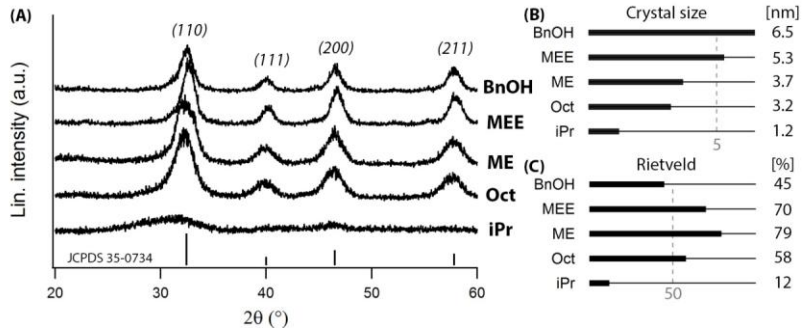

Figure 7.1. *(A) XRD diffractograms of cubic $SrTiO_3$ (JCPDS 35-0734) from the different precursors iPr, Oct, ME, MEE and BnOH after the microwave-assisted solvothermal synthesis at 270 °C for 4 hours with their (B) crystal size and (C) its crystallinity.*

7.3. Surface functionalization

The as-synthesized STO nanocrystals are aggregated, so a surface functionalization step is necessary to de-aggregate the nanocrystals and improve the stability for maximizing the applicability of STO nanocrystals. The precipitated nanocrystals after microwave reaction conditions (270 °C for 4h) were washed and led to a turbid and unstable suspension after redispersion in 4 mL toluene. To obtain a clear colloidal nanocrystal suspension, 0.2 mmol oleic acid was added to the milky and unstable suspension. Instantly, a transparent suspension was obtained independent on the used precursor after ultrasonic treatment. The nanocrystals are stabilized with oleic acid, a long-chain carboxylate acid, leading to a sterically stable and clear suspension in nonpolar solvents. As shown by DLS measurements (Figure 7.2a), the nanocrystals starting from ME, MEE and BnOH alkoxide precursors are aggregate-free while Oct precursor shows slightly agglomeration. Nevertheless, STO nanocrystals from iPr precursor cannot be stabilized with oleic acid and remain a turbid suspension. However, as seen in TEM images (Figure 7.3a), STO-iPr nanocrystals have pseudocubic morphology and seem to be agglomeration-free. These STO

nanocrystals should be agglomeration-free in the suspension because the large particles (coarsened due to the agglomeration) in the YBCO matrix would degrade the pinning properties and thus the superconducting properties in the final YBCO layer.

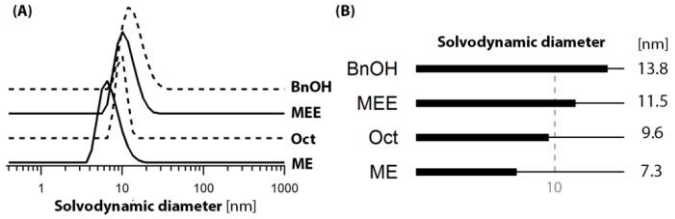

Figure 7.2. *(A) DLS analysis of the post-modified STO nanocrystals starting from ME, Oct, MEE and BnOH with (B) its solvodynamic diameters.*

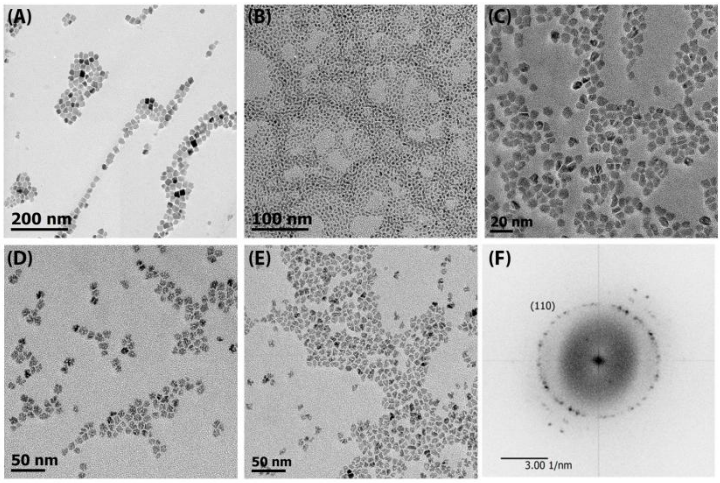

Figure 7.3. *TEM images of STO nanocrystals obtained after microwave assisted synthesis from (A) iPr precursor and using post-modification with oleic acid from the (B) Oct, (C) BnOH, (D) ME and (E) MEE precursors. (F) FFT pattern of STO nanocrystals obtained from MEE precursor.*

The solvodynamic diameter (nanocrystal + ligand shell, Figure 7.2b) of nanocrystals from the ME precursor is 7.3 nm while MEE, BnOH and Oct precursors show diameters of 11.5 nm, 13.8 nm and 9.6 nm resp. TEM micrographs of different nanocrystals except STO-iPr in Figure 7.3b-e show that the nanocrystals are aggregate-free and have a pseudo-spherical morphology. In addition, the FFT pattern (Figure 7.3f) of STO nanocrystals point out good crystallinity and the diffraction rings match with the STO structure. Energy-dispersive X-ray analysis (EDX) has been used to examine the composition of the

STO nanocrystals. With respect to the Ti-K-edge and Sr-K-edge, Sr as well as Ti were detected in the sample with a Sr:Ti ratio of 1:1. After thorough analysis, we confirmed that the type of alkoxide precursor has an influence on the final size of the nanocrystal and all produced cubic crystalline $SrTiO_3$ nanocrystals with a Sr:Ti ratio of 1:1.

7.4. Colloid stabilization

To determine the role of the oleic acid and to study the nanocrystals' surface chemistry, the stable STO suspension, starting from the ME precursor, was investigated by 1D ^{1}H NMR and 2D NOESY spectra. Two 1D ^{1}H NMR spectra are compared in Figure 7.4 corresponding to samples with STO nanocrystals treated at 270 °C for 4 hours starting from ME precursors in spectrum A and after 3 purifications in spectrum B.

According to spectrum A of the unpurified STO nanocrystals in toluene, it is clear that the oleic acid is bound on the nanocrystal surface as confirmed by the broad alkene resonance at 5.3 ppm. Bound ligands typically feature peak broadening due to excessive T_2 relaxation.[24] It is remarkable that there is no sharp peak present that is related to free oleic acid, which means that all of the oleic acid is bound to the nanocrystal surface. The resonances at 4.5 and 7.15 ppm are attributed to benzyl alcohol. The sharp peak of benzyl alcohol disappeared in NMR spectrum B of the purified STO nanocrystals.

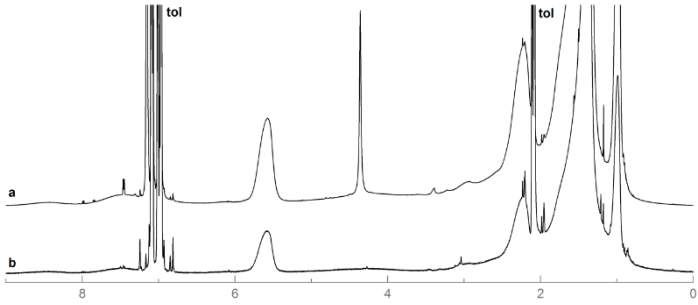

Figure 7.4. *^{1}H NMR spectra of STO nanocrystals starting from ME precursor treated at 270 °C for 4 hours in toluene stabilized with oleic acid before (A) and after (B) purification.*

To provide more insights in the interaction of the ligands with the surface, the unpurified and purified samples were also analyzed by 2D NOESY NMR (Figure 7.5) to characterize bound species. The clear negative nOe cross-peaks (7-9 ppm and 4-5 ppm) indicate that benzyl alcohol interacts with the surface.

However, according to the DOSY spectrum (Figure 7.6) benzyl alcohol has a high diffusion coefficient and is thus not strongly bound to the nanocrystals surface but exchanges fast between a free and a bound state. However, after the purification, these nOe cross-peaks are disappeared which means that benzyl alcohol is removed. Oleic acid on the other hand, features negative nOe cross peaks between its resonances and has a slow diffusion coefficient of 90 $\mu m^2 s^{-1}$ which is related to the solvodynamic diameter of 8 nm, corresponding to the values in TEM and DLS results. This confirms that oleic acid is tightly bound to the surface. The concentration of oleic acid was determined to be 7.5 mmol L^{-1} and together with the nanocrystal concentration (7 µM) and the nanocrystal size (5 nm) we calculated a ligand density of 4.5 ligand nm^{-2}.

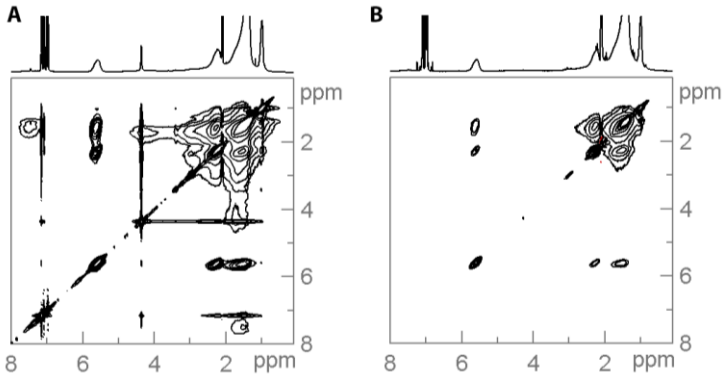

Figure 7.5. *Two-dimensional NOESY spectrum of the unpurified (A) and purified (B) $SrTiO_3$ nanocrystals*

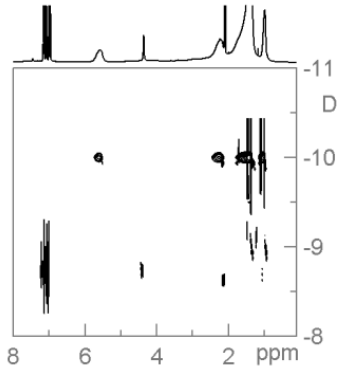

Figure 7.6. *DOSY spectrum of the purified $SrTiO_3$ nanocrystals in suspension.*

7.5. Ligand exchange and phase transfer of $SrTiO_3$ nanocrystals to methanol

Initially, agglomerate-free STO nanocrystals (8-10 nm in diameter) are stabilized via oleic acid in toluene. A phase transfer to a polar solvent, e.g. methanol is possible by precipitating the STO nanocrystals capped with oleic acid in toluene with acetone (1:4 by volume). After centrifugation at 5000 rpm for 2 min, the precipitate is mixed with methanol (1:1 by volume) and 35 mg Surfactis™ 11-104 (SF104). The mixture becomes transparent after an ultrasonic treatment of 30-60 minutes. The size distributions from DLS measurements before (black) and after (red) ligand exchange are given in Figure 7.7. The initial solvodynamic diameter has increased from 11.5 nm in toluene to 12.1 nm in methanol.

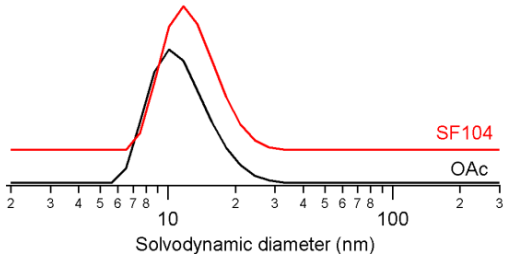

Figure 7.7. *DLS volume distribution of STO nanocrystals before (black) and after (red) ligand exchange/phase transfer.*

According to the 2D-NOESY spectrum of STO nanocrystal in methanol with SF104 (Figure 7.8), it becomes clear that the oleic acid (OAc) is no longer bound to the nanocrystals' surface (grey negative cross peaks at resonances below 2 ppm and at resonance 5.4 ppm indicated by the dotted circle). Moreover, the NOESY spectrum reveals the presence of bound SF104 (black positive cross peak at about 4.4 ppm indicated by the arrow). Although it should be mentioned that a large amount of free SF104 is still present in the sample due to the high intensity of the SF104 resonances (indicated in the 1D NMR spectrum).

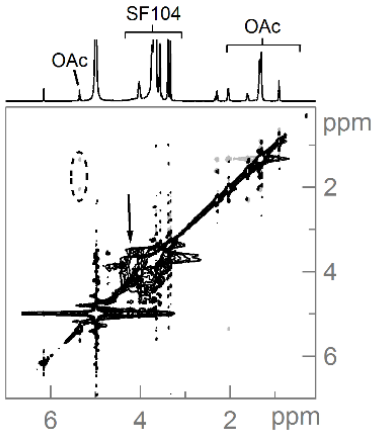

Figure 7.8. *2D NOESY spectrum of the STO nanocrystals stabilized with SF104 in methanol-d_4.*

7.6. Layer formation

After obtaining a stable STO-doped YBCO nano-suspension starting from a ME precursor with an YBCO concentration of 0.18 M, precursors with different nanocrystal additions (0, 5, 10 and 15 mol-%) were deposited on $LaAlO_3$ single substrates via spin-coating (2000 rpm and 1 min). However, as described in chapter 3 section 3.8, SF104 capped STO nanocrystals will probably coagulate during the growth of YBCO. These as-deposited layers were thermally treated for the pyrolysis. The heating rate during the pyrolysis was kept at 3-5 K min^{-1} up to 400 °C under a humid O_2 atmosphere. Subsequently, the pyrolyzed YBCO layers were first nucleated at 640 °C and then crystallized at 795 °C under 100 ppm O_2 in N_2 atmosphere with humidity of the dew point of 23 °C. In the last stage, the crystallized films were annealed at 450 °C for 2 hours in a dry O_2 atmosphere. More details of this thermal process with an additional dwelling step can be found in chapter four. The YBCO films after thermal treatment exhibit the (00ℓ) YBCO reflections as shown in the XRD patterns (Figure 7.9). It is shown that there are lots of secondary phases such as Y_2O_3 - 2θ = 29.2° (222) and 2θ = 33.8° (400) -, $BaCu_3O_4$ - 2θ = 29.1° (111) and 32.6° (400) - and $Y_2Cu_2O_5$ - 2θ = 31.3° (211) and 2θ = 33.2° (400) - present in YBCO film. By increasing the amount of STO nanocrystals, the (111) CuO peak at 2θ = 36.9° increases. The formation of secondary phases is due to the introduction of an additional dwelling step (see chapter four). However, it seems that the addition of higher loading STO nanocrystals results in the formation of more secondary phases, probably caused by a disturbance in the nucleation mechanism. The

superconducting properties of these films were measured inductively via Cryoscan™ with the voltage criterion of 50 µV and are shown in Table 7.2. It can be concluded that self-field J_c values at 77 K are slightly decreased in relation to an increased volume of STO nanocrystals. Based on these J_c values, it seems that the incorporation of STO nanocrystals and use of SF104 as ligands do not disturb the growth of YBCO as XRD patterns indicate good epitaxial structure.

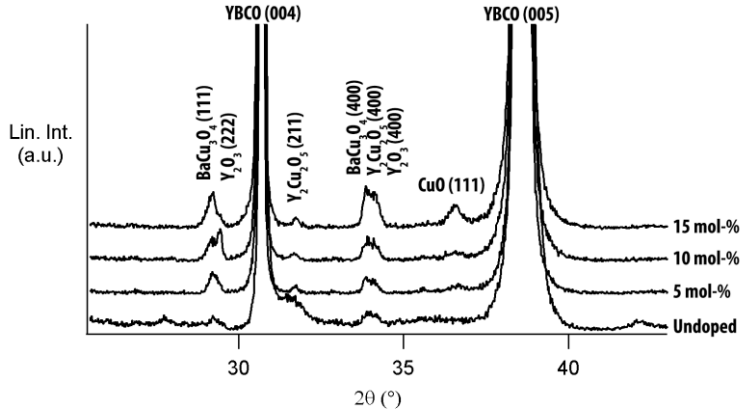

Figure 7.9. *XRD spectrum of 0, 5, 10 and 15 mol-% STO-doped YBCO film shows a good (00ℓ) texture with lots of secondary phases.*

Table 7.2. *Critical current density (J_c) of 0, 5, 10 and 15 mol-% STO-doped YBCO films on a LAO substrate, calculated via inductively measurements.*

STO nanocrystal mol-%	$J_{c,av}$ (0 T, 77 K) MA cm^{-2}
0	4.4
5	4.1
10	3.9
15	3.6

To investigate the influence of STO nanocrystals in the YBCO matrix, YBCO with 0, 5 and 10 mol-% STO nanocrystals on LAO substrates are coated with silver (1 micron) via lithography and laser-cut to nano-bridges of ~15-20 µm width and 800 µm length for the transport measurements via PPMS with E_c = 1 µV cm^{-1}. Figure 7.10a shows the magnetic field dependence of the critical current density at 77 K and $H//c$ of YBCO film with 0, 5 and 10 mol-% STO nanocrystals. Unfortunately, no pinning effect is observable when the magnetic field is increased, which means that STO nanocrystals do not act as pinning centers. It is also confirmed via the angular dependency at 77 K and 1 T on Figure 710b

where no improvement of the pinning effects is shown. When these samples are investigated via SEM (Figure 7.11), it is clear that the YBCO surface of STO-doped films is completely different compared to undoped YBCO film. The YBCO surface is not smooth anymore. From cross-sectional view of STO-doped film, it seems that there are large particles/secondary phases on the top of YBCO matrix.

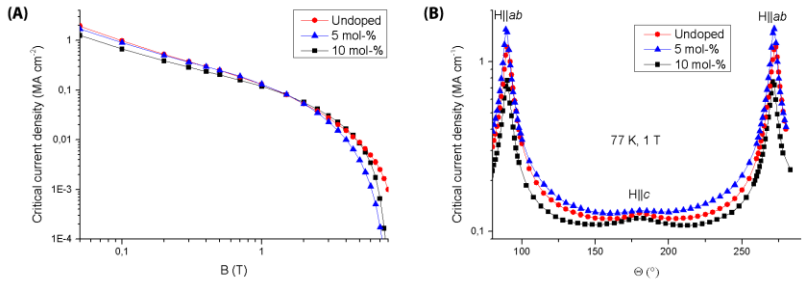

Figure 7.10. *Superconducting properties of 5 and 10 mol-% STO-doped YBCO film compared with an undoped YBCO film: (A) Magnetic field dependence of critical current density at 77 K and (B) angular dependence of J_c at 77 K and 1 T. [Measured at Karlsruhe Institute of Technology, E_c = 1 µV cm^{-1}]*

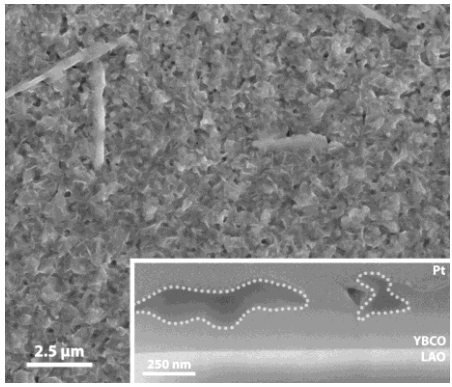

Figure 7.11. *Topographical SEM image of 10 mol-% STO-doped YBCO film after the full thermal process. Inset: cross-sectional SEM image, indicating lots of secondary phases on YBCO surface. (dotted)*

7.7. Behavior of $SrTiO_3$ nanocrystals during thermal process

To elucidate the behavior of the STO nanocrystals during the thermal process, XPS and TEM analysis were investigated to determine which type of secondary phases are formed and what the effect of STO nanocrystals during both thermal decomposition and YBCO crystallization would be. As mentioned in chapter 3

and section 3.4, the thermal decomposition of the YBCO precursor solution and the behavior of nanocrystals during the thermal decomposition is a crucial feature. However, STO nanocrystals can only be stabilized via SF104 at the moment and it is already reported in this work (chapter 3 section 3.4) that SF104 can affect the behavior of nanocrystals during the thermal decomposition, resulting in the coagulation of nanocrystals. Based on the XPS analysis (Figure 7.12) of the pyrolyzed STO-doped YBCO films, the STO nanocrystals are homogenously distributed in the Y-Ba-O-F amorphous matrix, together with CuO nanoparticles. However, it seems that the STO nanocrystals are pushed to the YBCO surface during thermal treatment and the YBCO growth and crystallization.

The cross-sectional microstructure of the STO-doped YBCO film is shown in Figure 7.13A. TEM lamellae were produced by FIB preparation and were studied via HAADF-STEM and EDX. As can be expected from the previous XRD analysis, YBCO grains show good (00ℓ)-texture and also good cube-on-cube orientation relationship with $LaAlO_3$ substrate. However, STO-doped YBCO film shows an enrichment of secondary phases and STO particles on the top of the YBCO matrix as indicated via EDX analysis. As seen in Figure 7.13a, STO particles can also settle on the YBCO/LAO interface and show a good cube-on-cube orientation relationship with $LaAlO_3$ substrate, yielding in an epitaxial STO structure (Figure 7.13b). It is confirmed via an FFT pattern of STO particles on the $LaAlO_3$ interface (inset Figure 7.13b).

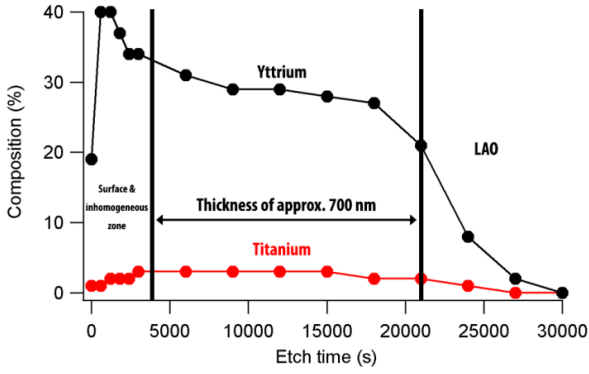

Figure 7.12. *Relative composition of Y and Ti in a 10 mol-% STO-doped YBCO film deposited on $LaAlO_3$ substrate (after pyrolysis). The composition of Y is varying due to the pores in the amorphous matrix after the pyrolysis.*

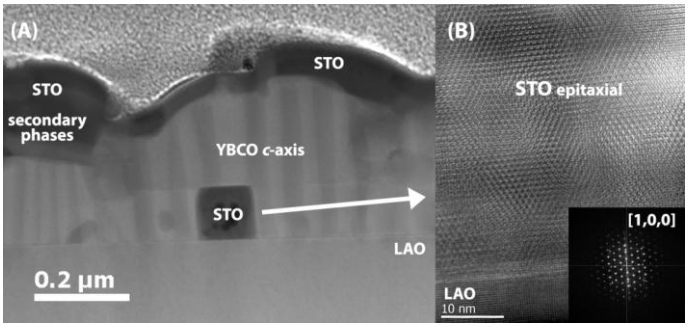

Figure 7.13. *(A) HAADF-STEM of STO-doped YBCO/$LaAlO_3$ (LAO) architecture analysis and (B) HRTEM image showing an epitaxial STO structure. (Inset shows FFT pattern of the STO structure on* $LaAlO_3$*)*

In comparison to ZrO_2 nanocomposite growth (cf. chapter 3 section 3.8), the difference between SF104 stabilized ZrO_2 nanocrystals and SF104 stabilized STO nanocrystals is that STO particles are pushed to the YBCO surface during growth while ZrO_2 nanocrystals are incorporated in the YBCO matrix leading to $BaZrO_3$ particles after the thermal process. So, this can probably be related to the smaller lattice mismatch between STO (3.91 Å) and $LaAlO_3$ (3.81 Å) compared to the lattice mismatch between $BaZrO_3$ (4.25 Å) and $LaAlO_3$ (3.81 Å). For this reason, the double metal oxide nanocrystals with higher lattice mismatch - e.g. $BaZrO_3$ (4.25 Å) and $BaHfO_3$ (4.17 Å) nanocrystals - should be introduced as the preformed nanocrystal approach. Another possibility is explained in the work of Cayado *et al.*[25] where a difference in CeO_2 nanocrystals (2 nm vs. 6 nm) appeared to have an effect on the nanocrystal behavior during the YBCO growth. The small (2 nm) nanocrystals are pushed to the YBCO surface whereas the large (6 nm) nanocrystals are incorporated in the YBCO matrix, leading to the formation of $BaCeO_3$ particles (4.38 Å). The behavior of nanocrystals during the YBCO growth, i.e. the interaction of nanocrystals at the growth interface, is influenced by several critical parameters such as the nanocrystal size and the growth rate. So, to confirm that the size of STO nanocrystals is smaller than the critical nanocrystal size (because of the pushing effect), 15 mol-% STO-doped YBCO precursor solutions were deposited on STO (3.91 Å) substrates and 50 nm CeO_2 (5.41 Å) capped sapphire (α-Al_2O_3) substrates. These as-deposited samples undergo a thermal process and the behavior of STO particles was determined via cross-sectional SEM images in Figure 7.14. Despite the absence of a lattice mismatch between STO nanocrystals and the STO substrate, the STO nanocrystals are also pushed to the YBCO surface as shown in Figure 7.14a.

Nevertheless, it is remarkable that STO nanocrystals are settled on the CeO_2 interface (Figure 7.14b) during the YBCO growth which seems that the critical nanocrystal size becomes larger when the lattice mismatch of the nanocrystals with YBCO increases. However, this accumulation effect can probably be eliminated by introducing a pure YBCO seed layer between the substrate and the YBCO nanocomposite film. This approach was introduced in the work of De Keukeleere *et al*.[26] for ZrO_2-doped TFA-YBCO nanocomposite films. Another method is to increase the YBCO film growth rate through adjusting the process parameters such as crystallization temperature, heating rate and water pressure. For this purpose, it is interesting to shift this research from $LaAlO_3$ substrate to the technical Ni-W substrate as it contains a top buffer layer of CeO_2 structure. However, it still remains a challenge to fabricate an YBCO nanocomposite film on the technical Ni-W substrate.

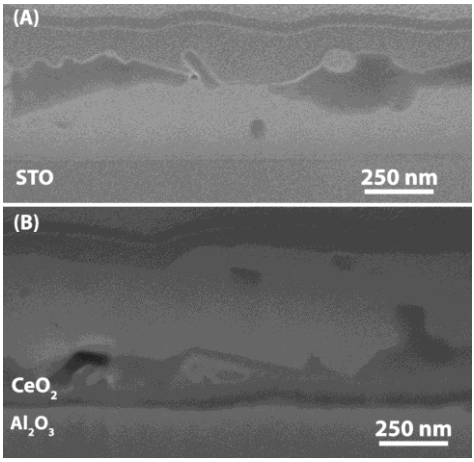

Figure 7.14. *Cross-sectional SEM image of 15 mol-% STO-doped YBCO on (A) $SrTiO_3$ substrate and (B) 50 nm CeO_2 capped sapphire substrate.*

7.8. Conclusion

In this chapter, we presented a new and successful synthesis of crystalline $SrTiO_3$ nanocrystals via the benzyl alcohol route using the more-efficient microwave-assisted solvothermal method. We examined the ability of tuning the crystal size by using different types of bimetallic Sr(II)-Ti(IV) alkoxides. All the as-synthesized $SrTiO_3$ nanocrystals have an average diameter in the range of 3 - 7 nm, yet are aggregated. Aggregate-free nanocrystal suspensions can be obtained after a post-modification treatment with oleic acid in apolar solvents (e.g. toluene). NMR studies confirm that the oleic acid is tightly bound to the nanocrystal

surface. It is also possible to transfer these STO nanocrystals to polar solvents (e.g. methanol) and YBCO precursor solutions via a ligand exchange with SF104.

However, after spin-coating this STO-doped YBCO precursor solution starting from a ME precursor on $LaAlO_3$ substrate, following a thermal treatment with an additional dwelling step, it resulted in good (00ℓ)-texture of YBCO with good critical current densities but did not exhibit improved pinning properties, indicating the STO nanocrystals are pushed to the YBCO surface or settled on the YBCO/LAO interface during the YBCO growth. It seems that the use of SF104 leads to the coagulation of nanocrystals. Moreover, it is remarkable that the single metal oxide (e.g. ZrO_2 and HfO_2) nanocrystals are embedded into the YBCO matrix due to its higher lattice mismatch while the STO nanocrystals with lower lattice mismatch are pushed to the YBCO surface on $LaAlO_3$ substrate. So, the incorporation of STO nanocrystals seems not straightforward. First, we need to evaluate the use of other ligands because the used ligand Surfactis™ leads to the coagulation of nanocrystals. Second, the size of the nanocrystals should be in the range of the critical nanocrystal size to avoid the pushing or accumulation effect. Third, the growth rate of YBCO must be increased via refining the thermal process in function of the type of nanocrystals. Fourth and last, the introduction of double metal oxide nanocrystals with higher lattice mismatch (e.g. $BaZrO_3$ and $BaHfO_3$) would probably incorporated in the YBCO matrix.

Further research will be required to synthesize agglomeration-free double metal oxide nanocrystals with higher lattice mismatch and to fabricate a homogenously distributed double metal oxide nanocrystals throughout the YBCO matrix with excellent superconducting and pinning properties. This should bring us one step closer to a benign and economical YBCO nanocomposite films in order to meet the requirements for power applications.

7.9. References

1. A. Arora, "Ceramics in nanotech revolution," *Adv. Eng. Mater.,* **6** [4] 244-47 (2004).
2. N. Setter and R. Waser, "Electroceramic materials," *Acta Mater.,* **48** [1] 151-78 (2000).
3. K. Nassau and A. Miller, "Strontium titanate: An index to the literature on properties and the growth of single crystals," *J. Cryst. Growth,* **91** [3] 373-81 (1988).
4. T. Tsurumi*, et al.*, "Artificial ferroelectricity in perovskite superlattices," *Appl. Phys. Lett.,* **85** [21] (2004).
5. M. Bibes, J. E. Villegas, and A. Barthélémy, "Ultrathin oxide films and interfaces for electronics and spintronics," *Adv. Phys.,* **60** [1] 5-84 (2011).
6. R. Muenstermann*, et al.*, "Realization of regular arrays of nanoscale resistive switching blocks in thin films of Nb-doped $SrTiO_3$," *Appl. Phys. Lett.,* **93** [2] 3110 (2008).
7. A. Kudo and Y. Miseki, "Heterogeneous photocatalyst materials for water splitting," *Chem. Soc. Rev.,* **38** [1] 253-78 (2009).
8. Q. Zhang*, et al.*, "Visible-Light-Active Plasmonic Ag-$SrTiO_3$ Nanocomposites for the Degradation of NO in Air with High Selectivity," *ACS Appl. Mater. Interfaces,* **8** [6] 4165-74 (2016).
9. G. Pollefeyt, "Chemical Solution Deposition of alternative buffer materials for coated conductors." in. Ghent University, 2015.
10. J. MacManus-Driscoll*, et al.*, "Strongly enhanced current densities in superconducting coated conductors of $YBa_2Cu_3O_{7-x}$+$BaZrO_3$," *Nat. Mater.,* **3** [7] 439-43 (2004).
11. X. Obradors*, et al.*, "Growth, nanostructure and vortex pinning in superconducting $YBa_2Cu_3O_7$ thin films based on trifluoroacetate solutions," *Supercond. Sci. Technol.,* **25** [12] 123001 (2012).
12. P. Vermeir, "Chemical solution deposition of superconducting $YBa_2Cu_3O_{7-\delta}$ layers in coated conductors." in. Ghent University, 2012.
13. J. Feys, "Digitally printed superconducting coatings and patterns." in. Ghent Unversity, 2014.
14. V. Somani and S. J. Kalita, "Synthesis and characterization of nanocrystalline Barium Strontium Titanate powder via sol-gel processing," *J. Electroceram.,* **18** [1-2] 57-65 (2007).
15. S. Zhang*, et al.*, "Formation mechanisms of $SrTiO_3$ nanoparticles under hydrothermal conditions," *Mater. Sci. Eng. B,* **110** [1] 11-17 (2004).
16. Y. Malghe, "Nanosized $SrTiO_3$ powder from oxalate precursor microwave aided synthesis and thermal characterization," *J. Therm. Anal. Calorim.,* **102** [3] 831-36 (2010).
17. M. Niederberger, G. Garnweitner, N. Pinna, and M. Antonietti, "Nonaqueous and halide-free route to crystalline $BaTiO_3$, $SrTiO_3$, and (Ba,Sr)TiO_3 nanoparticles via a mechanism involving CC bond formation," *J. Am. Chem. Soc.,* **126** [29] 9120-26 (2004).
18. W. L. Harrigan, S. E. Michaud, K. A. Lehuta, and K. R. Kittilstved, "Tunable electronic structure and surface defects in chromium-doped colloidal $SrTiO_{3-\delta}$ nanocrystals," *Chem. Mater.,* **28** [2] 430-33 (2016).

19. K. Fujinami*, et al.*, "Sub-10 nm strontium titanate nanocubes highly dispersed in non-polar organic solvents," *Nanoscale,* **2** [10] 2080-83 (2010).
20. D. Caruntu*, et al.*, "Solvothermal synthesis and controlled self-assembly of monodisperse titanium-based perovskite colloidal nanocrystals," *Nanoscale,* **7** [30] 12955-69 (2015).
21. T. Kimijima, K. Kanie, M. Nakaya, and A. Muramatsu, "Solvothermal synthesis of $SrTiO_3$ nanoparticles precisely controlled in surface crystal planes and their photocatalytic activity," *Appl. Catal. B Environ.,* **144** 462-67 (2014).
22. J. Okayama, I. Takaya, K. Nashimoto, and Y. Sugahara, "Conversion Process of Strontium–Titanium Bimetallic Methoxyethoxide Precursor into $SrTiO_3$ via Hydrolysis/Calcination," *J. Am. Chem. Soc.,* **85** [9] 2195-99 (2002).
23. J. J. Urban, W. S. Yun, Q. Gu, and H. Park, "Synthesis of single-crystalline perovskite nanorods composed of barium titanate and strontium titanate," *J. Am. Chem. Soc.,* **124** [7] 1186-87 (2002).
24. Z. Hens and J. C. Martins, "A Solution NMR Toolbox for Characterizing the Surface Chemistry of Colloidal Nanocrystals," *Chem. Mat.,* **25** [8] 1211-21 (2013).
25. P. Cayado*, et al.*, "Epitaxial $YBa_2Cu_3O_{7-x}$ nanocomposite thin films from colloidal solutions," *Supercond. Sci. Technol.,* **28** [12] 124007 (2015).
26. K. De Keukeleere*, et al.*, "Superconducting $YBa_2Cu_3O_{7-\delta}$ Nanocomposites Using Preformed ZrO_2 Nanocrystals: Growth Mechanisms and Vortex Pinning Properties," *Adv. Electr. Mater.,* **2** [10] 1600161 (2016).

Chapter eight

Conclusion and future outlook

8.1. General conclusion

Several articles are already published on how to synthesize the nanocrystals with desired properties, but a lack of acknowledge exist on how to use or incorporate these nanocrystals in the specific applications such as the formation of superconducting nanocomposite film. In the quest for the commercial breakthrough of coated conductors in power applications, we started to study and understand the missing link between the nanocrystal surface chemistry and the final nanocomposites performance. We successfully deposited the nanocomposite film via several CSD techniques and optimized the growth process of epitaxial YBCO and at the same time understood what the influence of the preformed nanocrystals and the growth of pinning-active nanocrystals in the YBCO matrix. However, additional research is necessary to optimize the final YBCO nanocomposite film with small particles in the YBCO matrix and high pinning force densities for making them applicable in high and alternating magnetic fields.

8.2. Main conclusions

8.2.1. Chemical solution deposition

In this thesis, we have shown that the chemical solution deposition technique was suitable to fabricate a superconducting film. However, the conventional preparation of TFA-YBCO precursor solution, as described by Roma *et al*., takes 72 hours to dissolve commercial YBCO powders, which is not ideal from an industrial point of view. So, we have introduced microwave heating to facilitate the dissolution of YBCO powder to an anhydrous TFA precursor. The microwave heating delivers more uniform heating during the dissolution and is very efficient compared to conventional heating by oil bath. This microwave heating reduces a preparation time by a factor of 72. This means we can fabricate a highly pure TFA-YBCO precursor solution in one hour instead of 72 hours as confirmed by a thorough analytical study. However, there are also other advantages such as the use of only a stoichiometric amount of TFAA and the removal of TFAH. This fast and reliable method can also deliver a low-fluorine (LF) content of YBCO precursor by adjusting the ratio between TFAA and propionic acid. The next step of this method is to scale up the TFA-YBCO dissolution by introducing of microwave continuous flow.

These TFA- and LF-YBCO precursor solutions are deposited on $LaAlO_3$ single substrate via CSD-based method by means of spin-coating. This method yields epitaxial YBCO thin films with J_c up to 4 MA cm^{-2} in self-field at 77 K for both

TFA- and LF-YBCO films after the thermal process. These properties are very promising and indicate that this microwave-assisted procedure can significantly improve the standard TFA-based and LF chemical solution deposition of YBCO thin films. Subsequently, we focused in this work on the LF-YBCO precursor solutions as it is more environmentally benign due to less release of toxic fluorinated compounds during the thermal process. To make this CSD method potential for low-cost long-length industrial production, we have shown in this work the possibility to adjust the YBCO inks in order to deposit YBCO inks on $LaAlO_3$ substrates using DOD piezoelectric ink-jet printing, leading to J_c values up to 3.0 MA cm^{-2} (self-field, 77 K) with a thickness of 500 nm after multideposition and one thermal process.

Nevertheless, these results from $LaAlO_3$ substrates should be transferred to industrial metallic Ni5W substrates for the commercial market. Yet, only a maximum J_c of 0.2 MA cm^{-2} can be obtained for a 450 nm thick YBCO film deposited on a Ni5W substrate via dip-coating technique. Nevertheless, compared to obtained results of 1.8-2.5 MA cm^{-1} for 2-3 times 500 nm deposited YBCO layer after thermal reel-to-reel process at d-Nano, there is still room for further optimization of the YBCO crystallization process at a lab scale.

8.2.2. Single metal oxide nanocrystals

In our research group, we were able to synthesis the single metal oxide ZrO_2 and HfO_2 nanocrystals via heating-up and microwave-assisted solvothermal synthesis to apply them as artificial pinning centers in high-temperature superconductors. However, in order to apply these synthesized nanocrystals stabilized with hydrophobic ligands in nonpolar solvent, a transfer to the more polar YBCO environment was necessary through a ligand exchange.

In this work, small crystalline cubic ZrO_2 nanocrystals with diameters of 3-5 nm were stabilized by a steric polar ligand (Copolymer and Surfactis™) or short carboxylates (tartaric and citric acid) in low-fluorine YBCO precursor solutions. From the resulting suspension, by a single coating step, we synthesized superconducting ZrO_2-doped YBCO nanocomposite films. During this process, we observed that nanocrystals stabilized by short carboxylate ligands resulted in poorly superconducting nanocomposites while the steric polar ligands lead to excellent superconductors. But, the use of Surfactis™ yielded in the coagulation of ZrO_2 nanocrystals during YBCO growth, resulting in the absence of pinning properties due to their large diameters. So, given the counter-intuitive relation between the nanocrystal surface chemistry and the final nanocomposites

performance, we expected that the use of ligands is crucial in order to obtain a good superconducting nanocomposite film with the ability to pin the vortices.

It is commonly known in the literature that a higher loading of nanocrystals in the YBCO matrix would lead to poor epitaxial growth properties due to nanocrystal behavior during the thermal process. To elucidate this effect, quench study was performed and investigated via XRD. This has shown that the addition of the ZrO_2 nanocrystals results in a delay in YBCO nucleation and growth because of the nanocrystal reactivity with Ba^{2+} between temperatures of 600 and 700 °C, leading to the formation of $BaZrO_3$ particles. This was observed by the less-pronounced BaF_2 (111) reflection on XRD patterns, indicating that less BaF_2 was present during the YBCO nucleation. For this reason, we have introduced an additional dwelling step to improve the YBCO nuclei density and to avoid the coarsening of nanocrystals. In contrast to most literature data, this extra dwelling step does not improve the distribution as well as the miniaturization of nanocrystals in the YBCO matrix, but does result in the improvement of superconducting properties.

So, it is clear that the critical current densities are increased by the 5 mol-% nanocrystal addition. This approach results in a high maximum pinning force density of 5.5 GN m^{-3}, which more than tripled compared to undoped YBCO thin films. The J_c in a moderate-to-high magnetic field is increased, and its anisotropy is lowered by the addition of nanocrystals. However, by higher loading of the nanocrystals in the YBCO matrix, it results in poorer superconducting properties as confirmed via transport measurements and is in line with the literature. It is explained to the more Ba^{2+} consumption of single metal oxide nanocrystals during the YBCO growth. This could cause a slow YBCO growth and Ba^{2+} deficiency in the YBCO matrix, leading to less epitaxial YBCO. Nevertheless, it is remarkable that a higher addition of nanocrystals (with a limited amount) can lead to better pinning properties due to the presence of more artificial pinning centers in the YBCO matrix.

Two different monoclinic HfO_2 nanocrystals were synthesized via microwave-assisted and heating-up synthesis and tested in the YBCO matrix in this work. HU-based synthesis delivers very small nanorods with a nanocrystal size of 2.6 nm in diameter and 8.0 nm in length, while MW-based synthesis yields more spherical nanocrystals with a nanocrystal size diameter of 6-8 nm. HU-based HfO_2 nanocrystals remain small (size of 5-20 nm) while MW-based HfO_2 nanocrystals have a tendency to coarsen in the YBCO matrix leading to a size of 15-30 nm. Small particles tended to promote a region of short intergrowths surrounding the particles, yielding in an increase of microstrain and thus pinning

properties. While the large particles (>25 nm) in the YBCO matrix resulted in more formation of undesired line defects such as stacking faults which can degrade J_c values of the YBCO nanocomposite films. So, in this work, we have shown that the nanocrystal size and its distribution are the key parameters to better control of the intergrowths and line defects. We can conclude that the results of HU-HfO_2-based nanocrystals incorporated in the YBCO matrix are promising because the $BaHfO_3$ particle size are in the range of 5-20 nm and results in the champion value of pinning force density (F_p^{max} = 17.11 GN m^{-3}**)** as far in this work. For this reason, it is attractive to transfer these results from spin-coated to ink-jet printing method. So, we have also shown it is possible to adjust the printing parameters depending on the addition of nanocrystals in order to deposit HfO_2-doped YBCO inks on $LaAlO_3$ substrates using a DOD piezoelectric ink-jet printing system. This ink-jet printing method leads to self-field J_c up to 3.0 MA cm^{-2} at 77 K with an increase of pinning force density with a factor of more than 5 due to the combined effect of $BaHfO_3$ particles in size of approximately 5-20 nm and a larger density of twin boundaries.

So, the preformed nanocrystal approach can be successfully applied for the CSD based LF-YBCO method, yet additional research is required to fully understand the influence of the higher loading of nanocrystals into the YBCO matrix and optimize the final YBCO nanocomposite films onto industrial metallic substrates. This should bring us one step closer to the effective and economically efficient application of high-temperature superconductors in high and alternating magnetic field applications, relevant in alternative energy generation.

8.2.3. Double metal oxide nanocrystals

Due to the reactivity of single metal oxide nanocrystals, these nanocrystals will affect the YBCO growth and coarsen to large particles in the YBCO matrix. The introduction of double metal oxide would offer a solution to tackle these disadvantages of single metal oxide nanocrystals. In this work, we are able to synthesize small crystalline $SrTiO_3$ nanocrystals via microwave-assisted synthesis using bimetallic Sr-Ti alkoxide. These as-synthesized nanocrystals were stabilized with oleic acid to ensure the colloidal stability in nonpolar solvent and transfer to more polar YBCO precursor solution via a ligand exchange with Surfactis™. Unfortunately, the use of Surfactis™ can lead to the coagulation of nanocrystals as discussed previously.

Nevertheless, $SrTiO_3$-doped YBCO precursor solution was spin-coated on $LaAlO_3$ substrate and thermal treated, resulting in good (00ℓ) YBCO texture. It also resulted to good J_c but shows no ability to pin the vortices. It is due to the

pushing or accumulation effect of $SrTiO_3$ nanocrystals during the YBCO growth. So, the incorporation of double metal oxide nanocrystals seems not straightforward. First, we need to take care of the use of different ligands because the used ligand Surfactis™ leads to the coagulation of nanocrystals. Second, the size of nanocrystals should be in the range of the critical nanocrystal size to avoid the pushing or accumulation effect. Third and last, the growth rate of YBCO must be increased via refining the thermal process in function of type nanocrystals. Further research will be required to obtain a homogenously distributed double metal oxide nanocrystals throughout the YBCO matrix with excellent superconducting and pinning properties.

8.3. Future outlook

Within this thesis, we have proven that it is possible to stabilize the single and double metal oxide nanocrystals in a low-fluorine YBCO precursor solution. The incorporation of single metal oxide nanocrystals lead to improved superconducting properties at low magnetic field. However, we believe that the introduction of the double metal oxide nanocrystals can improve the final properties of YBCO nanocomposite film. Due to no reactivity of double metal oxide nannocrystals, the coarsening of these nanocrystals can be avoided if they remain agglomerate-free. This should lead to small pinning centers in the range of a few nm, enhancing the ability to pin vortices more efficiently. Additional research is necessary to unravel the surface chemistry of double metal oxide nanocrystals because Surfactis™ cannot act as an ideal ligand during the fabrication of YBCO nanocomposite film. At the moment, the choice of stabilizing ligand is a very essential step and is the missing link between the nanocrystal synthesis and the nanocomposite formation. The opportunity of nanocrystal size tunability during the microwave-assisted synthesis may lead to an additional advantage in controlling the intergrowths and line defects. A more elaborated study is desired to understand the size effects on the pinning properties and to improve their application in the magnetic field.

Due to the different position of maximum pinning force density values in the magnetic field for several nanocrystal-doped nanocomposite films in this work, we were strongly convinced that the pinning properties could be improved by combining the addition of preformed nanocrystals and the formation of short Y124 intergrowths around the particles. This combination should lead to an enhancement of pinning properties. At the moment, it is also necessary to understand the complex relationship between vortex pinning properties and microstructural defects.

The next step is to simplify the cumbersome transfer of YBCO nanocomposite film starting from preformed nanocrystals from single crystal substrate to metallic tape. On single crystal substrate, no orientation variations of YBCO are notable whereas orientation of YBCO on the metallic tape is attributed to the granularity of underlying template. This transfer is still in early stage and is still unclear what the effects of nanocrystals are on the granularity and the orientation distribution of YBCO structure. Here, additional research is required to fully understand the influence of the nanocrystal addition for optimizing both YBCO precursor solution and reel-to-reel process. This brings us one step closer to the implementation of economically efficient coated conductors in high and alternating magnetic field applications.

Appendix A

Supplementary material

A1. Supplementary material of Chapter two

A1.1. NMR measurements

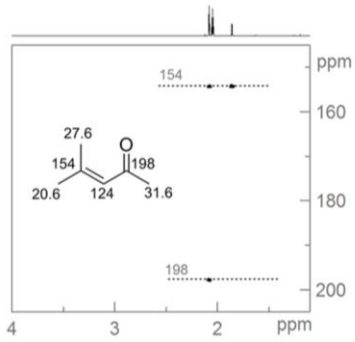

Figure A2.1. *HMBC spectrum of the degradation products of acetone refluxed with TFA at 60 °C for 3 days without YBCO powder, dissolved in acetone-d_6. The carbonyl peak clearly correlates to the proton resonance at 2.16 ppm (resonance d) while the quaternary alkene resonance correlates to resonances a and b (1.88 and 2.13 ppm).*

A1.2. Mass spectrometry analysis related to gas-chromatography

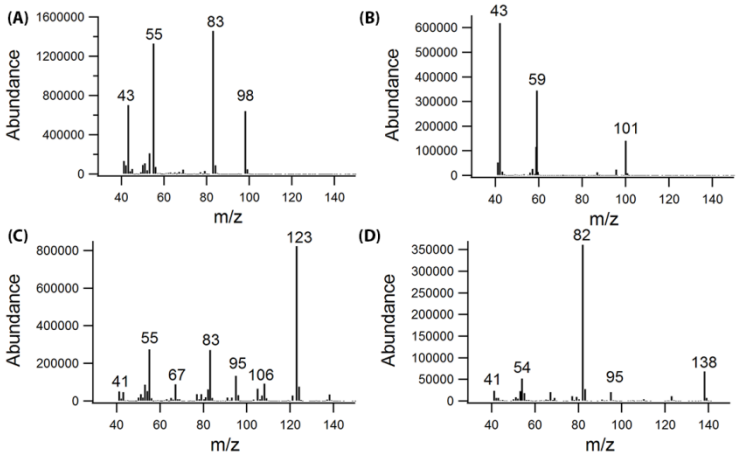

Figure A2.2. *MS data corresponding to the GC signal eluting at a retention time of (A) 3.827 min - indicating that this signal belongs to mesityl oxide -, (B) 4.301 min - indicating that this signal belongs to diacetone alcohol -, (C) 8.731 min - indicating that this signal belongs to phorone - and (D) 8.9 min - indicating that this signal belongs to isophorone -.*

A1.3. XRD patterns of TFA- and LF-YBCO

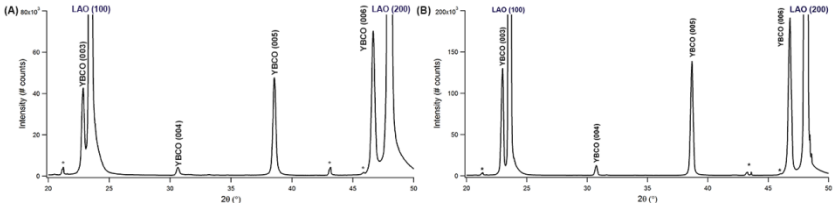

Figure A2.3. *The XRD diffraction* θ-2θ *of a fully grown (A) TFA-YBCO and (B) LF-YBCO thin film on a $LaAlO_3$ substrate. (LAO and YBCO reflections by the secondary radiation of x-ray tube are marked with an asterisk.)*

A1.4. Characterization of undoped YBCO obtained via single ink-jet printing deposition

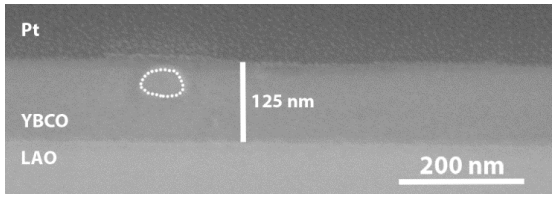

Figure A2.4. *Cross-sectional SEM image of one single ink-jet printing of YBCO layer after full thermal process. Secondary phases are marked with dotted lines.*

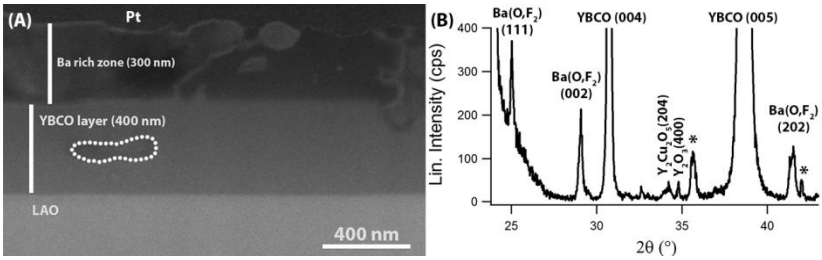

Figure A2.5. *(A) Cross-sectional SEM view and corresponding XRD spectrum (B) of YBCO layer obtained via 5 times of multi-deposition.*

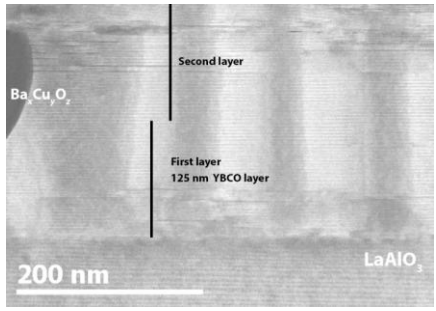

Figure A2.6. *TEM image of multi-deposited YBCO layer with one final thermal processing shows absence of distinct layers.*

A1.5. XRD patterns of YBCO on Ni5W tape

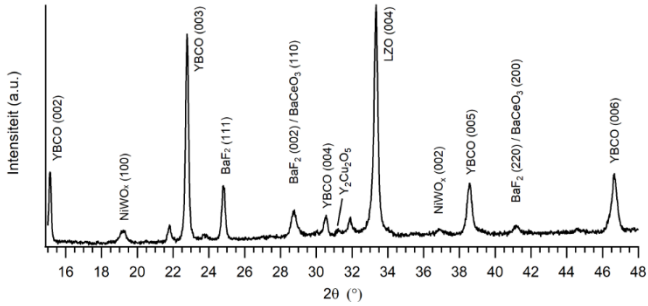

Figure A2.7. *The XRD diffraction* θ-2θ *of YBCO layer on Ni5W tape after the same thermal processing of $LaAlO_3$ substrate. (Heating rate with 5 K min-1 to 795 °C under wet 100 ppm O_2 in N_2 atmosphere with a dew point of 23 °C.*

A2. Supplementary material of Chapter three

A2.1. Rietveld quantitative analysis.

The samples were measured in a Bragg-Brentano geometry over an angular range of $2\theta = 20 - 65°$ (Cu-K_α radiation) using a 0.02° step size and 1 s/step counting time. Topas Academic V4.1 software was used for Rietveld quantitative analysis to calculate the crystalline fraction of ZrO_2 nanocrystals. By adding 10 wt% ZnO to the dried nanocrystals powders, weight fractions for amorphous and other phases in the specimen could be calculated using the composition and the cell parameters of the cubic ZrO_2 phases. The results were corrected with additional TGA of the same powders. The weight loss determined by TGA corresponds to the amount of organic fraction adsorbed to the precipitated powders.

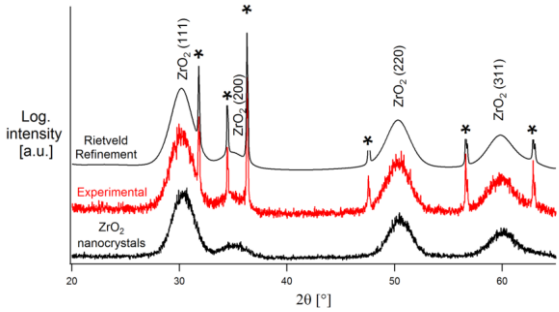

Figure A3.1. *Experimental XRD results of ZrO_2 nanocrystal powders and according Rietveld refinement. (ZnO internal standard phases are marked with an asterisk.)*

A2.2. NMR analysis of the copolymer stabilized nanocrystals

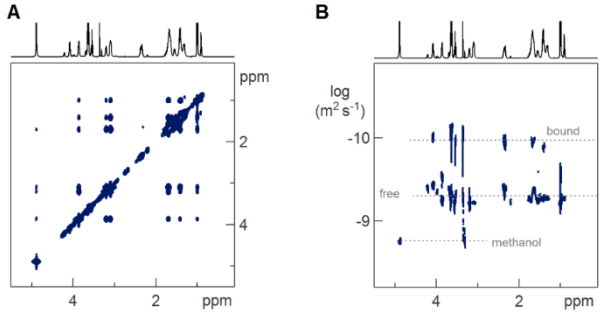

Figure A3.2. *(A) NOESY spectrum of zirconia nanocrystals stabilized with the steric dispersant in methanol-d_4. The negative cross peaks (same dark blue color as the diagonal) indicate interaction of the ligand with the nanocrystal surface. (B) DOSY spectrum of the same dispersion: the slowly diffusion coefficient indicates that the ligands are tightly bounded with the nanocrystal surface while the higher diffusion coefficient indicates the free ligands in suspension.*

A2.3. NMR analysis of the Surfactis™ stabilized nanocrystals

In the 1D spectrum (Figure A3.3a) tri-*n*-octylphosphine oxide is recognized by resonances between 0.7 and 2 ppm. The Surfactis™ resonances are in the range 3.3-4 ppm and P-H resonances are also observed. The latter is not strange as in the reference spectrum of Surfactis™ the compound H_3PO_3 was detected. Also in the phosphor spectrum of the ZrO_2 dispersion (Figure A3.3b) we note resonance d and e which probably belong to similar compounds. Indeed, both the P-H resonances and resonance d and e are related as seem in the HMBC (not shown here). Otherwise, the P peak of Surfactis™ (c) is retrieved at 18 ppm and two other phosphorus resonances (a and b) belong to stripped ligand, which were originally present. It is not yet clear which molecules those are. In DOSY (not shown here) there is still a fraction of tightly bound ligand for the CH3 resonance of "tri-*n*-octylphosphine oxide" indicating that not all original ligands have desorbed. The diffusion coefficient of 91 $\mu m^2\ s^{-1}$ can be converted to a diameter of 8.1 nm. This is somewhat larger than the original solvodynamic size in toluene of 5.9 nm. This can however be explained by the longer chain of Surfactis™ compared to tri-n-octylphosphine oxide. (23 versus 8 atoms long chain). As expected, the diffusion coefficient obtained from the CH2 resonances of Surfactis™ is exactly the same, confirming its strong binding. Zooming in on the resonances of Surfactis™ (Figure A3.3c), we can identify the CH2's at the beginning and end of the chain. The rest is in between. Also the CH3 resonances can be recognized. From the fine structure and NOESY spectrum (not shown here) we infer that this is not interacting with the surface. However, under those resonances, broader contributions are present which belong to tightly bound Surfactis™.

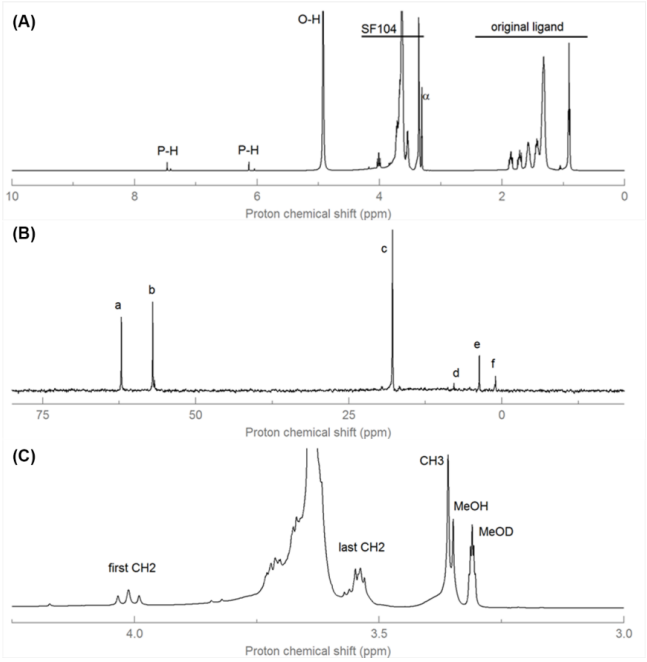

Figure A3.3. *(A) 1D ^{1}H spectrum and (B) ^{31}P spectrum of ZrO_2 nanocrystals stabilized with Surfactis™ (SF104) in MeOD-d_4, with (C) a zoom on SF104 resonances.*

A2.4. TEM of nanocrystals after ligand exchange/phase transfer

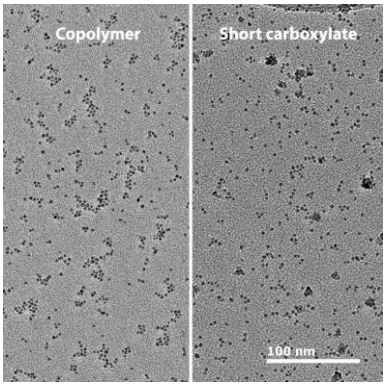

Figure A3.4. *TEM image of copolymer and short carboxylate stabilized nanocrystals in methanol, indicating that the short carboxylate stabilized nanocrystals exhibit slightly more agglomerations.*

A2.5. Thermogravimetric analysis measurements.

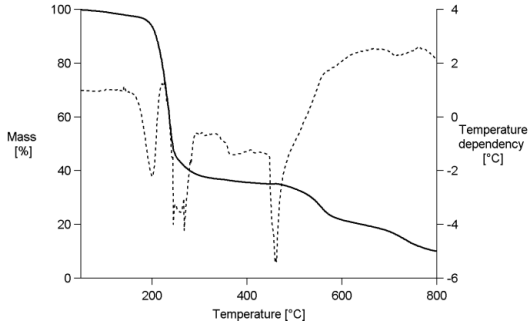

Figure A3.5: *TGA-DTA record of Surfactis™ with heating ramp of 10 K/min and air atmosphere.*

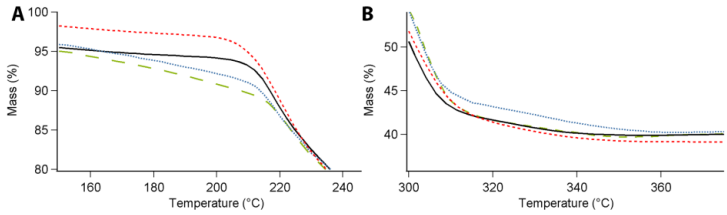

Figure A3.6. *Detailed TGA curves in the range of (A) 150-250 °C and (B) 300-375 °C of LF-YBCO nancomposite precursor with Copolymer (blue dotted line), with Surfactis™(red dotted line) and with citric acid (green dashed line) or undoped LF-YBCO precusor (black line).*

A2.6. X-ray photoelectron measurements.

XPS measurements were recorded on a Surface Science Instruments S-Probe spectrometer with monochromated Al radiation (1486 eV). The flood gun was set to 3 eV. A nickel grid was placed 3 mm above the samples in order to suppress charging of the samples. Experimental data were processed using the software package CasaXPS (Casa Software Ltd., UK). An area of $3 \times 3\ mm^2$ was sputtered for 500 s (steric dispersant capped ZrO_2 doped YBCO film) or 200 s (citric capped ZrO_2 doped YBCO film) with an Ar^+ ion gun (4 keV). After each consecutive sputter cycle an area of $250 \times 1000\ \mu m^2$ was analysed. Regions for C 1s, Y 3d, Zr 3p-3p1/2, La 4p1/2, La 3d5/2 and O 1s peaks were registered.

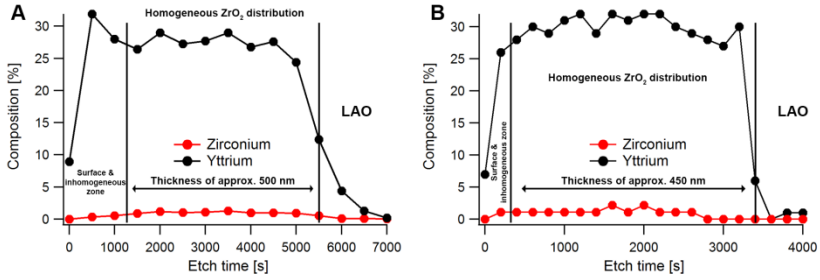

Figure A3.7. *Relative composition of Y and Zr in a 5 mol-% (A) steric dispersant capped and (B) citric acid capped ZrO_2 nanocrystal doped YBCO film deposited on LAO (after pyrolysis). The composition of Y is varying due to the pores in the amorphous matrix after the pyrolysis. So, the distribution of ZrO_2 nanocrystals is homogenous throughout the layer.*

A3. Supplementary material of Chapter four

A3.1. Time-of-Flight Secondary ion mass spectrometry

The distribution of ZrO_2 nanocrystals in amorphous $Ba_{1-x}Y_xF_{2+x}$ (matrix after pyrolysis and $YBa_2Cu_3O_7$ (YBCO) matrix after thermal process was determined via Time-of-Flight (TOF) Secondary Ion Mass Spectrometry (SIMS) using a TOF-SIMS IV from ION-TOF GmbH, equipped with a 25 kV Bi LMIG and 10 kV C_{60}^{++} sputter source. During the sputtering, the use of C_{60}^{++} clusters with a sputter current of 0.8-2.0 nA was introduced to identify the location of the nanocrystal. The raster size of the sputter beam was set at 300x300 µm2. Bi^+-ions were used as primary ions with a pulsed target current between 0.2 and 0.5 pA. The region of interest of the primary ion beam was set at the total surface of the raster of the sputter beam. The TOF analyzer was set in positive mode. SIMS measurements were finished when the La^+ peak from $LaAlO_3$ substrate was detected during the sputtering.

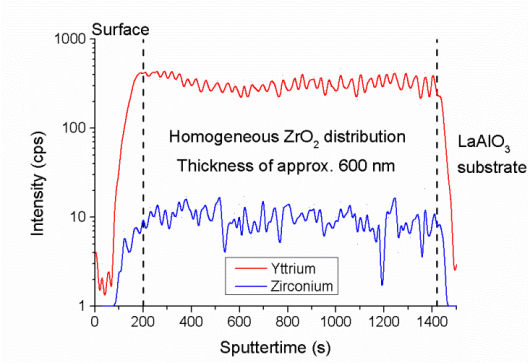

Figure A4.1. *The intensities of yttrium and zirconica in pyrolyzed matrix during SIMS analysis of ZrO_2-doped YBCO films.*

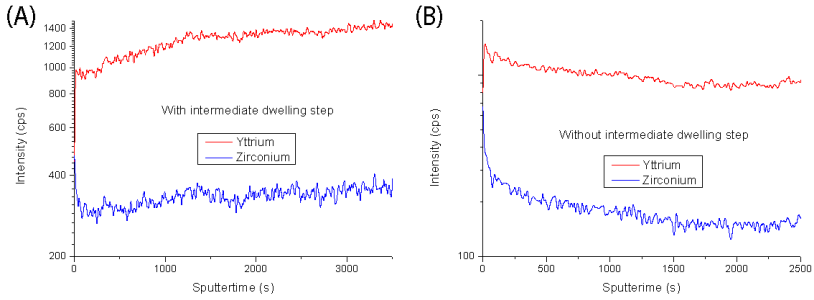

Figure A4.2. *The intensities of yttrium and zirconica in YBCO matrix during SIMS analysis of ZrO_2-doped YBCO films after the thermal process with (A) and without (B) the additional dwelling step.*

A3.2. Fitted curve of $BaZrO_3$ particles in the YBCO matrix

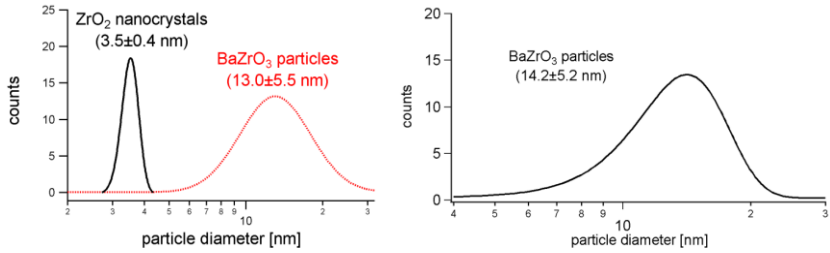

Figure A4.3. *Fitted curve of histogram of ZrO_2 nanocrystals after heating-up synthesis and $BaZrO_3$ particles in a YBCO matrix after thermal treatment with (left) or (right) without the additional dwelling step. The values of $BaZrO_3$ particles are estimated from cross-sectional images. The data was fitted using a Gaussian mode.*

A3.3. SEM images after the thermal process with or without an intermediate dwelling step.

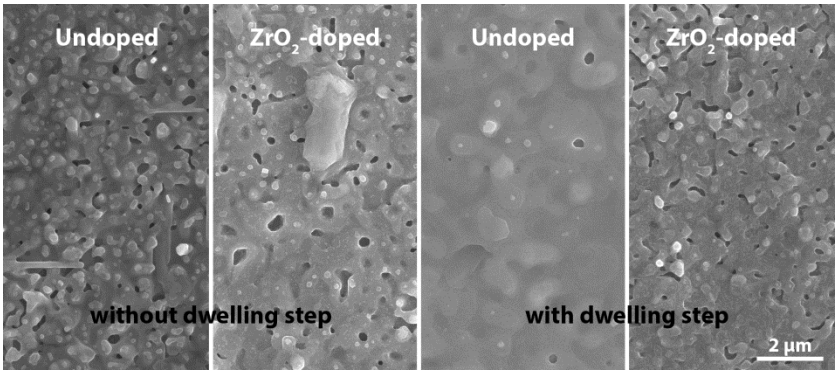

Figure A4.4. *SEM images of undoped and ZrO_2-doped YBCO films after thermal process with or without an additional dwelling step.*

A3.4. YBCO (103) pole figure scans.

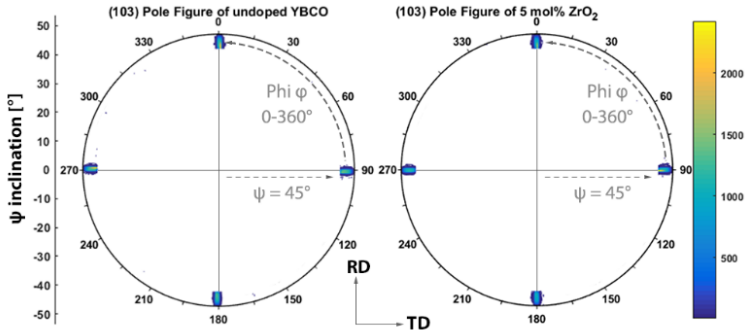

Figure A4.5. *YBCO (103) pole figure of undoped and 5 mol-% ZrO_2 nanocrystals doped YBCO show fourfold symmetry. The sample reference system was the (001) $LaAlO_3$ substrate. The psi (ψ) value was set on 45° due to the calculated angle between YBCO (103) and YBCO (001).*

A3.5. XRD ϕ-scan.

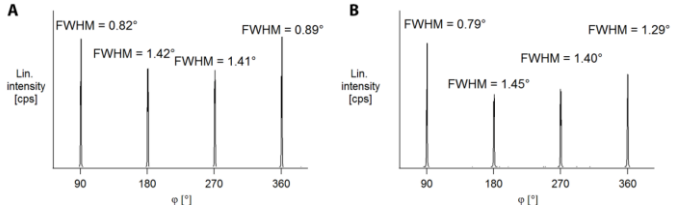

Figure A4.6: *XRD φ scans of YBCO (103) (ψ = 45.0°) extracted from Figure A4.5 indicating good in-plane alignment for (A) undoped YBCO and (B) 5 mol-% ZrO_2 nanocrystal added YBCO. The FWHM is around 0.8° for both samples, the smaller and broader peaks are due to slight misalignment of the sample.*

A3.6. Rocking (ω) curves.

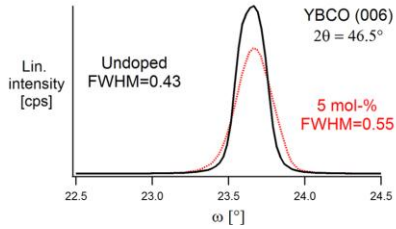

Figure A4.7. *Rocking curves of undoped YBCO (full black line) and 5 mol-% ZrO_2 nanocrystals doped YBCO (dotted red line). The most part of FWHM value of undoped is due to the twinning of the LAO substrates while a slight increase in FWHM of the nanocomposite is most likely due to the enhanced strain around the $BaZrO_3$ particles.*

A3.7. Fast Fourier Transformation (FFT) pattern.

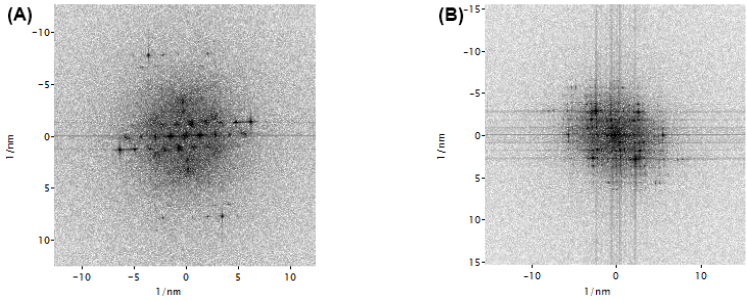

Figure A4.8. *FFT pattern of (A) $Ba_xCu_yO_z$ particles and (B) $BaZrO_3$ particles in the YBCO matrix, indicating a random orientation of the particles.*

A4. Supplementary material of Chapter five

A4.1. (*h*00) bright-field TEM

Figure A5.1. *(h00) bright-field TEM showing twin boundaries of undoped YBCO layer*

A4.2. Angular dependency of various mol-% ZrO_2-doped YBCO films

The line broadening effects were analyzed using the Williamson-Hall (WH) approach. The Kα2 contribution was stripped out using the Rachinger procedure incorporated in the EVA2.0 software. According to the WH approach, the line broadening is caused by the finite size of coherently scattering domains called volume averaged grain size $L_{<V>}$ and microstrain ε. Assuming that both give Lorenzian contributions to line broadening, the broadening effect is described as $\beta^* = 1/L_{<V>}+2\varepsilon d^*$, where $\beta^* = 2\cos\theta\times\beta\lambda$ is the reciprocal line breadth and $d^* = 2\sin\theta/\lambda$ is the reciprocal d spacing (λ is the wavelength). The microstrain values are listed in Table A5.1, indicating the microstrain is linear increased with increasing nanocrystal concentration. From the angular dependence transport J_c measurements, we observe a similar behavior as the peak at H||*ab* ($\Theta = 90°$) is broaden because of the addition of nanocrystals and is typical attributed to the effective pinning of stacking faults in YBCO matrix.

Table A5.1 *microstrain ε calculated according to the WH approach for various mol-% ZrO_2-doped YBCO films.*

ZrO_2 nanocrystals	ε_{00L}, %
0 mol-%	0.058
5 mol-%	0.084
7.5 mol-%	0.114
10 mol-%	0.141

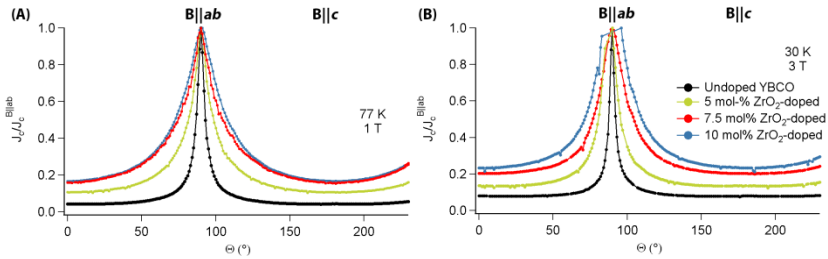

Figure A5.2 *Angular dependence of the critical current density, obtained at (A) 1 T and 77 K and (B) 3 T and 30 K for various mol-% ZrO_2-doped YBCO films.*

A5. Supplementary material of chapter six

A5.1. DLS measurements of HfO_2 nanocrystals in various polar solvents

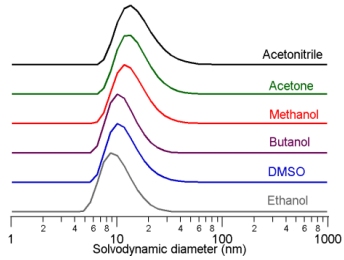

Figure A6.1. *DLS measurements of HfO_2 nanocrystals stabilized with TFA and glutamine in various polar solvents.*

A5.2. NMR measurements of HfO_2 nanocrystals

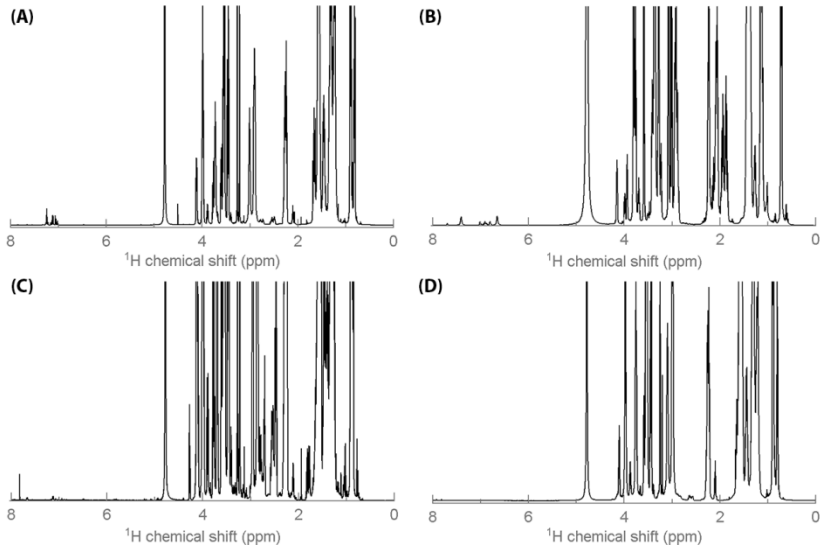

Figure A6.2. *1D ^{1}H NMR spectrum of (A) HU-based HfO_2 nanocrystals, (B) MW-based HfO_2 nanocrystals, (C) the steric dispersant copolymer and (D) copolymer stabilized ZrO_2 nanocrystals.*

A5.3. Characterization of HfO_2-doped YBCO film

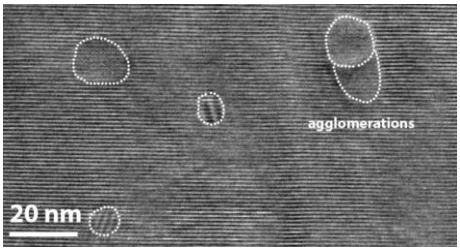

Figure A6.3. *TEM image showing a rare agglomeration of $BaHfO_3$ particles in the YBCO matrix.*

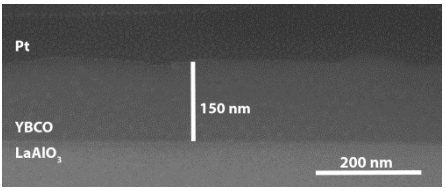

Figure 6.4. *FIB cross-sectional SEM image of one single deposition of 5 mol-% HfO_2-doped YBCO film after full thermal process.*

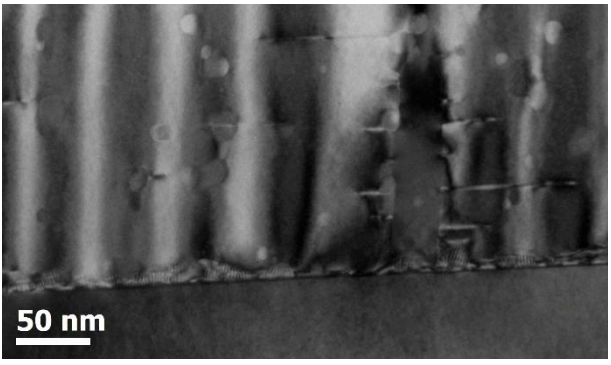

Figure 6.5. *(h00) bright-field TEM showing twin boundaries of HfO_2-doped YBCO layer. The density of twin boundaries nearly doubled by the addition of HfO_2 nanocrystals.*

Appendix B

Experimental methodology

B1. Characterization of the YBCO precursor solution

In this work, the metal ion concentration and stoichiometry of Y:Ba:Cu of YBCO precursor solution were verified by inductively coupled plasma-optical emission spectrometry (ICP-OES) analysis (SPECTRO Genesis). The density of the inks was analyzed using a 10 mL glass pycnometer (Duran) and the viscosity with a Brookfield DV-E viscometer (25 °C and 100 rpm). The surface tension of the inks and their contact angles on $LaAlO_3$ substrates were characterized with a Drop Shape Analyzer DSA30 (Krüss GmbH). The contact angles were measured using 0.5 µL droplets. The water content was determined by the Karl-Fischer method. To understand the thermal decomposition of the YBCO precursor solution, thermogravimetrical analysis (TGA) and differential thermal analysis (DTA) were used with a Netzsch Model STA 449 F3 Jupiter system with the heating rate of 10 °C/min under air atmosphere.

B2. Characterization of the solution without YBCO powder

Attenuated Total Reflection-Fourier Transform Infrared Spectroscopy (ATR-FTIR) were performed on a Perkin-Elmer FT-IR spectrometer spectrum 1000, equipped with a HATR module, Nuclear Magnetic Resonance (NMR) equipment and gas chromatography-mass spectrometry (GC-MS) device are used to analyze the by-products after the synthesis. GC-MS was conducted on an Agilent HP 6890 series with a HP 5972A single quadrupole mass spectrometer. 1 µL of sample was injected into a split/splitless liner with single taper, heated at 250 °C using splitless injection. Separation was performed using a Restek Rxi-5Sil MS column (30 meters long x 0.25 mm internal diameter x 0.25 µm film thickness) and helium as carrier gas at a constant flow rate of 1 mL min^{-1}. The oven was programmed as followed: starting at 40 °C where it was held for 2 minutes, followed by a gradient of 10 °C min^{-1} to 320 °C holding this temperature for 5 minutes. The transferline to the MS was held at 300 °C. The MS was set to scan for m/z ratios between 41 and 400, after a 3-minute solvent delay. NMR toolbox is described in section B7.

B3. Nanocrystal characterization

The dried metal oxide nanocrystal powders were characterized via X-ray diffraction (XRD) at a Thermo Scientific ARL X'tra X-ray diffractometer (Cu-K_α radiation) with Rietveld quantitative refinement (described in section A2.1 in Appendix A) to determine the crystal phase and its crystallinity degree. Dynamic light scattering analysis was performed on a Malvern Nano ZS in backscattering mode (173°). High-resolution TEM images were taken on a JEOL JEM-2200FS TEM equipped with an objective lens C_s corrector. The samples were prepared by dipping a 300-mesh holey carbon copper grid into the purified nanocrystal suspensions. To evaluate the temperature dependency of the decomposition of pure ligands and ligands capped nanocrystals in the LF-YBCO precursor during the pyrolysis, TGA analysis with DTA

were carried out using a Netzsch Model STA 449 F3 Jupiter. X-ray photoelectron spectroscopy (XPS) measurements were carried out using an S-Probe monochromatized spectrometer from Surface Science Instruments with an Al-K_α X-ray monochromatic source (1486.6 eV, more details in section A2.6 in Appendix A).

B4. Texture characterization

Texture and phase composition of the YBCO thin films were characterized by means of XRD on a Bruker D8 diffractometer (Cu-K_α). θ-2θ scans were measured between 2θ = 25° and 46° with a step width of 0.05° to analyse the purity of the thin films. In addition, θ-2θ with a finer step width of 0.02° and rocking (ω) curve scans on the YBCO (006) (2θ = 46.5°) peak were performed. The full width at half maximum (FWHM) values are determined by fitting a Gaussian to the experimental data. The (biaxial) crystal growth direction was determined by pole figure scans for YBCO (103) (2θ = 32.6°, Ψ = 45.0°).

B5. Microstructural characterization

Structural properties were characterized with an FEI Nova 600 Nanolab Dual Beam FIB-SEM, a JEOL JEM 2200-FS TEM at Ghent University and FEI Titan QuantEM microscope at University of Antwerp. For the TEM measurements, a cross-sectional lamella was cut via the FIB *in-situ* lift out procedure with an Omniprobe™ extraction needle and top cleaning. TEM has accelerating voltages of 60-300 kV which leads to an atomic resolution because the electrons exhibit a very small wavelength. It makes a very powerful technique for obtaining crystallographic information of the samples. In this work, two different TEM instruments were used. The TEM analysis of ZrO_2-doped YBCO film was investigated in-house with JEOL 2200FS TEM operating at 200 kV with a post-sample spherical aberration correction, whereas TEM analysis of HfO_2-doped YBCO films was investigated at University of Antwerp (EMAT) with FEI Titan QuantEM probe spherical aberration corrected microscope, allowing an extremely high resolution in STEM-mode. The Titan microscope was operated at 300 kV.

Several TEM-modes were used throughout this work to obtain a specific amount of information. Crystallographic information can be obtained by high-resolution TEM in combination with selected area electron diffraction patterns. Bright-field TEM was investigated to see the defects present in the matrix. Compositional information was observed via high-angle annular dark field (HAADF) STEM. This HAADF-STEM technique is highly sensitive to variations in the atomic number of atoms in the sample (Z-contrast images). Foreign phases in the YBCO matrix were determined via energy dispersive X-ray spectroscopy in HAADF-STEM. The image processing software *ImageJ* was used for the statistical measurement of nanocrystals in cross-sectional areas.

B6. Electrical characterization

The self-field critical current density J_c was evaluated inductively with a THEVA Cryoscan at 77 K with a voltage criterion of 50 µV. The field dependence of J_c was determined in magnetization and transport measurements at University of Turku, IFW Dresden and Karlsruhe Institute of Technology, which means that several methods to determine J_c values are used in this work. The obtained J_c values must be carefully compared with the other J_c values obtained by different methods.

University of Turku

The magnetic properties were measured with a Quantum Design Physical Property Measurement System (PPMS). The transition temperature was measured with an AC-magnetization scan with a 0.1 mT drive field in a zero applied field. The frequency of the drive was 113 Hz to minimize the distraction from the electricity grid. The critical temperature T_c was defined as the onset temperature of the in-phase component of the AC-magnetization at zero-field in the range of 10-100 K. The width of the magnetic transition was calculated as $\Delta T_c = T_{c,90} - T_{c,10}$. The DC-measurement was used to determine the critical current of the sample at constant temperature as a function of the applied magnetic field perpendicular to the direction of current flow. The J_c's of all samples are calculated using the Bean critical state model from the opening of the hysteresis loop up to 8 T.

For transport measurement, the critical current was measured using the horizontal rotator probe of the PPMS. In the measurements the voltage drop in a four-wire configuration is monitored as a function of the applied current. To protect the sample, the current is cut down as a critical voltage limit was exceeded. The Jc measurements were done in an applied field up to 9 T and the sample is rotated in maximum Lorentz force configuration, i.e. the current stripe is always perpendicular to the external field. The voltage limit for the critical current was 215 µV cm^{-1}. However, the high value does not change the shape of the angular dependencies and it is used to deal with the noise due to the measurement setup. Resistive measurements to obtain the critical temperature were measured in the function of temperature between 120 and 40 K using a 10 µA current. The probing current was kept as low as possible not to affect the measured resistivity curve. The samples were patterned using wet chemical etching.

IFW Dresden

Transport critical current densities were measured in maximum Lorentz force configuration on laser-cut bridges (l = 800 µm, w ~ 15-20 µm, E_c = 1 µV cm^{-1}) at magnetic fields up to 9 T in a Quantum Design Physical Property Measurements System. The irreversibility field H_{irr} was estimated with constant J_c criterion (50 A cm^{-}

^{2}) and cross-checked by the condition $n \rightarrow 1$ for $H \rightarrow H_{irr}$ (n being the exponent in $E(J) \sim J^{n}$ near J_c). Angular-dependent $J_c(B,\Theta)$ measurements were performed by rotating the sample with steps of 2° between 0° and 240° (with $B||c_{YBCO}$ at $\Theta = 0°$ and $B||ab$ at 90°) at 65 K/1, 3 5, 7 and 9 T, 77 K/1 T and 30 K/3 T. The magnetic field dependence of J_c in the maximum Lorentz force configuration was measured with logarithm steps of the increased magnetic field to see the effect of preformed nanocrystals more in details between 0 and 2 T.

Karlsruhe Institute of Technology

Transport critical current measurements were carried out in a 14 T Quantum Design Physical Property Measurement System in maximum Lorentz force configuration with an electrical field criterion of 1 μV cm^{-1}. The irreversibility field H_{irr} was estimated by a J_c criterion of 100 A cm^{-2} and cross-checked for the n value of the $E(J)$ characteristics, $E \sim J^{n}$, going to 1 near H_{irr}. The orientation dependence of the critical current density, $J_c(B,\theta)$, θ being the angle between sample normal and magnetic field, was measured at 30 K and 77 K by rotating the sample in applied magnetic fields of 1 T and 5 T between 280° and 80° with steps of 2° near $B||ab$ and 5° around $B||c$. The magnetic field dependence of J_c in the maximum Lorentz force configuration was measured with linear steps of the increased magnetic field.

B7. Nuclear Magnetic Resonance toolbox

Nuclear Magnetic Resonance (NMR) measurements were recorded on a Bruker Avance II Spectrometer operating at a ^{1}H and ^{13}C frequency of 500.13 MHz and 125.77 MHz respectively and featuring a ^{1}H, ^{13}C, ^{31}P BBI-Z probe. The sample temperature was set to 298.15 K. One dimensional (1D) ^{1}H and 2D ^{1}H-^{13}C Heteronuclear Single-Quantum Correlation (HSQC), 2D ^{1}H-^{13}C Heteronuclear Multiple-Bond Correlation (HMBC), Total correlation spectroscopy (TOCSY), Correlation spectroscopy (COSY) and Nuclear Overhauser Effect Spectroscopy (NOESY) spectra were acquired using standard pulse sequences from the Bruker library.

For the quantitative 1D ^{1}H measurements, 64k data points were sampled with the spectral width set to 16 ppm and a relaxation delay of 30 s. NOESY mixing time was set to 300 ms and 2048 data points in the direct dimension for 512 data points in the indirect dimension were typically sampled, with the spectral width set to 11.5 ppm. For 2D processing, the spectra were zero filled to a 4096×2048 real data matrix. Before Fourier transformation, the 2D spectra were multiplied with a squared cosine bell function in both dimensions, the 1D spectra were multiplied with an exponential window function. Concentrations were obtained using the Digital ERETIC method.

Diffusion measurements (2D DOSY) were performed using a double stimulated echo sequence for convection compensation and with monopolar gradient pulses. Smoothed rectangle gradient pulse shapes were used throughout. The gradient strength was varied linearly from 2-95 % of the probe's maximum value (calibrated at 50.2 G cm^{-1}) in 64 steps, with the gradient pulse duration and diffusion delay optimized to ensure a final attenuation of the signal in the final increment of less than 10 % relative to the first increment. The diffusion coefficients were obtained by fitting the appropriate Stejskal-Tanner equation to the signal intensity decay.

Appendix C

Scientific dissemination

C.1. Publications in international journals

1. De Keukeleere, K.; Pollefeyt, G.; Feys, J.; De Roo, J.; **Rijckaert**, **H.**; Lommens P. and Van Driessche, I., *Chemical solution deposition of functional ceramic coatings using ink-jet printing.* Pure and Applied Chemistry, 2015. **87**(3): p. 231-238.

2. Cayado, P.; De Keukeleere K.; Garzón, A.; Perez-Mirabet, L.; Meledin, F.; De Roo, J.; Vallés, F.; Mundet B.; **Rijckaert, H**.; Pollefeyt, G.; Coll, M.; Ricart, S.; Palau, A.; Gázquez, J.; Ros, J.; Van Tendeloo, G.; Van Driessche, I.; Puig, T. and Obradors, X., *Epitaxial $YBa_2Cu_3O_{7-x}$ nanocomposite thin films from colloidal solutions.* Superconductor Science and Technology, 2015. **28**(12): p. 124007.

3. De Keukeleere, K.; Cayado, P.; Meledin, A.; Vallès, F.; De Roo, J.; **Rijckaert, H.**; Pollefeyt, G.; Bruneel, E.; Palau, A.; Coll, M.; Ricart, S.; Van Tendeloo, G.; Puig, T.; Obradors, X. and Van Driessche, I., *Superconducting $YBa_2Cu_3O_{7-\delta}$ Nanocomposites Using Preformed ZrO_2 Nanocrystals: Growth Mechanisms and Vortex Pinning Properties.* Advanced Electronic Materials, 2016. **2**(10): p. 1600161.

4. De Roo, J.; Coucke, S.; **Rijckaert, H.**; De Keukeleere, K.; Sinnaeve, D.; Hens, Z.; Martins, J. C. and Van Driessche, I., *Amino Acid-Based Stabilization of Oxide Nanocrystals in Polar Media: From Insight in Ligand Exchange to Solution ^1H NMR Probing of Short-Chained Adsorbates.* Langmuir, 2016. **32**(8): p. 1962-1970.

5. **Rijckaert, H.**; De Roo, J.; Roeleveld, K.; Pollefeyt, G.; Bennewitz, J.; Bäcker, M.; Lynen, F.; De Keukeleere, K. and Van Driessche, I., *Microwave-assisted $YBa_2Cu_3O_7$ precursors: A fast and reliable method towards chemical precursors for superconducting films.* Journal of the American Ceramic Society, 2017. **100**(6): p. 2407–2418.

6. **Rijckaert, H.**; Pollefeyt, G.; Sieger, M.; Hänisch, J.; Bennewitz, J.; De Keukeleere, K.; De Roo, J.; Hühne, R.; Bäcker, M.; Paturi, P.; Huhtinen, H.; Hemgesberg, M. and Van Driessche, I., *Optimizing Nanocomposites through Nanocrystal Surface Chemistry: Superconducting $YBa_2Cu_3O_7$ Thin Films via Low-Fluorine Metal Organic Deposition and Preformed Metal Oxide Nanocrystals.* Chemistry of Materials, 2017. **29**(14): p. 6104-6113.

7. Malmivirta, M.; **Rijckaert, H.**; Paasonen, V.; Huhtinen, H.; Hynninen, T.; Jha, R.; Awana, VPS.; Van Driessche, I.; and Paturi, P., *Enhanced flux pinning in YBCO multilayer films with BCO nanodots and segmented BZO nanorods*. Scientific Reports, 2017. **7**: 14682

C.2. Patents

- EP1515716.9 - Nanoparticles for the Use as Pinning Centers in Superconductors

C.3. First author conference contributions

Hannes Rijckaert, Jelle Pelemans, Jens Hänisch, Rain Nast, Jonathan De Roo, Jan Bennewitz, Glenn Pollefeyt, Maximilian Hemgesberg, Michael Bäcker, Katrien De Keukeleere and Isabel Van Driessche. *Ink-jet printing of low-fluorine YBCO nanocomposite thin films with preformed HfO_2 nanocrystals*. (2017, september 17-21) Applied Superconductivity, 13th European Conference. Geneva (Switzerland). Poster

Hannes Rijckaert, Jonathan De Roo, Kevin Roeleveld, Glenn Pollefeyt, Jan Bennewitz, Michael Bäcker, Frederic Lynen, Katrien De Keukeleere and Isabel Van Driessche. *Microwave-assisted $YBa_2Cu_3O_7$ precursors: a fast and reliable method towards chemical precursors for superconducting thin films*. (2017, september 17-21) Applied Superconductivity, 13th European Conference. Geneva (Switzerland). Poster

Hannes Rijckaert, Glenn Pollefeyt, Max Sieger, Hannu Huhtinen, Katrien De Keukeleere, Jens Hänisch, Ron Feenstra, Jan Bennewitz, Jonathan De Roo, Ruben Hühne, Petriina Paturi, Maximilian Hemgesberg, Michael Bäcker and Isabel Van Driessche. *Elucidating vortex pinning in nanocomposite $YBa_2Cu_3O_{7-\delta}$ thin films derived from low fluorine metal organic deposition and preformed nanocrystals*. (2016, october 24-26) Chemical Research in Flanders. Blankenberge (Belgium). Poster

Hannes Rijckaert, Jonathan De Roo, Kevin Roeleveld, Glenn Pollefeyt, Jan Bennewitz, Michael Bäcker, Frederic Lynen, Katrien De Keukeleere and Isabel Van Driessche. *Microwave-assisted $YBa_2Cu_3O_7$ precursors: a fast and reliable method towards chemical precursors for superconducting thin films*. (2016, september 11-14) Coated Conductors for Applications. Aspen, Colorado (USA). Poster

Hannes Rijckaert, Glenn Pollefeyt, Max Sieger, Hannu Huhtinen, Katrien De Keukeleere, Jens Hänisch, Ron Feenstra, Jan Bennewitz, Jonathan De Roo, Ruben Hühne, Petriina Paturi, Maximilian Hemgesberg, Michael Bäcker and Isabel Van Driessche. *Elucidating vortex pinning in nanocomposite $YBa_2Cu_3O_{7-\delta}$ thin films derived from low fluorine metal organic deposition and preformed nanocrystals*. (2016, may 2-6) E-MRS Spring meeting. Lille (France). Poster

Hannes Rijckaert, Glenn Pollefeyt, Max Sieger, Katrien De Keukeleere, Jens Hänisch, Ron Feenstra, Jan Bennewitz, Jonathan De Roo, Ruben Huehne, Michael Bäcker, Maximilian Hemgesberg and Isabel Van Driessche.

Nanocomposite $YBa_2Cu_3O_{7-\delta}$ thin films using low fluorine MOD and preformed nanocrystals. (2016, march 22-24) Belgian and French Ceramic Societies, Annual meeting. Valenciennes (France). Talk

Hannes Rijckaert, Glenn Pollefeyt, Max Sieger, Katrien De Keukeleere, Jens Hänisch, Ron Feenstra, Jan Bennewitz, Jonathan De Roo, Ruben Huehne, Michael Bäcker, Maximilian Hemgesberg and Isabel Van Driessche. *Nanocomposite $YBa_2Cu_3O_{7-\delta}$ thin films using low fluorine MOD and preformed nanocrystals*. (2016, march 16-18) 13th Chemistry conference for Young Scientists. Blankenberge (Belgium). Talk

Hannes Rijckaert, Glenn Pollefeyt, Katrien De Keukeleere, Jonathan De Roo, Ron Feenstra, Jan Bennewitz, Michael Bäcker, Maximilian Hemgesberg and Isabel Van Driessche. *Understanding growth and nucleation of nanocomposite YBa2Cu3O7-δ thin films derived from low fluorine metal organic deposition*. (2015, september 6-10) Applied Superconductivity, 12th European conference. Lille (France). Poster

Hannes Rijckaert, Katrien De Keukeleere, Jonathan De Roo, Jonas Feys and Isabel Van Driessche. *Synthesis and stabilization of ZrO_2 and HfO_2 as artificial pinning centers in YBCO superconductors*. (2014, february 27-28). Poster

C.4. Other conference contributions

Katrien De Keukeleere, Hannes Rijckaert, Jens Hänisch, Pablo Cayado, Alexander Meledin, Max Sieger, Ferran Valles, Mariona Coll, Anna Palau, Javier Diez Sierra, Pedro Lopez Dominguez, Ruben Hühne, Jonathan De Roo, Petriina Paturi, Hannu Huhtinen, Gustaaf Van Tendeloo, Teresa Puig, Xavier Obradors, Maximilian Hemgesberg, Michael Bäcker and Isabel Van Driessche. *Progress towards $YBa_2Cu_3O_{7-\delta}$ nanocomposite thin films using chemical solution deposition and preformed nanocrystals*. (2017) Applied Superconductivity, 13th European Conference.

Matthias Van Zele, Hannes Rijckaert and Klaartje De Buysser. *Synthesis method for thermochromically active VO_2 nanoparticles.* (2017) 19th International Sol-Gel Conference

Katrien De Keukeleere, Jonathan De Roo, Sofie Coucke, Hannes Rijckaert, Davy Sinnaeve, Pascal Van Der Voort, Zeger Hens, José Martins and Isabel Van Driessche. *Zirconia nanocrystals: effect of metal precursor and the importance of its surface chemistry.* (2016) Chemical Research in Flanders.

Katrien De Keukeleere, Hannes Rijckaert, Jelle Pelemans, Max Sieger, Glenn Pollefeyt, Jens Hänisch, Ron Feenstra, Jan Bennewitz, Jonathan De Roo, Ruben Hühne, Michael Bäcker, Maximilian Hemgesberg and Isabel Van Driessche. *Superconducting low-fluorine $YBa_2Cu_3O_{7-\delta}$ nanocomposites using preformed MO_2 nanocrystals (M=Zr, Hf)*. (2016) Coated Conductors for Applications.

Katrien De Keukeleere, Glenn Pollefeyt, Hannes Rijckaert, Pablo Cayado, Alexander Meledin, Jonathan De Roo, Max Sieger, Ferran Valles, Mariona Coll, Anna Palau, Ruben Huehne, Ron Feenstra, Jan Bennewitz, Michael Baecker, Maximilian Hemgesberg, Gustaaf Van Tendeloo, Xavier Obradors, Teresa Puig and Isabel Van Driessche. *Incorporation of preformed nanocrystals in $YBa_2Cu_3O_{7-x}$ thin films using chemical solution deposition*. (2016) E-MRS Spring meeting.

Jonathan De Roo, Sofie Coucke, Hannes Rijckaert, Katrien De Keukeleere, Davy Sinnaeve, Zeger Hens, José Martins and Isabel Van Driessche. *Amino acid based stabilization of oxide nanocrystals in polar media: from insight in ligand exchange to solution ^1H NMR probing of small adsorbates*. (2016) E-MRS Spring meeting.

Glenn Pollefeyt, Hannes Rijckaert, Katrien De Keukeleere, Pablo Cayado, Alexander Meledin, Jonathan De Roo, Max Sieger, Ferran Valles, Mariona Coll, Anna Palau, Jens Hänisch, Ruben Hühne, Ron Feenstra, Jan Bennewitz, Gustaaf Van Tendeloo, Teresa Puig, Xavier Obradors, Michael Bäcker, Maximilian Hemgesberg, Klaartje De Buysser and Isabel Van Driessche. *Nanocomposite $YBa_2Cu_3O_{7-\delta}$ thin films using chemical solution deposition and preformed nanocrystals*. (2016) MRS Spring meeting.

Katrien De Keukeleere, Pablo Cayado, Alexander Meledin, Jonathan De Roo, Hannes Rijckaert, Glenn Pollefeyt, Max Sieger, Ron Feenstra, Jan Bennewitz, Jens Hänisch, Ruben Hühne, Maximilian Hemgesberg, Gustaaf Van Tendeloo, Michael Bäcker, Teresa Puig, Xavier Obradors and Isabel Van Driessche. *Incorporation of preformed nanocrystals in $YBa_2Cu_3O_{7-\delta}$ coated conductors*. (2015) Applied Superconductivity, 12th European conference.

Glenn Pollefeyt, Hannes Rijckaert, Max Sieger, Katrien De Keukeleere, Jonathan De Roo, Ron Feenstra, Jan Bennewitz, Jens Hänisch, Ruben Huehne, Michael Bäcker, Maximilian Hemgesberg and Isabel Van Driessche. *Nanocomposite $YBa_2Cu_3O_{7-\delta}$ thin films using low fluorine MOD and preformed nanocrystals*. (2015) Applied Superconductivity, 12th European conference.

Katrien De Keukeleere, Jonathan De Roo, Pablo Llosa, Hannes Rijckaert, Glenn Pollefeyt, Petra Lommens, Susagna Ricart, Xavier Obradors and Isabel Van

Driessche. Synthesis and incorporation of nanosized pinning centers for $YBa_2Cu_3O_{7-x}$ superconductors. (2015) MRS spring meeting,

Katrien De Keukeleere, Glenn Pollefeyt, Jonas Feys, Jonathan De Roo, Hannes Rijckaert, Petra Lommens and Isabel Van Driessche. *Chemical solution deposition of functional ceramic coatings using ink-jet printing*. (2015) Solid State Chemistry, 11th Conference.

Katrien De Keukeleere, Jonathan De Roo, Hannes Rijckaert, Jonas Feys and Isabel Van Driessche. *Solution synthesis of metal oxide nanoparticles for ex-situ pinning in $YBa_2Cu_3O_{7-x}$ (YBCO) superconductors*. (2014) E-MRS spring meeting.